

MODELING TECHNIQUES FOR COMPOSITIONALLY GRADED MARTENSITIC STEELS

MULTISCALE MODELING TECHNIQUES PERTAINING TO COMPOSITIONALLY
GRADED MARTENSITIC STEELS

By ROBERT CICORIA, B.A.Sc, M.Eng.

A Thesis Submitted to the School of Graduate Studies in Partial Fulfillment of the Requirements for the
Degree Doctor of Philosophy

McMaster University © Copyright by Robert Cicoria, January 2016

McMaster University DOCTOR OF PHILOSOPHY (2016) Hamilton, Ontario (Materials Engineering)

TITLE: Multiscale Modeling Techniques Pertaining to Compositionally Graded Martensitic Steels

AUTHOR: Robert Cicoria, B.A.Sc. ES (University of Toronto), M.Eng. (University of Toronto)

SUPERVISOR: Professor H.S. Zurob

NUMBER OF PAGES: xi, 157

Abstract

The introduction of composition gradients into the already hierarchical structure of martensitic steel leads to difficulties in modeling that arise from events occurring in the material at different length scales. In this thesis we isolate the features that are important to describing the mechanical properties of martensite and constitutively couple them through their respective length scales. The idea of a representative volume element is rigorously explored in which the microstructure is represented through a Masing model as well as more advanced structures akin to a nanocomposite. As such, we are able to keep track of microscopic yielding and internal stress evolution at the smallest scales (nanoscale through microscale). With the use of representative volume elements, we are able to track events at the largest scale as well by freely being able to change scale. As such, macroscopic phenomenon such as: thermal fields, composition fields, macroscopic loads, and the associated macroscopic phase distributions and stress distributions are evaluated. We conclude by demonstrating the power of this modelling technique in the design and optimization of compositionally graded steel structures via virtual prototyping.

Acknowledgements

I would like to express my thanks to my supervisor Dr. Zurob for his continual encouragement, support and advice throughout this project. Most importantly, he provided a great deal of support and patience in allowing me to explore topics I found to be of interest.

Additionally, I would like to thank David Embury, Yves Bréchet, Olivier Bouaziz, Peidong Wu, Arnaud Weck, and Dieter Stolle for their discussions and insights. Reza Roumina and Jean-Phillipe Masse for providing experimental data; as well as Victoria Jarvis and Chris Butcher for experimental assistance.

Finally, I would like to thank my family for their support over the years as well as their unwavering confidence; their enthusiasm did a lot to help fan my imagination and passion for discovery.

Table of Contents

Chapter 1 – Motivations	12
1.1 Problem Definition.....	13
1.2 Multiscale Approach	14
Chapter 2 – Macro-Meso Phenomenon	15
2.1 Finite Elements	16
2.1.1 Eight-Node Linear Hexahedral Elements (Isoparametric)	16
2.1.2 Twenty-Seven Node Quadratic Hexahedral Elements (Isoparametric)	17
2.1.3 Nine-Node Quadratic Quadrilateral Elements (Isoparametric)	18
2.2 Simulation of Diffusion Equation	19
2.2.1 Boundary Condition Types	20
2.2.2 Diffusion Stage	21
2.2.3 Quench Stage	21
Heat Transfer Coefficient	21
Latent Heat of Transformation.....	22
2.2.4 Finite Element Formulation.....	23
2.2.5 Explicit Transient Analysis	23
2.2.6 Stability Considerations.....	24
2.3 Mechanics Simulation	25
2.3.1 Small Strain Formulation – Small Strain Tensor	26
2.3.2 Total Lagrange Formulation – Green-Lagrange Strain.....	27
2.3.3 Determination of Equilibrium – Principle of Virtual Work.....	28
Small Strain Finite Element Derivation.....	28
Total Lagrange Finite Element Derivation	30
2.3.4 Finite Element System Matrices.....	31
Small Strain Theory Matrices	31
Total Lagrange Formulation Matrices	34
2.3.5 Finite Element Solution Methods.....	35
2.4 Constitutive Considerations	37
2.4.1 Additive Strain Decomposition.....	38
Integration Procedure.....	39
2.4.2 Modelling the Transformation	40
Kinetics of the Martensitic Transformation	40

Martensite Start Temperature	41
Stress-Assisted Transformation.....	41
2.4.3 Calculation of Dilatational Strains	43
2.4.4 Calculation of TRIP Strains	44
TRIP Mechanisms	44
Simulation Implementation	45
2.4.5 Plasticity.....	47
2.4.6 Return Mapping Algorithms.....	48
Effective Stress Function Algorithm	50
2.4.7 Solving for Equilibrium - Summation.....	51
2.5 Volumetric Locking Concerns.....	53
2.6 Numerical Integral Evaluation.....	54
2.6.1 Quadrature Rule Applied to Finite Element Integrals	55
2.6.2 Quadrature Rule Applied on a Finite Element Domain	57
2.7 Experimental Stress Analysis.....	58
2.7.1 Diffraction Physics and Experimental Setup.....	58
2.7.2 $\text{Sin}^2\Psi$ Method	59
2.7.2 Experimental Conditions	60
Material Assumptions	60
Plane Selection.....	60
2.8 Diffusion Simulations	61
2.8.1 Diffusion Processing Verification.....	61
2.9 Process Simulations	62
2.9.1 Comparison of Quench Rates.....	63
2.9.2 Quenching a Homogenous Steel Plate	64
2.9.3 Quenching Decarburized Steel Plates with Fixed Decarburization Time	64
2.9.4 Quenching Decarburized Steel Plates with Fixed Distribution Geometry	64
2.9.5 Quenching a Decarburized High Carbon Steel Plate.....	64
2.9.6 Quenching a Carburized Steel Plate	65
2.9.7 Quenching Decarburized Cylinders of Various Diameter and Surface Composition	65
2.9.8 Quenching a Decarburized Hollow Cylinder	65
2.9.9 Observations	75
2.10 Conclusions	76

Chapter 3 – Microstructure-Based Constitutive Modelling.....	77
3.1 Mechanical Behaviour of Martensite – A First Look.....	78
3.1.1 Uniaxial Mechanical Behaviour	78
Masing’s Hypothesis	79
3.1.2 Multiaxial Mechanical behaviour	81
3.1.3 Microstructural Examination.....	82
3.2 Overview - Modelling Techniques.....	84
3.2.1 Conventional Mixed Hardening.....	85
3.2.2 Work Hardening Field	85
3.2.3 Multi-Surface Plasticity	86
3.2.4 Direct Masing Model (Continuous Composite Model)	87
3.2.5 Micromechanical Model	89
3.3 Global Fitting Algorithms	90
3.3.1 No Free Lunch Theorem.....	91
3.3.2 Evolution-based Search Algorithm	92
3.3.3 Parallel Processing	93
Single Instruction Multiple Data (SIMD).....	93
3.4 Plasticity Surface Based Models.....	95
3.4.1 Strain Integration Algorithms.....	96
3.4.2 Mixed Hardening Plasticity.....	97
3.4.3 Work Hardening Field	99
3.4.5 Multi Surface Plasticity.....	101
3.5 Direct Masing Model.....	104
3.5.1 Building a Continuous Composite Model	105
Continuous Composite in One Dimensional Finite Elements	105
Masing Solid in Three Dimensional Finite Elements.....	107
3.5.2 Masing Model Performance.....	108
3.5.3 Anisotropic Behaviour and Tempering Behaviour.....	110
Modelling Anisotropy with Masing	112
3.6 Martensitic Micro-Cell Model	124
3.6.1 Macro-Meso Connection	125
Evolution of a Masing Type Macro-Meso Connection	126
3.6.2 Spatially Resolved Masing Assembly and Fitting Procedure	126

3.6.3 Micromechanical RVE Assembly and Fitting Procedure	127
Packet Tessellation.....	127
Block Assembly	128
Constitutive Applicability	128
3.6.4 Solving for Equilibrium in the Microcell	129
3.6.5 Fit to Experimental Data	130
3.7 Model Comparisons and Conclusions	132
3.8 Tiered Modeling Techniques.....	133
3.8.1 Representative Volume Element Cost Scaling.....	134
3.8.2 Tiered Model Costs	135
3.8.3 Computational Feasibility	137
Chapter 4 – Multi-Scale Coupled Simulations	138
4.1 Constitutive Scaling.....	139
4.1.1 Homologous Scaling of the Stress/Strain curve.....	139
4.1.2 Homologous Scaling of the Constitutive Model	141
4.2 Case Studies	142
4.2.1 Bending Test of an Asymmetrically Graded Beam	142
4.2.2 Bauschinger Testing of a Decarburized Plate	142
4.2.3 Examination of Presented Case Studies	147
4.3 Closing Remarks	148
References	149
Appendix – Material Properties Reference.....	155

Table of Figures

FIGURE 1.1 – PROCESS CONTROLS THAT GOVERN THE FINAL BEHAVIOUR OF A MARTENSITIC STEEL PART.	13
FIGURE 1.2 – IMPORTANT FACTORS THAT GOVERN THE MECHANICAL PROPERTIES OF COMPOSITIONALLY GRADED MARTENSITE, ALONG WITH THEIR ASSOCIATED LENGTH SCALES.	14
FIGURE 2.3 – ISOPARAMETRIC FORMULATION FOR 8-NODED LINEAR BRICK ELEMENTS.....	16
FIGURE 2.4 – ISOPARAMETRIC FORMULATION FOR 27-NODE QUADRATIC BRICK ELEMENTS	17
FIGURE 2.5 – ISOPARAMETRIC FORMULATION FOR THE 9-NODE 2D AXISYMMETRIC ELEMENT.. ..	18
FIGURE 2.6 – DEPICTION OF FIELD VARIABLES SOLVED VIA FINITE ELEMENT DISCRETIZATION OF THE SPATIAL DOMAIN.....	19
FIGURE 2.7 – 2D FEA SCHEMATIC DEPICTING THE DIFFERENCES BETWEEN A DIRICHLET AND NEUMANN BOUNDARY	20
FIGURE 2.8 – HEAT TRANSFER COEFFICIENT (H) FOR THE QUENCHING OF STEEL IN OIL AND WATER.....	22
FIGURE 2.9 – FORM OF THE QUASI-STATIC FINITE ELEMENT EQUATION THAT IS SOLVED OVER THE ENTIRE SPATIAL DOMAIN .	25
FIGURE 2.10 – STRAIN IN A ONE DIMENSIONAL ROD USING THE MATERIALS SCIENTIST AND SMALL STRAIN DEFINITIONS.	26
FIGURE 2.11 – EVOLUTION OF THE GREEN-LAGRANGE STRAIN THROUGH A UNIAXIAL STRETCH AND ROTATION.....	27
FIGURE 2.12 – FORMULATION OF THE JACOBIAN MATRICES.....	32
FIGURE 2.13 – DEFINITION OF THE STRAIN-DISPLACEMENT MATRIX [B]	32
FIGURE 2.14 – FORMATION OF THE INTEGRAND FOR THE ELEMENT STIFFNESS MATRIX.....	33
FIGURE 2.15 – STRAIN-DISPLACEMENT MATRIX FOR THE TOTAL LAGRANGE FORMULATION.	34
FIGURE 2.16 – MATRICES REQUIRED FOR THE CALCULATION OF THE NON-LINEAR COMPONENT OF THE STIFFNESS MATRIX....	35
FIGURE 2.17 – STIFFNESS MATRIX REFORMULATION POINTS FOR DIFFERENT SOLUTION METHODOLOGIES	36
FIGURE 2.18 – DEPICTION OF HOW THE MECHANICAL SOLUTION VALUES NEED TO BE EVALUATED AT EACH TIMESTEP.	39
FIGURE 2.19 – CCT CURVE DEPICTING THE TIME INDEPENDENT NATURE OF THE MARTENSITIC TRANSFORMATION.....	40
FIGURE 2.20 – PHENOMENOLOGICAL DEPICTION OF THE MARTENSITIC TRANSFORMATION.	41
FIGURE 2.21 – SHIFT IN MS VERSUS VARIOUS LOADING SCENARIOS.....	42
FIGURE 2.22 – THE CALCULATION OF THE MOST FAVORABLE ORIENTATION FOR THE FORMATION OF MARTENSITE.....	42
FIGURE 2.23 – DERIVATION OF THE VOLUMETRIC STRAIN.....	43
FIGURE 2.24 – DEPICTION OF RELATIVE CONTRIBUTIONS TO THE TOTAL OBSERVED TRIP STRAIN UNDER DIFFERENT LOAD LEVELS AS A FUNCTION OF TRANSFORMATION COORDINATE.	45
FIGURE 2.25 – TRIP STRAIN AS THE MARTENSITIC TRANSFORMATION PROGRESSES FOR VARYING LOAD LEVELS.....	46
FIGURE 2.26 – DEPICTION OF THE RADIAL RETURN MAPPING ALGORITHM ON THE DEVIATORIC STRESS COMPONENTS.	49
FIGURE 2.27 – EFFECTIVE STRESS FUNCTION INPUTS AND OUTPUTS.	50
FIGURE 2.28 – OVERVIEW OF THE PROCESS FOR SIMULATING THE QUENCHING OF GRADED STEELS.. ..	52
FIGURE 2.29 – SCHEMATIC OF A PRESSURE BAND PLOT.	53
FIGURE 2.30 – EVALUATION OF AN INTEGRAL VIA SAMPLING A FINITE NUMBER OF POINTS	54
FIGURE 2.31 – ORDER OF THE VOLUME INTEGRAL OVER THE NATURAL COORDINATE SPACE	55
FIGURE 2.32 - POSITION OF GAUSS INTEGRATION POINTS WITHIN THE NATURAL ELEMENT SPACE.....	57
FIGURE 2.33 – MANIFESTATION OF A 3X3X3 INTEGRATION RULE IN A CUBOIDAL ELEMENT	57
FIGURE 2.34 – EXPERIMENTAL SETUP OF A SURFACE X-RAY DIFFRACTION EXPERIMENT.....	58
FIGURE 2.35 – STRAIN MEASUREMENT AS A FUNCTION OF $\sin^2\psi$	59
FIGURE 2.36 – TETRAGONALITY OF IRON MARTENSITE AS A FUNCTION OF CARBON CONTENT.. ..	60
FIGURE 2.37 – DEPICTION OF CARBON COMPOSITION GRADING EXPERIMENT.	61
FIGURE 2.38 – SIMULATION OF THE QUENCH RATES OF OIL AND WATER THROUGH A 15MM PLATE OF STEEL.....	63
FIGURE 2.39 – RESIDUAL STRESSES IN A HOMOGENOUS WATER -QUENCHED PLATE	66
FIGURE 2.40 – RESIDUAL STRESSES IN A HOMOGENOUS OIL -QUENCHED PLATE	67
FIGURE 2.41 – DECARBURIZED 300M ALLOY OF VARYING PLATE THICKNESS (WATER QUENCHED).....	68
FIGURE 2.42 – DECARBURIZED 300M ALLOY OF VARYING PLATE THICKNESS (OIL QUENCHED)	69
FIGURE 2.43 – PROPORTIONALLY DECARBURIZED 300M ALLOY OF VARYING PLATE THICKNESS (WATER QUENCHED).....	70
FIGURE 2.44 – THIN PLATE OF HIGH CARBON STEEL THAT HAS BEEN DECARBURIZED (WATER QUENCHED).....	71
FIGURE 2.45 – CARBURIZED 3.2MM PLATE (WATER QUENCH)	71
FIGURE 2.46 – THIN RODS (7MM) THAT HAVE BEEN DECARBURIZED TO VARIOUS SURFACE CONCENTRATIONS (WATER).....	72
FIGURE 2.47 – THIN RODS (10MM) THAT HAVE BEEN DECARBURIZED TO VARIOUS SURFACE CONCENTRATIONS (WATER).....	73
FIGURE 2.48 – DECARBURIZED HOLLOW CYLINDERS WITH DIFFERENT SURFACES MASKED (WATER QUENCHED)	74
FIGURE 3.49 – MONOTONIC DATA FROM 41XX STEEL SERIES. DATA WITH A LIGHT 150°C TEMPER IS SHOWN.....	78
FIGURE 3.50 – BAUSCHINGER TEST CONDUCTED ON US1080 0.24WT.%C STEEL (AS OIL-QUENCHED).	79

FIGURE 3.51 – MASING’S HYPOTHESIS TESTED ON BAUSCHINGER DATA FOR 0.24 WT.% CARBON MARTENSITIC STEEL	80
FIGURE 3.52 – HARDENING RATES FOR AS-QUENCHED USIBOR 0.24WT.%C STEEL SAMPLES AT DIFFERENT ORIENTATION RELATIVE TO A DEFINED PRESTRAIN DIRECTION	81
FIGURE 3.53 – DEPICTION OF LATH MARTENSITE WITH THE VARYING LENGTH SCALES OF THE MICROSTRUCTURE.....	82
FIGURE 3.54 – NANO-HARDNESS MAP OF LATH MARTENSITE.....	83
FIGURE 3.55 – CRACKING OF PLATES IN ACICULAR MARTENSITE.....	83
FIGURE 3.56 – DEPICTION OF VONMISES PLASTICITY WITH BOTH ISOTROPIC AND KINEMATIC HARDENING COMPONENTS.	85
FIGURE 3.57 – DEPICTION OF A YIELD SURFACE THAT IS TRANSLATING IN A FIELD OF WORK HARDENING VALUES.	86
FIGURE 3.58 – PLASTIC FLOW OCCURRING IN A MULTI-SURFACE PLASTICITY MODEL	87
FIGURE 3.59 – ONE DIMENSIONAL CONTINUOUS COMPOSITE WITH SUBELEMENTS THAT HAVE VARYING YIELD STRENGTHS... ..	88
FIGURE 3.60 – DEPICTION OF CONTINUOUS YIELDING IN A ONE-DIMENSIONAL MASING SOLID	88
FIGURE 3.61 – DEPICTION OF BLOCK SUBELEMENTS DISTRIBUTED INTO THE PACKET SUBSTRUCTURE.	89
FIGURE 3.62 – SCHEMATIC DEPICTION OF NO FREE LUNCH THEOREM FOR TWO ALGORITHMS.....	91
FIGURE 3.63 – GENE STRUCTURE OF A MASING MODEL PARAMETER SET	92
FIGURE 3.64 – ILLUSTRATION OF GENE RECOMBINATION IN CONSTRUCTING THE DESCENDANT POPULATION.	93
FIGURE 3.65 – DEPICTION OF DATA ORGANIZATION UNDER A SIMD PROCESSING PARADIGM	94
FIGURE 3.66 – IMPLICIT RETURN MAPPING PERFORMED ON MULTIPLE PLASTICITY SURFACES.....	95
FIGURE 3.67 – ALGORITHMIC IMPLEMENTATION OF A GENERALIZED RETURN MAPPING PROCEDURE.....	96
FIGURE 3.68 – BAUSCHINGER TEST FOR 0.24WT.%C MARTENSITIC STEEL.....	97
FIGURE 3.69 – SIMULTANEOUS MIXED HARDENING FIT TO USIBOR BAUSCHINGER DATA USING A VOCE HARDENING LAW.	98
FIGURE 3.70 – BAUSCHINGER PORTION OF THE FIT TO USIBOR DATA FOR THE WORK HARDENING FIELD MODEL.	99
FIGURE 3.71 – MULTIAXIAL PORTION OF THE FIT TO USIBOR DATA FOR THE WORK HARDENING FIELD MODEL.....	100
FIGURE 3.72 – A DEPICTION OF HOW A MULTI-SURFACE PLASTICITY MODEL CORRESPONDS TO THE EXPERIMENTALLY MEASURED WORK HARDENING RATES OF PRE-STRAINED MARTENSITIC STEEL (0.24WT.%C).....	101
FIGURE 3.73 – BAUSCHINGER PORTION OF SIMULTANEOUS FIT TO MULTISURFACE MODEL (USIBOR).....	102
FIGURE 3.74 – MULTIAXIAL PORTION OF SIMULTANEOUS FIT TO MULTISURFACE MODEL (USIBOR).....	103
FIGURE 3.75 – EXAMPLE ILLUSTRATING THE FORMATION OF RESIDUAL STRESSES IN A ONE DIMENSIONAL MASING SOLID. ...	105
FIGURE 3.76 – PHILOSOPHY OF A ONE-DIMENSIONAL MASING ELEMENT	106
FIGURE 3.77 – SUPERIMPOSED SUBELEMENTS DEFINING A THREE DIMENSIONAL MASING SUPERELEMENT.....	107
FIGURE 3.78 – BAUSCHINGER PORTION OF SIMULTANEOUS FIT TO THE DIRECT MASING MODEL (USIBOR).....	108
FIGURE 3.79 – MULTIAXIAL PORTION OF SIMULTANEOUS FIT TO THE DIRECT MASING MODEL (USIBOR).....	109
FIGURE 3.80 – TENSILE TESTS AT 0°, 45°, AND 90° TO THE ROLL DIRECTION FOR AS-QUENCHED USIBOR (0.24WT.%C).....	110
FIGURE 3.81 – DEPICTION OF HOW INTERNAL STRESSES CAN CAUSE FORWARD/REVERSE LOADING ANISOTROPY	111
FIGURE 3.82 – COMPARISON OF TENSION AND COMPRESSION LOADING CURVES FOR USIBOR 0.24WT.% CARBON FOR DIFFERENT DEGREES OF TEMPERING	111
FIGURE 3.83 – SUMMARY OF FITTING METHOD USED TO MODEL ANISOTROPY IN USIBOR 0.24WT.%C STEEL.	112
FIGURE 3.84 – AS-QUENCHED – 1% BAUSCHINGER TEST – USIBOR 0.24 WT.%C	113
FIGURE 3.85 – AS-QUENCHED – 2% BAUSCHINGER TEST – USIBOR 0.24 WT.%C	114
FIGURE 3.86 – AS-QUENCHED – 2% COMPRESSION TEST – USIBOR 0.24 WT.%C.....	115
FIGURE 3.87 – 150°C TEMPER - 1 HOUR – 1% BAUSCHINGER TEST – USIBOR 0.24 WT.%C.....	116
FIGURE 3.88 – 150°C TEMPER - 1 HOUR – 2% BAUSCHINGER TEST – USIBOR 0.24 WT.%C.....	117
FIGURE 3.89 – 150°C TEMPER - 1 HOUR – 2% COMPRESSION TEST – USIBOR 0.24 WT.%C	118
FIGURE 3.90 – 300°C TEMPER - 1 HOUR – 1% BAUSCHINGER TEST – USIBOR 0.24 WT.%C.....	119
FIGURE 3.91 – 300°C TEMPER - 1 HOUR – 2% BAUSCHINGER TEST – USIBOR 0.24 WT.%C.....	120
FIGURE 3.92 – 300°C TEMPER - 1 HOUR – 2% COMPRESSION TEST – USIBOR 0.24 WT.%C	121
FIGURE 3.93 – DISTRIBUTIONS OF VONMISES STRESSES AND YIELD STRENGTHS FOR MASING SUBELEMENTS FITTED TO EXPERIMENTAL DATA OF VARIOUS TEMPER CONDITIONS.	122
FIGURE 3.94 – DEPICTION OF THE MACRO-MESO CONNECTION PARADIGM	125
FIGURE 3.95 – REPRESENTATIVE VOLUME ELEMENTS.	126
FIGURE 3.96 – VERONOI TESSELLATION USING RANDOM SEEDS BEFORE AND AFTER AGGLOMERATION.....	127
FIGURE 3.97 – PROCEDURALLY GENERATED BLOCK STRUCTURE OF A SINGLE MARTENSITE PACKET.....	128
FIGURE 3.98 – DEPICTION OF INTERNAL FORCES IN A PERIODIC REPRESENTATIVE VOLUME ELEMENT.....	129
FIGURE 3.99 – FITS OF VARIOUS REPRESENTATIVE VOLUME ELEMENTS TO THE 0.24WT.% USIBOR DATA	131
FIGURE 3.100 – PERFORMANCE EVALUATION OF MODELS SUMMARIZED IN TABLE 3.6.	137

FIGURE 4.101 – COMPARISON OF THE YIELD STRENGTHS AND ULTIMATE TENSILE STRENGTHS OF LITERATURE 43XX SERIES STEEL COMPARED TO THOSE OBTAINED FROM HOMOLOGOUS SCALING OF USIBOR 0.24WT.%	139
FIGURE 4.102 – HOMOLOGOUS STRESS/STRAIN CURVES TO USIBOR 0.24WT.% C.....	140
FIGURE 4.103 – SCALING PARAMETER AS A FUNCTION OF CARBON CONTENT WITH LINEAR TREND DEPICTED.....	140
FIGURE 4.104 – HOMOLOGOUS SCALING OF A MASING DISTRIBUTION OF ELEMENT STRENGTHS.....	141
FIGURE 4.105 – FORCE/DEFLECTION PLOT OF AN ASYMMETRICALLY CARBURIZED BEAM.	143
FIGURE 4.106 – FORCE/DEFLECTION PLOT OF AN ASYMMETRICALLY DECARBURIZED BEAM.....	144
FIGURE 4.107 – BAUSCHINGER TEST OF A DECARBURIZED PLATE THAT IS DECARBURIZED/QUENCHED FROM TWO SIDES.	145
FIGURE 4.108 – BAUSCHINGER TEST OF A DECARBURIZED ROD THAT IS DECARBURIZED/QUENCHED FROM FOUR SIDES.	146

Chapter 1 – Motivations

Scientific inquiry in the 20th century was largely defined by large, insulated leaps in a number of scientific fields. Often, scientists and engineers would be exceptionally trained in a single scientific field and that would be sufficient for the development of scientific and technological gains; however, the story of 21st century science is taking on a different narrative. In order for progress to be made, conventional barriers between fields are being broken down. For example, with the development of nanotechnology, the barriers between chemistry, biology, and physics are no longer clearly defined. As such, this thesis is assaulting one such barrier; namely, the barrier between materials science, mechanical engineering, and computational science. In order to engineer the most truly high performing structures, knowledge of all these fields is required. The philosophy behind this assertion is the idea that materials science and mechanical engineering are really addressing the same issues, but on different length scales. In order for a structure to be optimized, all length scales must be addressed. The incorporation of the computational science component is imperative for the optimization itself. Over the last several decades, many computational techniques have been developed both for performing “thought experiments” on materials at different length scales and performing global optimizations of metrics in a multivariable space. With a judicious selection of techniques appropriate to the most critical events occurring at different length scales, one can fully simulate the behaviour of the structure to an arbitrarily high level of accuracy corresponding to the available level of computational power. If one were to combine this simulation power with global optimization techniques; one can effectively perform “perfect engineering” bounded by only the computational power available and quality of physical models that can be implemented.

1.1 Problem Definition

Martensitic steel poses an interesting challenge for engineers. It is a family of materials that have flow strengths amongst the highest possible for steels; however, it is quite easy for this material to exceed its fracture strength during loading if even moderately alloyed with carbon. For this reason, this material is often engineered to extract the highest possible strength while still maintaining a reasonable amount of ductility. This is accomplished with very careful alloying and judicious selection of tempering treatments. Historically, this process of optimization has been conducted empirically with meticulous experimental work. Such work has resulted in high performance martensitic alloys such as 300M, the 43xx series, and Usibor. These alloys are homogenous in composition and have predictable properties independent of application (provided they are processed within specification); hence their use in a wide variety of industries. Data sheets for these materials are provided in the Appendix due to their extensive use in this research.

With the advent of materials that have non-homogenous composition, we are faced with the problem of optimizing the composition field to produce the most favorable material properties. This problem is complicated by the fact that the resultant material is not purely just the sum of its parts; but rather, significant nonlinear effects take place to define the behaviour. These nontrivial effects manifest from sources such as macroscopic quench-induced stresses (Ruud 2002), composition gradient effects on fracture behaviour (Kolednik 2000); and constrained deformation between regions of different strengths (Masing 1923). These effects all combine to produce a material that is ultimately anisotropic mechanically with properties that vary from feature inputs such as: part geometry, alloying composition gradients, and the quenching procedure (in the case of martensitic steel).

Clearly, it is not feasible to optimize every possible component part that needs to be designed through iterative empirical means. The parameter space is simply too large with the possibility of varying: the part geometry, diffusion treatment (composition field), quench treatment, and even tempering process. The work of this thesis promotes the idea of virtual prototyping; that is, we are attempting to capture the important physical processes that occur in such a material with well-placed models that generate a suitable material description. With these models in place, we should be able to map a parameter configuration consisting of part geometry, diffusion treatment, quench process, and tempering process to obtain an output of expected mechanical behaviour. This would allow engineers to design parts computationally that are well suited to their demands. The problem statement is illustrated in Figure 1.1 for martensitic steel.

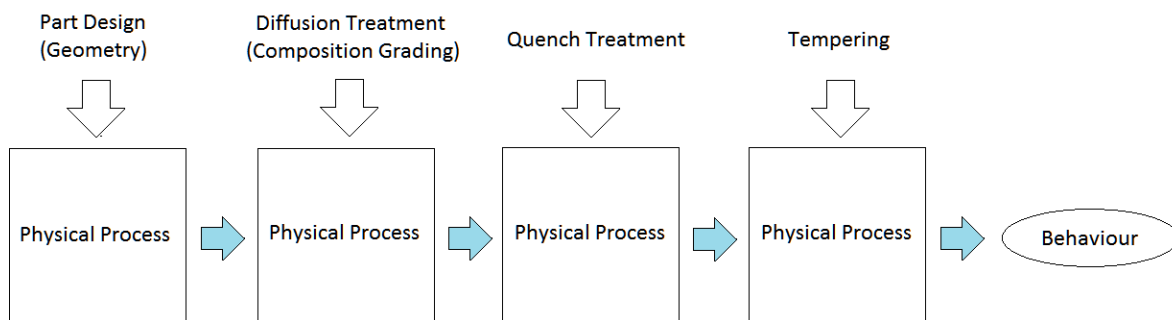


Figure 1.1 - A diagram depicting all the process controls that govern the final behaviour of a martensitic steel part.

1.2 Multiscale Approach

While we have defined the problem, we have not yet discussed the manner in which we are to tackle it. When examining martensite, we see that martensite is intrinsically a tiered material. Lath martensite in particular has a structure that is defined from the micron scale (prior austenite), all the way down to the nanometer scale (laths) (Krauss 1999). If we compound the fact that a compositionally graded material has a composition gradient that varies on the millimeter scale and larger, it is clear that any material description will have to capture important phenomena that occur at different length scales. In this thesis we take a multitier approach to capturing such phenomena. Specifically, we properly couple models that have domains on different length scales to achieve a full material description. Figure 1.2 shows the important qualities that should exist in the overall model, along with the associated length scale each pertains to.

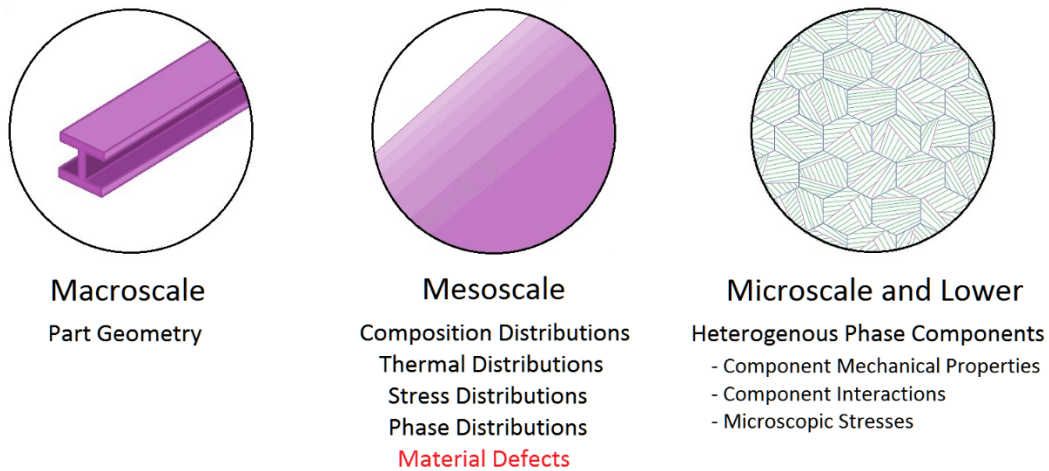
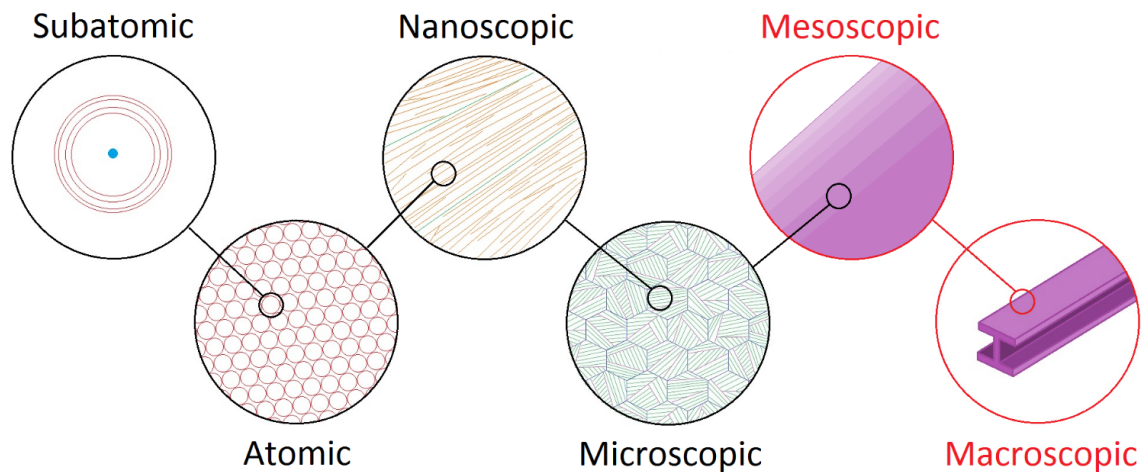


Figure 1.2 - Important factors that govern the mechanical properties of compositionally graded martensite, along with their associated length scales. Material defects tend to dictate fracture behaviour and as such, are not explicitly dealt with here.

In essence, each of these features must be modeled to a degree that gives respect to their relevance in the overall material properties. For instance, a simple polycrystalline metal may not need to explicitly keep track of microstructural phenomenon such as the deformation and stresses of each component crystal. In this case, such features can be homogenized into an isotropic elasticity model or plasticity model and real life mechanical behaviour can still be well described. As we will see in the coming sections, the degree to which we need detail in modelling our martensitic material depends upon how sensitive mechanical properties are to generalized small scale homogenizing assumptions. The degree to which we can get away with simplicity is highly context dependent and as such, we use different models for the different phases of the material processing procedure (Figure 1.1) The next section of this thesis deals with those processes that can be well described via the simplest models requiring the least amount of detail at low scales. In the following sections, we add upon the complexity until an adequate material description is obtained.



Chapter 2 – Macro-Meso Phenomenon

Our quest to understand the behaviour of martensite is one that we must undertake at various length scales in order for us to achieve a competent and computationally feasible material description that is applicable to the design and simulation of large parts. It was mentioned earlier that the processing history of the martensitic steel part has a large impact on its room temperature service behaviour. In this chapter, we concern ourselves with those phases of the processing history that are easily describable without looking too closely at the microstructure of these steels. In essence, we want to apply models that are built upon computationally cheap, homogenized microstructural descriptions to any process that can be well explained in such a manner. More specifically, we wish to apply homogenization ideas such as: isotropic elasticity, J2-plasticity (vonMises plasticity), continuum diffusion, mixing laws, and far field (average) stresses to any process we are able. Luckily, the manufacturing processing steps, diffusion and quenching, can be modelled in such a manner; this is because the composition/thermal gradients exist on a length scale large enough for us to rely on bulk diffusion coefficients. Additionally, in the case of quenching, the volume change from the phase transformation is so small, and the residual quenching stresses so far reaching, that we can use simple mechanical models for the elasticity and plasticity. Conversely, we cannot model room temperature loading in such a manner since the plastic strains are large. In order to accomplish that task, we must build constitutive models that look to the microstructure for insight; such a feat will be tackled in the next chapter.

In this chapter, we resolve ourselves to build a strong finite element simulator for modeling both the diffusion and quenching stages of the part processing. This is done with the explicit goal of obtaining the unique macroscopic-scale residual stresses that arise from quenching the geometry. At this point, we do not concern ourselves with the stresses that arise at the nano/micro scale from the phase transformation. Such stresses will be dealt with in the next chapter where the microstructure is considered.

2.1 Finite Elements

The Finite Element Method makes use of objects called elements to discretize the domain. These elements are designed with interpolation functions which will interpolate nodal quantities throughout the domain of the element. With an assemblage of these elements, the entire domain is described via nodal quantities alone, using interpolation “shape” functions applicable to each region (element). In both our diffusion and mechanics simulations, we make use of 3D continuum brick elements and 2D quadrilateral axisymmetric elements to discretize the domain. The formulation of these elements is something that is well established in the finite element literature. For our purposes, we will use isoparametric finite elements exclusively; that is, the geometry is interpolated via the same interpolation functions as the primary solution quantities. In each solution procedure, the primary nodal quantities are mass content, temperature, and displacements. Additional quantities that are computed in the solution are inferred from these basic quantities. In formulating the elements, most descriptions make use of a natural element configuration that allows us to easily set up an algorithm for the evaluation of the integrals required for the finite element calculations. The specifics of these formulations are discussed in detail next.

2.1.1 Eight-Node Linear Hexahedral Elements (Isoparametric)

The linear brick element is the simplest type of 3D brick. As the name implies, these elements make use of 3D-linear interpolation functions for the description of both element geometry and property fields; these properties can be temperature, nodal displacements, or carbon content depending on which type of simulation one is performing. These elements are very cheap and simple to implement, however, they suffer from reduced accuracy by virtue of their linear interpolation functions. From the literature, when used for mechanics simulations, these elements provide good predictions for displacement, however stress predictions are not great (Bathe 2006); additionally, they are more prone to volumetric locking¹ than higher order elements. Figure 2.3 below depicts the shape functions for this element as well as the interpolation procedure.

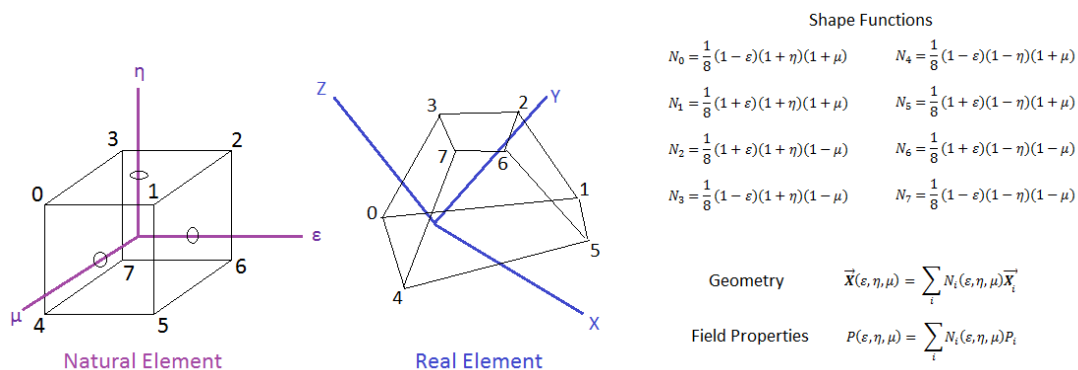


Figure 2.3 – Isoparametric Formulation for 8-Noded Linear Brick Elements. The natural and true configurations for the element are depicted, as well as their respective coordinate systems. Note that the interpolation functions for the geometry and field properties are the same.

¹ Volumetric locking is an increase in stiffness arising from artificial geometric constraints imposed by the interpolation functions. This will be addressed in detail in Section 2.5.

An important aspect of the finite element formulation depicted in this figure is the mapping of the finite element from a natural cuboidal configuration with its own coordinate system to the real element; the natural cube in this system spans from -1 to 1 in each dimension. In the isoparametric formulation, all quantities, including geometry, are mapped from this configuration; by doing this, we can easily carry out the integrals required for the FEA problem formulations by numerically integrating in the natural configuration and then projecting to the real coordinate frame. The numerical integration procedure is discussed in detail in Section 2.6.

2.1.2 Twenty-Seven Node Quadratic Hexahedral Elements (Isoparametric)

The 27-node quadratic brick element is of the Lagrangian family of elements; named as such because it derives its shape functions from Lagrangian interpolation. Although these elements are far more expensive than their linear counterparts, the quadratic interpolation functions allow for greatly enhanced accuracy. Figure 2.4 below shows how these elements are formulated. As can be seen, center nodes are required for the interpolation functions. These elements perform very well with good predictions for nodal quantities and stresses in mechanical analysis; the quadratic displacement field allows for linear variations in stress throughout.

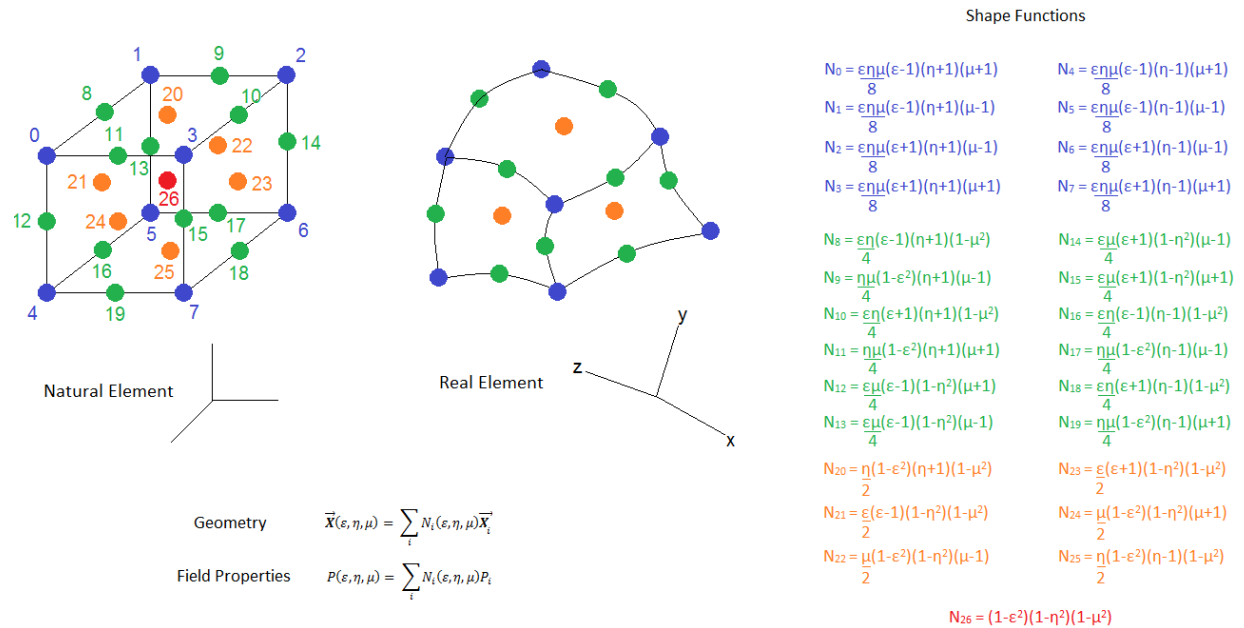


Figure 2.4 - Isoparametric Formulation for 27-Node Quadratic Brick Elements. Note that the quadratic interpolation of the geometry allows for curved elements.

The 27-node quadratic brick element contains 81-coupled degrees of freedom when used for displacement interpolation. As such, this large number of degrees of freedom leads to a larger global stiffness bandwidth and hence much more expensive solution both in memory, and in computational time. When used in an explicit integration scheme that does not have a stiffness matrix², the stable time

² Stiffness matrix refers to the primary solution matrix of the simulation in question. It only truly represents “stiffness” in a mechanics simulation.

step constraint is much more restrictive (Bathe 1986) as compared to a linear element of similar size. Additionally, this element requires more integration points than its linear counterpart in order to achieve convergence; further increasing computational cost. In all, owing to its requirements, this element is well suited for nonlinear analysis (ie. quenching simulations) where an increased number of integration points is desirable and the increased costs are justified. These elements are used whenever possible in this thesis.

2.1.3 Nine-Node Quadratic Quadrilateral Elements (Isoparametric)

There are many situations in which axisymmetry allows us to make use of two-dimensional axisymmetric elements. These elements significantly reduce computational costs over 3D elements, so they should be used whenever possible. As can be seen in Figure 2.5, this type of element is effectively a two dimensional analogue of the 27-node 3D brick element. This 2D element is rotated about an axis of revolution to create an effective 3D element. Due to its axisymmetric assumption, both the geometry and loading³ of the part must be axisymmetric for this type of simulation to be applicable; this makes this element well suited to diffusion and quench simulations of cylinders and rings due to axisymmetric thermal, diffusive, and mechanical loading.

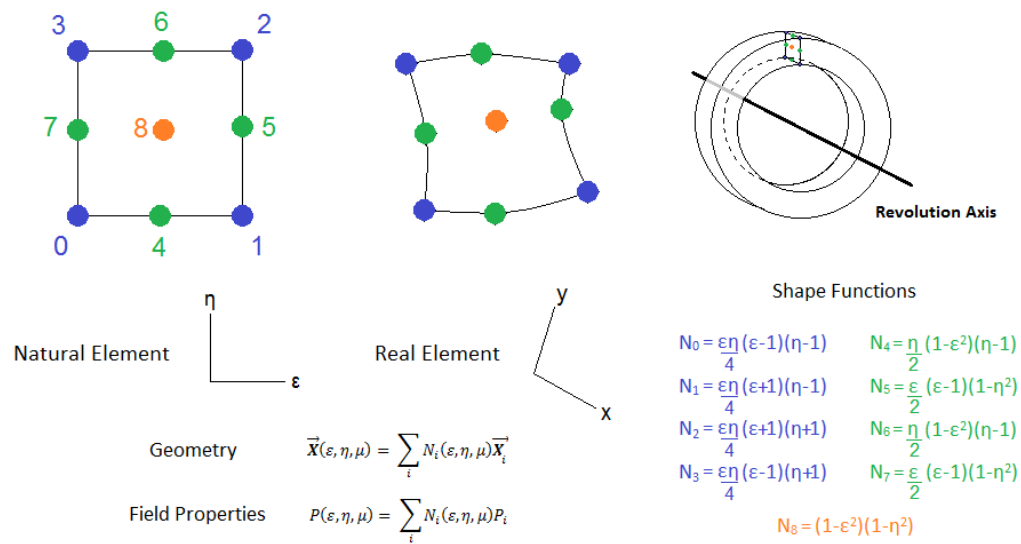


Figure 2.5 – Isoparametric formulation for the 9-Node 2D Axisymmetric Element. This element has quadratic interpolation functions in a two dimensional plane that is rotated about an axis of revolution to define an axisymmetric volume. As such, nodal points are more accurately described as nodal rings.

Simplifying the problem to two dimensions has the benefit of reducing the degrees of freedom, system bandwidth, number of integration points, and the dimensionality of the governing equations; as such, problems that are computationally unfeasible with conventional 3D elements can be done very easily using these elements.

³ Loading refers to the boundary conditions of the simulation in question. For thermal and diffusion simulation it refers to flux boundary conditions, whereas in mechanics simulations it refers to actual loads.

2.2 Simulation of Diffusion Equation

The diffusion equation plays a large part in the processing simulation of our martensitic steels. At the macroscopic level, the gas carburizing/decarburizing steps are governed by Fick's law, and the heat transfer during quenching is governed by the heat equation. Both laws have the exact same mathematical form (parabolic differential equation) and thus use the same solution method. Similar to the mechanics problem, we have opted for a finite element solution to these equations. Instead of solving for displacements primarily, as in the mechanics problem, we are solving for mass concentrations and temperatures directly at the nodal points. The form of the equations we will be solving for are depicted below in Figure 2.6.

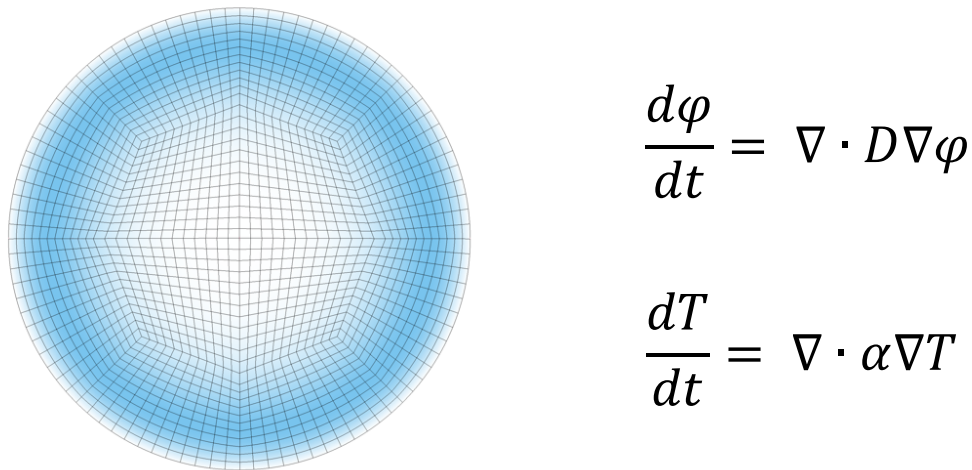


Figure 2.6 – Depiction of field variables solved via finite element discretization of the spatial domain. For our purposes, the carbon distribution (Φ) and temperature distribution (T) will be solved via their respective parabolic descriptions (depicted right). (D is the mass diffusion coefficient and α is the thermal diffusivity).

These problems will be solved dynamically, that is, we are after the transient solution as opposed to the steady state solution. For this reason, we need to discretize the time domain via the finite difference method. Additionally, we will opt for an explicit solution technique. Explicit techniques are ideal for highly nonlinear problems owing to their strict time step upper bound (Bathe 1986). This makes this paradigm ideal for both the diffusion phase and quenching simulations because of the rapidly changing conditions. For instance, in the diffusion simulation, the diffusion coefficient for carbon in iron will have a concentration dependence and thus change with time. In the case of quenching, all pertinent variables: heat capacity, thermal conductivity, and density all have dependencies on phase and temperature which are changing as the solution progresses. For these reasons, the small timestep demanded for an explicit solution technique is required anyway.

In this section, we will show how the specifics of our problem fit into this solution paradigm. In particular, we take a look at what aspects of a quench and diffusion simulation are required in order to assemble a good model. Afterwards, we will examine how the finite element solution to the diffusion equation is assembled.

2.2.1 Boundary Condition Types

When dealing with the diffusion of either heat or mass through a body, one ultimately must deal with the boundaries of the problem. When dealing with these boundaries, there are two types to consider; the Dirichlet boundary condition, and the Neumann boundary condition (Figure 2.7).

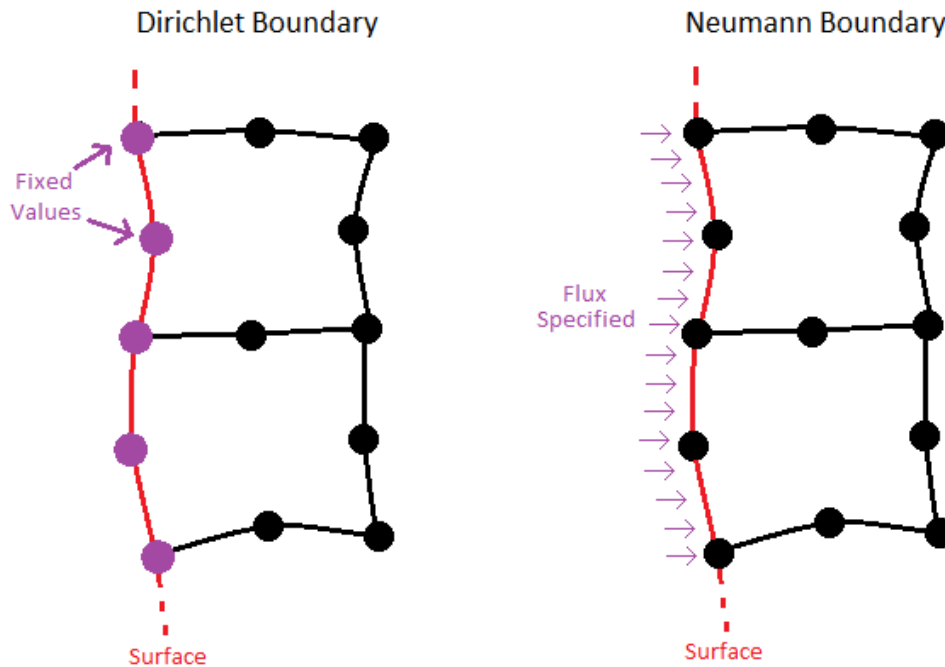


Figure 2.7 - 2D FEA Schematic depicting the differences between a Dirichlet boundary and Neumann boundary. Note that the Dirichlet boundary simply specifies nodal values on the surface whereas the Neumann boundary has a specified flux governed by a surface transfer equation. In the Neumann case, the surface nodal values are not fixed but must be found as part of the solution

The Dirichlet boundary condition is the simplest type of boundary condition. It simply specifies the value the solution must take upon that boundary. This type of boundary condition is ideal for mass diffusion simulations because the rate of diffusion is so much slower than the rate of replenishment/depletion across the boundary.

The Neumann type boundary condition specifies the flux through the boundary in question. This type of boundary condition is critical for heat transfer applications because often, the heat transfer throughout the material is much faster than transfer through the boundary. In our formulation, we will make use of the convective flux type boundary. The equation governing this boundary type is shown below in Equation 2.1, where T_s is the surface temperature, T_R is the reservoir temperature, and h is the convection coefficient; h is strongly dependent on the quench medium and is surface temperature dependent.

$$\dot{Q} = h(T_S - T_R) \quad \text{Eq. 2.1}$$

The advantage to using a linear boundary expression is that most literature values report convection coefficients (h), with this type of expression in mind.

2.2.2 Diffusion Stage

In martensitic steel processing, the diffusion of carbon is the first stage to occur. This is a high temperature process in which we simulate the treatment of the steel in various carbon-carrying atmospheres on the length scale of hours. The atmosphere composition is allowed to vary with time so that the surface composition of carbon is changing with time; we do this to obtain carbon composition gradients within the material. In order to simulate this, we use Dirichlet boundary conditions to simulate the carbon activity on the surface; these fixed surface values are allowed to change with time to reflect the changing atmosphere. It is an acceptable assumption that the surface carbon boundary is fixed (Karabelchtchikova and Sisson 2006), especially for treatments that are more deeply penetrating. It is also a much simpler boundary to implement computationally.

As we can see from the problem equation (Figure 2.6), the only material quantity needed for simulation is the carbon diffusion constant in iron. A variety of published data exist for this value obtained from experiment as a function of temperature and carbon content (Bhadeshia 1981; Parris and McLellan 1976). After simulating the model with the prescribed boundary conditions, we will have a fully interpolated field of carbon concentration throughout the part. This will then allow us to proceed to the quench stage of our simulation.

2.2.3 Quench Stage

Unlike the diffusion stage, the quench stage involves a heat transfer simulation that is coupled with calls to solve for mechanical equilibrium; as shown in Figure 2.28. This is necessary because some phenomena involving heat transfer, such as stress-assisted shifts in M_s , are dependent on the mechanical stress state. Additionally, the final material stress state is strongly path dependent. In this section, we will examine key variables required for a competent heat transfer simulation in transforming austenite.

Heat Transfer Coefficient

The actual modelling of the heat transfer problem is straightforward with literature data on heat capacity, thermal conductivity, and density freely available for the applicable phases of the steel. A more challenging problem to solve is the boundary condition since the heat transfer through the quench surface boundary will govern the entire simulation. To tackle this problem, we have opted for a convective Neumann type boundary as we have mentioned previously. This type of boundary requires us to supply the heat transfer coefficient through the boundary. This coefficient is strongly dependent on surface temperature with values for oil quench being an order of magnitude lower than values for water. Additionally, the dependence on the type of material being quenched makes it difficult to obtain reliable values for our steel. However, we have managed to locate some reasonable data for this coefficient as shown in Figure 2.8. The values of the heat transfer coefficient vary considerably between authors; however, they seem to share the same qualitative features. Namely, low convection at high temperatures during a vapor blanket stage and high convection at medium temperatures due to nucleate boiling of the quenchant (Passarella et al. 2014; Simsir 2008).

With all the data available for the simulation of the heat transfer, it is a straightforward matter to perform the finite element simulation of this aspect of the process. As in the carbon diffusion simulation, we obtain a temperature distribution field as a function of time. If we include the mechanics simulation that is running concurrently to the heat transfer simulation, we obtain all the necessary field data for us to make evaluations on the state of an as-quenched martensitic part; namely, internal stress distributions, changes in geometry, plastic flow, and phase.

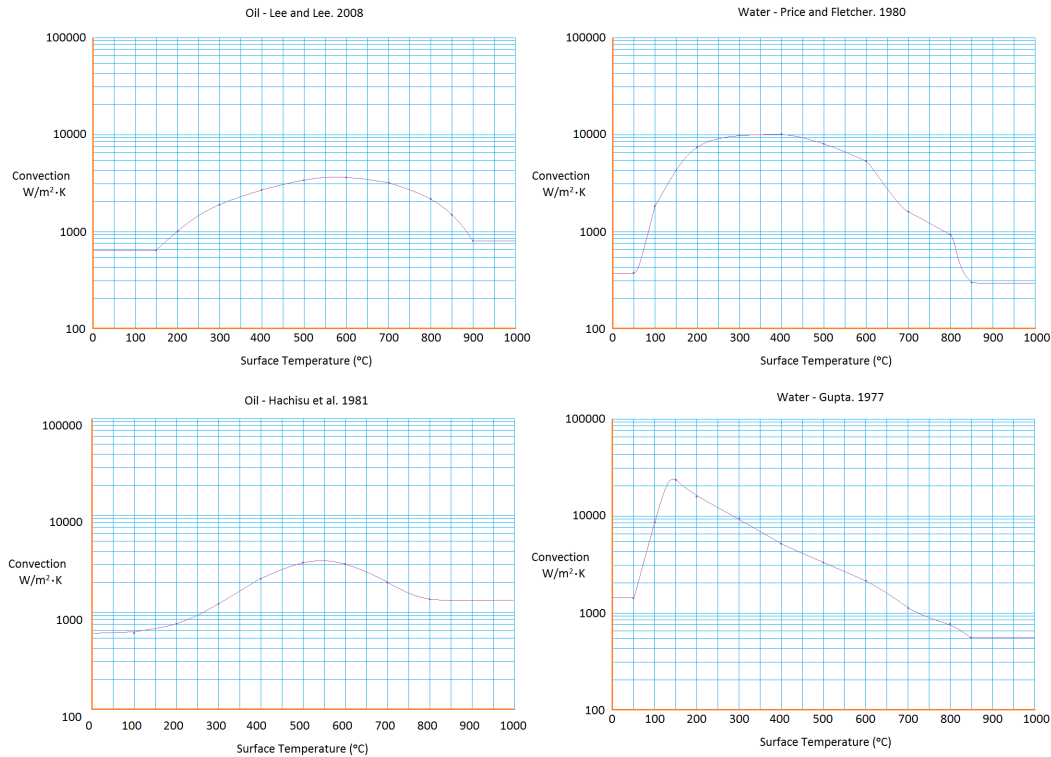


Figure 2.8 – Values of the heat transfer coefficient (h) for the quenching of steel in oil and water as a function of surface temperature. Various literature sources (Hachisu, Sakai, and Taguchi 1981; Lee and Lee 2009; Price and Fletcher 1980; Gupta 1977).

Latent Heat of Transformation

The martensitic transformation, like all transformations, has a latent heat of transformation associated with it. This transformation has a small but non-negligible effect on the temperature of a quenched object throughout the quenching process (maximum effect of less than 100°C found in this work). An expression for the change in enthalpy is shown below in Equation 2.2 (Lee and Lee 2009) for this phase transformation as a function of temperature. This expression is applicable to 4340 steel and must be appropriately scaled with the Ms of other grades of steel.

$$\Delta H^{\gamma \rightarrow \alpha'} = 0.041T^2 - 0.078T - 5079.947 \left(\frac{J}{mol} \right) \quad \text{Eq. 2.2}$$

Although the change in enthalpy is only equal to heat evolution at constant pressure, we will use the value as heat and assume the errors are small.

2.2.4 Finite Element Formulation

We have discussed the nature of our solution method; now what is remaining is to discuss the actual finite element solution. The finite element formulation of our problem is achieved by applying the Galerkin method to the heat conduction equation. By doing this and applying the divergence theorem (Nikishkov 2010), we obtain Equation 2.3 below which is the transient heat equation in the weak finite element form. Notice that the included integrals are dependent on the element type we choose (as they make use of the shape functions, N , shown earlier in Section 2.1). The matrices $[N]$ and $[B]$ are vectors of the shape functions and their spatial derivatives at each integration point respectively. The integrals displayed here are evaluated numerically using gaussian quadrature for each element (discussed in Section 2.6). Each element's contribution is then combined into the global solution spanning the system degrees of freedom.

$$[C][\dot{T}] + [K_T][T] = [R_C] - [K_C][T] + [R_E] \quad \text{Eq. 2.3}$$

Where,

$$[C] = \int_V \rho C [N]^T [N] dV - \text{Capacitance Matrix}$$

$$[K_T] = \int_V [B]^T [K] [B] dV - \text{Conductivity Matrix}$$

$$[R_C] = \int_S h T_R [N]^T dS - \text{Convective Boundary Reservoir Term}$$

$$[K_C] = \int_S h [N]^T [N] dS - \text{Convective Boundary Surface Term}$$

$$[R_E] = \int_V Q [N]^T dV - \text{Internal Heat Evolution Term}$$

There are a number of schemes that are able to solve this equation, however we will use a fully explicit forward-Euler scheme due to its simplicity in implementation and ability to handle nonlinear problems effectively. The strict timestep requirement of this scheme is acceptable because of this nonlinear requirement; that is, all of the terms, C , k , h , and Q are rapidly changing functions of temperature and time.

2.2.5 Explicit Transient Analysis

In an explicit transient analysis, we proceed with solving the next time step of the solution by considering the governing equation at the current time (t). This leads to an equation of the type shown below (Equation 2.4).

$$[C]^t [\Delta T] = \Delta t ([R]^t - ([K_C]^t + [K_T]^t) [T]^t) \quad \text{Eq. 2.4}$$

This expression becomes simple to solve if we lump the capacitance matrix entries on the diagonal. Specifically, that implies that we make the approximation that all the heat capacity lies at the nodes (Bathe 1986). By doing this, the system of equations becomes decoupled and we can very rapidly

solve the degrees of freedom. Due to the dependence of the intrinsic system quantities on time, we reevaluate all the system matrices at every timestep. It should be noted that the mass diffusion problem is solved in an analogous manner by using an equivalence between thermal diffusivity and the mass diffusion constant.

2.2.6 Stability Considerations

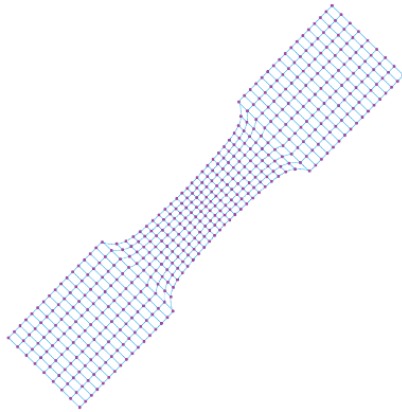
The Forward-Euler scheme we have previously discussed is only conditionally stable, that is, there is a critical timestep above which the solution will produce nonsense. Fortunately, it is possible to approximate the critical timestep with our elements by looking at the one-dimensional stability criterion. In one dimension, the critical time step is given by Equation 2.5 below for a linear element.

$$\Delta t_{crit} = \frac{l^2}{2\alpha} \quad \text{Eq. 2.5}$$

This expression states that the critical timestep is inversely proportional to the thermal diffusivity (or diffusion constant) and quadratically proportional to element size (l). This expression is applicable to 3D situations if we approximate the element size “ l ” as the smallest dimension in the 3D element. Since the smallest length scale will control the largest permissible timestep, we are really seeking the smallest length scale that exists in the entire finite element mesh. This can be done heuristically by measuring distances in each element in the mesh.

It should be noted that the expression above is applicable to linear elements only. For high order elements, like the 27-node hexahedron, the critical timestep is actually much smaller. A conservative estimate for the critical timestep in these elements is $1/8^{\text{th}}$ of the linear critical timestep (Bathe 1986); this is because the center node carries more “stiffness”⁴ in these elements.

⁴ Stiffness refers to the diffusivity in a diffusion simulation.



$$[K][u] = [F_{ext}] - [F_{int}]$$

Figure 2.9 – Form of the quasi-static finite element equation that is solved over the entire spatial domain

2.3 Mechanics Simulation

The mechanics aspect of our quench simulation is crucial for determining the residual stresses in the as-quenched part. As such, we now focus our efforts into discussing the finite element description of the mechanics problem. In solving the mechanics problem, we are searching for the nodal displacements that generate the stress/strain field required for equilibrium (Figure 2.9). A great deal of research has gone into creating finite element formulations for solving stress fields. Each has their own strengths and weaknesses; however, what is common between all of them is that they all use a virtual work principle combined with energy conjugate stress and strain measures to derive the equations of equilibrium. We will rely on quasi-static analysis exclusively for our quench simulations due to the extremely low loading frequencies relative to the sample natural frequencies. In formulating the finite element description, the difficulty arises when one examines the limitations of each stress and strain measure and their applicability to various magnitudes of strain and rotation. Additionally, a material constitutive law applicable to the stress and strain measures used is required; a requirement that can pose some difficulty in certain situations.

In this chapter we will discuss two types of formulation used widely in finite element literature. The first, small strain analysis, is very simple to formulate and uses both the Engineering Strain and Engineering Stress measures. The basic requirement to this strain theory is that we assume both small strains and small rotations. These requirements can be met in certain quench simulations; for others with a large degree of warping, the small rotation assumption is violated. In those situations, we rely on another description, called the Total Lagrange Formulation which assumes small strains but arbitrarily large rotations. The advantage to this formulation is that we can use the same constitutive models as the small strain formulation (Bathe 2006). More advanced formulations that allow both large strains and large rotations are outside the scope of this thesis as they require more careful examination of the material constitutive law. Luckily, the materials we are examining in this thesis typically experience strains of about 1% in quenching and below 10% in loading (due to their limited ductility). This results in a very small constitutive error for the quench models and marginal error for loading.

2.3.1 Small Strain Formulation – Small Strain Tensor

To begin this section, we are going to consider an infinitesimally small volume present within a quenching steel part. If one were to track this volume throughout the quench process, one may likely notice that it continually changes shape/volume and moves rigidly via translation and/or rotation. If we assume that any rotations are small throughout, and any changes in shape/volume are small, we can quantify this deformation accurately via the small strain tensor. The small strain tensor is given below in Equation 2.6.

$$\varepsilon_{ij}^{SM} = \frac{1}{2} \left(\frac{du_i}{dX_j} + \frac{du_j}{dX_i} \right) \quad \text{Eq. 2.6}$$

Upon inspection of the small strain tensor, we see that it is invariant under rigid translation, however, rotations will result in a non-zero false strain; it is for this reason that rotations must be small. Additionally, the derivatives must be with respect to some reference configuration. In this sense, this strain definition is effectively an engineering strain with respect to a reference configuration. This strain measure can be used in quenching simulations due to the small displacements of a quenching part, granted there is minimal warping. The fact that we assume small strains gives rise to a particular type of finite element formulation that can make use of infinitesimal strain theory; this type of formulation is called the Small Strain Formulation.

The Small Strain Formulation has two distinct features. The first feature, namely the small strain requirement has been discussed previously and is due to the exclusive use of the small strain tensor. The second feature is a Lagrange feature and implies that all quantities are referenced to a static reference configuration. This reference configuration is normally taken as that which exists at the beginning of the simulation, but it need not be. Figure 2.10 below illustrates this trait simply in one dimension. We see that the rod at time $t = 0$ is the reference element, any displacements in the rod at this time or any other are mapped back to this configuration for determination of the strains. This is permissible since changes in element geometry are small.

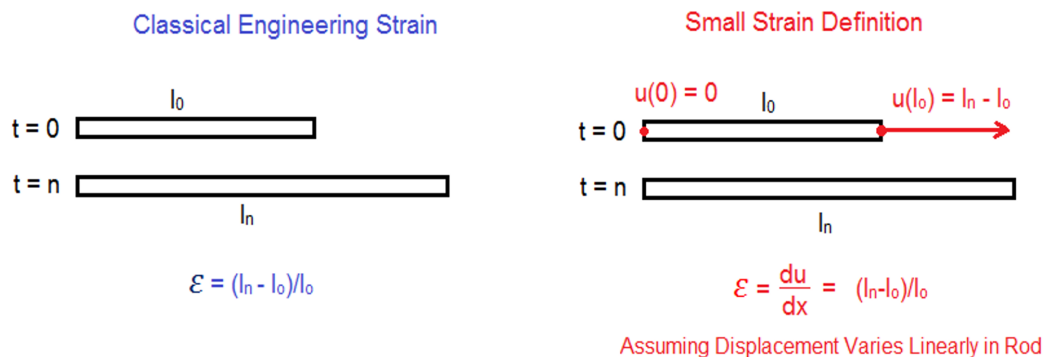


Figure 2.10 – Engineering strain in a one dimensional rod using the materials scientist convention and the small strain definition. In each case the reference configuration is taken to be the rod at time $t = 0$.

From the equivalency shown in Figure 2.10 between materials scientist definitions of strain and mechanical engineering definitions of strain, we see that the small strain tensor is that most encountered in practice.

2.3.2 Total Lagrange Formulation – Green-Lagrange Strain

The Total Lagrange Formulation is an improvement upon the Small Strain formulation that allows for arbitrarily large rotations without adding much complexity to the problem; specifically, constitutive models used for the Small Strain Formulation can still be easily substituted into the Total Lagrange Formulation. This formulation is still limited in that real material strains must still be small due to the constitutive approximations used (Bathe 2006; de Borst et al. 2012).

The base point for the Total Lagrange Formulation is a strain measure called the Green-Lagrange Strain. This strain measure, shown below in Equation 2.7, is similar to the small strain measure except that it contains quadratic terms in addition to the linear ones. These quadratic terms allow for a volume element to undergo rotation without the rotation being misrepresented as a false strain.

$$\epsilon_{ij}^{GL} = \frac{1}{2} \left(\frac{du_i}{dX_j} + \frac{du_j}{dX_i} \right) + \frac{1}{2} \left(\frac{du_k}{dX_i} \cdot \frac{du_k}{dX_j} \right) \quad \text{Eq. 2.7}$$

The Green-Lagrange Strain is referred to as a material strain quantity because it references all strains back to a reference configuration. This is exemplified in Figure 2.11. As can be seen, if a rod were to undergo a rotation and a stretch, the stretch would be mapped back to the reference orientation and geometry. For this reason, a specifically defined reference configuration is required; similar to the small strain case.

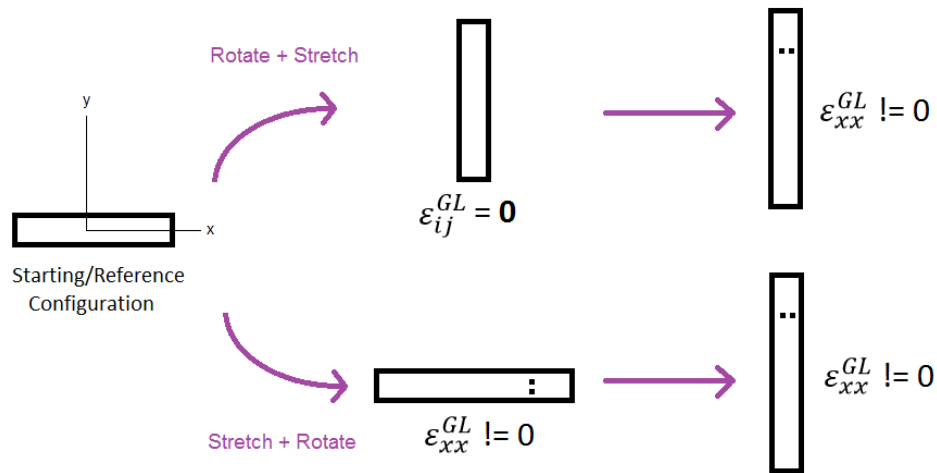


Figure 2.11 - Example demonstrating the evolution of the Green-Lagrange Strain through a uniaxial stretch and rotation. Note that the rotation has no effect on the strain measure and the stretch will always appear in the xx-component of the strain since the stretch maps back to the x-direction in the reference orientation. Comparatively, the small strain measure would become nonsense after the introduction of the rotation.

The Green-Lagrange measure gives a mapped, true representation of strain. What is needed now is a measure of stress which operates in the same manner; that is, a stress measure which maps surface tractions in the deformed state back to a reference configuration. A stress measure that operates in this manner would be energy conjugate with the Green-Lagrange strain and thus be applicable in a finite element derivation based upon virtual work. The stress measure that satisfies this requirement is called the 2nd Piola-Kirchhoff Stress and is related to the Cauchy “True” stress via Equation 2.8. In this expression, F is the deformation gradient tensor from the reference to the current state.

$$\sigma_{ij}^{CAUCHY} = |F|^{-1} F \sigma_{ij}^{PK2} F^T \quad \text{Eq. 2.8}$$

A finite element simulation that uses the Total Lagrange Formulation operates totally in the space of Green-Lagrange strains and 2nd Piola-Kirchoff stresses; therefore, the approximation we must make when dealing with metals exists in the constitutive model where we assume a linear elastic relationship between the Green-Lagrange strain and 2nd Piola-Kirchhoff Stress; Equation 2.9 below.

$$\sigma_{ij}^{PK2} \approx D_{ijkl} \varepsilon_{kl}^{GL} \quad \text{Eq. 2.9}$$

This relationship is only realistic for small values of the Green-Lagrange Strain; this is the case because the Green-Lagrange strain is nonlinear in the displacements and has quadratic components. A linear constitutive model would quickly become unrealistic at large strain values. Since the quadratic terms approximate zero in the small strain limit (no rotation example), we recover the linear strain behaviour for small strains and the constitutive law is consistent with real material behaviour. Additionally, in the limit of small strain, the 2nd Piola-Kirchhoff Stress reduces to a pure rotation of the Cauchy stress and hence they represent the same thing, just with a different coordinate orientation.

$$\sigma_{ij}^{CAUCHY} \approx R \sigma_{ij}^{PK2} R^T \text{ for small strains} \quad \text{Eq. 2.10}$$

The Total Lagrange Formulation thus represents the same thing as the small strain formulation when strains are small with the caveat that the material orientation is fixed to the reference frame. It is because of this fact that any model used for a small strain formulation can be directly substituted into a Total Lagrange Formulation by simply substituting the 2nd Piola-Kirchhoff stress for the Engineering stress and Green-Lagrange Strain for Linear Strain. The only disadvantage to this formulation over the small strain formulation is a bit more complexity in deriving the finite element equations, as we will see in the next section.

2.3.3 Determination of Equilibrium – Principle of Virtual Work

Throughout the course of our simulations, it will become necessary for us to determine mechanical equilibrium within the object of interest. In order to do this, the finite element mechanics solver determines the displacements necessary for equilibrium. This equilibrium requirement is based upon the “Principle of Virtual Work” and is derived slightly differently for the Small Strain and Total Lagrange Formulations; recall that the small strain formulation uses the linear strain tensors and engineering stress as work conjugate measures, whereas the Total Lagrange Formulation uses the 2nd Piola-Kirchhoff stress and Green-Lagrange strain as work conjugate measures.

Small Strain Finite Element Derivation

We begin with the derivation for small strain displacement-based finite elements. The principle used for determination of equilibrium is called the Principle of Virtual Work. The principle states that in order for an object to be in a state of equilibrium, the work done by the internal forces must equal the work done by the external forces at any point in the material for any arbitrary displacement field. This is quantified in Equation 2.11 below for the structure at an arbitrary point in time.

$$\int_{V_0} \delta \varepsilon_{ij}^T \sigma_{ij}^{t+\Delta t} dV = \delta u^T F_{ext} \quad \text{Eq. 2.11}$$

In this equation, the arbitrary displacement field is represented by the virtual nodal displacements. In the finite element adaptation of the principle, the virtual displacement field is applied via virtual nodal displacements and interpolated via the shape functions. Using the definition of the small strain tensor, we can expand the virtual strain field back into a form that utilizes the nodal displacements; where the matrix B is a matrix that converts nodal displacements into strains. This form is shown below in Equation 2.12.

$$\delta u^T \int_{V_0} B^T \sigma_{ENG}^{t+\Delta t} dV = \delta u^T F_{ext} \quad \text{where} \quad \delta \varepsilon^T = \delta u^T B^T \quad \text{Eq. 2.12}$$

From comparison of the left side and the right side, it is immediately evident that equilibrium requires that the external forces are balanced by an internal force quantity at the nodal points. This internal force quantity is a virtual work consistent internal force that arises from the integral on the left hand side. The final equilibrium requirement is shown below in Equation 2.13.

$$\int_{V_0} B^T \sigma_{ENG}^{t+\Delta t} dV = F_{ext} \quad \text{Eq. 2.13}$$

This equation can be solved for the configuration at time (t+1) provided the following information is known. Namely, the external forces at time (t+1), and the stress at time (t). This can be shown by expanding Equation 2.13 with regard to a known initial stress and a stress increment.

$$\int_{V_0} B^T (\sigma_{ENG}^t + \Delta \sigma_{ENG}) dV = F_{ext} \quad \text{Eq. 2.14}$$

Rearranging the equation with known terms on the right and unknowns on the left, Equation 2.14 takes form below.

$$\int_{V_0} B^T \Delta \sigma_{ENG} dV = F_{ext} - \int_{V_0} B^T \sigma_{ENG}^t dV \quad \text{Eq. 2.15}$$

This expression can be easily interpreted as follows; the quantity on the right hand side is a measure of how far from equilibrium the system is, in its current state. The term on the left side is the correction to this imbalance as it represents the change in stress field necessary to achieve equilibrium. In order to solve this expression, one more step is necessary; we must express the change in stress in terms of nodal displacements since they are our principal unknowns. This is easily accomplished by relating the change in stress to a change in strain via a constitutive model. The final solvable form for this expression is shown below in Equation 2.16 and takes the form of $[A][x]=[b]$; a problem easily solved via linear algebra techniques.

$$\int_{V_0} B^T D B dV * [u] = [F] - \int_{V_0} B^T \sigma_{ENG}^t dV \quad \text{Eq. 2.16}$$

The constitutive model makes its appearance via the component D in the expression above. In a purely elastic analysis, this matrix is simply the elastic constitutive matrix. In an elastoplastic analysis in which the structure is deforming on the yield surface, this matrix may become an elastoplastic tangent

matrix. Ultimately, the goal of this matrix is to “guess”⁵ what the changes in stress will be for any changes in strain in the materials current configuration. For linear problems, the above expression is solved directly and exactly. For non-linear problems, an iterative scheme is required that utilizes a tangent stiffness matrix or variation thereof. This will be addressed further in the next section.

In the finite element literature, the integral on the left hand side is referred to as the global stiffness matrix and can be interpreted as a matrix that relates any nodal displacements to the generation of internal forces. The expression in its reduced form is shown below in Equation 2.17.

$$[K][u] = [F] - \int_{V_0} B^T \sigma_{ENG}^t dV \quad \text{Eq. 2.17}$$

We have presented this derivation assuming small strains and with an initial stress to make it consistent with the way in which we have approached the quench problem in the previous sections. The small strain assumption is noted both in the fact that the integrals are evaluated with respect to the original reference volumes, and with the fact that changes in stress depend on changes in engineering strain. The presence of an initial stress is included because it is possible for a material to be prestrained at the beginning of a new timestep. Phase transformation strains are what give rise to the initial stress and ultimately, the need for seeking equilibrium since externally applied forces are usually zero in a quench simulation.

Total Lagrange Finite Element Derivation

Recall that the Total Lagrange Formulation gives the added bonus of allowing large rotations into our small strain problems. This benefit does however come with a price in the derivation of the Virtual Work Principle with the presence of nonlinear terms which must be neglected. Ultimately, this implies that the solution procedure for even a linearly elastic material will need to be iterative if rotations are involved. To begin our derivation, we express the virtual work balance in terms of the appropriate stress strain measures in Equation 2.18.

$$\int_{V_0} \delta \varepsilon_{ij_{GL}}^T \sigma_{ij_{PK2}}^{t+\Delta t} dV = \delta u^T F \quad \text{Eq. 2.18}$$

We then perform separations of our stress terms, and then separate our variation in the Green-Lagrange strain into a linear and nonlinear variation.

$$\int_{V_0} \delta \varepsilon_{ij_{GL}}^T \Delta \sigma_{ij_{PK2}} dV + \int_{V_0} \delta \varepsilon_{ij_{GL}}^T \sigma_{ij_{PK2}}^t dV = \delta u^T F \quad \text{Eq. 2.19}$$

$$\int_{V_0} \delta \varepsilon_{ij_{GL}}^T \Delta \sigma_{ij_{PK2}} dV + \int_{V_0} \delta \varphi_{ij_{GL-NonLinear}}^T \sigma_{ij_{PK2}}^t dV = \delta u^T F - \int_{V_0} \delta e_{ij_{GL-Linear}}^T \sigma_{ij_{PK2}}^t dV \quad \text{Eq. 2.20}$$

Upon examination of each of the terms in Equation 2.20, we see that some terms on the left side will ultimately be non-linear in the displacements; these terms are dropped from the expression and what we end up with is effectively a linearized tangent matrix. The terms on the right hand side can

⁵ The stiffness matrix on the left hand side of Equation 2.16 is a matrix that guesses how stresses will become related to strains. As such, it takes no unique form when looking to solve more complex constitutive models.

be evaluated exactly and represent the out of balance load vector that must be corrected. The final matrix form of the virtual work expression is shown next in Equation 2.21.

$$\left(\int_{V_o} {}^tB_L^T D {}^tB_L dV + \int_{V_o} {}^tB_{NL}^T \sigma_{PK2}^t {}^tB_{NL} dV \right) [u] = [F] - \int_{V_o} {}^tB_L^T \sigma_{PK2}^t dV \quad \text{Eq. 2.21}$$

This expression differs from the small strain derivation in that we have an expression for B_L that is equivalent to B in the small strain case but includes initial displacement effects for the Green-Lagrange strain measure. Additionally, we have another contribution to the stiffness matrix which accounts for how changes in geometry affect internal forces from existing stresses; this component has been linearized to only account for stresses present at the previous timestep/iteration. Since a Total Lagrange Expression accounts for geometrical nonlinearity, several equilibrium iterations may be required to obtain a suitable solution; this is due to linearization in the stiffness matrix in geometric terms. In the next section, we will expound on the form of these matrices for continuum elements used in quench modelling.

2.3.4 Finite Element System Matrices

In the previous section we laid out the finite element equations that need to be solved. Now we must couple the terms of the equation to the actual finite element domain we formulated at the beginning of the chapter. A key feature of FEA is that derivatives of interpolated quantities manifest as being functions of the derivatives of the shape functions. This feature is demonstrated in the formulation of the strain-displacement matrix and the Jacobian.

Small Strain Theory Matrices

With small strain theory, we need to set up matrices needed to evaluate the integrals in the finite element problem formulation. Specifically, we are solving

$$\int_{V_o} B^T DB dV * [u] = [F] - \int_{V_o} B^T \sigma_{ENG}^t dV \quad \text{Eq. 2.22}$$

This lends itself to two integrals which must be evaluated numerically:

$$[K] = \int_{V_o} B^T DB dV = \sum_{i=0}^{GP} w_i * detJ * B^T DB \quad \text{Eq. 2.23}$$

$$[F]_{Int} = \int_{V_o} B^T \sigma_{ENG}^t dV = \sum_{i=0}^{GP} w_i * detJ * B^T \sigma_{ENG}^t \quad \text{Eq. 2.24}$$

The weighting and gauss point rules are described in detail in Section 2.6. Until then, simply regard the integrals as weighted sums using specific points in the domain. The Jacobian matrix we have also not discussed yet; the Jacobian matrix is a matrix of complete partial derivatives representing the transformation from the natural to the real coordinate space. Its structure is shown in Figure 2.12.

Computing this matrix is very straightforward and is necessary not only because we require the determinant for the integrals, but because the integral matrices require the partial derivatives contained

The final integral that needs to be evaluated is the internal force integral. This integral represents the current effect on stresses present in the model before equilibrium is attained. Like the stiffness matrix integral, we make use of the strain-displacement matrix; however, we multiply with the stress state arranged in a vector.

$$\begin{aligned}
 [B]^T &= \begin{bmatrix} N_0^x & 0 & 0 & N_0^y & 0 & N_0^z \\ 0 & N_0^y & 0 & N_0^x & N_0^z & 0 \\ 0 & 0 & N_0^z & 0 & N_0^x & N_0^y \\ \vdots & & & N_1 & & \\ \vdots & & & \vdots & & \\ \vdots & & & N_n & & \\ \vdots & & & \vdots & & \\ \vdots & & & \vdots & & \end{bmatrix} & \quad [D] = \begin{bmatrix} D_{11} & D_{12} & D_{13} & D_{14} & D_{15} & D_{16} \\ D_{21} & D_{22} & D_{23} & D_{24} & D_{25} & D_{26} \\ D_{31} & D_{32} & D_{33} & D_{34} & D_{35} & D_{36} \\ D_{41} & D_{42} & D_{43} & D_{44} & D_{45} & D_{46} \\ D_{51} & D_{52} & D_{53} & D_{54} & D_{55} & D_{56} \\ D_{61} & D_{62} & D_{63} & D_{64} & D_{65} & D_{66} \end{bmatrix} & \quad [B] = \begin{bmatrix} N_0^x & 0 & 0 \\ 0 & N_0^y & 0 \\ 0 & 0 & N_0^z \\ N_0^y & N_0^x & 0 \\ 0 & N_0^z & N_0^y \\ N_0^z & 0 & N_0^x \\ \vdots & & \\ \vdots & & \\ \vdots & & \end{bmatrix} \begin{matrix} N_1 \dots N_n \dots \end{matrix} \\
 [B]^T [D] [B] &= \begin{bmatrix} N_0^x (D_{11} N_0^x + D_{14} N_0^y + D_{16} N_0^z) & N_0^x (D_{12} N_0^x + D_{14} N_0^y + D_{15} N_0^z) & N_0^x (D_{13} N_0^x + D_{15} N_0^y + D_{16} N_0^z) \\ + N_0^y (D_{41} N_0^x + D_{44} N_0^y + D_{46} N_0^z) & + N_0^y (D_{42} N_0^x + D_{44} N_0^y + D_{45} N_0^z) & + N_0^y (D_{43} N_0^x + D_{45} N_0^y + D_{46} N_0^z) \\ + N_0^z (D_{61} N_0^x + D_{64} N_0^y + D_{66} N_0^z) & + N_0^z (D_{62} N_0^x + D_{64} N_0^y + D_{65} N_0^z) & + N_0^z (D_{63} N_0^x + D_{65} N_0^y + D_{66} N_0^z) \\ \vdots & \vdots & \vdots \end{bmatrix} \begin{matrix} N_1 \dots N_n \dots \end{matrix}
 \end{aligned}$$

Figure 2.14 – Formation of the integrand for the element stiffness matrix. This matrix is $3n \times 3n$ corresponding to the nodal degrees of freedom present in the element. Upon integration, this matrix relates nodal displacements to the generation of internal forces. The matrix $[D]$ is a linearized constitutive matrix corresponding to a tangent stiffness of the material upon additional strain.

Total Lagrange Formulation Matrices

The matrices used in the small strain formulation appear here as well, however with some small modification that make them suitable for the nonlinear Green-Lagrange strain measure. The integrals to be assembled are shown below. Note that the integrals are performed for the reference volume.

$$[K]_L = \int_{V_0} {}^tB_L^T D_0 {}^tB_L dV_0 = \sum_{i=0}^{GP} w_i * detJ * {}^tB_L^T D_0 {}^tB_L \quad \text{Eq. 2.25}$$

$$[K]_{NL} = \int_{V_0} {}^tB_{NL}^T {}^tS_0 {}^tB_{NL} dV_0 = \sum_{i=0}^{GP} w_i * detJ * {}^tB_{NL}^T {}^tS_0 {}^tB_{NL} \quad \text{Eq. 2.26}$$

$$[F]_{Int} = \int_{V_0} {}^tB_L^T \sigma_{PK2}^t dV_0 = \sum_{i=0}^{GP} w_i * detJ * {}^tB_L^T \sigma_{PK2}^t \quad \text{Eq. 2.27}$$

These matrices are assembled as shown previously with some minor differences. For instance, the B_L matrix (Figure 2.15) now contains additional terms to reflect the fact we are using a strain measure with an initial displacement effect. The superscripts and subscripts in tB represent the B matrix at time t referenced to the configuration at time $t = 0$. The F terms in the matrix are the deformation gradient entries from the reference configuration to the configuration at time t . With all these terms, this matrix will be able to track the linear changes in the Green-Lagrange strain from the current strain state upon imposition of new displacements.

$${}^t[B]_L = \begin{bmatrix} F_{11} \frac{dN_0}{dx} & F_{21} \frac{dN_0}{dx} & F_{31} \frac{dN_0}{dx} & \vdots \\ F_{12} \frac{dN_0}{dy} & F_{22} \frac{dN_0}{dy} & F_{32} \frac{dN_0}{dy} & \vdots \\ F_{13} \frac{dN_0}{dz} & F_{23} \frac{dN_0}{dz} & F_{33} \frac{dN_0}{dz} & \vdots \\ F_{11} \frac{dN_0}{dy} + F_{12} \frac{dN_0}{dx} & F_{21} \frac{dN_0}{dy} + F_{22} \frac{dN_0}{dx} & F_{31} \frac{dN_0}{dy} + F_{32} \frac{dN_0}{dx} & \vdots \\ F_{12} \frac{dN_0}{dz} + F_{13} \frac{dN_0}{dy} & F_{22} \frac{dN_0}{dz} + F_{23} \frac{dN_0}{dy} & F_{32} \frac{dN_0}{dz} + F_{33} \frac{dN_0}{dy} & \vdots \\ F_{13} \frac{dN_0}{dx} + F_{11} \frac{dN_0}{dz} & F_{23} \frac{dN_0}{dx} + F_{21} \frac{dN_0}{dz} & F_{33} \frac{dN_0}{dx} + F_{31} \frac{dN_0}{dz} & \vdots \end{bmatrix} \quad N_1 - N_n$$

$$\text{where } [F] = \begin{bmatrix} 1 + \frac{du_x^t}{dx} & \frac{du_x^t}{dy} & \frac{du_x^t}{dz} \\ \frac{du_y^t}{dx} & 1 + \frac{du_y^t}{dy} & \frac{du_y^t}{dz} \\ \frac{du_z^t}{dx} & \frac{du_z^t}{dy} & 1 + \frac{du_z^t}{dz} \end{bmatrix}$$

Figure 2.15 – Strain-Displacement Matrix for the Total Lagrange Formulation. The differences from the small-strain matrix arise from the initial displacement effect from the reference configuration. The F terms are the entries in the deformation gradient tensor from the reference configuration to the configuration at time t .

We have a new matrix in this formulation that adds a nonlinear contribution to the stiffness matrix (K_{NL}). This matrix tracks changes to internal forces caused by prior existing stresses acting on a changed model geometry. The required matrices are shown in Figure 2.16. Since the stress measure is symmetric, this contribution will also be symmetric.

$${}^tS = \begin{bmatrix} \sigma_{PK211}^t & \sigma_{PK212}^t & \sigma_{PK213}^t & & & & & & \\ \sigma_{PK221}^t & \sigma_{PK222}^t & \sigma_{PK223}^t & & 0 & & & & \\ \sigma_{PK231}^t & \sigma_{PK232}^t & \sigma_{PK233}^t & & & & & & \\ & & & \sigma_{PK211}^t & \sigma_{PK212}^t & \sigma_{PK213}^t & & & \\ & 0 & & \sigma_{PK221}^t & \sigma_{PK222}^t & \sigma_{PK223}^t & & 0 & \\ & & & \sigma_{PK231}^t & \sigma_{PK232}^t & \sigma_{PK233}^t & & & \\ & & & & & & \sigma_{PK211}^t & \sigma_{PK212}^t & \sigma_{PK213}^t \\ & 0 & & & 0 & & \sigma_{PK221}^t & \sigma_{PK222}^t & \sigma_{PK223}^t \\ & & & & & & \sigma_{PK231}^t & \sigma_{PK232}^t & \sigma_{PK233}^t \end{bmatrix}$$

$$B_{NL} = \begin{bmatrix} \frac{dN_0}{dx} & 0 & 0 & \frac{dN_n}{dx} & 0 & 0 \\ \frac{dN_0}{dy} & 0 & 0 & -\frac{dN_n}{dy} & 0 & 0 \\ \frac{dN_0}{dz} & 0 & 0 & \frac{dN_n}{dz} & 0 & 0 \\ 0 & \frac{dN_0}{dx} & 0 & 0 & \frac{dN_n}{dx} & 0 \\ 0 & \frac{dN_0}{dy} & 0 & -0 & \frac{dN_n}{dy} & 0 \\ 0 & \frac{dN_0}{dz} & 0 & 0 & \frac{dN_n}{dz} & 0 \\ 0 & 0 & \frac{dN_0}{dx} & 0 & 0 & \frac{dN_n}{dx} \\ 0 & 0 & \frac{dN_0}{dy} & -0 & 0 & \frac{dN_n}{dy} \\ 0 & 0 & \frac{dN_0}{dz} & 0 & 0 & \frac{dN_n}{dz} \end{bmatrix}$$

Figure 2.16 - Matrices required for the calculation of the geometrically non-linear component of the stiffness matrix. The stress matrix is a 9x9 matrix whereas B_{NL} is 9 x 3n in size; where n is the number of nodes in the element.

An important realization concerning the matrices that we have set up for our finite element problem is that they have a time dependence to them and make use of quantities referenced to a certain time. Additionally, our stiffness matrix is often linearized and thus only provides a good approximation for the displacements required for solution; this approximation gets worse as the working conditions differ from that used to set up the matrices. As such, the solution matrix does need to be updated to avoid divergence. In the next section, we elucidate the iterative solution procedure needed to solve the finite element equation and discuss how we handle both the physical and geometrical nonlinearities in the problem.

2.3.5 Finite Element Solution Methods

In the finite element method, we are ultimately trying to solve the expression below (Total Lagrange form shown):

$${}^t[K][u] = [F]_{ext} - \int_{V_0} {}^tB_L^T \sigma_{PK2}^t dV_0 \quad \text{Eq. 2.28}$$

The right hand side of this expression is the unbalanced load vector and the displacements [u] are displacements necessary to achieve equilibrium. Within a given step, the right hand side is calculated perfectly, and indicates the deviation from equilibrium. We set up the stiffness matrix [K] and solve for equilibrium. After the displacements are updated and the corresponding stress and strain

states are updated, we reevaluate the right hand side of Equation 2.28 using the new updated quantities for the $t+\Delta t$ time step corresponding to iteration (i).

$$[F]_{ext} - \int_{V_0} {}^{t+\Delta t (i)} B_L^T \sigma_{PK2}^{t+\Delta t (i)} dV_0 \quad \text{Eq. 2.29}$$

What will often be seen is that the right hand side has not been reduced to zero after the first iteration. This is because of geometrical nonlinearities and nonlinearities in the constitutive model. Therefore, a second iteration is required to attain additional displacement corrections. This procedure is repeated until the residual forces are small enough to deem negligible.

One aspect of this iterative scheme that we have not discussed is how to handle the stiffness matrix. Assembling and factoring the stiffness matrix is by far the most expensive part of the finite element procedure, however, in order to obtain full Newton-Rhapson convergence characteristics, this matrix needs to be recalculated at each iteration step. In practice however, it may be more efficient to only calculate the global stiffness matrix at the beginning of each new time step (modified Newton-Rhapson Method) or only once (Initial stiffness method). However, divergence may be encountered with these other schemes. In practice, it is optimal to update the global stiffness matrix at staggered points in the solution procedure (Bathe 1986). These solution techniques are depicted below in Figure 2.17.

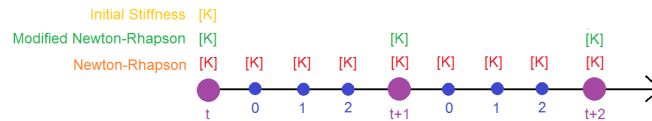
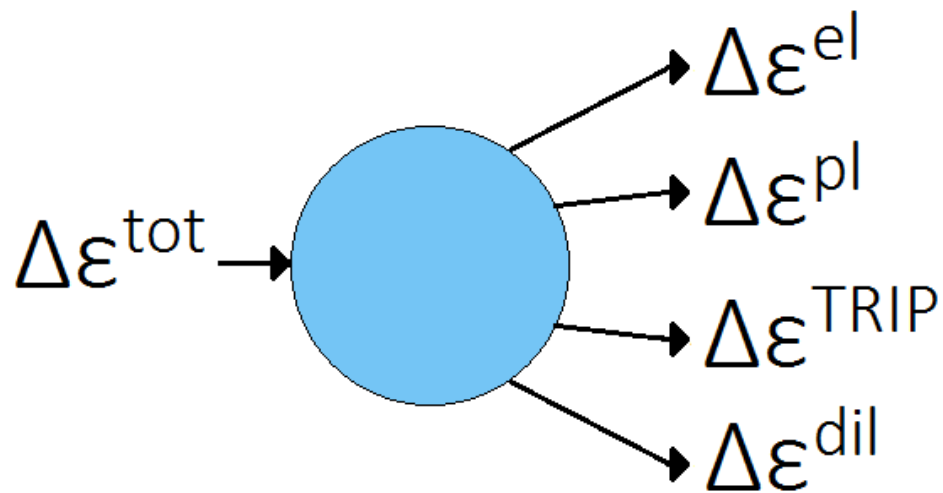


Figure 2.17 – Stiffness matrix reformulation points for different solution methodologies



2.4 Constitutive Considerations

The constitutive model is arguably the most significant part of any mechanical simulation as it is here we are able to directly input the observed reality of how materials behave. When assembling the constitutive model for a quench simulation, we have to consider what kind of strains the material is expected to exhibit and how we are to obtain them. Recall that in this chapter we are attempting to formulate this model in terms of macroscopic descriptions only due to the length scale of the phenomena we are examining. As such, our identification of mechanical phenomena must operate at this level. When reading this section keep in mind that these several things must be taken into account:

1. The microstructure of the material exists on a length scale much smaller than the part and elements we are working with.
2. The material consists of multiple changing phases that are intermingled on a much smaller length scale than the element.
3. The material experiences strains associated with elasticity, plasticity, phase transformations, and temperature changes.

These three basic postulates for our constitutive description imply/allow the following:

1. Mechanical behaviour can be homogenized (isotropic elasticity, J2-plasticity)
2. Mixture laws can be used to infer basic material properties.
3. The global strain must be decomposed into its constituents.
4. Material behaviour is nonlinear.

With these considerations in mind, we will now begin the construction of the constitutive model. An obvious starting point is elucidation of material strains, the mathematical description of their evolution and the mechanics of their decomposition.

2.4.1 Additive Strain Decomposition

In the previous sections, we were able to quantify the total strain exhibited on a volume element via definitions of the Small Strain and Green-Lagrange strain tensors. Additionally, we were able to set up a system for solving for global equilibrium given a proper constitutive relationship between additional strains and stresses. With this in mind, it is now worth considering what type of strains make up the total observed strain and how to set up our quench model to handle them. In the context of a quench, one may consider mechanical strains, both elastic and plastic, as well as strains introduced from thermal expansion/contraction. Additionally, a unique strain introduced in this context is that which arises from the phase transformation. This strain can have both a volumetric component, as well as a deviatoric component (TRIP). All these strain components are represented in Equation 2.30 below in an additive manner.

$$\boldsymbol{\varepsilon}^{tot} = \boldsymbol{\varepsilon}^{el} + \boldsymbol{\varepsilon}^{pl} + \boldsymbol{\varepsilon}^{thermal} + \boldsymbol{\varepsilon}_{vol}^{phase} + \boldsymbol{\varepsilon}_{dev}^{phase} \quad \text{Eq. 2.30}$$

Any observed strain present in a volume element is ultimately a combination of all the aforementioned strains. The reason why we can represent these strains additively is because we are working with strains that are related back to a sole reference configuration. For the purposes of this work, we are going to lump some of the terms into more manageable groupings. Since both thermal dilatation and the volumetric component of the phase transformation contain only hydrostatic terms, they will be lumped into a term which reflects the change in density of the material as a function of phase and temperature. The new total strain expression is represented below in Equation 2.31.

$$\boldsymbol{\varepsilon}^{tot} = \boldsymbol{\varepsilon}^{el} + \boldsymbol{\varepsilon}^{pl} + \boldsymbol{\varepsilon}^{dil} + \boldsymbol{\varepsilon}_{TRIP}^{phase} \quad \text{Eq. 2.31}$$

Within this expression, the elastic strains may be both volumetric and deviatoric; the dilatational strains are hydrostatic only, and the plastic and TRIP strains are deviatoric only. Via rearrangement of Equation 2.31, from any observed strain state, the stresses present may be calculated via Equation 2.32.

$$\boldsymbol{\sigma}_{ij} = D_{ijkl} * \left[\boldsymbol{\varepsilon}_{ij}^{tot} - \boldsymbol{\varepsilon}_{ij}^{pl} - \boldsymbol{\varepsilon}_{ij}^{dil} - \boldsymbol{\varepsilon}_{ij}^{TRIP} \right] \quad \text{Eq. 2.32}$$

In our computational paradigm, we are going to solve for the quantities in this expression at discrete time points with global system equilibrium in mind. Most of these quantities are intrinsically path dependent and as such, contribute to the material non-linearity during deformation. Specifically, deviatoric strains brought on by phase transformation are dependent on the stress state and plastic flow strains are dependent on the material yield surface. Luckily, one component, the inelastic dilatational strain component, is solvable at the beginning of a time step since it only relies on the temperature field. If a phase transformation model that includes the effect of stresses is incorporated (stress-induced transformation), then this is not the case.

Integration Procedure

A stable, efficient, and accurate integration procedure is required to solve for these strains at the required solution times. Without going into the details of any specific integration procedure here (we will discuss these later), we will show how these variables need to be solved at any given material point in both an explicit scheme and an implicit scheme.

Consider that at time t , all the solution variables are known. In the context of a global equilibrium iteration, the solver makes a guess at the strain increment required for equilibrium. It is the job of the integration procedure to partition this strain increment into all the separate component strains to find the variables at time $t+\Delta t$. In a fully explicit scheme, variables that depend upon other solution variables use the known values at time t . In an implicit scheme however, we use the unknown values at time $t+\Delta t$; in this case, the variables are coupled and need to be solved simultaneously. These procedures are illustrated schematically in Figure 2.18.

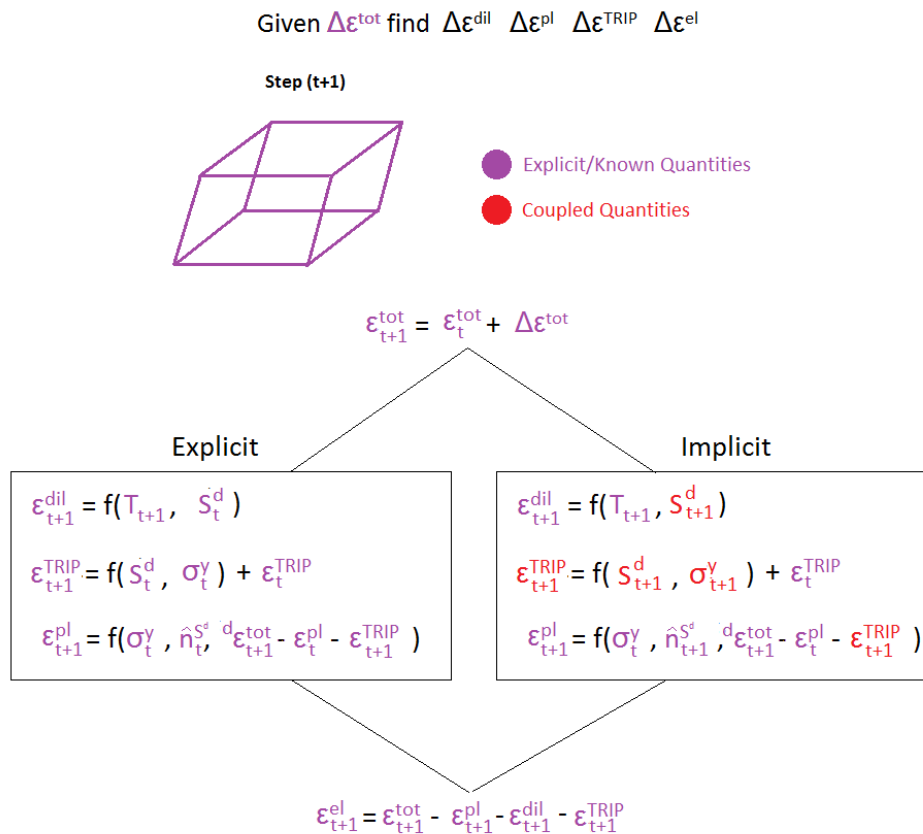


Figure 2.18 – Generalized depiction of how the mechanical solution values need to be evaluated at each timestep. An explicit and implicit scheme are presented noting the differences between the two. The variables in the implicit scheme can be solved sequentially whereas the variables in the implicit scheme are coupled and need to be solved simultaneously.

The advantage of the explicit scheme is that it is faster and simpler to implement. It does however suffer from instability if the timestep is taken to be too large. The implicit scheme features coupled nonlinear equations and thus requires an iterative solution scheme. The advantage lies in the better behaviour of the solution for larger timesteps. In this thesis, we will use an implicit integration scheme exclusively. The exact method will be presented in Section 2.4.6.

2.4.2 Modelling the Transformation

In formulating our constitutive model for how a two phase mixture of austenite and martensite would behave mechanically through a transformation, we must first determine how we will model the transformation itself. Namely, how the martensitic transformation progresses as a function of all the state variables; time, temperature, stress state and carbon content.

Kinetics of the Martensitic Transformation

The kinetics of the martensitic transformation are unlike those associated with most other transformations. Being a displacive transformation, the transformation front moves very rapidly throughout the lattice, on the order of the speed of sound, owing to the lack of diffusion required to assemble the new phase. For this reason, the transformation is nucleation controlled and is time independent. Nucleation begins when the temperature of the austenite reaches a critical threshold upon cooling where the martensitic phase is more energetically favorable. Upon crossing this temperature (M_s temperature), the transformation only progresses with further cooling, not time (Figure 2.19). A very popular expression to model the extent of transformation as a function of temperature was put forth by Koistinen and Marburger (Koistinen and Marburger 1959). They fit experimental data phenomenologically to an exponential function of the form shown in Equation 2.33.

$$f_{\alpha'} = 1 - e^{-0.01(M_s - T)} \quad \text{Eq. 2.33}$$

Although this expression is fit from data and was not physically founded, the function fits the observed experimental data very well, especially for the first 80 % of the transformation. After which, it underestimates the amount of martensite present. For this reason, it may be prudent to introduce a small correction at low temperatures.

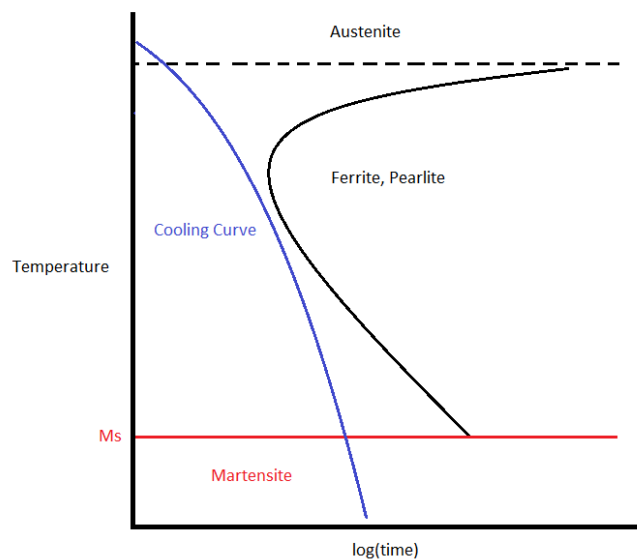


Figure 2.19 – CCT Curve depicting the time independent nature of the martensitic transformation. The degree of martensite formation is dependent on how low the temperature reaches below M_s .

Martensite Start Temperature

As we saw in the previous section, the only material parameter the Koistinen-Marburger expression needs is the martensite start temperature. The M_s temperature is extremely composition dependent with values varying hundreds of degrees with microalloying. Additionally, the prior austenite grain size has a small effect on this value with a maximum shifting of about 50°C from a grain size of 0 to 200µm for 0.1 wt%C steel (Capdevila, Caballero, and García De Andrés 2003); the shift is significantly less for higher carbon contents. In low alloy steels, carbon by far has the most dominating effect on M_s ; coincidentally, it is the alloying constituent we are compositionally grading during processing. As such, a most basic expression for M_s should include a dependence on carbon content. Fortunately, it has been found (Krauss 1999) that the M_s varies linearly with carbon content in the 0-1 wt.% range; therefore, the most simple expression we will use for M_s is shown below in Equation 2.34.

$$M_s = 490.44 - 474 * (wt. \%C) \quad \text{Eq. 2.34}$$

This expression gives a good average M_s for the types of steel we are working with and the grain size range we expect to see in the course of our experiments. With that said, it is still possible to refine the M_s expression further by including the effects of stress state on the transformation. We will examine this effect in the next section.

Stress-Assisted Transformation

In the previous section, we discussed the athermal nature of the martensitic transformation. In particular, we showed how the martensitic transformation is independent of time and proceeds solely as a function of temperature via a Koistinen-Marburger phenomenological expression. Historically however, it has been found that temperature is not the sole parameter that dictates the progress of the martensitic transformation. In fact, it has been found that the application of stress will shift the martensite start temperature in a manner proportional to the magnitude of the applied shear and dilatational stress components on the habit plane. Patel and Cohen were the first to model this behavior accurately in their famous 1953 paper in which they consider the thermodynamic effects of a applied stress on a transforming volume (Patel and Cohen 1953). The work of Patel and Cohen considers that the martensitic transformation has both a shear and dilatational component for any given lath. One can consider that an applied stress may have a component normal to this particular habit plane and a component acting in shear. This effect is illustrated in Figure 2.20 below.

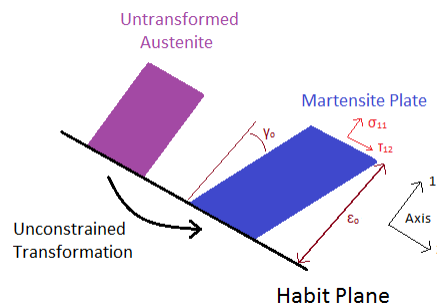


Figure 2.20 – Phenomenological depiction of the martensitic transformation; the untransformed austenite undergoes a large shear strain with a small dilatation with respect to the transformation habit plane. Stresses on the plane can be decomposed into a normal component and a shear component which act along the transformation strains and perform work.

The stress components acting along the transformation strains have the ability to do work which may either aid the martensitic transformation or oppose it. This is seen in the cases of uniaxial tension and compression versus hydrostatic compression. In the case of hydrostatic compression, the transformation is hindered as demonstrated by the lowering of the M_s temperature; this can be understood considering the 4% dilatation that defines the transformation; the compressive strains act to work against this expansion hence, the transformation must provide additional driving force. Conversely, uniaxial loading would have an opposite effect for this exact reason. In the case of uniaxial loading, tension and compression both aid the transformation with tension having a larger effect; this effect is illustrated in Figure 2.21.

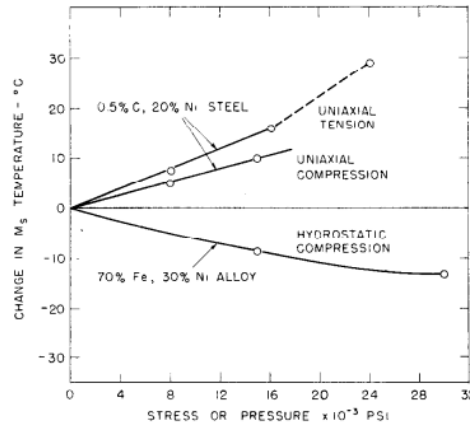


Figure 2.21 (Patel and Cohen 1953) – Shift in M_s versus various loading scenarios

This can be understood by considering the shear aspect of the transformation. In uniaxial loading, there is a shear stress that acts depending on the orientation of the habit plane with respect to the loading direction (Mohr's Circle, Figure 2.22). There will be a particular orientation in which the work from the shear component and normal component is highest. Since the shear strain is the largest component and the shear stress will always aid the transformation, both uniaxial tension and compression will aid the transformation with the normal tensile/compressive stresses, aiding/inhibiting the transformation in a small manner respectively. This is quantified in Figure 2.22 below for a general stress state shown with regard to the principal orientation.

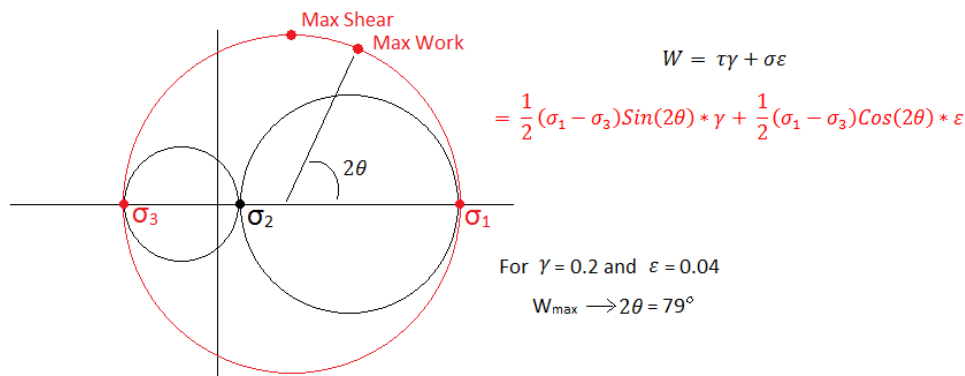


Figure 2.22 – The calculation of the most favorable orientation for the formation of martensite inside a fully 3-Dimensional stress state. The expression for this work boost is given with regard to a Mohr's circle interpretation and is at its maximum at an orientation of 79° (rotated about σ_2 -axis) for martensitic steels.

As Figure 2.22 depicts, the angle of maximum work boost is $2\Theta = 79^\circ$ about the σ_2 -axis for martensitic steels. Using this calculated work value, one can determine the shift in M_s based upon how the free energy of transformation varies with temperature. The first martensitic plates to form would be expected to have habit planes with this orientation. At the point of interest, the free energy of transformation varies linearly with temperature; hence, one can easily compute the shift in M_s due to the work boost. For Iron-Nickel alloys, this boost is approximately $5.56 \text{ (J/mol)/}^\circ\text{C}$ (Patel and Cohen 1953).

While we can calculate the shift in M_s with respect to the applied stress state, it would be naïve to assume that this shift is constant throughout the entire transformation. The reason for this is that the internal stresses will begin to dominate over the externally applied stresses as the transformation proceeds; additionally, it may be more difficult for the remaining austenite to transform to martensite along the favorable orientations as the volume becomes occupied. A simple substitution of the new M_s into the Koistinen-Marburger expression would ultimately be fallacious; however, due to the small shifts in M_s due to stresses, these errors are assumed small in the context of a quenching simulation.

2.4.3 Calculation of Dilatational Strains

Earlier, we discussed how both isotropic thermal expansion/contraction and phase transformations result in a purely dilatational strain of the material. This strain can be calculated purely upon the density differences between the material in the reference state and current state. Equation 2.35 depicts this calculation below in incremental form, while Equation 2.36 depicts how it is partitioned in a purely dilatational form.

$$\varepsilon_{n+1}^{vol} = \varepsilon_n^{vol} + \Delta\varepsilon^{vol} = \varepsilon_n^{vol} + \left(\frac{\rho_n}{\rho_{n+1}} - 1\right) \left(\frac{\rho_0}{\rho_n}\right) \quad \text{Eq. 2.35}$$

$$\varepsilon_{ij}^{dil} = \frac{\varepsilon^{vol}}{3} \delta_{ij} \quad \text{Eq. 2.36}$$

In the finite element code, we do not calculate the non-elastic strain components explicitly, rather, we only calculate the changes in each quantity between steps so that we may calculate the change in elastic strain. It is for this reason why the incremental form of the volumetric strain calculation is presented. In Figure 2.23 below, we present how this equation is obtained by considering the mass invariance of an expanding volume element. Both the total form and incremental form are depicted so that the equivalence between the two may be tested.

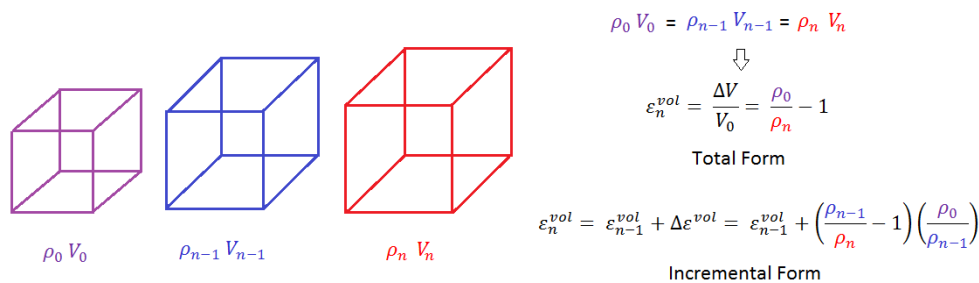


Figure 2.23 – Derivation of the Volumetric Strain from the consideration of a mass balance and the definition of volumetric strain. The incremental form is used in the finite element code due to the ease of working with changes in strain.

2.4.4 Calculation of TRIP Strains

The phase transformation of materials undoubtedly results in the volume change of a volume element due to differences in density between the parent and product phase. This observed nonlinear strain that accompanies the transformation is volumetric and is observed regardless of the circumstances of the transformation; most importantly, this strain is fully reversible upon a reversal of the phase transformation. In this section, we wish to address another strain component that often accompanies the transformation. This strain component is entirely deviatoric and is referred to as the “Transformation-Induced Plasticity” component (TRIP). This component, unlike the volumetric component, depends upon the material stress state while it is undergoing the transformation and for this reason, its magnitude and direction is context dependent. In general, it is not reversible and can be quite large in magnitude. In this section we will discuss the mechanisms responsible for this deformation as well as bring forward the latest literature attempts to model them.

TRIP Mechanisms

There are two specific mechanisms in the literature which have been shown to have a contribution to the generation of TRIP strains. The first mechanism, referred to as the *Greenwood-Johnson Effect* (Greenwood and Johnson 1964), is common to most phase transformations and is a contribution that stems from plastic yielding in the parent phase as it accommodates the newly forming phase. The second contribution is referred to as the *Magee Effect* (Magee 1966) and it is unique to the martensitic transformation. The Magee (orientation) Effect is caused by selection of favorable variants during transformation. In the previous section we discussed the concept of stress-assisted transformation; the energy considerations brought about by Patel and Cohen are the driving force for this preferred variant effect. It is ultimately the anisotropy of this variant selection that leads to the shape change of the material.

Experimentally, the factor that drives this TRIP phenomenon has been shown to be the mesoscopic stress state in the material as it undergoes transformation. Specifically, most models that attempt to predict the evolution of the TRIP strain throughout the transformation will give it a proportional dependence to the applied stress deviator. This relationship is depicted below in Equation 2.37 for a constant applied load.

$$\varepsilon_{ij}^{TRIP} = \frac{3}{2} K * S_{ij} \quad \text{Eq. 2.37}$$

In this expression, S_{ij} is the deviatoric component of the applied stress, K is a constant that depends on the specific mechanism(s) of the phase transformation. This expression was derived from early work measuring TRIP via uniaxial testing and is very popular (Simsir 2008). It has persisted despite its shortcomings; namely that it lacks load path change considerations. Some authors have attempted to compensate for this by including a back stress in S_{ij} (Fischer et al. 2000). Experimental data for such a model is very difficult to obtain however.

In constructing K for this expression, awareness of the two deformation mechanisms is crucial. One must be aware that they both may have different strength contribution depending on the transformation coordinate and the level of applied stress. This is illustrated nicely in Figure 2.24.

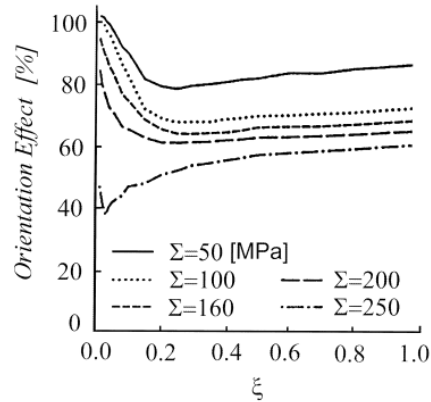


Figure 2.24 (Fischer et al. 1998) – Depiction of Relative Contributions to the total observed TRIP strain under different load levels as a function of transformation coordinate.

From this figure, we see that the Magee effect makes up the majority of TRIP strains when under low stress; however, the contribution drops in favor of Greenwood-Johnson at high applied stresses. Additionally, the contribution of each changes with the maturity of the transformation. Nonetheless, there exist many different expressions for the K constant. These literature models usually only consider the Greenwood-Johnson effect in their formulation. One such model is shown below.

$$K = \frac{5}{9} \frac{\delta}{\sigma_y^0} \quad \text{Eq. 2.38}$$

In this model, δ represents the volume change of the transformation and σ_y^0 is the yield strength of the parent phase. A more elaborate model, developed by Fisher (Fischer et al. 2000) incorporates the shear effect of the martensitic transformation (Equation 2.39).

$$K = \frac{5}{4} \frac{\sqrt{\delta^2 + \frac{3}{4}\gamma^2}}{\sigma_y^*} \quad \text{Where, } \sigma_y^* = \sigma_y^n \left(\frac{1 - \sigma_y^o / \sigma_y^n}{\ln(\sigma_y^n / \sigma_y^o)} \right) \quad \text{Eq. 2.39}$$

This model incorporates the Greenwood-Johnson and Magee effects. It is clear that the large shear strain, γ , present in the martensitic transformation is taken into account. It does however assume a constant contribution of each deformation mechanism.

Simulation Implementation

In our discussion thus far, we have neglected how the strain develops as a function of transformation coordinate; that is, we have neglected to scale the strength of the TRIP effect as a function of transformation progress. We have only discussed the TRIP equation assuming instantaneous and complete transformation. In Figure 2.25, we observe the TRIP strain as a function of transformation coordinate for the martensitic transformation in steel. We see that its development is highly nonlinear. A number of phenomenological expressions have been put forth to fit this behaviour; the most popular of which by Abrassart (Abrassart 1972) is shown next in Equation 2.40.

$$\varphi(f_m) = f_m(3 - 2\sqrt{f_m}) \quad \text{Eq. 2.40}$$

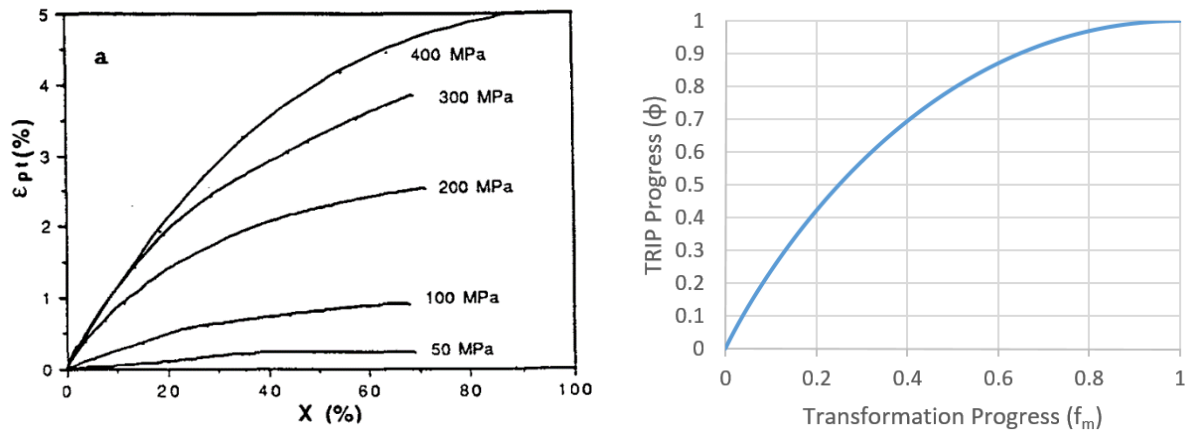


Figure 2.25 – (a) (E. Gautier 1995) TRIP strain as the martensitic transformation progresses for varying load levels. (b) Phenomenological description of the curve based up on the model by Abrassart (Abrassart 1972).

What is particularly interesting when looking at this function is that the straining proceeds most rapidly at the onset of transformation. This can be understood by considering that at the onset, the applied stress has the most influence on the transforming regions whereas internal stresses will begin to dominate later on.

This is the expression that we will use in our quench simulations due to its fit for the martensitic transformation in steels. This expression will be coupled with that of Equation 2.37 to give a rate form expression for the development of plastic strain, shown below in Equation 2.41.

$$\dot{\epsilon}_{ij}^{TRIP} = \frac{3}{2} K \frac{d\varphi}{df_m} \frac{df_m}{dt} S_{ij} \quad \text{Eq. 2.41}$$

This expression, developed by Leblond (Leblond, Devaux, and Devaux 1989), has been popularly used in quenching simulations with the assumption that we can vary S_{ij} throughout the simulation. A consequence of using this expression is that no TRIP strain will develop if there is no deviatoric stress present. This is experimentally consistent in constant loading situations, however, in unloading, in which the macroscopic stress is reduced to 0, TRIP strain has been experimentally found to develop in materials as a result of internal stresses (Fischer et al. 1998). In the mechanical formulation of our quench simulation, we will modify the rate-form of the Leblond Equation (Equation 2.41) into an incremental form compatible with our time stepping procedure. This transformation is based upon an implicit time-stepping.

$$\dot{\epsilon}_{ij}^{TRIP} = \frac{3}{2} K \frac{d\varphi}{df_m} \frac{df_m}{dt} S_{ij} \rightarrow \Delta \epsilon_{ij}^{TRIP} = \frac{3}{2} K_{n+1} (\varphi_{n+1} - \varphi_n) S_{ij}^{n+1} \quad \text{Eq. 2.42}$$

Clearly, the time stepping for the quench simulation must remain small to avoid drift of the solution; however, the use of an implicit scheme does allow for good convergence properties. The difficulty with this method lies in the fact that the stress state at the end of the timestep is not known

apriori. As such, an iterative solution process is required to solve this equation within the global finite element context. We will discuss this solution procedure in Section 2.4.6 where we invoke the “Effective Stress Function” method.

With regard to the significance of TRIP strains in the solution process, TRIP strains, like plastic strains, are deviatoric in nature and flow along the deviatoric stress direction. For this reason, the evolution of TRIP strains will have the effect of reducing the effective deviatoric stress during a phase transformation. This will act to bring the stress state further away from the yield surface and should have a significant effect in the quenching simulations.

2.4.5 Plasticity

When we seek the solution for equilibrium within our quenched object, it is likely (and expected) that the stresses determined by the solution procedure will exceed the yield strength of the material. When this occurs, the solution as it stands is incomplete and we must take corrective measures to map the stress state back to the yield surface. We have a situation referred to as physical non-linearity and it is understood simply as a non-linear relationship between stress and strain. What actually occurs is that we have the generation of plastic strains in addition to the elastic strains during the strain increment. The tangent stiffness matrix we use for the determination of equilibrium is in fact a linearized stiffness matrix which may only account for elastic strains (initial stiffness method) or linear plastic hardening (Newton-Rhapson method). The end result no doubt is that the solution predicted by the tangent stiffness matrix is not exact and is only an approximation to the correct solution. Via iterative means however, we can converge upon the exact solution. We have discussed this process in Section 2.3.5.

Let us examine the problem in a situation in which we only have elastic and flow strains (neglect the other strain types we have discussed for now). At the end of the previous load step, the system is in equilibrium; this is taken as our reference point ($t = n$). When we enter the next load step however, an imbalance is introduced; upon correcting for this imbalance, both elastic and plastic strains will inevitably be introduced. Our solver will have guessed a total strain increment and we will need to partition it into elastic and plastic strains; more specifically, we are looking to find the change in strain since step (n).

$$\begin{aligned}\varepsilon_{n+1}^{el} &= \varepsilon_n^{el} + \Delta\varepsilon^{el} \\ \varepsilon_{n+1}^{pl} &= \varepsilon_n^{pl} + \Delta\varepsilon^{pl}\end{aligned}\tag{Eq. 2.43}$$

$$\text{where, } \Delta\varepsilon^{tot} = \Delta\varepsilon^{el} + \Delta\varepsilon^{pl}$$

Given that the displacements incurred during the global step iteration result in a change in total strain, it is sufficing to say that the stresses at the end of the step are a function of both the stresses at the beginning of the step and the total strain incurred during the step; the hardening variables at the beginning of the step (α) also dictate the final resting point of the yield surface.

$$\sigma_{n+1} = f(\alpha_n, \sigma_n, \Delta\varepsilon^{tot})\tag{Eq. 2.44}$$

The form of Equation 2.44 is convenient since it conveys that the stress state is a non-linear function of the initial stresses and the step strain within the step. What this function actually does is split the total strain into an elastic and plastic component while staying consistent with the physical laws governing plasticity. Since the quantities at the beginning of the load step are constant, an important realization is that the stress state only depends on the total strain, or displacement field in a nonlinear manner.

The tangent stiffness matrix does not take into account this nonlinearity, hence the solution we obtain will be not be in equilibrium; however, if we update the stress state via Equation 2.44 we will see that we are closer to equilibrium upon recalculation of the residual load vector. We can thus repeat the process and obtain an even better solution. In repeating the process, we can use the original stiffness matrix we started with (initial stiffness method) or opt to reformulate the stiffness matrix using the new information regarding tangent stiffness (Newton-Rhapson method); both methods will converge upon the correct solution assuming the tangent matrix is not too far removed from the actual stiffness.

2.4.6 Return Mapping Algorithms

In our discussion in the previous section, we neglected to discuss how the function in Equation 2.44 is evaluated; that is, how we partition the strain increment into a consistent elastic and plastic contribution. This is because we do not evaluate the function explicitly but instead undergo a process referred to as a radial return mapping algorithm. This algorithm, like the expression states, will take the total strain increment as input as well as the elastic strain at the beginning of the global load step and partition the strain increment into an elastic and plastic component. The type of algorithm we use in our simulations is called a Euler Implicit Radial Return Mapping Algorithm (de Borst et al. 2012; de Souza Neto, Peric, and Owen 2008). We implement this algorithm for an isotropic vonMises type material with an associative flow rule. In mathematical terms, this algorithm will solve the following problem:

$$\text{Given: } \varepsilon_n^{el}, \bar{\varepsilon}_n^{pl}, \text{ and } \Delta\varepsilon^{tot} (\text{step strain increment}) \quad \text{Find: } \varepsilon_{n+1}^{el}, \text{ and } \Delta\gamma$$

where,

$$\bar{\varepsilon}_{n+1}^{pl} = \bar{\varepsilon}_n^{pl} + \Delta\gamma \quad \text{Plastic Increment}$$

$$\sigma_{n+1}^{vm} - \sigma_y(\bar{\varepsilon}_{n+1}^{pl}) \begin{cases} \leq 0 \text{ for } \Delta\gamma = 0 \text{ (elastic increment)} \\ = 0 \text{ for } \Delta\gamma \neq 0 \text{ (plastic increment)} \end{cases} \quad \text{Consistency Condition} \quad \text{Eq. 2.45}$$

$$\Delta\varepsilon^{pl} = \Delta\gamma \sqrt{\frac{3}{2} \frac{\sigma_{n+1}^{dev}}{\|\sigma_{n+1}^{dev}\|}} \quad \text{Implicit Associative Flow Rule}$$

We see that solving this system of equations will result in the split of the strain increment into the elastic and plastic contributions while maintaining the consistency condition and flow rule for the plasticity. In order to solve this system, we make use of the elastic-predictor, plastic-corrector, return map method. In this method, we initially assume that the entirety of the strain increment is elastic, we define these associated quantities as trial quantities (Equation 2.46). If this assumption holds for the consistency condition (state inside the yield surface), we take these trial quantities as the final stress/strain state with a plastic increment of zero.

$$\varepsilon_{TRIAL}^{el} = \varepsilon_n^{el} + \Delta\varepsilon^{tot} \quad \text{Eq. 2.46a}$$

$$\sigma_{TRIAL} = D^e : \varepsilon_{TRIAL}^{el} \quad \text{Eq. 2.46b}$$

If the trial quantities do not satisfy the equations, we must apply a correction that allows for plastic strain; the so called plastic-corrector phase. For isotropic vonMises materials, this phase is greatly simplified by noting that the correction only applies to the deviatoric strains; additionally, the deviatoric components of the trial states and actual states are collinear in associative plasticity. They differ by only a scalar multiple. This is represented mathematically in Equation 2.47.

$$\sigma_{n+1}^{HYDRO} = \sigma_{TRIAL}^{HYDRO}$$

$$\sigma_{n+1}^{DEV} = \sigma_{TRIAL}^{DEV} - \Delta\gamma 2G \sqrt{\frac{3}{2}} \frac{\sigma_{n+1}^{dev}}{\|\sigma_{n+1}^{dev}\|} \rightarrow \text{Implies } \frac{\sigma_{n+1}^{dev}}{\|\sigma_{n+1}^{dev}\|} = \frac{\sigma_{TRIAL}^{dev}}{\|\sigma_{TRIAL}^{dev}\|} \quad \text{Eq. 2.47}$$

By substitution of these quantities, we see that our system of equations will reduce to only one equation with $\Delta\gamma$ as the only unknown, namely,

$$0 = \sigma_{TRIAL}^{vm} - 3G\Delta\gamma - \sigma_y(\varepsilon_n^{pl} + \Delta\gamma) \quad \text{Eq. 2.48}$$

This equation can be solved by iterative means in order to find the plastic increment. Since the derivatives are easy to compute, the Newton-Rhapson method is ideal. Once solved, by using our relations in Equation(s) 2.43, we can easily sub in to find the appropriate strain values at time n+1, as well as the material stresses.

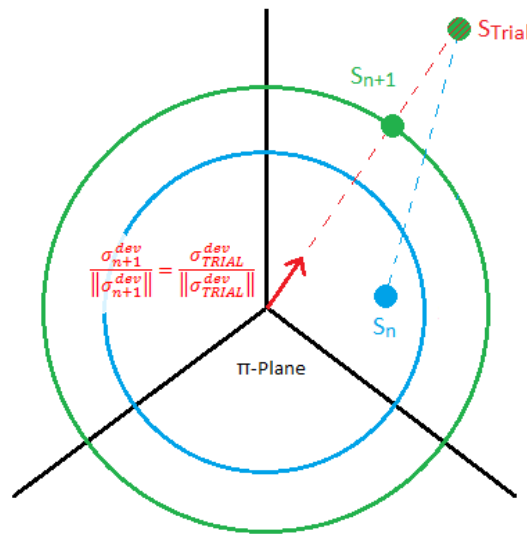


Figure 2.26 - Depiction of the radial return mapping algorithm on the deviatoric stress components. The colinearity of the trial and final stress states is shown with the distance between them being the plastic increment along the flow direction (N_{n+1}). Consistency is seen to be maintained with the final stress state lying on the hardened yield surface.

This entire return mapping procedure can be easily visualized in the stress space along the deviatoric plane. As we can see in Figure 2.26, the initial trial stress rests outside the yield surface. This stress state is mapped back toward the yield surface, by noting the flow direction for the implicit method at time (n+1) is collinear with the trial stress state. The final stress state rests on the yield surface, enforcing our consistency condition for plastic flow.

Effective Stress Function Algorithm

The return mapping algorithm we saw in the previous section is effective for partitioning the total strain increment into elastic and plastic components; however, in our quench simulation we must also solve for the TRIP strain component since its magnitude depends upon the final stress state at time $t+\Delta t$. The Effective Stress Function (ESF) algorithm is an effective method for simultaneously solving for both plastic strains and TRIP strains throughout the time step interval. This algorithm, developed by Kojic (Kojić and Bathe 1987), was originally designed to solve for concurrent creep phenomenon. However, since creep and TRIP are mathematically very similar, it is easily adaptable to our purposes. For brevity, we will focus on the fully implicit form of this algorithm which is effectively very similar to the return mapping algorithm we previously discussed.

In this algorithm, we solve a single nonlinear equation of vonMises effective stress. The equation takes the form as shown below in Equation 2.49.

$$\left(\frac{1}{2G} + \gamma + \lambda\right)^2 \sigma_{vm}^2 - \frac{3}{2} \varepsilon_{dev}^{trial} : \varepsilon_{dev}^{trial} = 0 \quad \text{Eq. 2.49}$$

Notice that the equation makes use of a trial strain state like the return mapping algorithm does. The values γ and λ represent the plastic flow and the TRIP flow respectively and depend upon the value for σ_{vm} . This equation is solved effectively by a bifurcation procedure in which we converge upon the appropriate stress value (Kojić and Bathe 1987). In testing different stress points, the TRIP equation can be solved for the TRIP increment and the plastic flow can be determined from the work hardening rate; thus allowing us to test the values in the effective stress function. It should be noted that this effective stress method was originally developed for creep instead of TRIP but, the mathematics are nearly similar, thus allowing its use. The output of the effective stress function is thus summarized below given solution inputs. This procedure is performed at every integration points after step strains are determined.

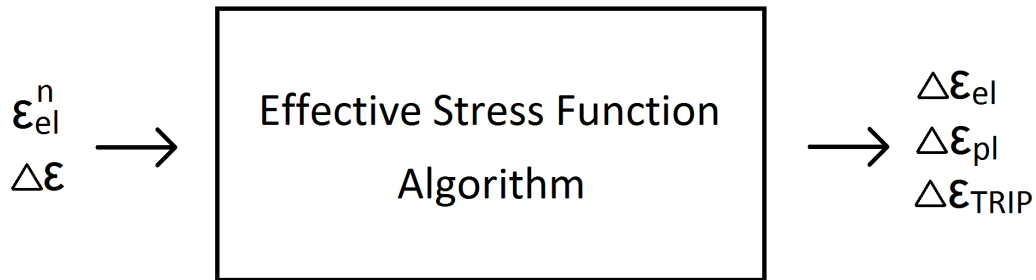


Figure 2.27 – Effective Stress Function inputs and outputs. All constitutive quantities are determined by the procedure in a manner consistent with their respective governing laws.

As we have mentioned previously, we have opted for the fully implicit form of this procedure since it seems to be well compatible with the initial stiffness solution method and is easily understood conceptually in terms of the radial return mapping methods discussed earlier.

2.4.7 Solving for Equilibrium - Summation

In this section, we will discuss the method by which all mechanical operations are performed during the quenching simulation. Upon the calling of the mechanical module by the quench simulation, the system will have undergone a short period of time since the last time mechanical equilibrium was sought. In this time, temperatures have changed, and phase composition has changed; this will result in a change in the material constitutive law as well the generation of fixed inelastic strain components. These strain components have been discussed previously and result from: thermal dilatation, and phase change dilatation. Figure 2.28 depicts these last comments and shows that the determination of these quantities is the first step in the mechanical process. After which, we run our mechanical equilibrium solver to find the remaining strain components at time $t+\Delta t$.

From the flow chart in Figure 2.28, we begin our mechanics module with an update of the constitutive model for current conditions. The constitutive model is the simplest component to update. In the conventional formulation of the elements the constitutive model can be expressed using a chosen law of mixture for the phases utilizing the current temperature and phase state; thus material properties such as stiffness, Poisson's ratio, flow strength, and hardening can be computed by mixing the respective values for the involved phases.

After the constitutive model is updated, it is necessary to find the changes in all the strain values since the last time a mechanical equilibrium step was performed. This is done so that we can obtain the pre-equilibrium stress state from the elastic strains. At the beginning of the mechanical stage, no nodal displacements have yet been computed, thus the change in total strain since the last mechanical step is zero.

$$\Delta \varepsilon^{tot} = 0$$

By invoking the effective stress method discussed in the previous section, we obtain a first guess at the stresses and strains in the structure at time $t+\Delta t$. The stress state in the structure is likely not in equilibrium after this procedure (load vector is not close to zero)⁶, thus the equilibrium iterations begin. What we have just obtained are the 0th iteration starting point guesses for equilibrium. Future iterations will result in changes in the displacements and total strains of the structure. We proceed iteratively until the integration nets a set of elastic stresses which are in equilibrium; thus signifying the end of the mechanical step. At this point we return to the heat transfer solver until the next mechanical timestep is called.

⁶ Load vector refers to the difference between the external loads and internal forces. It is a measure of imbalance from equilibrium.

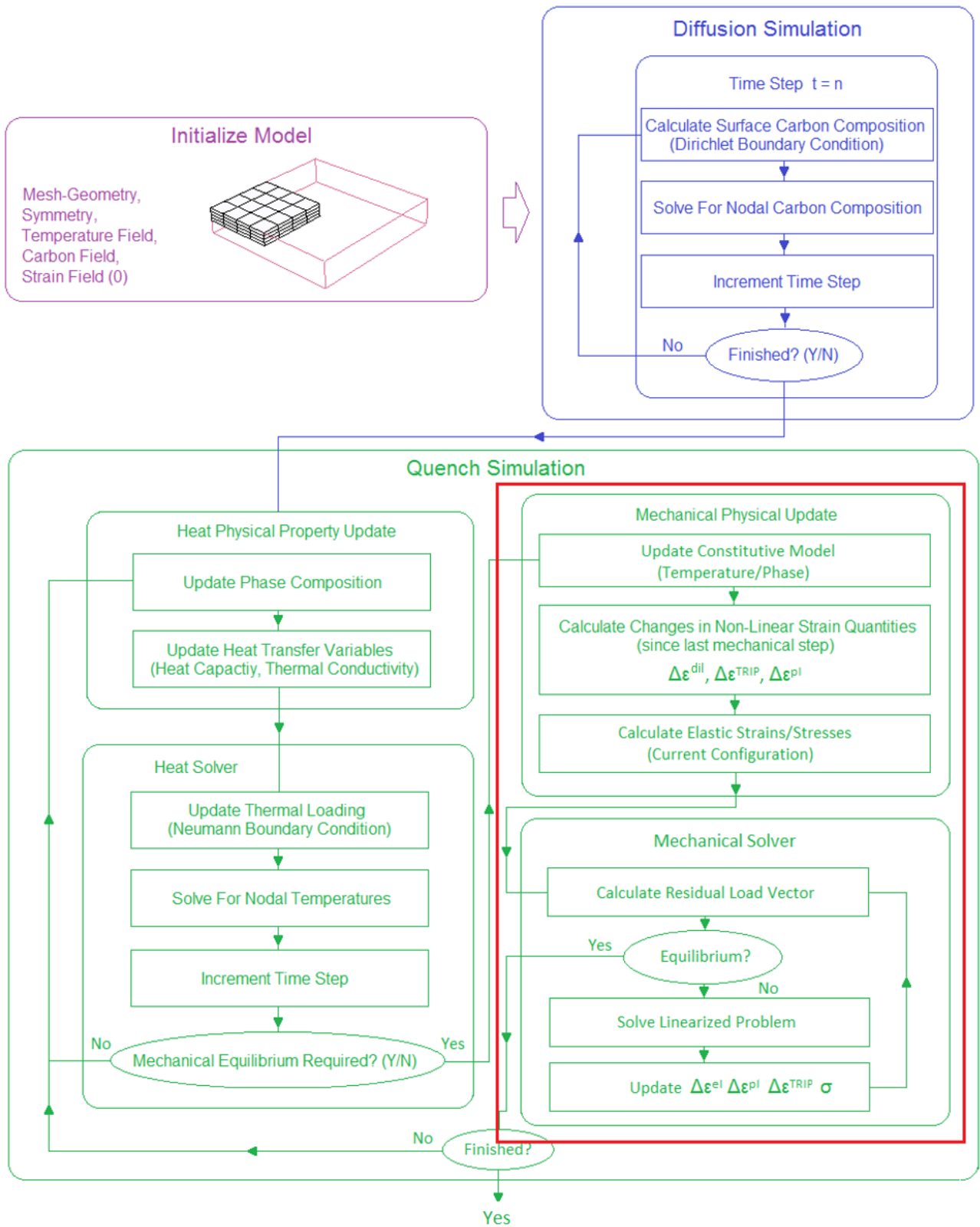


Figure 2.28 – Overview of the Process for Simulating the Quenching of Graded Steels. The red box depicts the region in which all strain components are determined and is the focus of this section.

2.5 Volumetric Locking Concerns

Up to this point, we have discussed the pure displacement formulation of the finite element method. This formulation is highly effective for most materials, however, it inherits a specific problem which may be of concern. This problem occurs when the ratio of the bulk modulus to the shear modulus of a material approaches infinity; that is, when the material approaches near incompressibility. In this situation, a phenomenon may occur called Volumetric Locking. When this happens, the solution to the finite element problem is too stiff and the pressure field of the solution becomes highly inaccurate due to the decoupling of pressure from the displacement field.

This is a concern for us because we include incompressible plasticity in our analysis. However, it has been shown (Bathe 2006) that a good solution is still possible given a sufficiently high density mesh in this situation; albeit a mesh with much higher density than necessary for compressible analysis. Also, flexible high order elements such as the 27-noded brick discussed earlier tend to perform better than others when confronted with this situation. It has been suggested (Sussman and Bathe 1986) that one make use of pressure band plots in which bands of constant hydrostatic pressure are plotted as a means to prove that volumetric locking has not occurred (Figure 2.29).

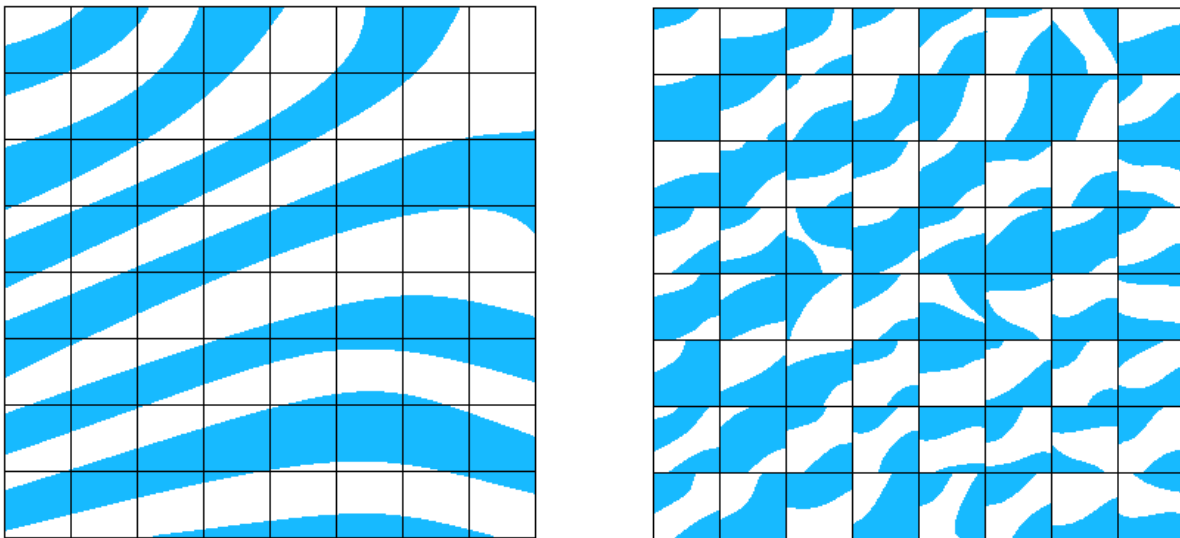


Figure 2.29 – (Left) Schematic of a pressure band plot depicting good mesh properties; (Right) Schematic of pressure bands on a locked mesh. Note the inconsistent pressure field.

In the cases where the volumetric locking cannot be alleviated, there are other formulations of the finite element method which use pressure as separate degrees of freedom. Reduced integration techniques also seem to help with this problem. We will not discuss these techniques here but we point out that these methods do exist if faced with this problem. Overall, when evaluating the effectiveness of a finite element mesh, the global predictor of accuracy is continuity of the stress field between elements. When we present results in this thesis, we will show the stress fields calculated directly from the gauss points without any averaging. This is done to convince the reader that the solution is accurate when they see a smooth stress distribution.

2.6 Numerical Integral Evaluation

In the previous sections, we have seen that the finite element formulations for diffusion and mechanics problems require the integration of both volume and surface integrals throughout the domain. Clearly, analytical integration is not suitable due to the complexity of the problem, however, there exist several integration schemes that are well suited to our needs. In particular, the method of gauss quadrature is well suited to the type of elements we are using. The philosophy behind gauss quadrature is quite simple, the true integral can be approximated (or evaluated exactly) by sampling specific points in the domain and interpolating with a polynomial. This concept is illustrated in Figure 2.30 below. What is clear from this figure is that a judicious selection of integration points will evaluate the integral exactly. Gaussian quadrature formalizes this concept. In essence, the gaussian quadrature rule builds an interpolating polynomial based on the desired number of integration points; ultimately, by using the correct integration points and weights, you are integrating this polynomial. Because of this, Gaussian quadrature rules have the favorable property that they will integrate a polynomial of $(2n-1)$ exactly, where n is the number of integration points. This allows us to perform our integrations exactly with the correct number of integration points appropriate for our element and integral; assuming the element is not distorted from a cuboid natural shape or parallelepiped. As the element gets more distorted, the integration will lose accuracy, however, it has been shown that convergence will still be possible, provided the distortions are not too large (Bathe 1986).

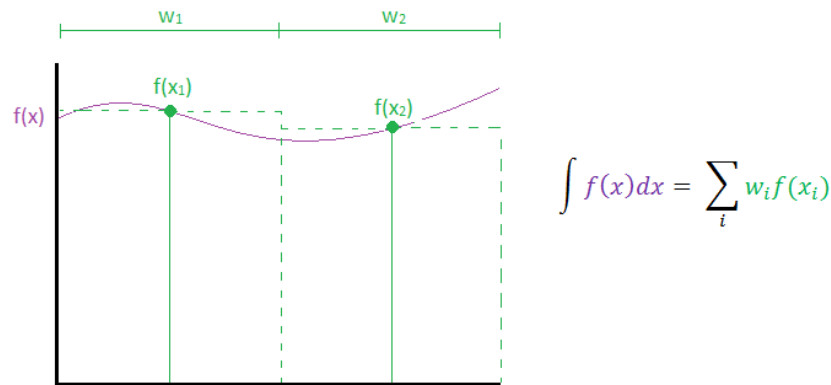


Figure 2.30 – Evaluation of an integral via sampling a finite number of points with respective weights in one dimension

Recall that we like to work with our elements in their natural coordinate space. Since we are dealing with mainly volume integrals in our formulations, we transform the integrals from the real volume into an equivalent integral in the natural coordinate space. This is clarified below in Equation 2.50.

$$\iiint_V f(x, y, z) dx dy dz = \iiint_{V_N} \frac{dx dy dz}{d\varepsilon d\eta d\mu} f(\varepsilon, \eta, \mu) d\varepsilon d\eta d\mu \quad \text{Eq. 2.50}$$

Recall that our volume element extends from -1 to 1 in all dimensions of the natural coordinate space. That makes this integral easy to evaluate using Gaussian quadrature. Specifically, the integral transforms into a sum over all integration points of the form shown in Equation 2.51.

$$\iiint_{V_N} \frac{dx dy dz}{d\varepsilon d\eta d\mu} f(\varepsilon, \eta, \mu) d\varepsilon d\eta d\mu = \sum_{\varepsilon} \sum_{\eta} \sum_{\mu} \det J * w_{\varepsilon} w_{\eta} w_{\mu} * f(\varepsilon, \eta, \mu) \quad \text{Eq. 2.51}$$

The integral in the original volume thus transforms into a sum over the natural volume where we evaluate the function at the integration points and sum the values with the corresponding weightings. The additional term $\det J$ is the determinant of the Jacobian and represents the volume scaling from the natural coordinate system to the real coordinate system. Surface integrals, which are sometimes required, are evaluated in an analogous manner.

2.6.1 Quadrature Rule Applied to Finite Element Integrals

The two/three dimensional numerical integration of finite elements using gaussian quadrature is a straightforward process. As we saw in the previous section, a gaussian quadrature rule of order n will integrate a polynomial of order $(2n-1)$ exactly. With this in mind, we must look at both the finite element integrals, and the type of element being used in order ascertain the minimum integration order required to exactly integrate an undistorted element. The form of a typical finite element volume integral is shown below in Figure 2.31. As can be seen, when integrating over the natural coordinate space, the shape functions depend on the natural coordinates; hence, higher order elements have higher order shape functions. These shape functions then feed into the problem formulation which will dictate the final order of the polynomial being integrated. In the case of undistorted elements, the Jacobian is constant, thus it has no contribution to the problem order.

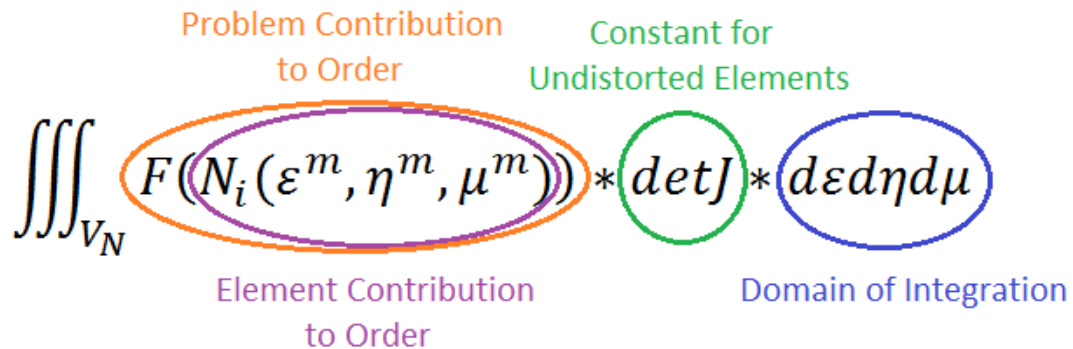


Figure 2.31 – Volume integral over the natural coordinate space typical of those performed in finite element solutions. Both the order of the shape functions and order of the problem formulation contribute to the order of the polynomial being integrated. For undistorted elements, the Jacobian is constant and does not contribute to the order.

Using the type of analysis performed above, the minimum integration order is two for linear elements and three for quadratic elements. These values were obtained by examining each of the integrals required for the solution of the diffusion and mechanics problems. These integrals are summarized in Table 2.1. Although the required integration order is calculated for undistorted elements, convergence can still be expected for elements with small distortions; albeit with small errors. A higher integration order than required can be used; this has the advantage of increased accuracy in a nonlinear problem as well as better performance with distorted elements.

Problem Integral	Linear Order	Required Gauss Rule	Quadratic Order	Required Gauss Rule
$[K_T] = \int_V [B]^T [k] [B] dV$	2	2	4	3
$[R_C] = \int_S h T_R [N]^T dS$	1	1	2	2
$[K_C] = \int_S [N] h [N]^T dS$	2	2	4	3
$[R_E] = \int_V Q [N]^T dV$	1	1	2	2
$[K] = \int_{V_o} [B]^T [D] [B] dV$	2	2	4	3
$[F]_{Int} = \int_{V_o} [B]^T \sigma_{ENG}^t dV$	1	1	2	2
$[F]_{surf,vol} = \int_{S,V} [N] f d(S, V)$	1	1	2	2

Table 2.1 – The required gauss order of the integrals encountered in our finite elements formulations for different elements.

2.6.2 Quadrature Rule Applied on a Finite Element Domain

We quickly examine how a two-point and three-point integration rule manifest on a three dimensional finite element. In multiple dimensions, the rules extend for each dimension, therefore, an order-two element has a total of eight integration points. Figure 2.32 below depicts the placement of the integration points in the element as well as their respective weights. Luckily, in the case of a 2x2x2 integration rule, all the weights are one.

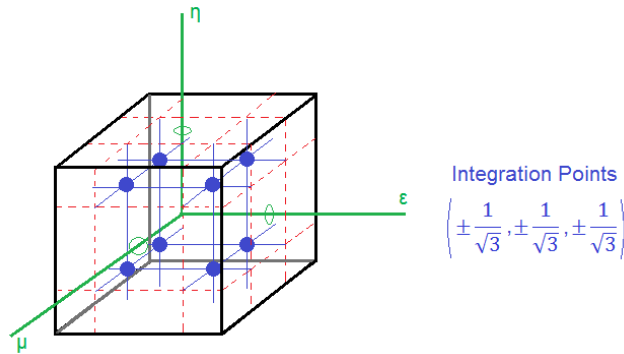


Figure 2.32 - Position of Gauss Integration Points within the natural element space. Eight integration points (two per dimension) are necessary for the 8-noded brick element.

The 27-node element we had discussed earlier requires a three-point minimum integration rule for convergence. The location of the integration points as well as the respective weights are shown below in Figure 2.33.

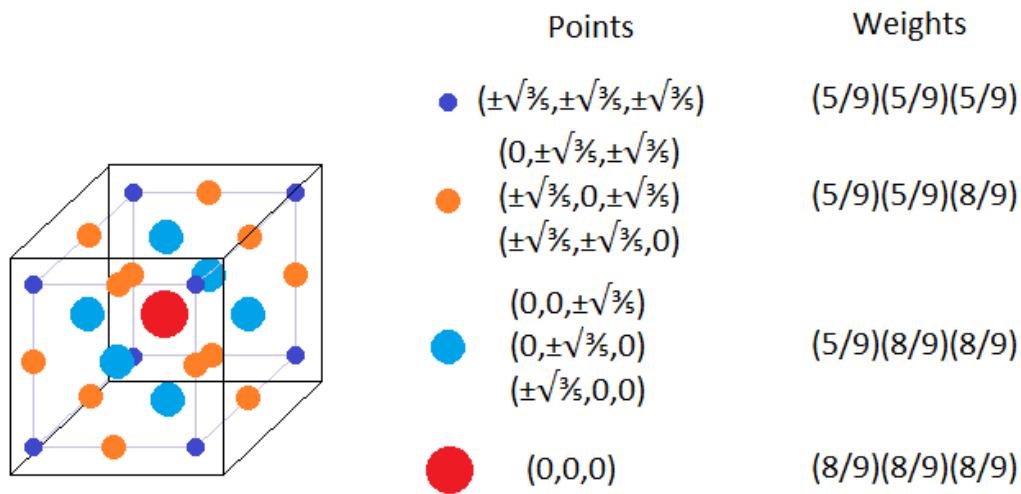


Figure 2.33 – Manifestation of a 3x3x3 integration rule in a cuboidal element. Note the variation in weighting (signified by point size) as opposed to the 2x2x2 rule.

The integration rules we have discussed are the minimum required for the respective elements shown; of course it is always possible to use a higher order integration rule. Gauss weights and positions for arbitrarily high orders are published and easily accessible.

2.7 Experimental Stress Analysis

Many techniques exist for measuring residual stresses that yield direct or approximate stress measurements. These techniques include but are not limited to: particle diffraction (x-ray, neutrons), Barkhausen noise analysis, ultrasonic wave analysis, optical analysis, and hole drilling (Anderoglu 2004; Hauk 1997). In this thesis, we will rely solely on x-ray diffraction as a stress measuring technique; this is because x-ray diffraction is among the highest resolution techniques available for measuring stresses. The method relies upon measuring the lattice strains caused by stresses via shifts in diffraction angle. By using the proper elastic constants for the material and diffraction plane, the stress tensor is converted from diffraction angle shifts. The only limitation to this technique lies in the small penetration depth of x-ray energies available from benchtop sources (on the order of $30\mu\text{m}$ for 7 keV x-rays); for this reason, we are limited to performing surface measurements.

2.7.1 Diffraction Physics and Experimental Setup

The fundamental law governing diffraction is referred to as the Bragg Law. The Bragg Law considers what happens to radiation of a given wavelength when it impinges upon an ordered lattice of specific lattice spacing. When considering the beam path, it is clear that there is a relationship between wavelength (λ), lattice spacing (d), and incident angle (θ) that gives maximum constructive interference. When the effect of successive lattice planes is considered, a high intensity diffracted beam will emit when the Bragg's Law (Figure 2.34) is satisfied.

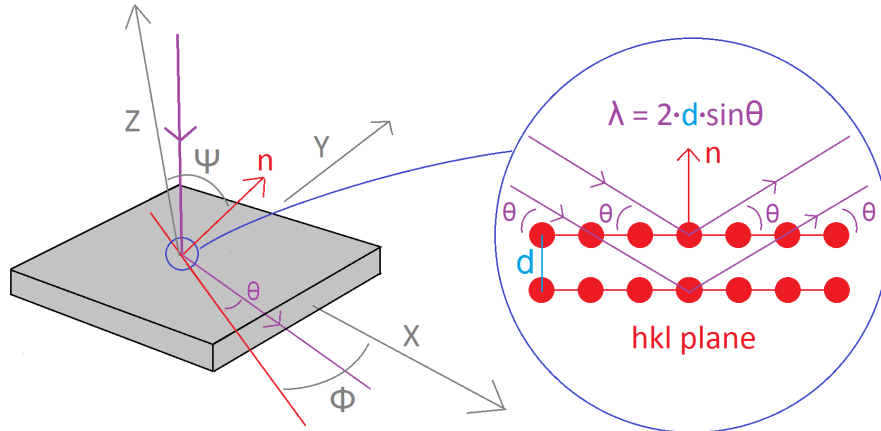


Figure 2.34 - Experimental setup of a surface x-ray diffraction experiment. The lab frame is depicted (xyz) along with the sample rotation and tilt. Bragg Diffraction is observed when the Bragg condition is satisfied for a properly oriented (hkl) plane.

In this figure we see a typical experimental setup for a surface diffraction experiment. An x-ray beam of fixed energy is directed at the sample. The sample is rotated and tilted from the laboratory reference frame through angles Φ and Ψ respectively (Bruker 2009). Diffraction is observed at the detector when the conditions match the Bragg relation. What is of particular interest is that the lattice spacing “ d ” should stretch under a stress; this leaves $\sin\theta$ to change to satisfy the Bragg condition since λ is constant. Thus if one were to measure this diffraction angle shift, one could obtain the strain in the normal (n) direction. With enough of these measurements, one has enough information to construct the full strain tensor in the lab reference frame. We will quantify this method in the next section.

2.7.2 Sin²Ψ Method

The sin²Ψ method is used to populate the stress/strain tensor. This method uses the data from multiple tilt angles to fit the strain components. To see how this works, we first look at the definition of strain, and the Bragg law; we combine them into one expression for the strain along the measured orientation as a function of peak shift (Equation 2.52).

$$\varepsilon_{\Phi\Psi} = \frac{d-d_0}{d_0} \quad + \quad d = \frac{\lambda}{2\sin\theta} \quad \rightarrow \quad \varepsilon_{\Phi\Psi} = \frac{\sin\theta_0}{\sin\theta} - 1 \cong \frac{-\Delta\theta}{\tan\theta_0} \quad \text{Eq. 2.52}$$

If we combine the above expression with the definition of a strain rotation to the primary (xyz) coordinate system and we incorporate the elastic constants for a cuboidal lattice, we obtain the master expression shown below in Equation 2.53 (Anderoglu 2004; Fitzpatrick et al. 2005).

$$\begin{aligned} \varepsilon_{\Phi\Psi} = & \frac{s_2}{2} (\sigma_{xx}\cos^2\Phi + \sigma_{yy}\sin^2\Phi + \sigma_{xy}\sin2\Phi - \sigma_{zz})\sin^2\Psi \quad \text{Eq. 2.53} \\ & + \frac{s_2}{2} (\sigma_{xz}\cos\Phi + \sigma_{yz}\sin\Phi)\sin2\Psi + s_1(\sigma_{xx} + \sigma_{yy}) + \left(\frac{s_2}{2} + s_1\right)\sigma_{zz} \end{aligned}$$

This expression can be simplified considerably if we make specific assumptions. For instance, since we are operating on the surface, there is no normal stress. We can also assume no shear strains; in which case we obtain a linear expression. If we allow shear, we have an ellipse courtesy of the sin²Ψ term. These are illustrated in Figure 2.35.

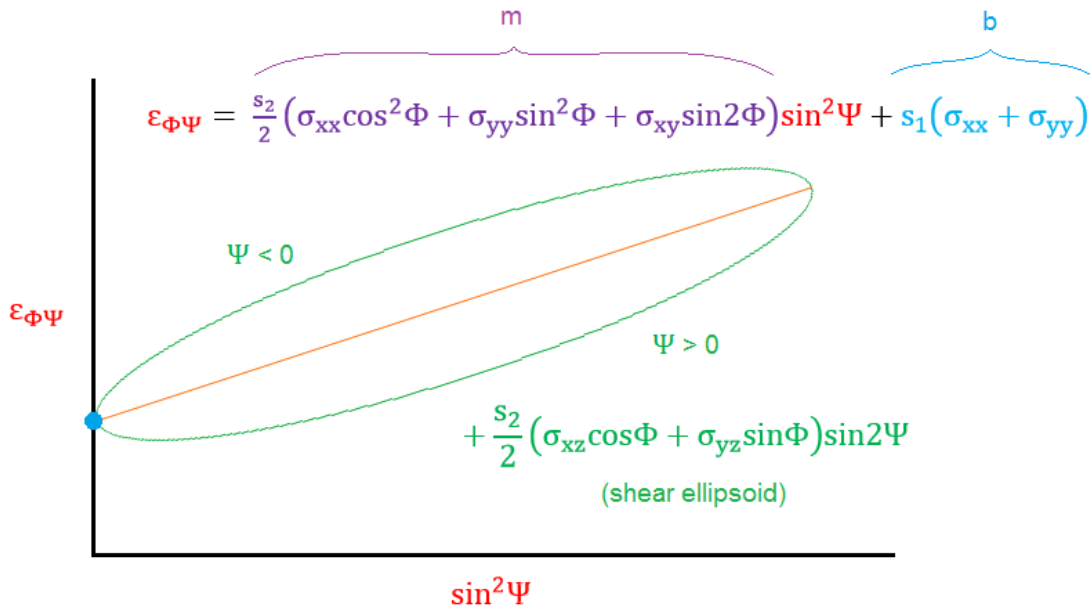


Figure 2.35 – Strain measurement as a function of sin²Ψ. Note in the absence of out of plane shear the expression reduces to a line. If shear is present, there is splitting into an ellipse owing to the sin²Ψ term.

If we combine our strain measurement from the peak shift expression with the master stress-strain relation expression, we can solve for the unknown stress quantities. The number of measurements required is dependent on the complexity of the stress state with a shear-free analysis requiring as few as two tilts (linear).

2.7.2 Experimental Conditions

We saw in the previous section how x-ray diffraction is used to measure stresses in a material. We will now lay out the experimental conditions used in this thesis for the measurement of stresses on the surface of as-quenched martensite.

Material Assumptions

Martensite is classically understood to be a body-centered tetragonal phase with tetragonality that depends on the amount of carbon content. However, it has been reported in the literature that martensite below a critical carbon threshold has a cubic lattice instead of a tetragonal one. This is likely due to carbon diffusion to grain boundaries and dislocations soon after the martensitic phase is formed. This is fortunate for us because the expressions derived previously are for cuboidal lattices. As such, we can use x-ray elastic coefficients for ferrite to analyze our data.

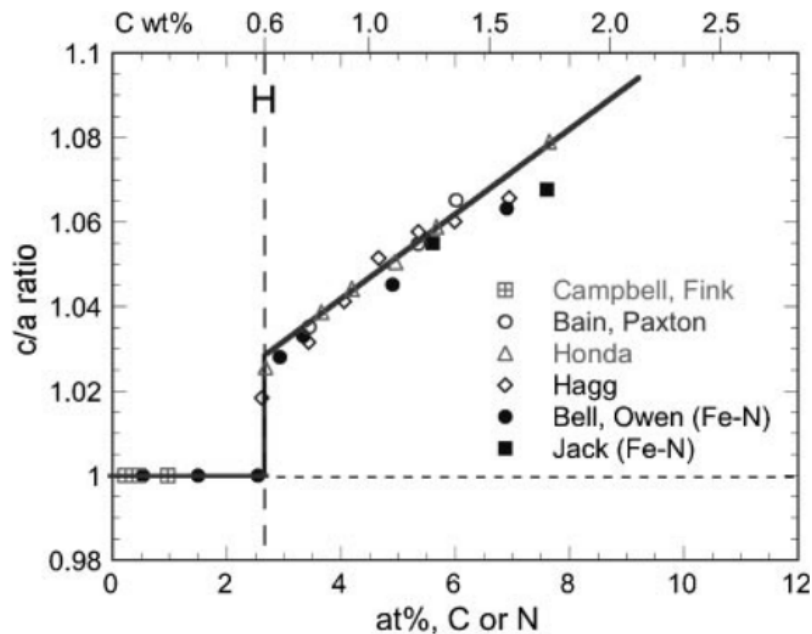


Figure 2.36 (Sherby et al. 2008) – Tetragonality of Iron Martensite as a function of carbon content. Note that below a critical carbon content the lattice is BCC.

Plane Selection

In order to perform our stress measurement, we must choose a plane for which to observe our diffraction peak shifts. From Equation 2.52, we see that a higher angle plane is preferable due to larger peak shifts at high angles. For this reason, we have chosen the 200 plane at a 2θ angle of 123.4° . The following x-ray elastic coefficients were used for this plane:

$$E = 220264 \text{ MPa}, \quad \nu = 0.280, \quad s_1 = -1.271 \times 10^{-6}, \quad \frac{1}{2}s_2 = 5.811 \times 10^{-6}$$

This plane has a good compromise between peak intensity and diffraction angle, thus giving an optimized strain measurement with the lowest error possible.

2.8 Diffusion Simulations

In this section, we will demonstrate the accuracy of our diffusion simulations as well as demonstrate the uniqueness and limitless possibilities of the attainable structures. Earlier, we made the argument that these simulation tools were necessary for structural optimization. We will see first-hand why this is the case in this section.

2.8.1 Diffusion Processing Verification

In order to verify the accuracy of our processing simulations, we have performed a two-dimensional multistage diffusion treatment process on a square rod. We make use of masking structures to obtain more pronounced carbon distribution features. Figure 2.37 below depicts the treatment schedule and shows the comparison between experimental and computed results.

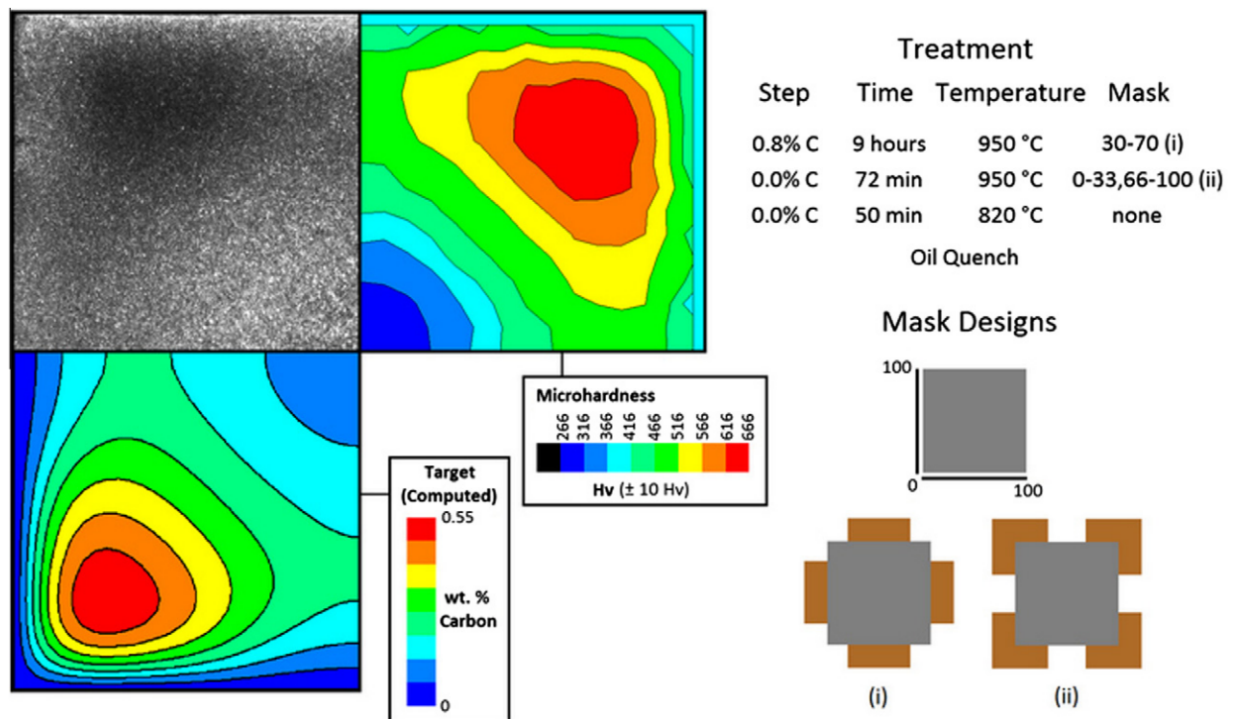
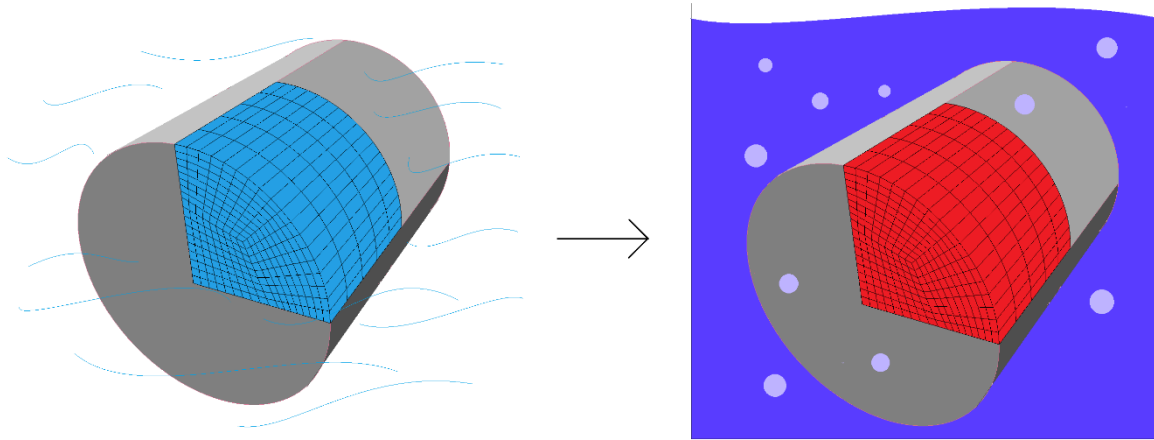


Figure 2.37 (Cicoria, Chehab, and Zurob 2013) - Clockwise from bottom left: computed carbon profile within the square cross-section; etched surface of a fabricated sample revealing relative carbon contents; microhardness of a fabricated sample; treatment schedule; and mask diagram. The final step was undertaken at a lower temperature so that low-carbon regions would exist as ferrite.

We see good agreement between the computed and measured carbon profiles. Our confirmation of this agreement is depicted in the measured microhardness map of the cross-section and the linear relationship between hardness and carbon content (Krauss 1999). We also have visual confirmation of the agreement from etching the surface. Since we performed the last step in the two phase (ferrite + austenite) region, regions with higher carbon content appear darker due to larger amount of austenite present before transformation to martensite.



2.9 Process Simulations

Up until now, we have developed the tools necessary for us to perform high quality simulations of compositionally graded steels undergoing their processing treatments. Additionally, we have developed the tools to verify these simulations with x-ray stress analysis data. For these reasons, we are now in a position to demonstrate the efficacy of our first steps in our attempt to model the constitutive behaviour of martensite. Specifically, at this point, our goal is to obtain the internal stress field present in an as-quenched martensite of arbitrary composition and geometry. Since the macroscopic internal stresses present in as-quenched martensitic materials can be very large, such stresses are essential in determining the behaviour of such components under further loading/testing.

In addition to presenting the results of the simulations, we will also present x-ray analysis data that will give validity to our simulation results. Our simulations are performed with a variety of carbon distributions given on plate, cylinder, and ring geometries in increasing order of complexity. Moreover, the quenchant is varied through slow and fast quenchant. It will be evident that the internal stresses are strongly geometry and process dependent; hence, we will see the justification of developing reliable numerical tools to adequately predict behaviour.

The starting materials we will be using for our diffusion and quenching simulations are aerospace alloy 300M (0.4wt.%C) and Usibor (0.24wt.%C); data sheets for these materials are provided in the Appendix. These steels are thoroughly hardenable in the thickness ranges we are using; for this reason, we do not expect any additional phases after quenching, save for retained austenite at high carbon contents.

2.9.1 Comparison of Quench Rates

In determining the residual stresses present in an as-quenched martensite, it has historically been known that the quenchant used has a significant effect on the internal stresses (Pan 2002). To quantify this effect, a quenching simulation was performed on a 15mm thick plate of austenite at 800°C; both with water as a medium and oil as a medium. The thermal distribution through the thickness of the plates is shown below in Figure 2.38 at different times; it is clear that water produces much steeper thermal gradients in the material and achieves cool temperatures much more rapidly than oil. In large parts, the introduction of a steep thermal gradient will affect the residual stresses due to the differential transformation times through the thickness and the thermal strains themselves.

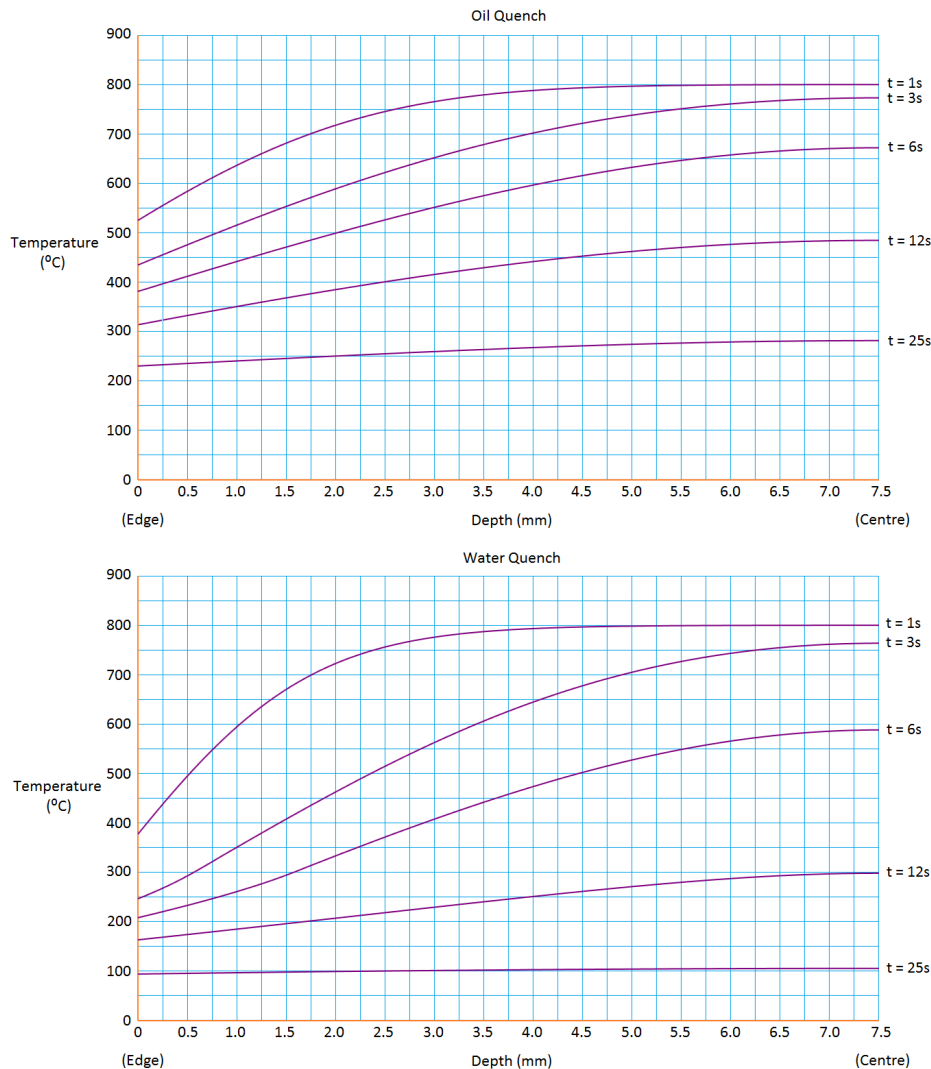


Figure 2.38 – Simulation of the quench rates of oil and water through a 15mm plate of steel starting at 800°C.

The thermal gradients we have seen can be expected to produce residual stresses even in homogenous steel samples. As a baseline to compare between the severity of the two cases, residual stresses are calculated for both quenchantes pertaining to a material with a uniform carbon content. (Figures 2.39, 2.40).

2.9.2 Quenching a Homogenous Steel Plate

As our first type of quenching simulation, we will quench steel plates with a homogenous carbon distribution. The simulations were performed as a function of plate thickness and carbon content for two different quenchants (water and oil). The results of the simulations are shown in Figures 2.39 and 2.40. As conventional wisdom would confirm, the slower quench (oil) typically resulted in lower residual stresses. Water generated surface compression in thicker plates; this compression was amplified with dropping carbon content. The reason for this seems to be that the transformation begins in a temperature range where the thermal gradient is largest when the carbon content is low. Additionally, the thermal gradient is largest in thicker plates. Nonetheless, despite the sizeable surface compression, this compression does not extent very deep into the material.

2.9.3 Quenching Decarburized Steel Plates with Fixed Decarburization Time

The purpose of this study was to determine how plate thickness affects the residual stress distribution when the decarburization time remains fixed. This was done for three different plate thicknesses and for both water and oil quenchants. It is apparent that decarburization results in surface tension regardless of any other variable. In general, the surface tension state increase with increasing plate thickness. This result is reasonable since the surface will be stretched by a larger amount of bulk in thicker plates. An interesting result that was found for decarburized structures is that the stress state in oil quenched samples was larger than in the water quenched samples (Figures 2.41 and 2.42). In this case it seems that a larger thermal gradient has a mitigating effect on stresses through the quench. This further reinforces the need for these simulations as this process phenomenon is not obvious.

2.9.4 Quenching Decarburized Steel Plates with Fixed Distribution Geometry

This study was similar to the previous one except that the carbon diffusion time was matched with the plate thickness in order to achieve geometric similitude of the carbon distribution between plates (Figure 2.43). An interesting result here is that the residual stress distribution after quenching seems to maintain its form but scroll to the right as the plate thickness increases. This information could be useful when extrapolating/interpolating to different plate thicknesses.

2.9.5 Quenching a Decarburized High Carbon Steel Plate

In this study we examine the effect of decarburizing a steel that initially has a very high carbon content (0.75%) (Figure 2.44). The carbon content is such that there will be a significant amount of retained austenite remaining after a room temperature quench. We see that this retained austenite has a mitigating effect on internal stresses for this particular geometry and composition gradient.

2.9.6 Quenching a Carburized Steel Plate

In this study we show how a carbon profile inversion affects the residual stresses in martensitic steel. A steel sample that was depleted of carbon (through an initial decarburization step) is carburized at 0.32 wt.% carbon for two hours (Figure 2.45). We see that this sample exhibits surface compressive residual stresses after a quench. From this, it is evident that we have a fair amount of control over the surface stress state. With drops or increases in surface carbon content leading to tension/compression respectively.

2.9.7 Quenching Decarburized Cylinders of Various Diameter and Surface Composition

The quenching of a cylinder as opposed to a plate is interesting because the stress state is not expected to be shear-free on the surface. For this reason, we have done a full study in which we alter the diameter and surface carbon content of a steel cylinder (Figures 2.46 and 2.47). Like the plate, the decarburization results in surface tensile stresses that increase in magnitude with the amount of surface decarburization. The difference here is that the axial and hoop stresses differ with axial stresses being somewhat smaller than the hoop stresses. Additionally, the residual stress distribution seems to “scroll” to the right as the surface decarburization value decreases. Paradoxically, reducing the diameter of the cylinder results in increased residual stresses. This is contrary to the behaviour seen for plates.

2.9.8 Quenching a Decarburized Hollow Cylinder

Our last study involves quenching cylinders that have had their centers drilled. We examine the changes that develop when only the outside is decarburized and quenched versus the entire structure (Figure 2.48). What is interesting is that the surface residual stresses change considerably when the core is decarburized and quenched as well; despite being a considerable distance from the outer surface. This further reinforces our assertion that geometrical effects on residual stresses are enormous.

Homogenous Plate (Water Quenched)

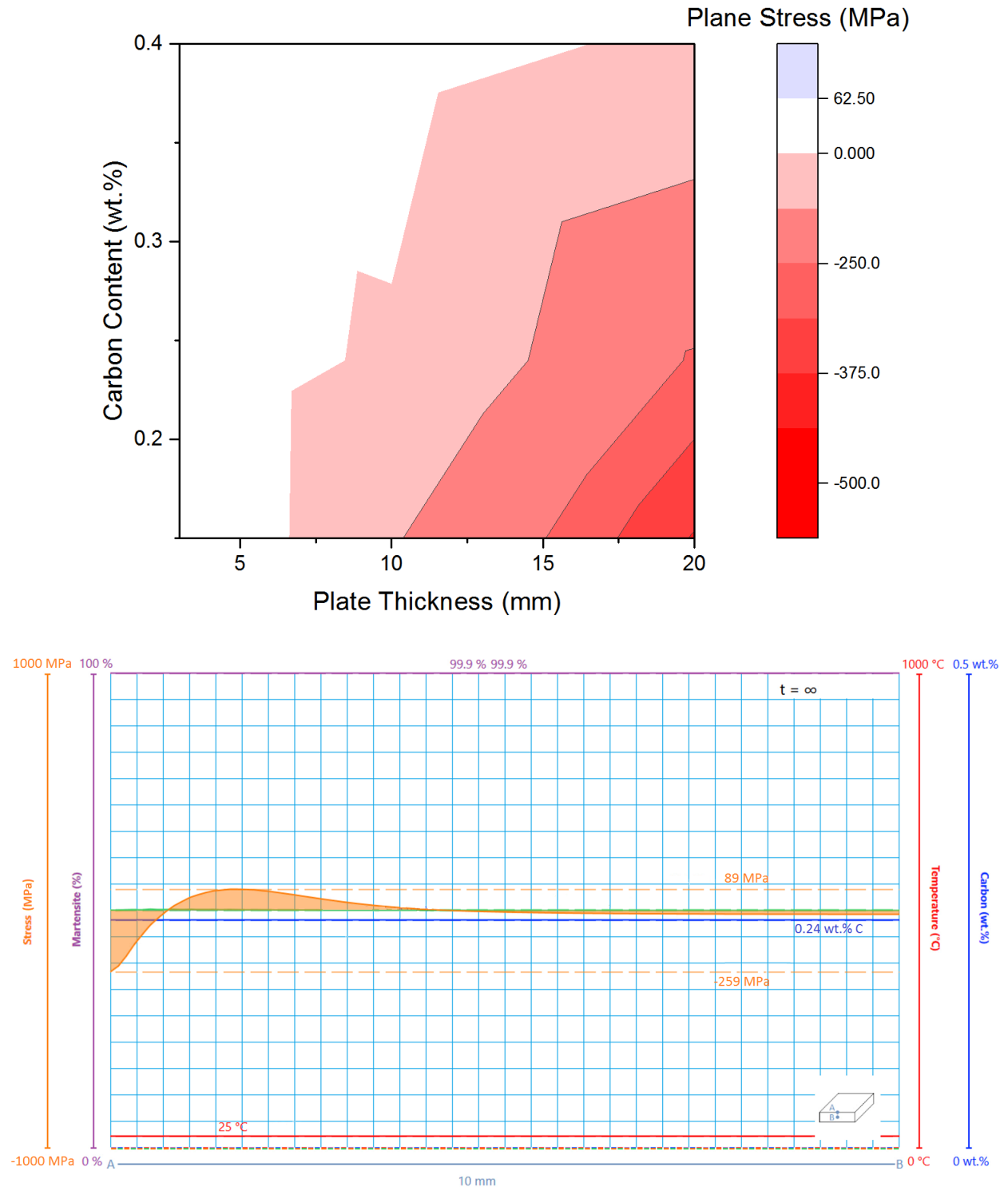


Figure 2.39 – Top – Contour map depicting simulated surface residual stresses in a **water-quenched** plate as a function of plate thickness and carbon content. Bottom – Through thickness profile of all solution variables during the water quench of a 20mm thick homogenous plate of 0.24 wt.% carbon content (Animation Online).

Homogenous Plate (Oil Quenched)

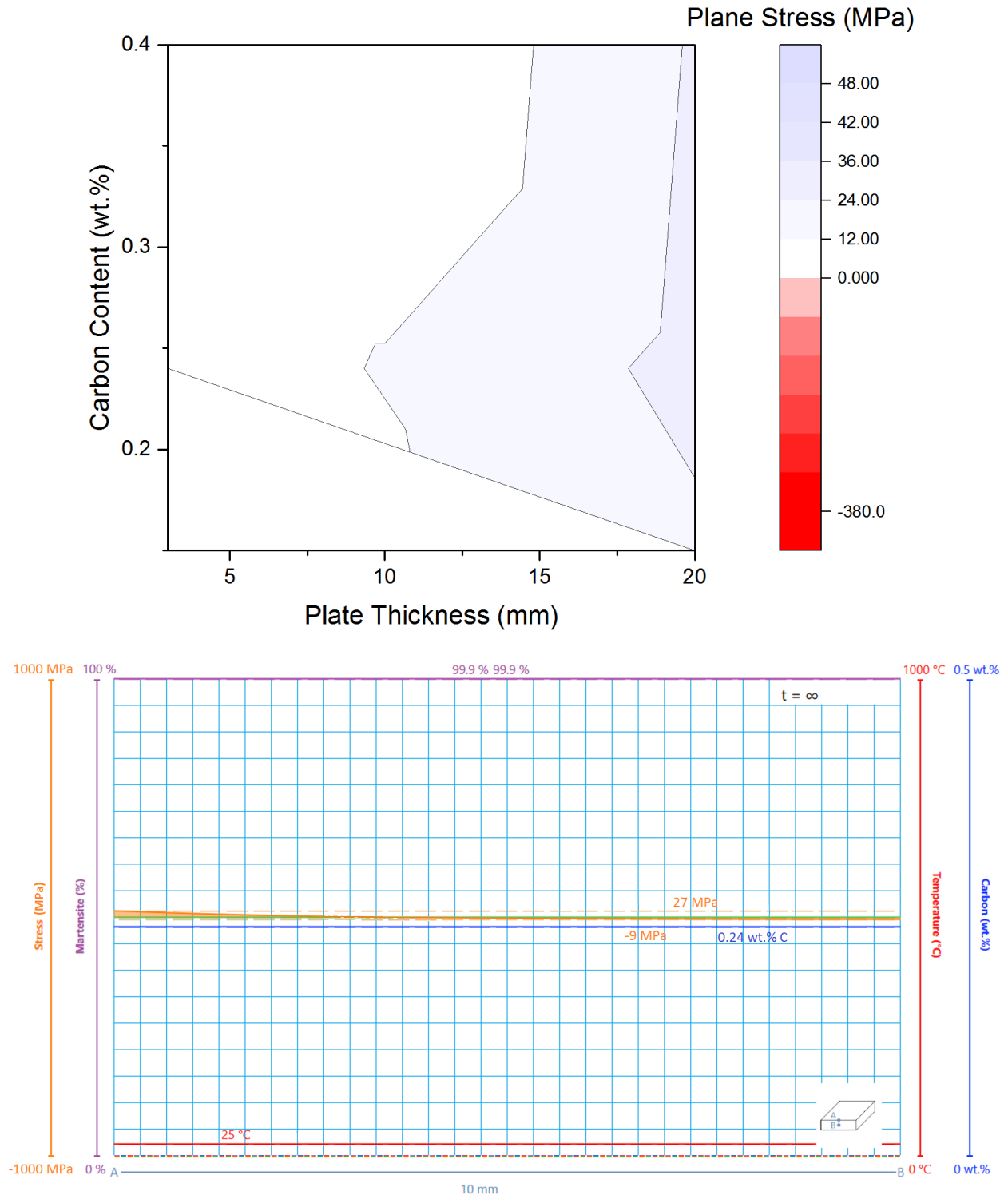


Figure 2.40 - Top – Contour map depicting simulated surface residual stresses in an oil-quenched plate as a function of plate thickness and carbon content. X-ray for 1.6 mm plate of 0.24wt.% C is 25 MPa ± 40 MPa; computed is 0 MPa. Bottom – Through thickness profile of all solution variables during the oil quench of a 20mm thick homogenous plate of 0.24 wt.% carbon content (Animation Online).

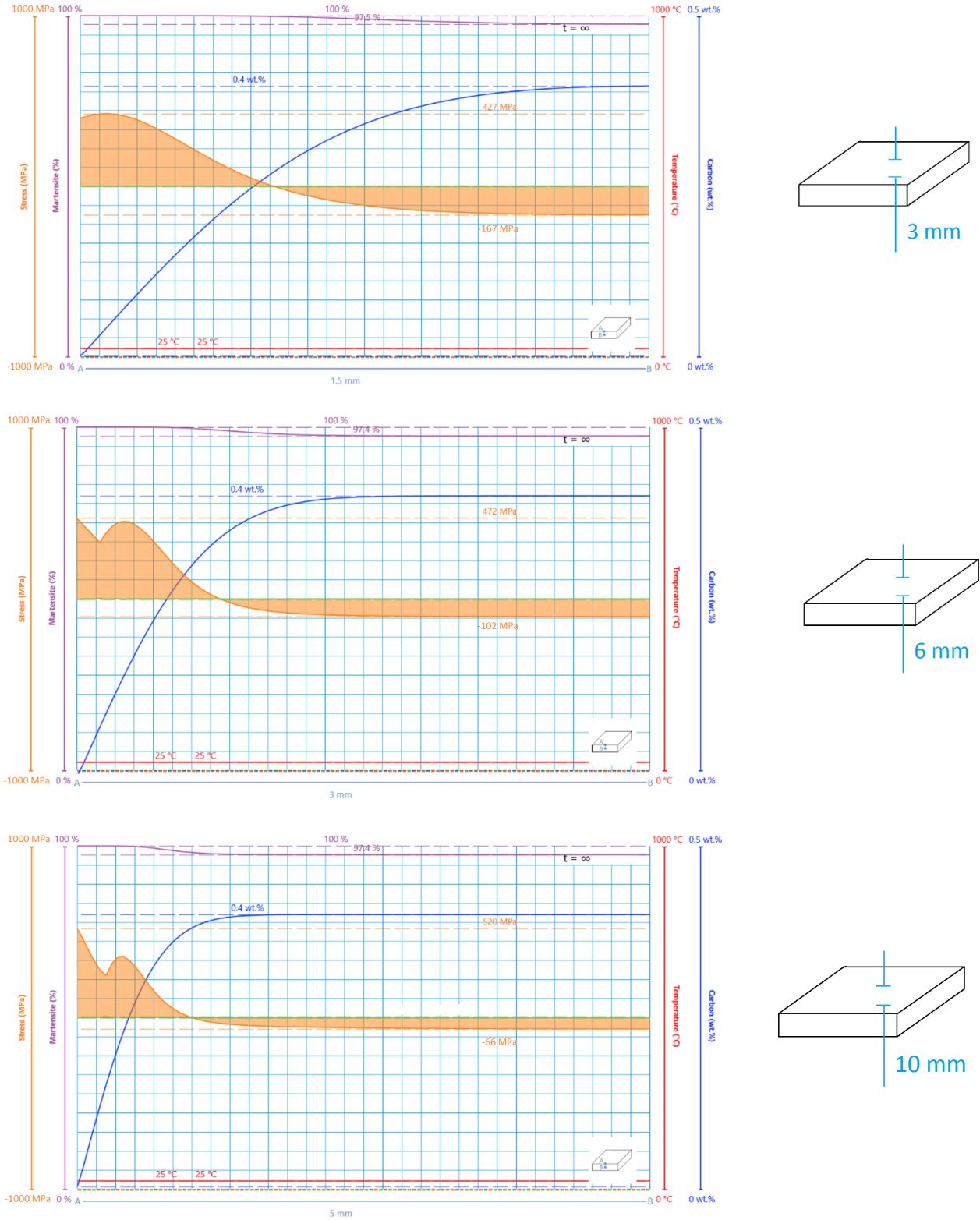


Figure 2.41 – Decarburized 300M alloy of varying plate thickness that has been decarburized for two hours and quenched in water. (Animation Online)

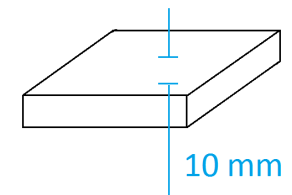
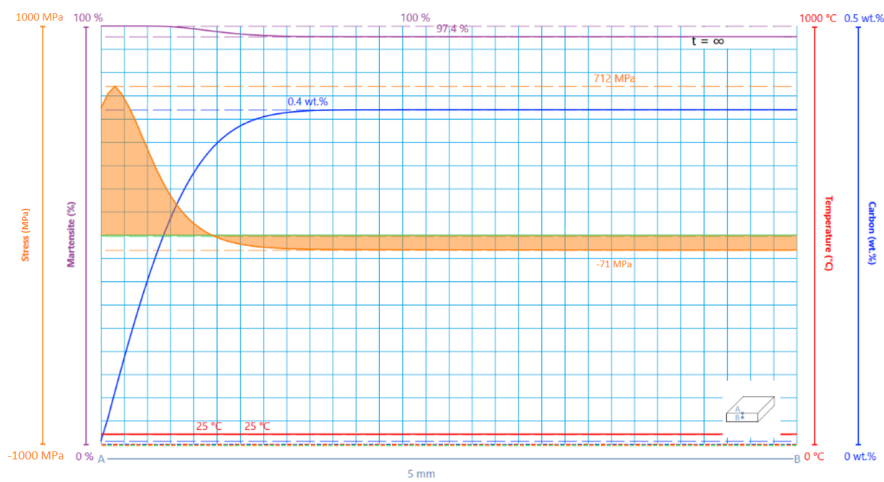
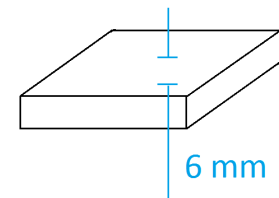
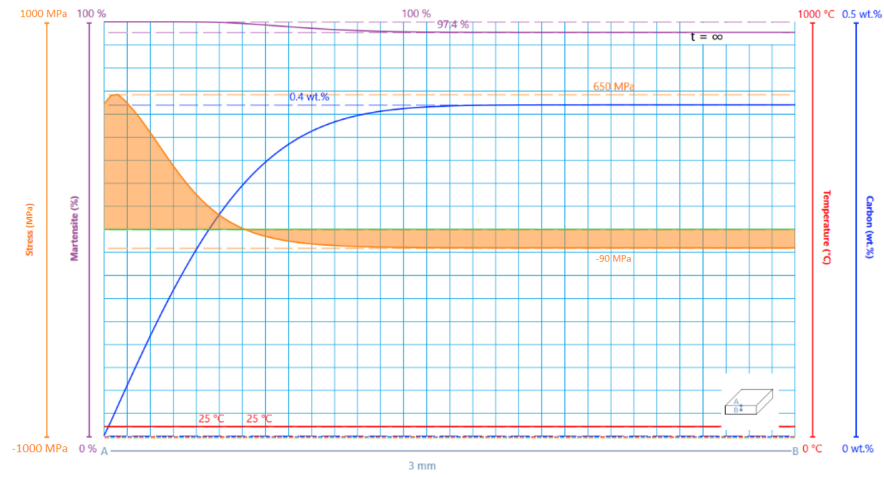
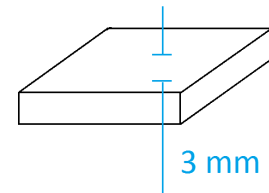
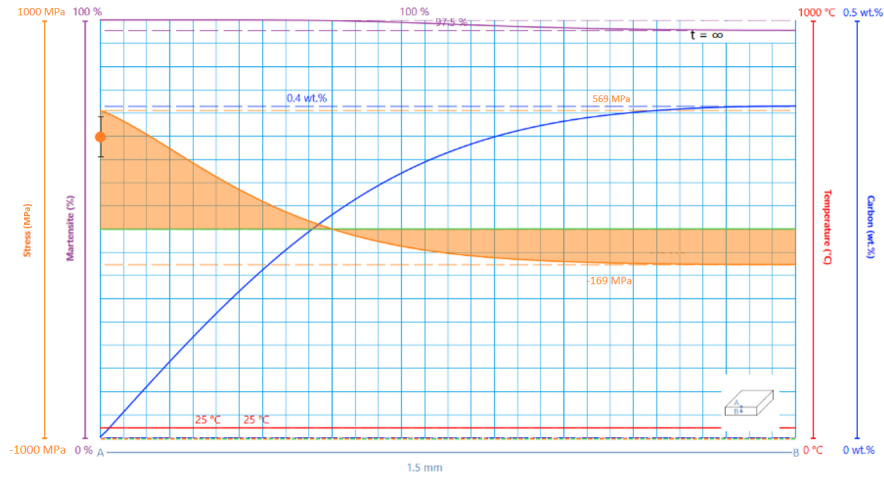


Figure 2.42 – Decarburized 300M alloy of varying plate thickness that has been decarburized for two hours and quenched in oil. (a) X-ray 441 ± 70 MPa. (Computed 560 MPa) (Animation Online)

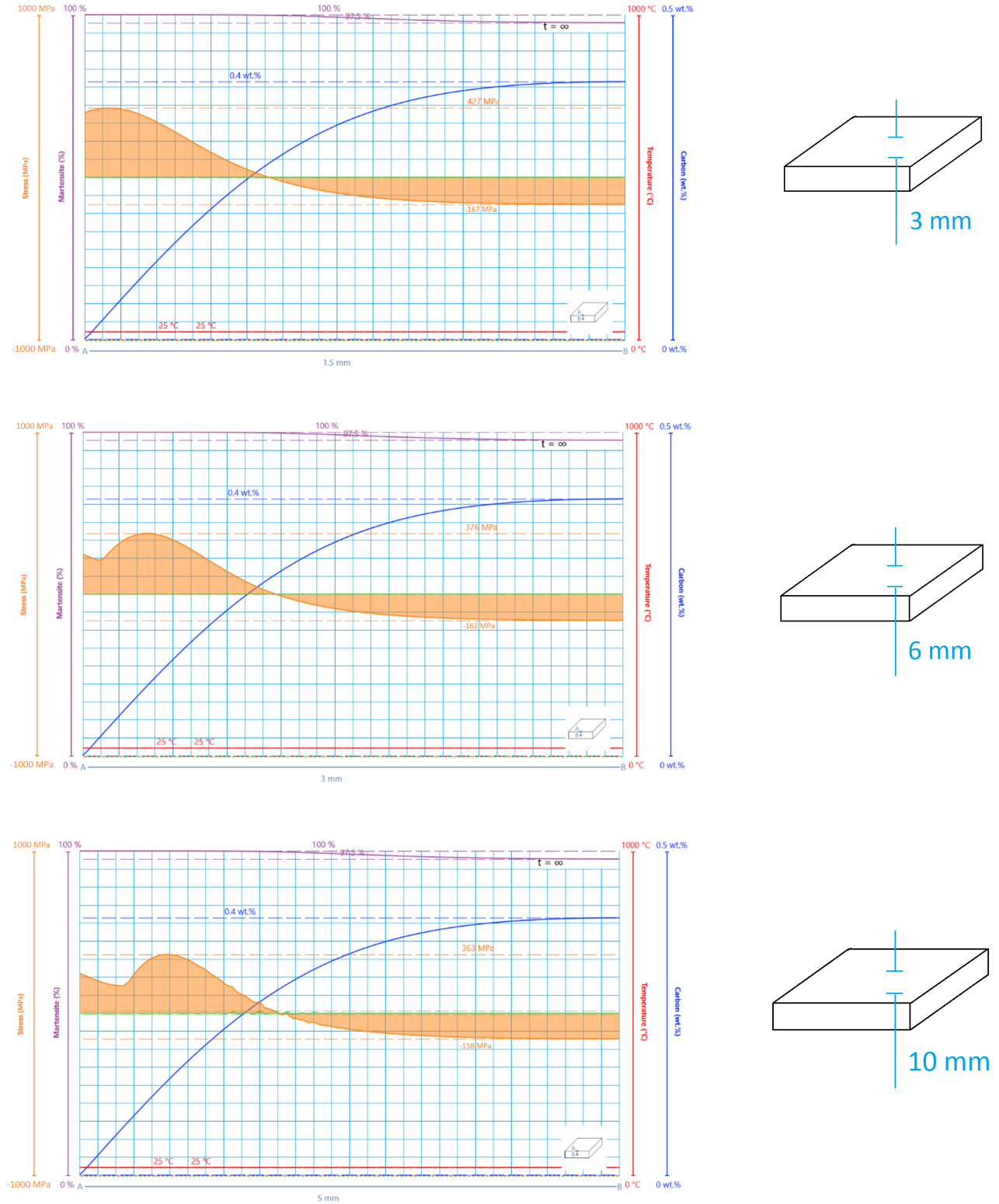


Figure 2.43 - Decarburized 300M alloy that has been decarburized for a proportional time as to achieve geometric similitude with the plate thickness. Quenched in water. (Animation Online)

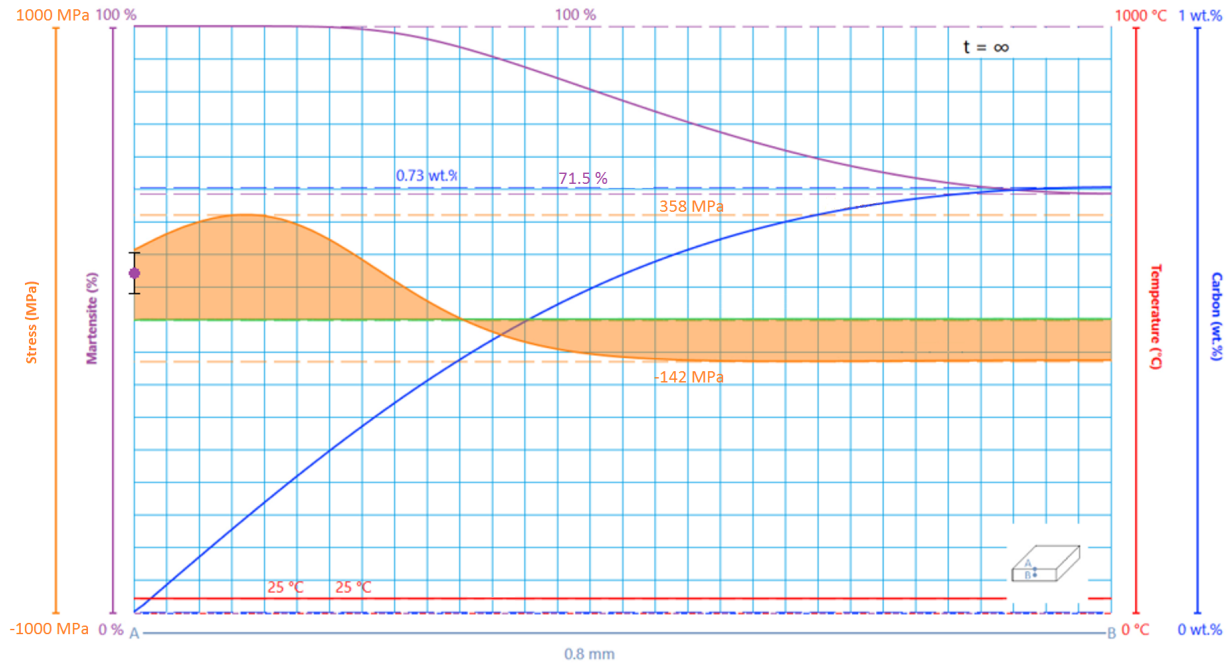


Figure 2.44 - Water quenched thin plate (1.6mm) of high carbon (0.75wt.%) steel that has been decarburized for 50 minutes. Note the retained austenite at room temperature. Xray 150 ± 30 MPa (225 MPa Computed). (Animation Online)

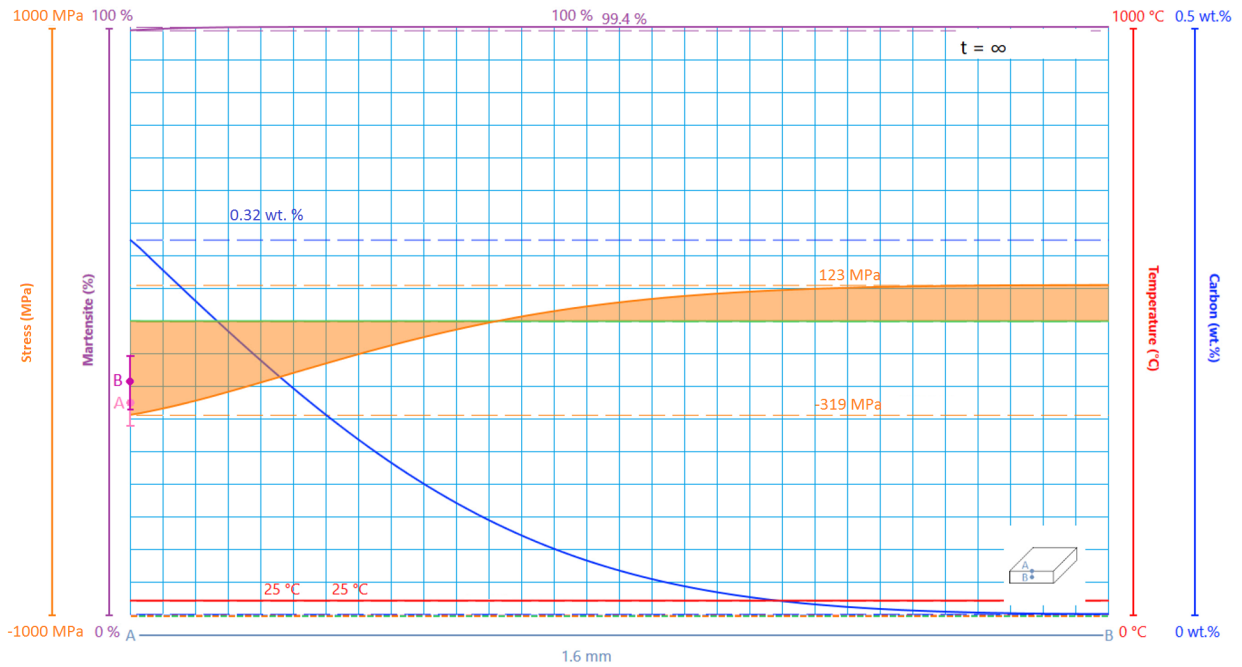


Figure 2.45 - Through thickness profile of all solution variables during the water quench of a 3.2mm thick carburized plate. X-ray data of both sides is shown for the surface with measurements of: A = -274.8 ± 70 MPa, B = -214.1 ± 84 MPa. Computed is -319 MPa. (Animation Online)

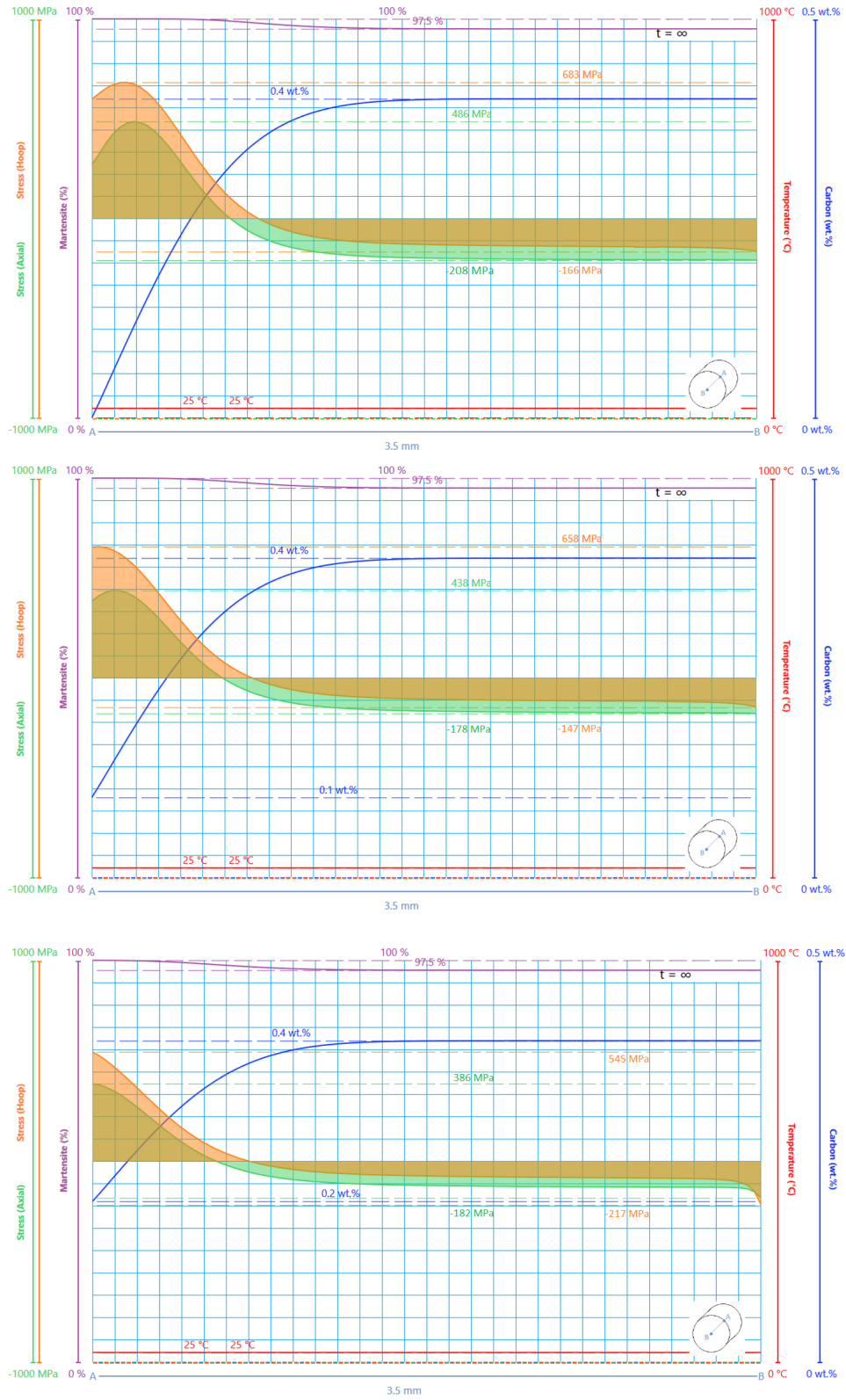


Figure 2.46 – Water quench of a 7mm diameter thin rod that has been decarburized to various surface concentrations. (a) 0.0 wt.% Carbon. (b) 0.1 wt.% Carbon. (c) 0.2 wt.% Carbon. (Animation Online)

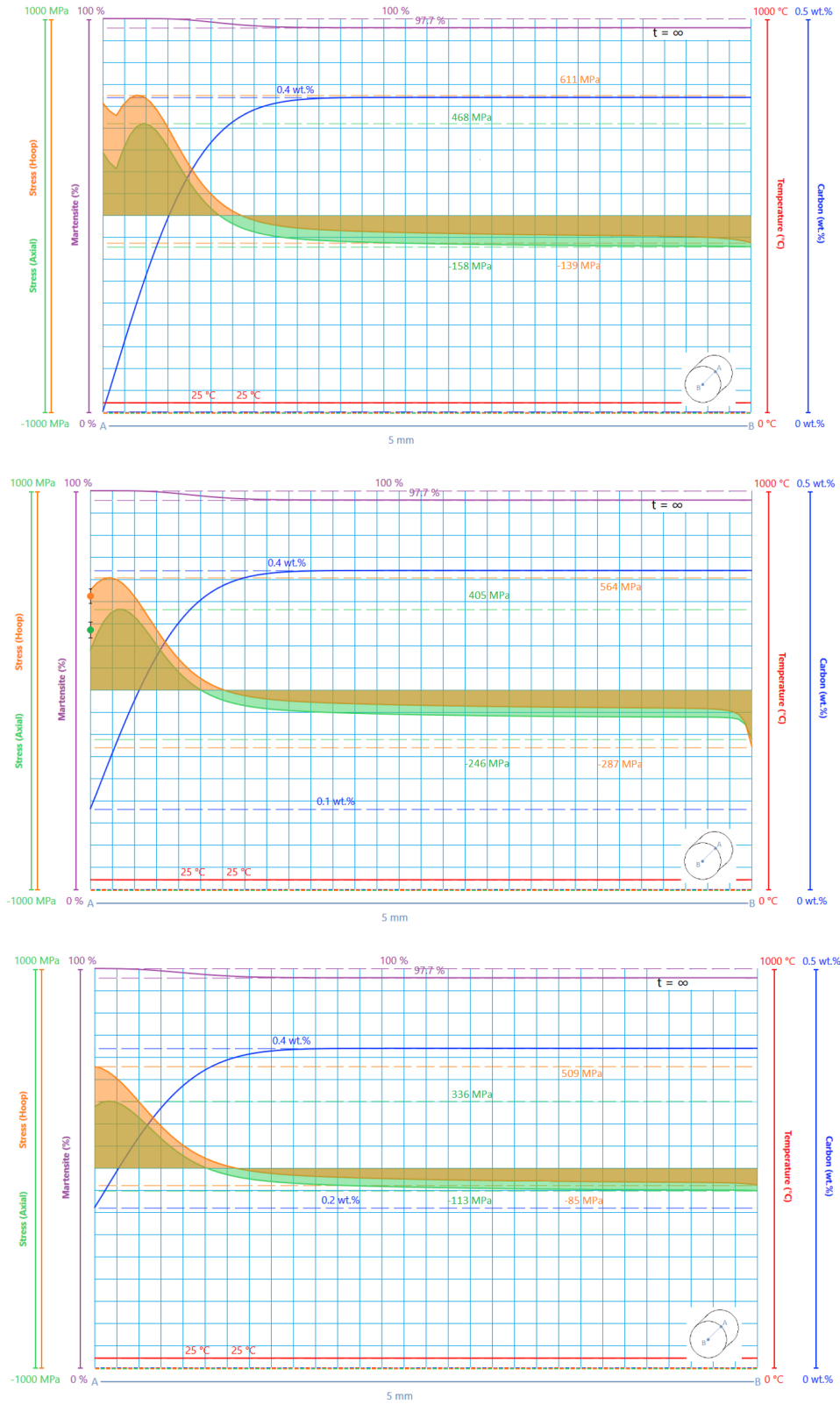


Figure 2.47 - Water quench of a 10mm diameter thin rod that has been decarburized to various surface concentrations. (a) 0.0 wt.% Carbon. (b) 0.1 wt.% Carbon. Xray: hoop 457.5 ± 30 MPa (495 Computed), axial 318.7 ± 35 MPa (220 Computed). (c) 0.2 wt.% Carbon. (Animation Online)

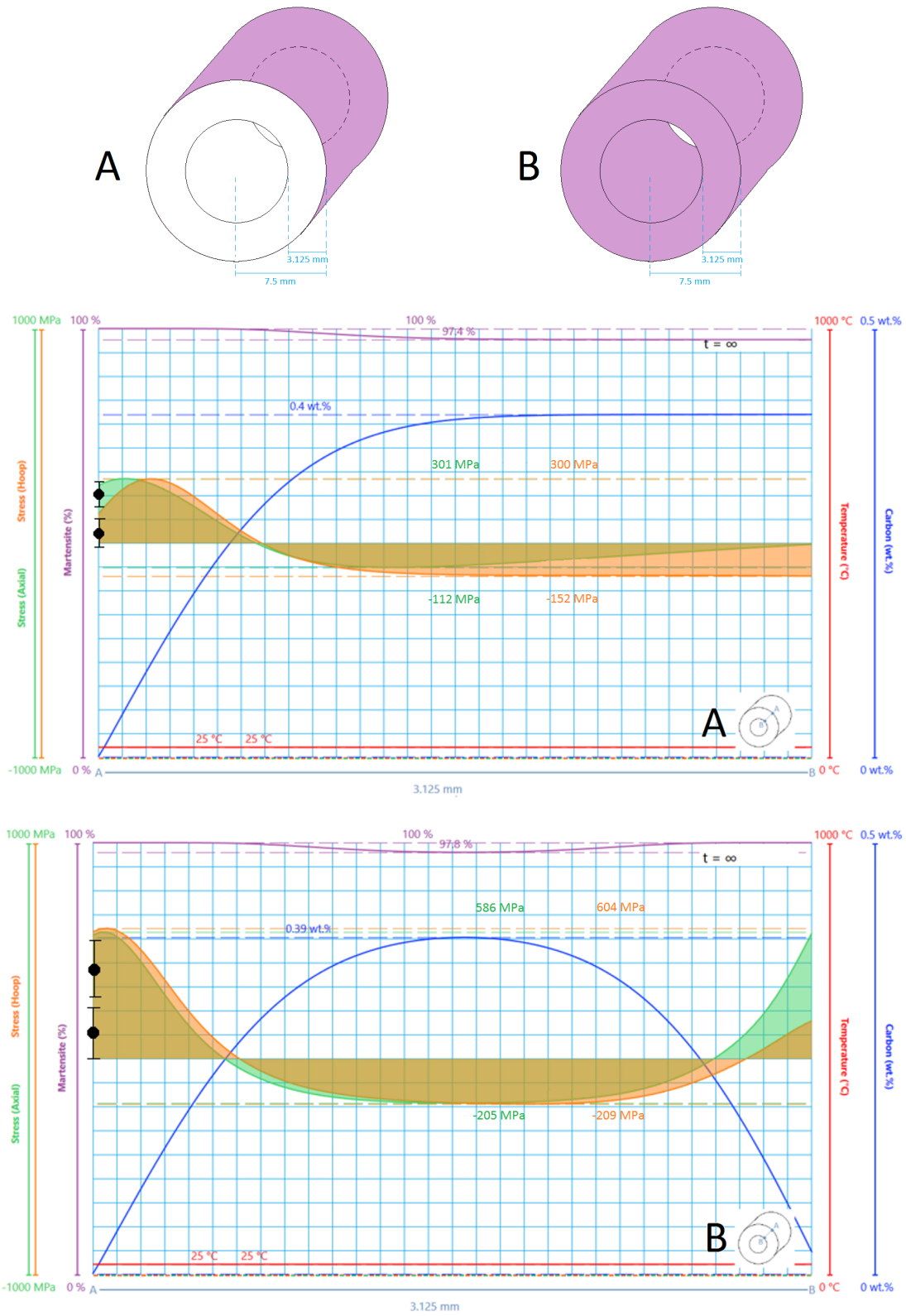


Figure 2.48 – (a) Water quench of a decarburized hollow cylinder with internal and side surfaces masked from decarburization and heat transfer. X-ray: 236 ± 30 MPa, 31.3 ± 30 MPa (Computed 280 MPa, 150MPa). (b) Water quench of a decarburized hollow cylinder with all surfaces exposed to decarburization and heat transfer. X-ray: 400 ± 100 MPa, 125 ± 100 MPa. (Computed 575 MPa, 570 MPa). (Animation Online)

2.9.9 Observations

In our study of residual stresses, we have examined the effects of many variables; namely part geometry, carbon distribution and quenchant. Resultantly, we have made some important observations that really reinforce the need for having simulating tools of this type.

1. Conventional wisdom that a softer quench is gentler is only true for homogenous materials.

It has long been accepted that a slower quenchant will reduce residual stresses at the risk of potentially reducing hardenability. This reduction of residual stresses has been found to be true when working with homogenous samples. However, this line of thinking fails when considering samples with carbon distributions. This result makes sense because ultimately, residual stresses arise when parts of the material change volume at different times. In a homogenous sample, the only source for this difference is a thermal gradient. In a graded sample both the carbon distribution (variable Ms) and thermal gradient cause this effect; it is conceivable that the thermal effect can either contribute or subtract from the intrinsic gradient effect in this case.

2. Trends only exist for a fixed geometry and distribution type

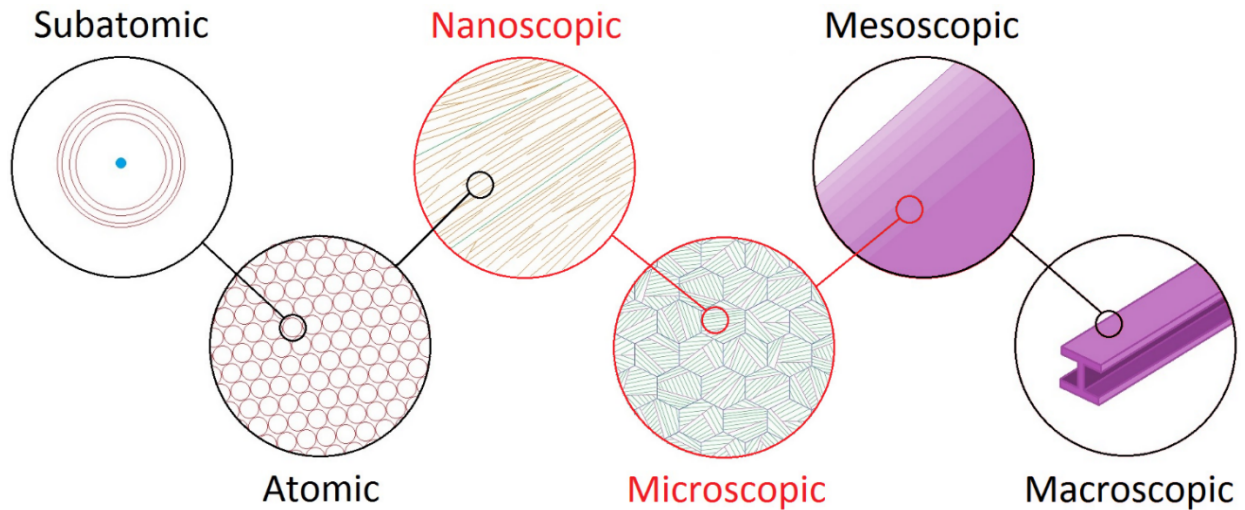
When examining the trends that result from modifying our process variables we see some behaviours such as the scrolling behaviour that was previously mentioned. Additionally, we see fairly predictable changes in surface stress values with subtle changes in process time and surface carbon values. The problem exists when we change large features such as the geometry or distribution profile. Any trends that we may have observed for one geometry may be completely shattered or even inverted with different geometries. This observation really reinforces the main argument that we are purporting; namely that there is a rich area of structural optimization to be found here and that computational techniques are absolutely essential in performing it. The process is simply too complicated for a scientist or engineer to reason qualitatively.

3. Geometry dependent deviations exist between measured and computed stress values

It is worth noting that although the x-ray data has very good precision, the correlation to the simulation may be marginal in some instances due to non-reproducibility's of the quench process. This is especially true for complicated geometries such as cylinders and rings since the quenchant strikes the surface of these objects in an erratic manner, causing deviations from ideal behaviour.

2.10 Conclusions

With this chapter, we have taken the first steps to having a fully reliable computational model for martensite. With only macroscopic generalizations, we have been able to attain the construction of a reliable and accurate tool for the determination of post processing internal stresses present in martensite. Our next step will be to construct a tool that will allow us to take these structures and perform structural loading to see how the structures behave. In the next chapter we will tackle this problem by taking a close look at the microstructure and constructing a constitutive model that is based upon microstructural features; this will allow us to model the room temperature observed large strain behaviour of martensite.



Chapter 3 – Microstructure-Based Constitutive Modelling

The last chapter saw us making significant progress in our quest to model the mechanical behaviour of martensitic steels. We were able to achieve a good mathematical description of the post-processed state of the material using nothing but generalized macroscopic material descriptions. We were able to do this because the transient processing phenomenon existed on a scale much larger than the microstructure. In this chapter, we are tasked with now setting up a material description for a martensitic steel that is experiencing loading that results in the development of significant irreversible plastic strains. We cannot approach this in the same manner we tackled the quenching stage because of the extent of the plastification and the fact that plastic flow is intrinsically a microstructural phenomenon. While plasticity can be dealt with macroscopically, we will see in this chapter that such models are inadequate for martensite undergoing non-monotonic loading. As such, our approach will consist of performing an examination of martensitic microstructural features while considering literature attempts to model such features. Finally, we will compare the performance of using: conventional plasticity models, advanced plasticity models (Masing derived models) in various incarnations, and Representative Volume Element models under various loading regiments, with an emphasis on fidelity and relative computational resources required.

3.1 Mechanical Behaviour of Martensite – A First Look

A good starting point for modeling martensite's large strain behaviour is to examine a simple monotonic loading curve. Figure 3.49 shows the monotonic loading behaviour of lightly tempered martensite of various strengths. A striking feature of this material is that there is no clear distinction between an elastic and plastic loading regime; rather, the material exhibits continuous yielding. The tangent is gradually dropping from what appears to be a very early point in straining. From a monotonic loading curve alone, one could develop various hypotheses for the behaviour; the most promising of which are based-upon the inhomogeneous microstructure. A pure dislocation-based work hardening mechanism is discouraged due to the non-physical work hardening rates that would be required. Indeed, if one were to reverse loading of the curves, as is shown in the next section, such a model is seen to be wholly inadequate. Additionally, one notices a large vertical stretch of the curves upon increasing carbon content; if work hardening were to be the blame, one would expect the initial yielding to increase with Carbon and the hardening capacity to somewhat decrease. Instead both the initial yielding and the hardening capacity increase drastically. In this section, we will seek alternative explanations for such behaviour.

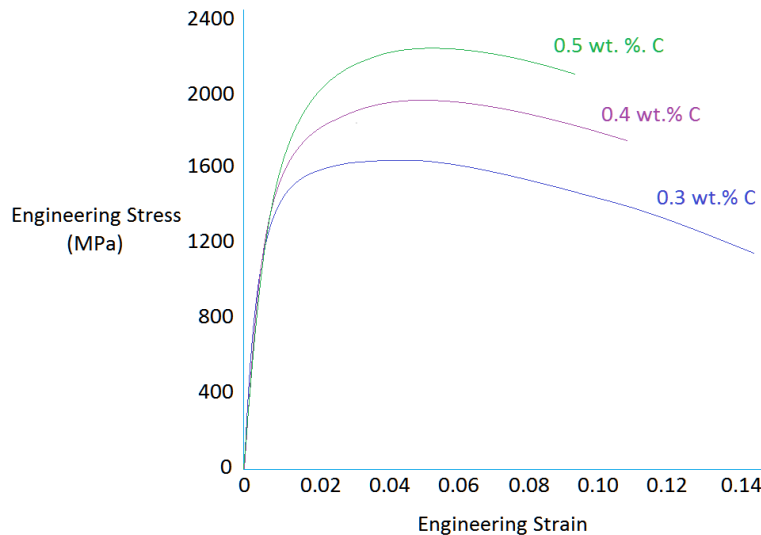


Figure 3.49 – Monotonic data from 41xx steel series. Data with a light 150°C temper is shown to demonstrate large strain behaviour. Data from (Krauss 1999).

3.1.1 Uniaxial Mechanical Behaviour

In order to gain more insight into the problem, we examine a full Bauschinger curve of as-quenched martensite (Figure 3.50). We see from this curve that if we were to examine a range of hardening rates in the forward direction, and find the equivalent range in the reverse direction, the range in the reverse direction would in fact be over a larger strain. This begs the question, how would a hardening mechanism be not only replenished, but also maintained over a larger strain range in the reverse direction? Additionally, how would the point of initial yielding be reduced in the reverse direction? In order to answer these question, we turn to the work of George Masing (Masing 1923, 1926). In essence, Masing proposed that such behaviour could be modeled as an agglomeration of elements with different strengths; each undergoing different strain modes simultaneously. The global

reduction in hardening rate with strain is the result of elements gradually reaching the plastification regime. Such a description is consistent with current microstructural explanations of the Bauschinger effect in a wide variety of materials; namely, stresses building up between multiple phases and dislocation pileups generating incompatibility stresses at phase boundaries.

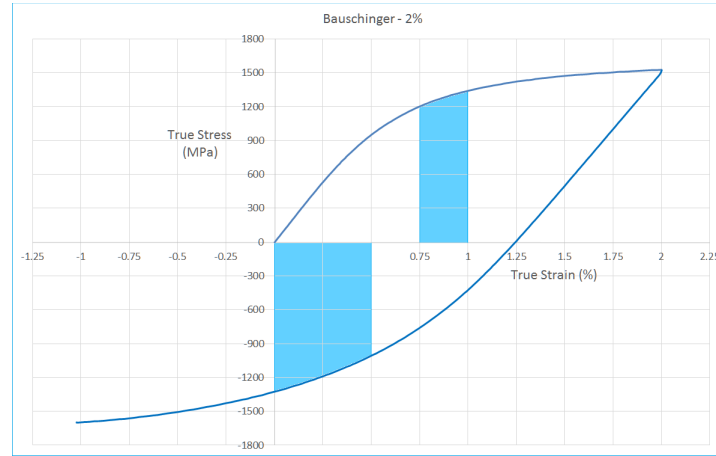


Figure 3.50 – Bauschinger Test conducted on Usibor 0.24wt.%C steel (as oil-quenched). Regions of equivalent hardening rate are highlighted in both the forward and reverse directions. (Bauschinger data courtesy Reza Roumina)

Masing’s Hypothesis

Back in the early 20th century, George Masing attempted to model macroscopic plasticity as a collection of elastic and perfectly plastic elements connected in parallel (Masing 1923). This attempt at modeling plasticity was significant because it was the first attempt that was able to adequately model gradual yielding behaviour as well as qualitatively proper Bauschinger behaviour of real material’s uniaxial response. In performing this study, he came upon an interesting result that came to be known as Masing’s hypothesis or postulate (Iwan 1967; Montans and Borja 2002; Mróz 1967; Tseng and Lee 1983). This hypothesis states that if one were to model plasticity in this manner, the curve obtained in reverse loading is a homologue of the forward loading curve and scaled by a parameter η (homology factor). This condition is defined mathematically below.

$$\text{if } \sigma = f(\epsilon) \text{ then } \bar{\sigma} = \eta * f\left(\frac{\bar{\epsilon}}{\eta}\right) \text{ where, } (\bar{\sigma}, \bar{\epsilon}) \text{ define a reverse loading axis}$$

$$\eta < 2 \text{ – cyclic softening}$$

$$\eta = 2 \text{ – stable cyclic behaviour}$$

$$\eta > 2 \text{ – cyclic hardening}$$

Many macroscopically defined plasticity models are related in some manner to Masing’s work. Besseling (Besseling 1958) extended this work to a two dimensional surface and considered stacked plane elements of different strength. From that point, more complex plastic surface models were developed. These models span the regime of multisurface plasticity models introduced by Mroz (Mróz 1967) which define a warping work hardening field; as well as bounding surface plasticity models introduced by Krieg (Krieg 1975) that have a work hardening rate that is dependent on the distance from the load surface to the bounding surface. In fact, these models are tested to satisfy Masing’s hypothesis and are all effectively three-dimensional incarnations of Masing’s parallel element model.

A limitation of using these models to define plasticity occurs if one's material does not behave in ideal Masing manner; ultimately it could be very difficult to expand a macroscopic model to explain deviations. As such, we will take a look at how martensite behaves in Bauschinger tests and compare it to a Masing type model. The comparison is made in Figure 3.51.

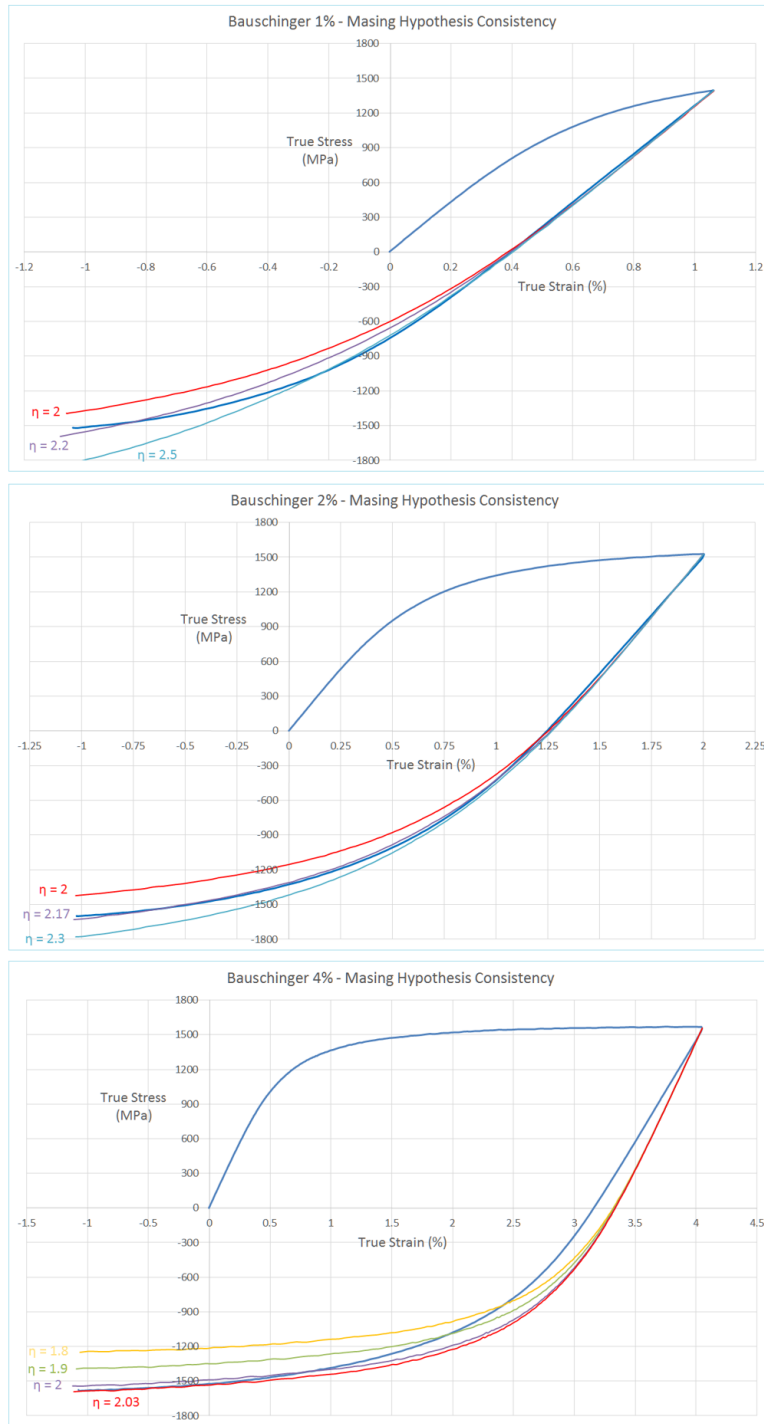


Figure 3.51 – Masing’s Hypothesis tested on Bauschinger Data for Usibor 0.24 wt.% Carbon Martensitic Steel (as oil-quenched). Various homology factors are tested including Masing’s stable factor of 2. Note the inconsistent fit behaviour between the model and the data at high strains; with only the 1% and 2% tests performing ideally. (Bauschinger data courtesy Reza Roumina)

The comparison of Bauschinger data to a Masing explanation is very suitable; especially at low strains. Although, the model begins to deviate from the data at high reversal strains it would appear (buckling of the sample may contribute to this). Nonetheless, the proximity of the data to Masing's model implies that a mechanism of differential yielding between subelements has an important contribution to the overall behaviour. The deviations likely apply because the deforming elements are not arranged in parallel as Masing assumed, but rather as the complex microstructure dictates. Due to the influence of Masing-like behaviour, the first three-dimensional plasticity models we test for martensite will be based upon Masing's work. Before we do that however, we will take a look at fully multiaxial loading behaviour of martensite and then examine the microstructure for additional insight.

3.1.2 Multiaxial Mechanical behaviour

In the last section we examined the Bauschinger behavior of as-quenched martensite. This corresponds to a prestrain followed by a load reversal of 180° . If we look at the hardening rates of different loading orientations after the material has been prestrained approximately 2% and unloaded, we see definite anisotropic hardening behaviour (Figure 3.52). The point of offset yielding is reduced with rotation, and the hardening capacity is increased. Thus, any extension of Masing's observations will have to accommodate such behaviour. However, the behaviour seems smoothly consistent with rotation and we know that the extreme angles are consistent with Masing.

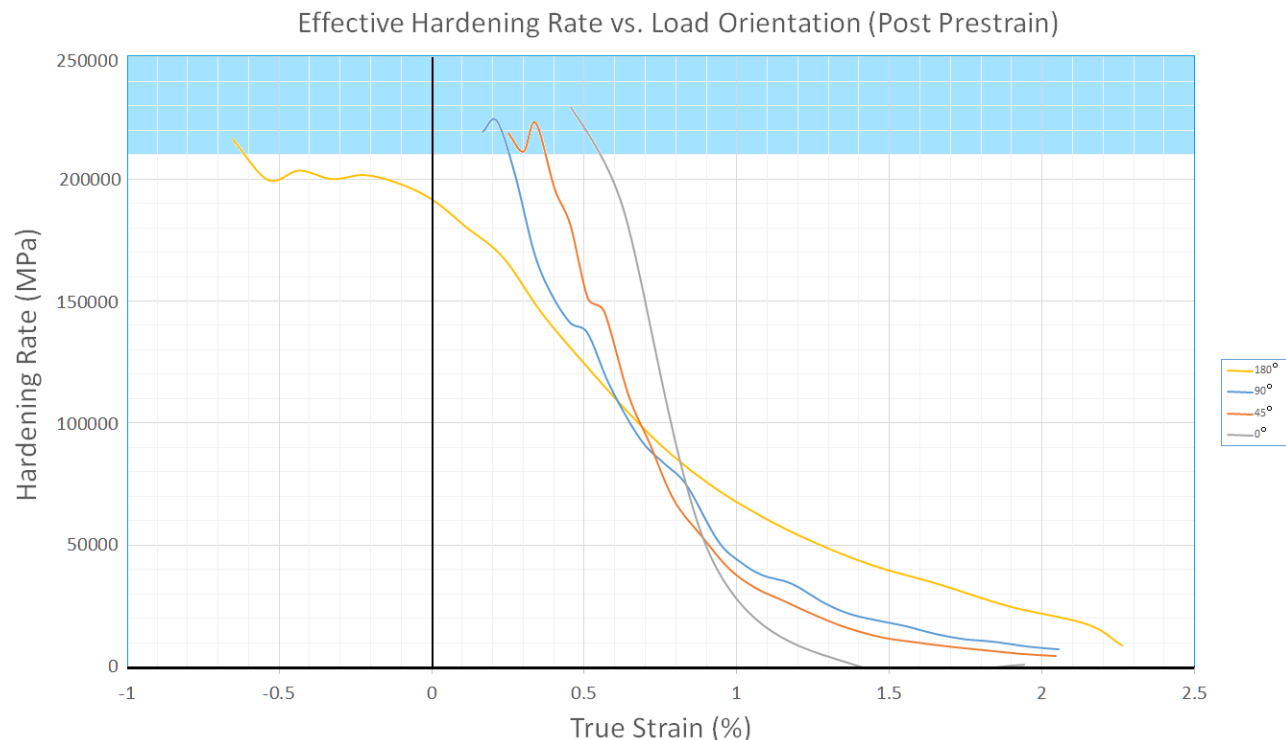


Figure 3.52 – Hardening Rates for as-quenched Usibor 0.24wt.%C steel samples that are loaded at different orientation relative to a defined prestrain direction in the deviatoric plane (180° rotation is compression relative to initial tension). Data has been scaled to accommodate material from different batches. Notice the yield strength and hardening capacity exhibit significant anisotropic behaviour.

3.1.3 Microstructural Examination

We just made some significant observations regarding the mechanical behaviour of martensite from a phenomenological perspective. In this section we examine the microstructure of martensite and the mechanism by which it forms to see if there is a strong basis to considering Masing's model.

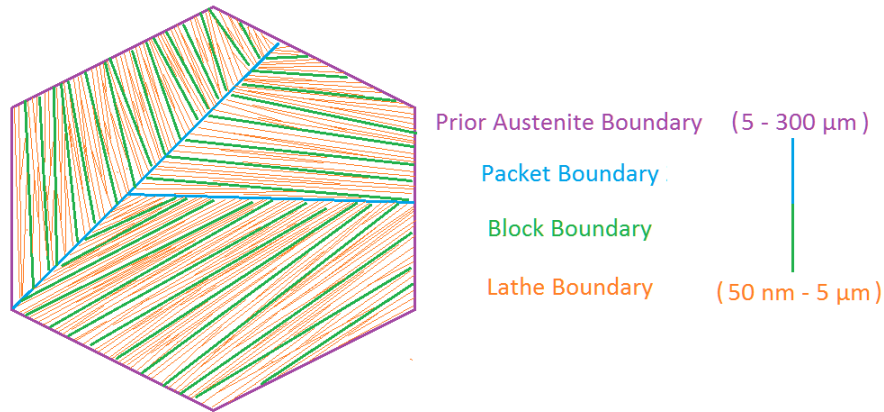


Figure 3.53 – Schematic depiction of lath martensite with the varying length scales of the microstructure.

It is well known that martensitic steel with low carbon content has a characteristic lath structure (Badinier 2013; Krauss 1999; Morsdorf et al. 2015; Sherby et al. 2008). This structure has hierarchy with divisions of the prior austenite grain into a packet, block and then lath substructure (Figure 3.53). When examining the lowest level of the hierarchy (the laths), it is found that these laths can have a vastly different thickness within the same material. In fact, this size can range from tens of nanometers to several microns (Badinier 2013; Morsdorf et al. 2015). The reason put forward for this in the literature is that laths that form at different points relative to M_s on cooling have different characteristic features. Additionally, one can imagine that a lath that forms first will undergo more auto-tempering than one that forms closer to room temperature. As such, it is reasonable to deduce that the microstructure can vary between laths as well. This is significant because it implies that the resistance to yielding will vary throughout the microstructure of martensite; both because of Hall-Petch effects and differing amounts of carbon segregation.

Already one can see that the use of a Masing type model is justified; we have discussed how elements with different yield strengths can exist in the microstructure and these elements will deform heterogeneously. Direct experimental evidence exists in the literature regarding the idea of varying hardness between laths. In an experiment done by Morsdorf (Morsdorf et al. 2015), the nano-hardness of various laths was shown to vary by as much as 100%. Figure 3.54 depicts these measurements spread over the domain of a prior austenite grain. Since the size of the nano-diamond indenter was 200 nm, it is conceivable that lathes smaller than this size would have an even higher hardness than those measured.

A key difference between the microstructure observations and Masing's model is that the laths are not arranged in a parallel arrangement as Masing's model would have us assume. As such, the model cannot be expected to perform perfectly (as was demonstrated in Section 3.1.1); nonetheless, working-in the real geometry of the laths is a good starting point for improving the model; a task we will undertake at the end of this chapter.

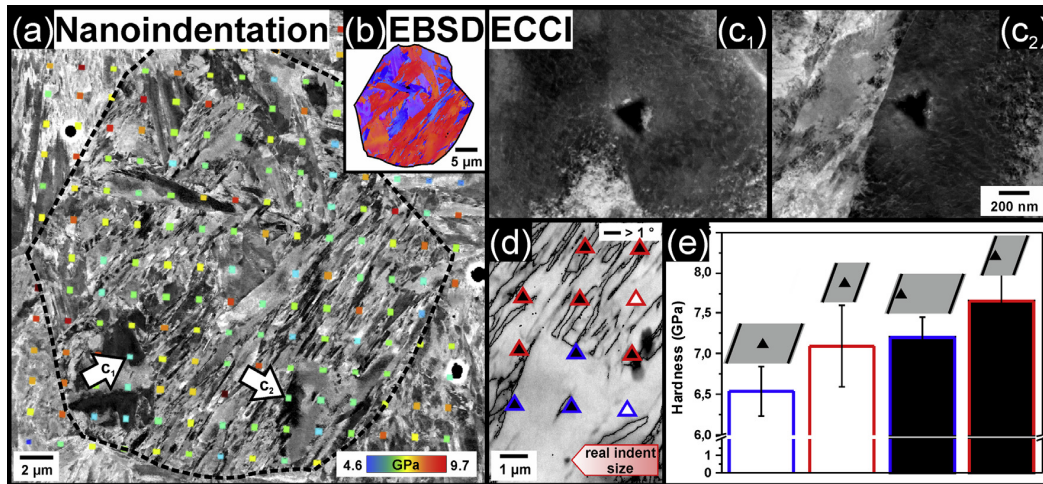


Figure 3.54 (Morsdorf et al. 2015) – (a) Nano-hardness map of lath martensite showing the large variation in lath hardness. (b) EBSD of prior austenite grain. (c1) and (c2) depict indentations in the bulk and next to a grain boundary respectively. (d) and (e) depict indent data for large and small laths both in the bulk and near a boundary.

Before leaving this section and delving into the specifics of modelling martensite, a second microstructural feature should be discussed. It was shown in the last chapter that the martensitic transformation has a large shear component. Accommodating a large shear in an austenite matrix requires a considerable amount of plastic accommodation; numerical simulations of the martensitic transformation have confirmed this fact (Yamanaka, Takaki, and Tomita 2010). Now, if we know that there is a large amount of plastic accommodation occurring, we know from the last chapter that plastic accommodation and residual stresses go hand in hand, so it is not unreasonable to expect that the martensite laths/plates are under a considerable amount of stress in their as-quenched configuration. Adding further evidence to such an assertion are micrographs of acicular martensite in which it is clearly shown that there are regions where plates are impinging upon other plates and cracks resulted (Figure 3.55); such is strong testimony to the presence of these internal stresses. Although we mainly deal with lath martensite in this thesis, such behaviour could reasonably be expected to extend to this microstructure as well. This is significant because when formulating models, it needs to be taken into account that subelements in the structure are not necessarily in a relaxed state.

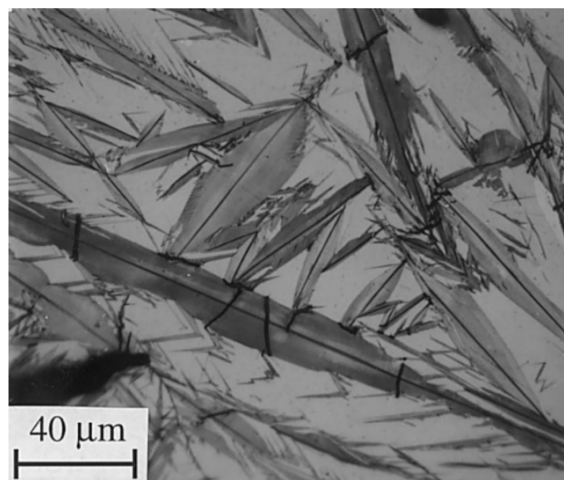
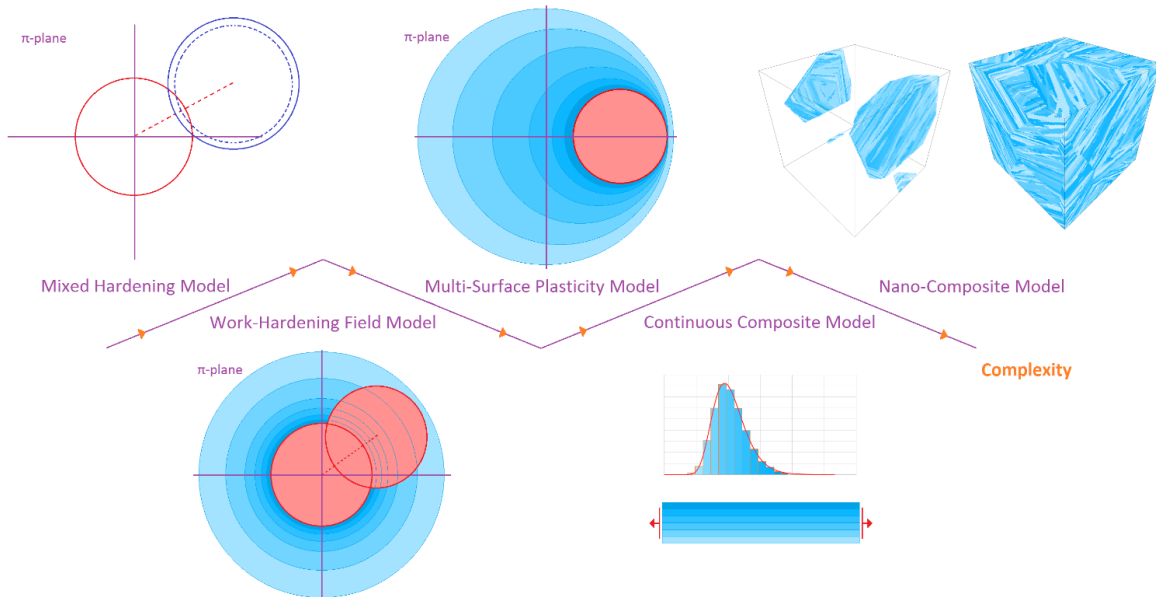


Figure 3.55 (Krauss 1999) – Cracking of plates in acicular martensite



3.2 Overview - Modelling Techniques

We will now introduce the modeling techniques we will use in this chapter to mathematically accommodate the experimental mechanical behaviour of room temperature martensitic steels. We brought up previously that these models have varying levels of complexity. Indeed, we will see that this complexity increases as we decide to introduce more microstructural features into the model; that is, the model becomes more physically based. From our discussions in the previous section, the key concepts to be focused on in this regard are: Non-homogeneous yielding, plasticity mechanism activation, spatial inhomogeneity, and evolved internal stresses.

In a realist sense, the fidelity and complexity of any given model should increase as the mechanics more closely match what is observed in reality. It is no surprise that the cheapest models, which make broad stroked statements, have a more abstract resemblance to a yielding martensitic steel (such as the Masing parallel arrangement of subelements); whereas a complex model which incorporates as many features as possible, such as a nanocomposite model, resembles a yielding piece of martensite at the microstructural level. In this chapter, we are after a macroscopic description, however, we will see that a good description is not possible without a competent microstructural description “under the hood” so to speak. The required degree of complexity however is not clear and determining it is the main focus of this chapter. For this reason, we will introduce five models in increasing order of complexity as: a conventional mixed hardening model (minimal microstructural considerations), a work-hardening field model (abstract pseudo-Masing), a multi-surface plasticity model (abstract Masing), a continuous composite model (true Masing), and various structures based upon Representative Volume Elements (maximum feasible microstructural considerations). Each will now be detailed.

3.2.1 Conventional Mixed Hardening

A conventional mixed hardening model is a staple of plasticity modelling. These models are very widely used with implementations in both metal and non-metal plasticity. What defines these models is a phenomenological concept of a yield surface; a surface that is defined in stress space that dictates that plastic flow will occur when the stress-state reaches it. The position and shape of the surface as well as the plastic flow direction upon contact with the surface are all dependent on the specific model used; however, in the case of most metals, a vonMises-type surface with a plastic flow direction normal to the surface has been historically very effective for mechanical descriptions.

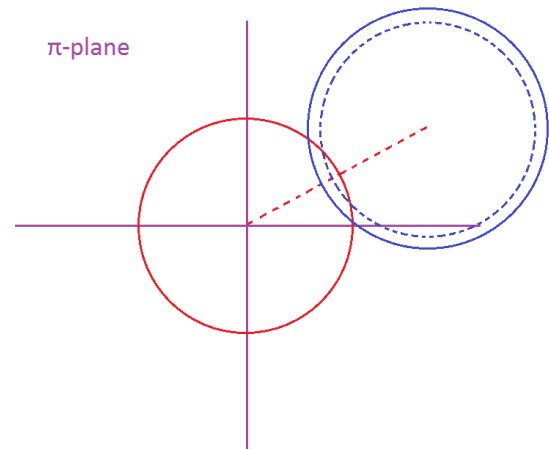


Figure 3.56 – Depiction of VonMises plasticity with both isotropic and kinematic hardening components.

We discussed vonMises plasticity in the previous chapter; the yield surface is a hypersphere in the deviatoric stress space of radius $r_s = \sqrt{2/3}v_y$ where v_y is the uniaxial yield strength of the material. Upon the evolution of plastic flow, the phenomenon of hardening is incorporated by a growing (isotropic hardening) or shifting (kinematic hardening) of the yield surface (Prager 1955; Ziegler 1959). In these models, the yield point may be anisotropic, however, the hardening rate is generally isotropic; that is, the hardening rate does not depend on where the yield surface is breached. The evolution of such hardening is usually obtained from experimental data and is typically based upon a parameter that tracks the amount of plastic flow, such as the vonMises-equivalent plastic strain. This type of model is entirely macroscopically defined. Consideration for events at the microstructural level are almost entirely ignored with perhaps only the rationale that plastic flow occurs via dislocation motion under shear being the only physical insight afforded by the model, as well as the notion of internal stresses evolving under plastic flow (kinematic hardening) (Barlat 2007). Nonetheless, the model usually performs very well with minimal fitting parameters; it serves as a jumping off point for our investigations into martensitic behaviour. This type of model satisfies Masing's rule for stable cyclic behaviour only when a constant work hardening rate is used.

3.2.2 Work Hardening Field

In a small deviation from a classical mixed hardening model, we will now define the work hardening rate of the material as being dependent on the point in deviatoric stress space that the yield surface is contacted, as opposed to variables related to the plastic history of the material. This type of model is our first anisotropic hardening model and has the advantage of now providing a work hardening rate that depends on both **when** and **where** the yield surface is contacted, instead of just **when** it is contacted (Figure 3.57). For instance, forward loading could result in initially high hardening rate that gradually diminishes; upon reverse loading, the yield surface is breached on the opposite side where there is a higher hardening rate; thus the material hardens at a high initial rate again. This feature was not present in the prior mixed hardening model and will be seen to be very important for the modeling of martensitic mechanical behaviour on reverse loading. In summation, this model is still

phenomenologically defined like the first model, however, we add further insight of events occurring at the microstructure to add to the description. One could rationalize the behaviour is dislocation pinning and freeing for example. This model features no increase in fit parameters over the last and only a minor increase in computational effort to evaluate. However, this model will never satisfy Masing's rule for stable cyclic behaviour; unless of course, the field is constant.

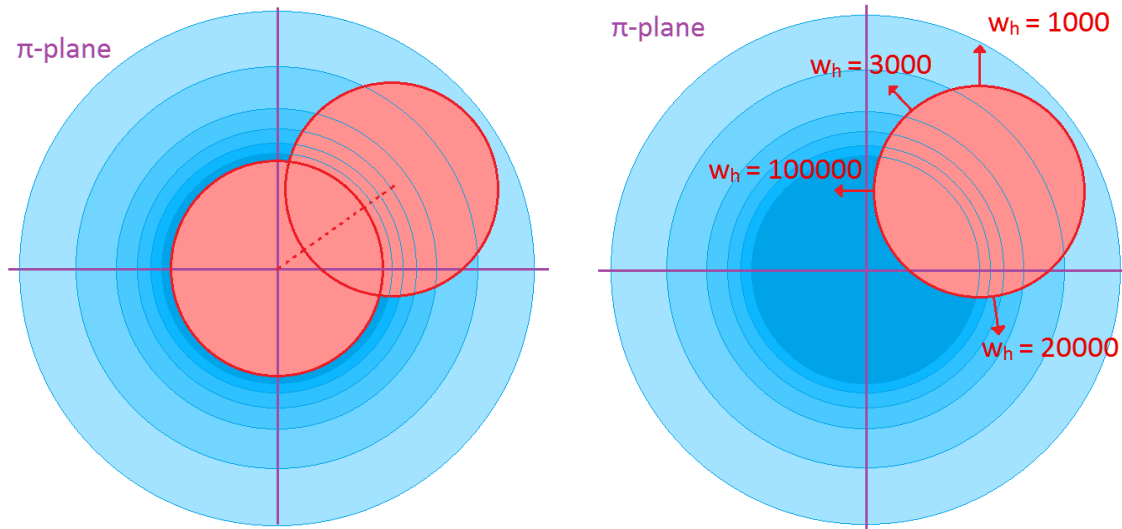


Figure 3.57 – Depiction of a yield surface that is translating (hardening) in a field of work hardening values. Note that the work hardening rate is dependent on where the surface is contacted.

3.2.3 Multi-Surface Plasticity

Despite its name, a multi-surface plasticity model is very closely related to the work hardening field model we just discussed. This type of model is truly derived from Masing's work and is guaranteed to exhibit a Masing curve homology rule. In this model, we have multiple hardening surfaces encapsulating the primary yield surface. These additional hardening surfaces move with the primary surface upon contact and dictate the work hardening rate when they are reached (Figure 3.58). Mroz and Krieg (Krieg 1975; Mróz 1967) both implemented this model with subtle superficial differences that are essentially based upon having a finite number of hardening surfaces (Mroz) or an infinite number (Krieg). This is effectively very similar to the work-hardening field model except that this work hardening field that the surfaces define can shift and stretch upon motion of the yield surface. This model can be interpreted microstructurally the same way as the prior model except that since the yield surfaces cannot cross, we will always have the maximum work hardening rate available (albeit for different amounts of hardening) upon a change in load orientation. This helps prevent non-physical events such as low hardening followed by high hardening that is possible in the field model.

A neat interpretation of a multi-surface plasticity model is that each concentric surface corresponds to the activation of a new plastic flow mechanism. This new mechanism corresponds to reduced plastic resistance and in turn, lower effective work hardening. The nature of this plastic

resistance is up for interpretation and can be thought of in many different ways. For instance, we can say that a new slip system is activated when a specific surface is reached. Additionally, in a multiphase system we could say that plastic slip of an additional phase is activated upon reaching the next yield surface and that the high work hardening rate seen prior is actually a mixture of elastic straining of the non-flowing phases mixed with plastic flow of the flowing ones; this is the interpretation that Masing would provide. This latter interpretation of the surfaces is appealing for martensite because we have seen that the hardness of elements in the microstructure varies considerably for reasons relating to differences in lath size, auto-temper time, and possible residual stresses⁷. Like the previous model, this one requires the definition of the work hardening field as fit parameters. It is a little more intensive computationally as the shifts in all the yield surfaces must be computed and stored.

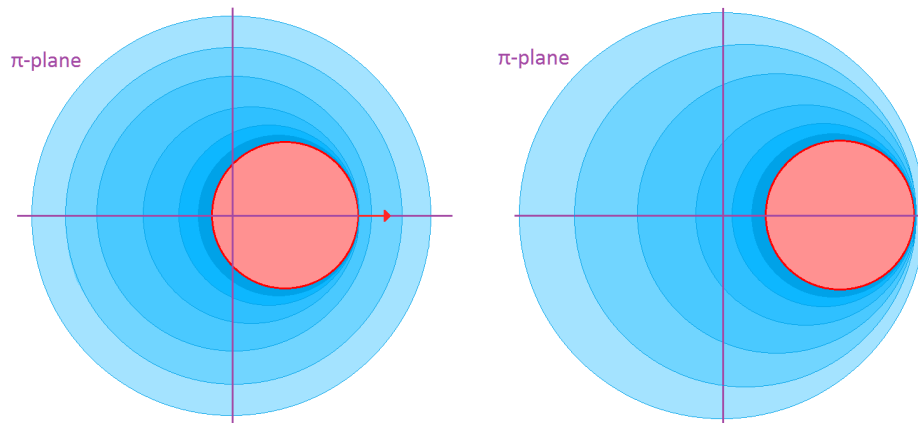


Figure 3.58 – Plastic flow occurring in a multi-surface plasticity model. Note that all surfaces in contact with the flowing control surface are also flowing and the work hardening rate is governed by the largest contacted surface.

In the case of only kinematic motion of the primary yield surface, this model will exactly correspond to a homology parameter of two ($\eta=2$) in Masing’s Rule (stable cyclic behaviour). If the surfaces are able to expand or contract, this will correspond to cyclic hardening ($\eta>2$) or softening respectively ($\eta<2$).

3.2.4 Direct Masing Model (Continuous Composite Model)

This is the first model where we attempt to examine the behaviour of discrete elements at the microstructural level and combine them directly for macroscopic behaviour. Although this model should behave identically to a multisurface model, we implement the Masing model in this manner as a stepping stone to our next microstructural model; as such, with this model we no longer make use of the macroscopic yield surface used in the previous three models. A key feature of a model of this type is the idea that the behaviour of the macroscopic object is ultimately a weighted sum of smaller elements that represent a fraction of the underlying structure. In the context of martensite, we mentioned previously that an important point for a model was the consideration that elements within the

⁷ The existence of microscopic residual stresses alters the “effective” yield strength of an element in a certain loading direction.

microstructure would be yielding at different points and the effective hardening seen was really just a combination of elastic and plastic deformation. This lends itself well to the Masing type model because we can model each fraction separately and generate the resultant macroscopic behaviour via a sum of the behaviour of the subfractions.

In this model, the only thing that must be defined is the constitutive model for the subfractions. An extremely simple constitutive model is appropriate in this context, such as simple vonMises plasticity. When strain is applied to the structure, it is applied to each subfraction separately. The resultant stress state is the weighted mean of the stress state of the subelements; this is the macroscopic assumption we make in this model. This model is very easy to visualize in one dimension and effectively translates into an iso-strain composite model in this context; this is illustrated in Figure 3.59. In this figure, each subfraction has a different yield stress which falls on a yield stress distribution; when the structure is strained, an apparent tangent modulus is seen which is between that of perfect elastic straining and fully evolved plasticity. This is illustrated in Figure 3.60 in which we see that the slope of the macroscopic stress-strain curve drops as more subelements reach their yield criteria. The fact that this happens without us defining a specific macroscopic work hardening rate that is excessively large like those seen in the previous models makes this model less abstract from a physical point of view. Additionally, due to the generation of residual stresses between subelements, a Bauschinger Effect can be seen in this material description without any explicit definition of kinematic hardening at the subelement level. These residual stresses effectively take the place of the back-stresses in a kinematic motion of the macroscopic yield surfaces in the models we just discussed previously.

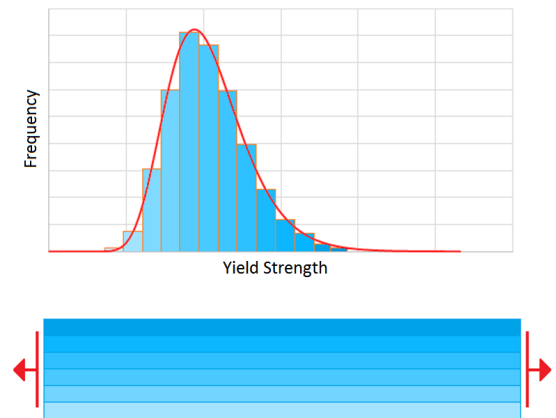


Figure 3.59 – One dimensional continuous composite with subelements that have varying yield strengths (Direct Masing Model)

The effects that occur in this model are very desirable, however, this model still suffers from the fact that there is no spatial definition of the plasticity that occurs (the iso-strain assumption); we will do away with this assumption in further models. Nonetheless, the gains made by this model are very rich considering that it removes a considerable amount of abstraction from the multi-surface plasticity model. We have only discussed the model in one dimension, however, the reasoning is fully extendable to three dimensions and we will do this clearly in Section 3.5;

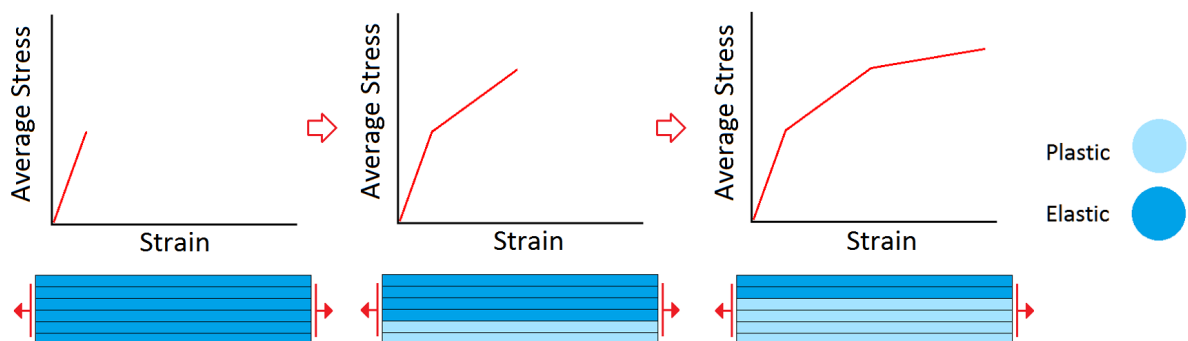


Figure 3.60 – Depiction of continuous yielding in a one-dimensional Masing solid with associated macroscopic stress strain behaviour.

3.2.5 Micromechanical Model

The most complex model we will consider is a micromechanical model in which the interactions that occur at the microstructural level are explicitly accounted for at some scale. All the reasoning that went into creating the Masing Model applies in this model; in fact, the only real difference between this model and the Masing model is the spatial assignment of the subelements. Masing assumed a parallel arrangement of subelements, whereas we now do away with that assumption. In essence, the foundation of this model is the idea that we can create a representative volume element (RVE) that is comprised of heterogeneous subelements (Kouznetsova, Brekelmans, and Baaijens 2001). This RVE will represent the constitutive behaviour of a macroscopic portion of material; that is, any arbitrary macroscopic strain applied to the RVE will result in deformations and microscopic stresses in the subelements that make up the RVE. The global macroscopic stress is the volume average of these stresses in the unit cell. This procedure is referred to as first order homogenization (Gitman, Askes, and Sluys 2008) and is essentially the process of assuming continuum macroscopic behaviour from a heterogeneous microstructure. In order to evaluate these microscopic stresses, a numerical technique, such as the finite element method, must be employed to solve for equilibrium within the cell (Smit, Brekelmans, and Meijer 1998). The fact that we must do this makes this model orders of magnitude more expensive computationally than the other presented models; however, it has the advantage (or disadvantage) of forgoing any closed form macroscopic constitutive relations. Any assumptions that exist, exist entirely at the microstructural level with regard to the constitutive behaviour, and positioning of the subelements in the RVE.

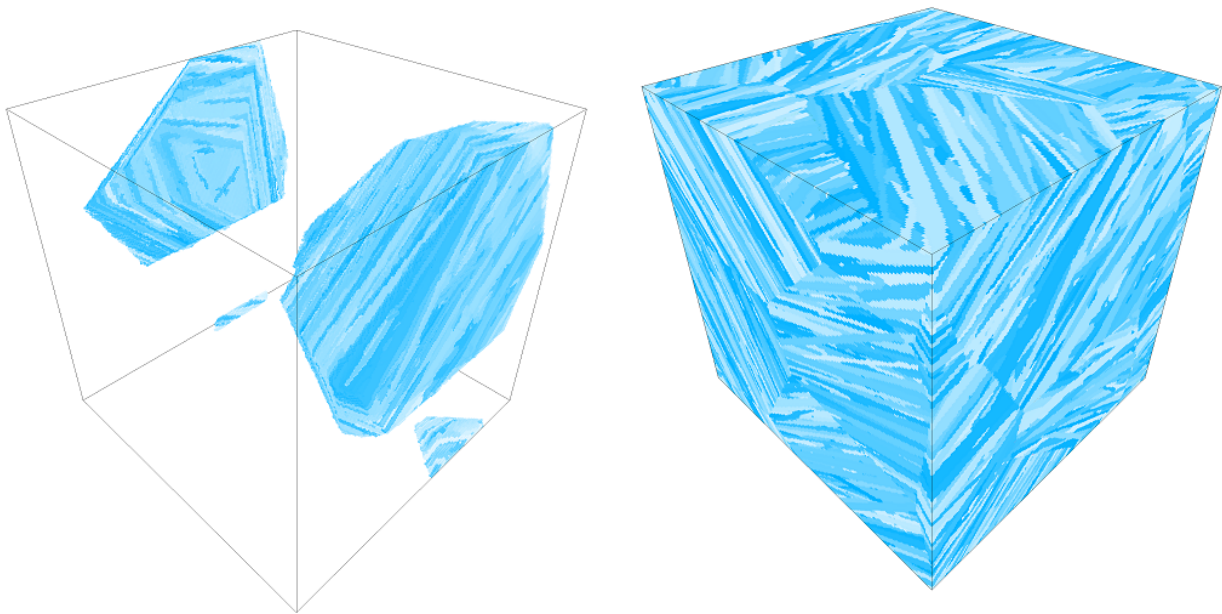


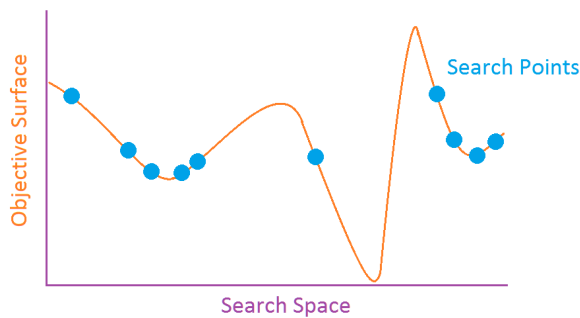
Figure 3.61 – Depiction of block subelements distributed into the packet substructure characteristic of lath martensite. Note that the structure fulfills the necessary periodicity requirement.

Figure 3.61 gives an example depiction of a micromechanical unit cell (RVE). In this example, we see various subelements with yield strengths that differ. As in the Masing model, these subelements may also have pre-stresses applied to them as well. The spatial arrangement of these subelements should be done in a manner that approximates the microstructure of the real material. Additionally, our

RVE should have a periodic mesh and periodically defined microstructure; the reason being that periodic boundary conditions have been shown to exhibit more favorable behaviour of the RVE; with a smaller RVE being required for good behaviour (Kouznetsova et al. 2001). In our implementation, the subelements of the RVE represent the block structure of martensitic steels. Their shape is such as a block would appear in lath martensite, and they are arranged into the appropriate packet structure. It would also be possible to define the structure at the nanoscale with definitions of the martensitic laths; however, at this point, such an undertaking is not computationally feasible; and, as we will see in Section 3.6, not necessary to obtain a good macroscopic constitutive model. The detailed implementation of this model is explained in Section 3.6.

3.3 Global Fitting Algorithms

In the previous section, we introduced many types of models to explain the constitutive behavior of martensitic steel. What is common to all these models is that they each have adjustable parameters that need to be obtained. In many cases, these parameters are obtained directly (such as a work hardening surface for monotonic loading), however, our more complex models have a large possibility space of parameters and it is not clear what these parameters should be. It is a simple matter to bound the parameters but their exact values should be set to those which give optimal fidelity to experimental data.



Model	Search Space
Mixed Hardening	$1_{\text{surf}} * (\sigma_y, \{H_k\}, \{H_i\})$
Work Hardening Field	$1_{\text{surf}} * (\sigma_y) + \{ H = f(\sigma_{ij}) \}$
Multi Surface Plasticity	$N_{\text{surf}} * (\sigma_y, \{H_k\})$
Masing Model	$N_{\text{elements}} * (\sigma_y, \{H_k\}, \{H_i\})$
Micromechanical Model	$N_{\text{elements}} * (\sigma_y, \{H_k\}, \{H_i\})$ + Geometry

Table 3.2 – Adjustable parameters for each model and search space representation. N refers to the number of objects; σ refers to the object yield strength; H refers to a collection of either isotropic or kinematic hardening parameters.

In a large multivariable space such as the one we are dealing with, it is not feasible to use a gradient descent algorithm since it is very easy to find a solution which is only locally optimal. Instead we must use an algorithm which attempts to find the globally optimal parameter set (solution). The table above depicts the fit parameters that need to be found for each model, as well as an abstract representation of a search space, showing how different parameter combinations have varying fit performance. The objective of a global fitting algorithm is to find the absolute minimum of the objective space shown.

A large number of global fitting algorithms exist; the quality that they all have in common is that they make no guarantee that the global optimum will be found in a fixed period of time, nor that the best solution found is indeed the global optimum (Sivanandam and Deepa 2008). Nonetheless, they often find a very good solution with a reasonable use of computational resources. In general, all these algorithms feature a tradeoff between breadth and depth based exploration of the solution space; with a completely random search representing a fully breadth based search and gradient descent algorithms representing a full depth based search. In this work, we have opted to use a genetic algorithm to search the solution space for parameters. The motivations for choosing this algorithm are discussed next along with comparisons to other algorithms.

3.3.1 No Free Lunch Theorem

A common question people ask when choosing a search algorithm is “Which algorithm does the best?”. Unfortunately, a mathematical result called the **No Free Lunch Theorem For Optimization** (Wolpert and Macready 1997) shows that it is impossible for any given search algorithm to perform strongly across all possible problems. Stated differently, it implies that all algorithms will perform **on average** the same over all possible problems. When interpreting this theorem, the key result is that while the average performance of all the algorithms is the same over all problems, the algorithms may perform differently for any specific problem in question. This modifies the original question to “Which algorithm does the best for my problem?”. Unfortunately, unless someone has studied the performance of various algorithms on your specific problem, one is out of luck to choose a specific algorithm to use. Heuristically however, one is able to draw upon the experiences of others treating similar problems to make an educated choice for an algorithm.

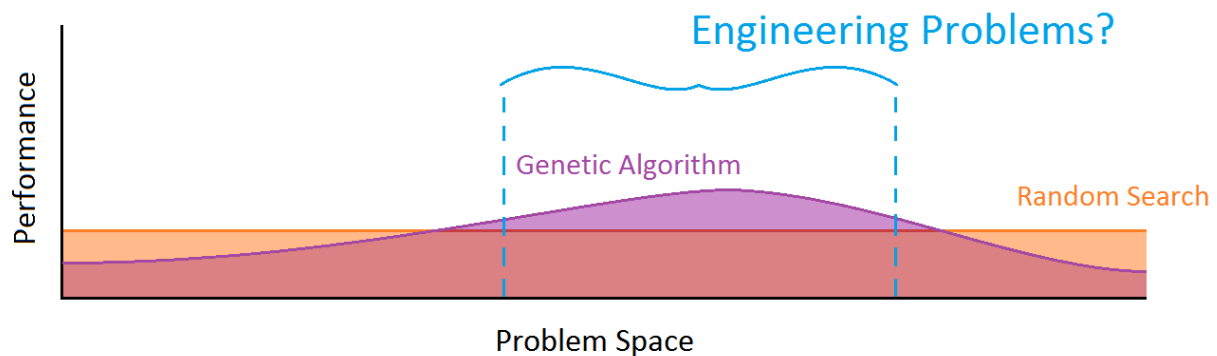


Figure 3.62 – Schematic depiction of No Free Lunch theorem for two algorithms. Note that the area under both curves is the same and since a random search performs equally for all algorithms, a genetic algorithm must necessarily do better for some problems and worse for others.

One algorithm that appears often in the literature is called a genetic algorithm, or evolution type algorithm. This algorithm has performed reasonably well across a wide range of engineering optimization problems (Chun, Kim, and Lee 2002; Ganguly et al. 2009; Goldberg and Kuo 1987) and is a good candidate for optimizing our plasticity models. Other models that are popular include: simulated annealing, hive search, and harmony search, to name a few. Note however that we have no real incentive to choose one over another with the information available.

3.3.2 Evolution-based Search Algorithm

We have opted to use an evolution-type algorithm for optimizing our parameter set to experimental data. An advantage of this type of algorithm, in addition to its generally good performance in engineering problems, is that it is intuitively easy to understand with a biology analogy. In this algorithm, the parameter set we are trying to fit is analogous to a set of genes (Figure 3.63); the genes make up an individual, and this individual has a specific performance against defined fitting criteria. The individuals that make up the population are evaluated by their performance and the best performing members become the “parents” of the next generation. When the next generation is assembled, the gene pool is made up of the parent generation with an allowable deviation that represents genetic mutation (Figure 3.64). The cycle of generations repeats until a solution that is deemed acceptable is found. Recall that with these types of algorithms there is no indication that the found solution is in fact the global optimum; however, progressively better solutions will be found with time.

When constructing the genetic algorithm, the sizes of the parent and descendant populations are adjustable parameters, as well as the probability of mutation. In general, larger parent and descendant populations reduce the probability of the solution becoming trapped in a local optimum. With regard to the mutation parameter, recall that we brought up the idea of breadth vs. depth when conducting a global search; the mutation parameter is effectively a parameter to control the extent of each. One can imagine that no mutation would result in no new breadth-based exploration of the solution space and effectively implies a gradient descent that converges on a local optimum with each subsequent generation as genes are lost. On the other extreme, a very high mutation would result in a descendant generation that is in no way coupled to the parent generation. In this situation, the genetic algorithm reduces to a true random search and is entirely breadth based. It is desirable to find a good balance between the two and finding a good value for these parameters requires some experimentation by the user.

With the structure of the algorithm in place, the only remaining task that we have not discussed is the evaluation of performance. This is the most expensive part of the search, as it requires a simulator to run with the parameters of each descendant. In effect, we need to simulate the experiments with the model parameters encoded in each descendant to see how good the simulation matches the experimental data. The comparison is made with a quantifiable metric; in our case, a least squares analysis. Despite being expensive, this algorithm lends itself well to parallel processing by virtue of the fact that each descendant is evaluated independently. In the next section, we will discuss how to leverage this fact to make otherwise computationally prohibitive fits feasible.

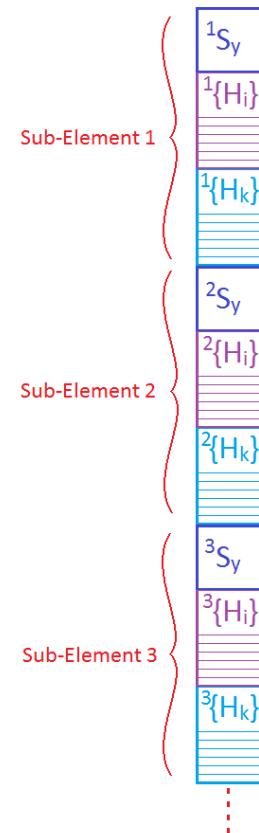


Figure 3.63 – Gene Structure of a Masing Model parameter set. Note that this collection of genes makes up a single member of the evolution algorithm’s population.

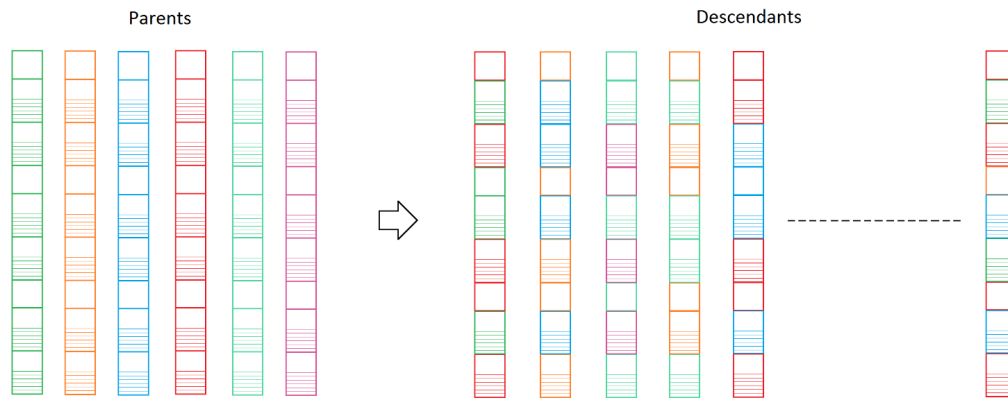


Figure 3.64 – Illustration of gene recombination in constructing the descendant population. The parents are the top performing members of the prior generation and contain the gene pool for the next generation. In addition to acquiring the genes from the parent generation, the descendants also have a chance to undergo a mutation with each of their genes. Note that this example depicts each descendant as having two parents each; this is not necessary and the number of parents can be any $n > 1$.

3.3.3 Parallel Processing

The use of the most advanced computational techniques is imperative when dealing with such computationally intensive procedures as a global search. For instance, in this thesis, a generation size of 2048 descendants is used; each of these descendants is fitted to approximately five experiments and approximately 100 generations are required to find a strong parameter set. That multiplies to 1,024,000 simulations that need to be conducted to perform a fit! The enormity of the task is reduced if one leverages the parallel nature of the problem. In particular, we have made use of a programming technique that leverages the parallel nature of a computer’s graphics processing unit (GPU) to speed up computations; this allows us to achieve significant performance gains (10x-100x) without resorting to the use of a supercomputer.

Single Instruction Multiple Data (SIMD)

A computer’s GPU implements a specific kind of processing architecture referred to as Single Instruction Multiple Data (SIMD). Essentially, what this means is that a GPU is capable of running processes on many pieces of data simultaneously, as long as the operations are identical. This sort of processing paradigm is referred to as data parallelism and is well suited to scientific applications. This is the case because scientific simulations need to run identical instructions over a large domain (for example, updating a quantity during the current timestep). In the case of an evolution algorithm, we are running simulations on each member of the population. Since the instructions for running the simulations are identical for each, we can perform such instructions on a SIMD processor.

A SIMD processor has approximately 100x the processing power of a conventional processor of the same generation. For instance, at the present moment (2016), the most advanced CPU features 8 parallel processors capable of 50 GFLOPS of single precision compute power. On the other hand, the most advanced GPU features 4096 SIMD processors that are capable of 10,000 GFLOPS of compute

power. These processors cost approximately the same; with the caveat being the GPU cores can only work on data parallel tasks. Fortunately, data parallelism is ubiquitous in scientific problems.

Over the course of this thesis, we have implemented many of our numerical simulations by using this technique. The finite element solutions to the heat equation and mechanics equations are implemented this way; as well as the optimization problem we are currently discussing. Figure 3.65 depicts the processing paradigm of SIMD processors schematically for implementing a genetic algorithm. It shows how the members of the descendant population are organized into small groups that correspond to the hardware defined workgroup size. A workgroup is a collection of SIMD cores that execute the simulation instructions together. Workgroups operate independent of one another and will fetch the next batch of data elements upon completion until the domain of unprocessed elements is exhausted. This structure ensures scalability such that the same programs can be used over multiple GPU's in supercomputers if warranted.

Data elements can correspond to many different things, depending on the scientific application. For instance, they may correspond to: discrete points in a finite difference method simulation, rows in a matrix factorization operation; nodes in a finite element simulation, gauss points in a finite element simulation, or atoms in an N-body simulation, etc. In this thesis, such elements have taken many different identities to ensure fast and efficient high resolution simulations of our martensitic steel's optimization, manufacturing and loading processes.

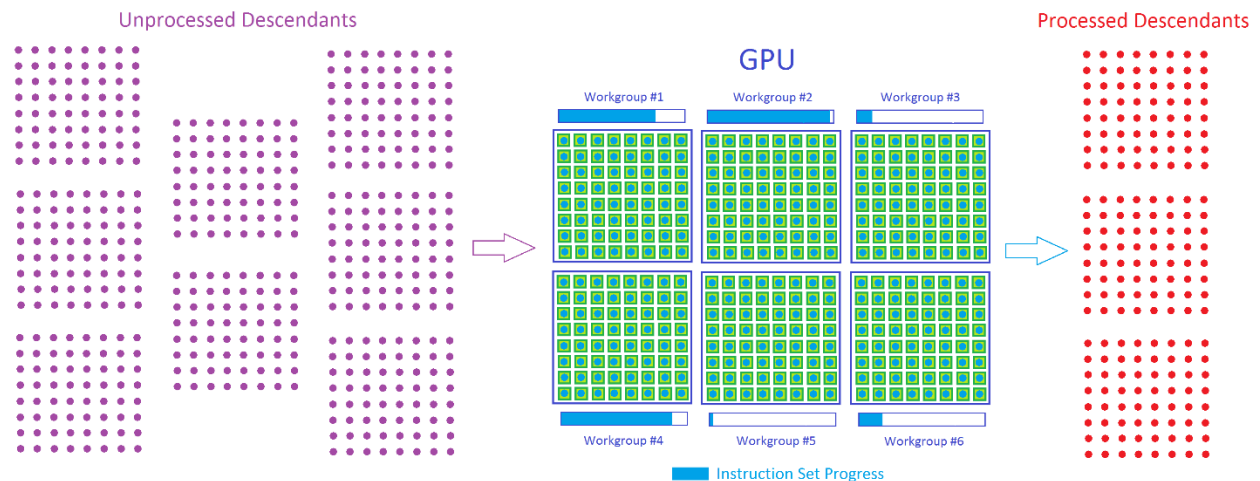


Figure 3.65 – Depiction of data organization under a SIMD processing paradigm. The SIMD cores of the GPU are organized into work groups of size x . All SIMD cores in a workgroup execute instructions together in parallel. When a work group is completed, it processes the next batch of data. In this example, the circles represent the parameter data associated with a specific member of the population in a genetic algorithm. The instruction set is the complete simulation program that the work group executes. Note that the circles represent descendants in this context only. In another context, they may represent spatial points in a finite difference calculation for example, with the workgroups evaluating the heat equation at those points.

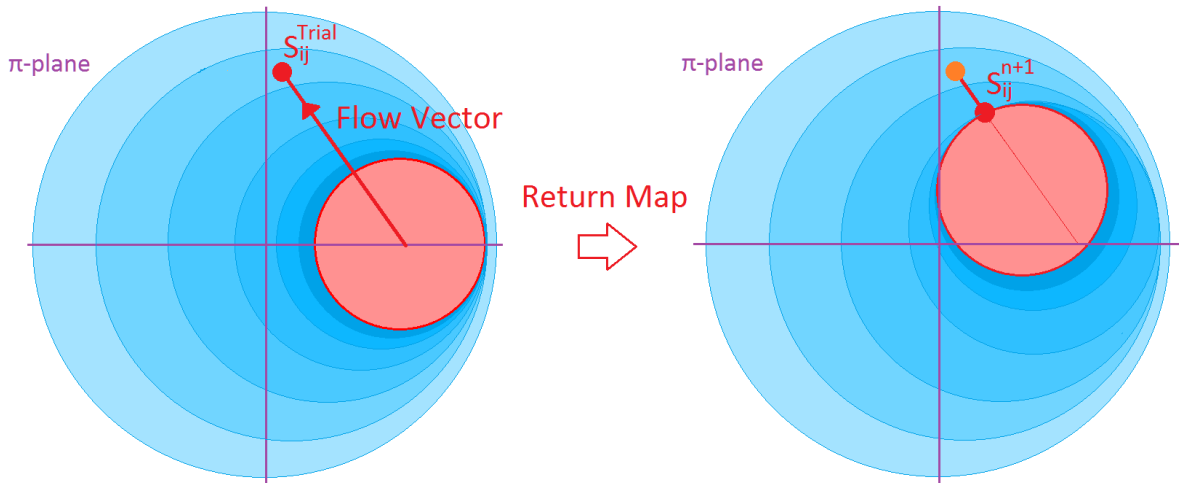


Figure 3.66 – Implicit Return Mapping performed on multiple plasticity surfaces. The flow direction is normal to the control surface.

3.4 Plasticity Surface Based Models

The first three of the five models we are analyzing are based upon the manipulation of one or more plasticity surfaces. In this chapter, we will discuss the details of these models and analyze their behaviour with regard to performance, costs, and limitations in the face of increasingly complex loading scenarios. The reason we lump these three models together is that they are implemented into a finite element program very easily without any modification of the finite element derivation or procedures. That is, they are entirely contained within a constitutive subroutine in a finite element analysis. Our implemented integration procedure for these models is presented with a described pseudocode implementation, so that they may be easily implemented by others in a commercial finite element user subroutine. The algorithms are all based upon the implicit return mapping technique (Figure 3.66) presented in Chapter Two and are solved via Newton-Raphson Iteration. The same procedure is used because only subtle differences are needed to adjust for the different plasticity surface types.

3.4.1 Strain Integration Algorithms

In this section, we present the strain integration algorithm used to execute our various plasticity models. As was discussed in Chapter Two, we are implementing a fully implicit return mapping algorithm that projects a given strain/stress state to the appropriate location in stress space while maintaining consistency with the plasticity requirements.

Return Mapping Algorithm

1. Calculate Deviatoric Trial Stress State - $S_{ij}^{(0)}$
2. Guess λ (Plastic Increment) = 0
3. while $|^{(1)}S_{vm}^{(0)} - 3G\lambda - ^{(1)}H_{yield} - f_{iso}(\lambda) - f_{kin}(\lambda, S_{ij})| > \epsilon_{tol}$

$$\frac{dF}{d\lambda} = -3G - H_{tan}^{iso} - H_{tan}^{kin}$$

$$\lambda := \lambda - \frac{F^{(i-1)}}{\frac{dF}{d\lambda}}$$

$$F^{(i)} = ^{(1)}S_{vm}^{(0)} - 3G\lambda - ^{(1)}H_{yield} - f_{iso}(\lambda) - f_{kin}(\lambda, S_{ij})$$
4. Update Plasticity Parameters for each plasticity surface (e)
 - Update Isotropic Hardening
 - Update Kinematic Hardening
5. Update Stress State

$$S_{ij} = S_{ij}^{hydro} + S_{ij}^{(0)} - 3G\lambda * \frac{^{(1)}S_{ij}^{(0)}}{^{(1)}S_{vm}^{(0)}}$$

Kinematic Hardening Integration

1. Evaluate $f = \int_0^\lambda H_{tan} d\lambda$

Conventional	Field Type
$H_{tan} = g(\lambda)$	$H_{tan} = g(S_{ij})$

Update Isotropic Hardening Parameters

For each (e)

1. Find fraction of hardening that occurred while in contact with (e)
2. Update Hardening Parameters

$$^{(e)}\lambda = f * \lambda$$

Update Kinematic Hardening Parameters

For each (e)

1. Find fraction of hardening that occurred while in contact with (e)
2. Calculate Backstress Evolution

$$^{(e)}\Delta S_{ij}^{back} = f * H_{rdkin} * \frac{^{(1)}S_{ij}^{(0)}}{^{(1)}S_{vm}^{(0)}}$$

Figure 3.67 – Algorithmic implementation of a generalized return mapping procedure that is suitable for all three plasticity models used in this section. Notice that the algorithm essentially iterates via Newton-Raphson iteration for plastic consistency. That is, the trial stress state is mapped back to a point on the yield surface via the flow direction at (n+1), while keeping track of the motion and dilatation of the yield surface(s). The important part that differs between models is the evaluation of the tangent hardening modulus and integration of the hardening along the flow path.

A return mapping procedure solved via Newton-Raphson iteration is presented in Figure 3.67 above. This algorithm implements vonMises plasticity with isotropic and kinematic (Ziegler) hardening. In the course of a finite element procedure, the global solution solver will request that a strain increment be added to the current strain state. This algorithm will consider the strain increment and return an elastic strain/stress that is physically consistent with our plasticity model in use. The largest difference between our plasticity models comes in how hardening is evaluated. In conventional mixed plasticity, the hardening is a function of a hardening evolution expression alone. Alternatively, in field and multisurface plasticity, the accumulated plastic strain is inconsequential; the only factor that governs the tangent work hardening rate is the location in stress space as hardening occurs. In this thesis, we use a Voce law in our analysis of mixed hardening single surface plasticity. With regard to field and multisurface plasticity, each surface(radius) is assigned a constant work hardening tangent modulus; the resolution of the domain is increased via the addition of additional surfaces (radii).

3.4.2 Mixed Hardening Plasticity

We mentioned earlier that mixed hardening vonMises plasticity is essentially the simplest plasticity model available to use. The presence of an isotropic component is necessary because of obvious hardening during the plasticity phase of monotonic loading. However, isotropic hardening is not sufficient on its own because it is clear that upon unloading, the yielding point is significantly reduced in the reverse direction; see Figure 3.68.

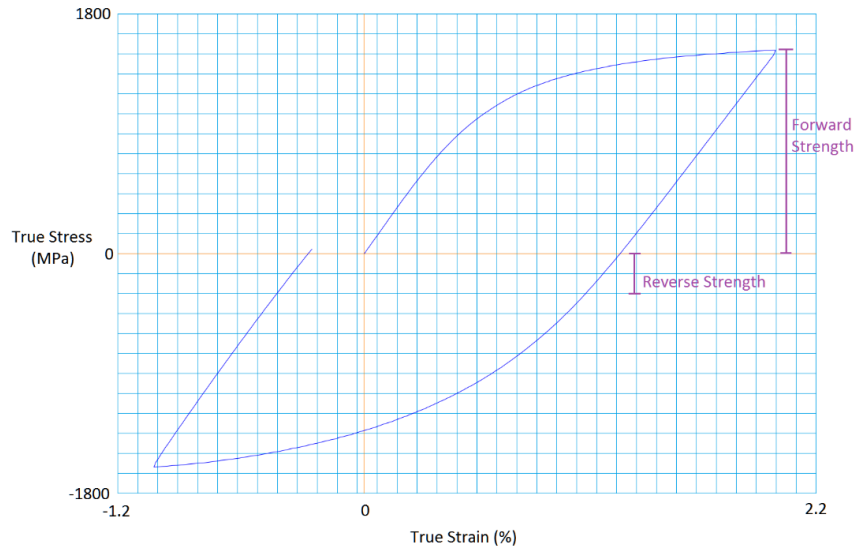


Figure 3.68 - Bauschinger test for 0.24wt.%C martensitic steel. Notice the reduction in offset yield strength in reverse loading.

If one desires to fit only monotonic data, isotropic hardening will always give a perfect description; the reason for this being that the work hardening rate can always be defined piecewise and inserted directly from tensile tests. In the case of reverse loading, or any change in loading direction, significant deviations will naturally occur due to the lack of physical meaning in the work hardening expression. For this reason, we will directly perform a Bauschinger fit to three data sets using our mixed hardening model.

Figure 3.69 shows the fitting result for mixed hardening plasticity to a collection of Usibor Bauschinger tests. It is quite evident from these images that this model is quite unsatisfactory in describing this material; although, linear hardening does satisfy Masing's stability condition. When non-linear hardening is used to capture the shift in yield strength associated with hardening, the fundamental problem with this model is that the hardening⁸ capacity is exhausted in reverse. Notice that upon reverse loading, the yielding curve continues upon the rate it experienced in the forward direction. That is, the hardening mechanisms do not seem to refresh on a load change like the experimental data suggests. It is for this reason that we have abandoned hardening based upon plastic history in our future models and base the hardening rate upon the position in the stress space. In the next section, we will make this change explicitly with the work hardening field model; in which nothing else is changed from this model except the hardening paradigm.

⁸ We refer to "hardening" purely as a change in stress state with strain. It is not appropriate to relate it to classical mechanisms of hardening such as work hardening.

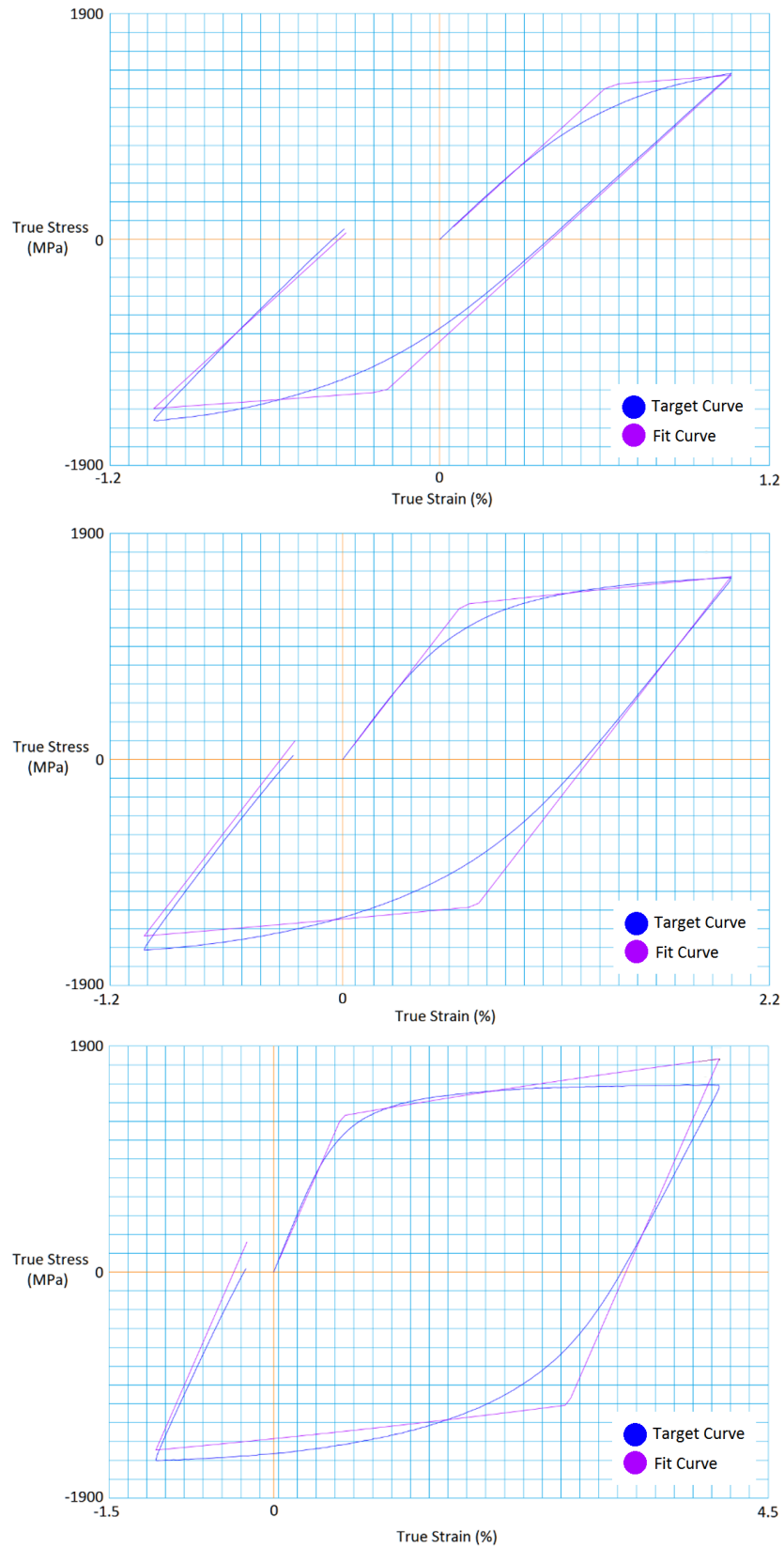


Figure 3.69 – Simultaneous mixed hardening fit to Usibor Bauschinger data using a Voce hardening law.

3.4.3 Work Hardening Field

In this section, we make a new change to the hardening paradigm in which the rate is now stress state defined as opposed to plastic history defined. This is our first anisotropic hardening model and very loosely corresponds to a Masing model. The hardening parameters as a function of position in the stress space are fitted radially around the center of the deviatoric plane. The results presented in Figures 3.70 and 3.71 depict a simultaneous fit to Usibor experimental data along different strain paths.

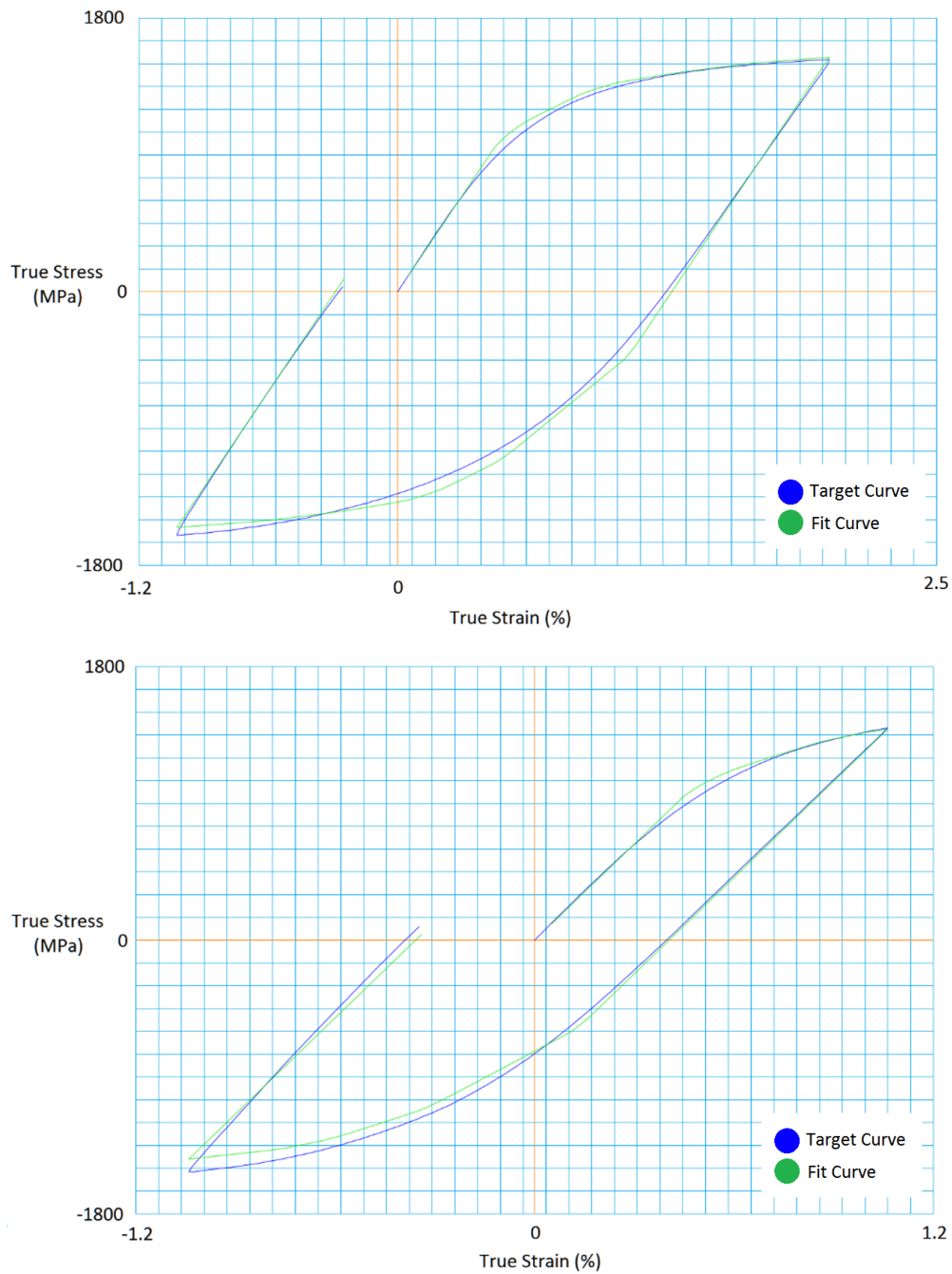


Figure 3.70 - Bauschinger portion of the simultaneous fit to Usibor data for the work hardening field model.

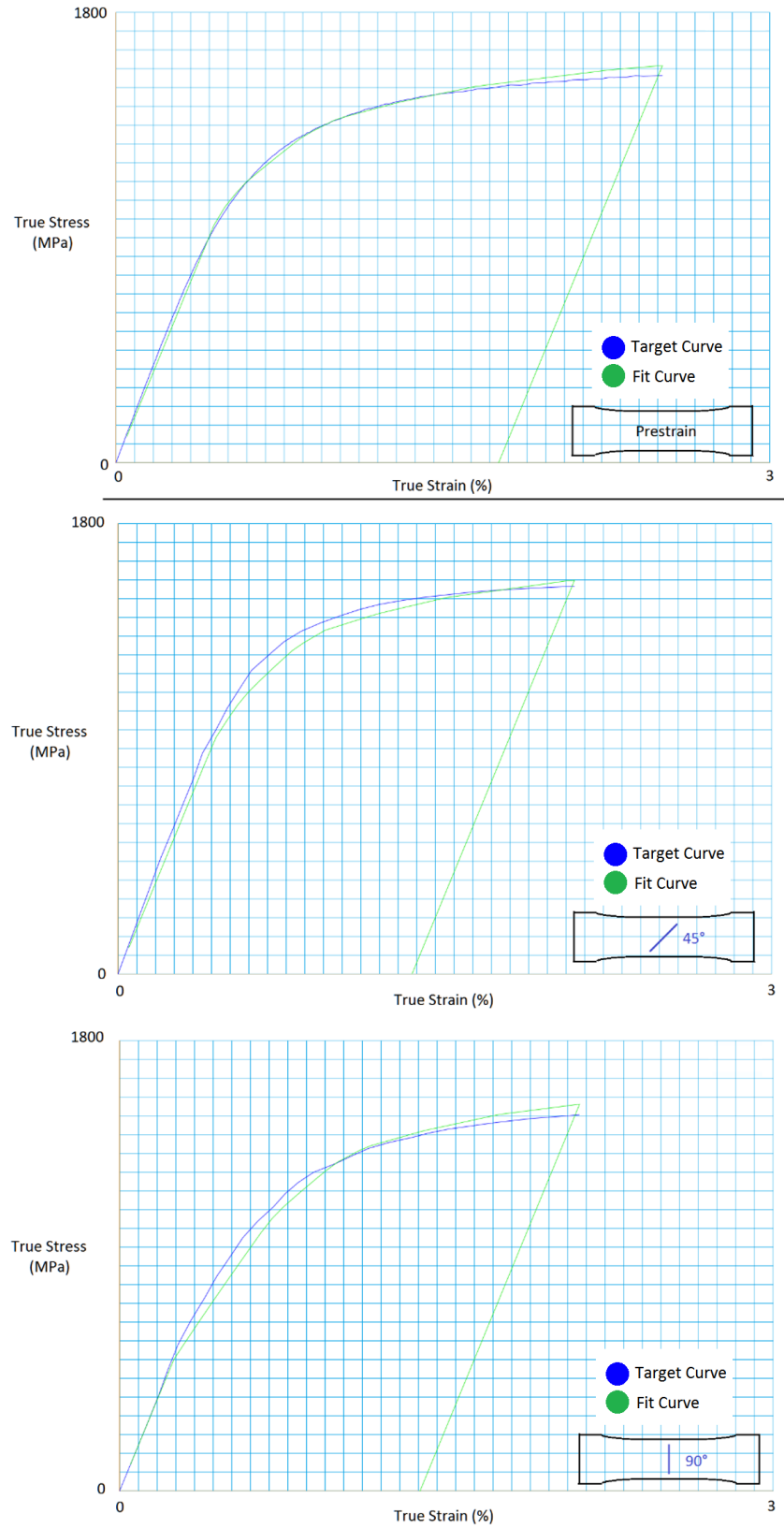


Figure 3.71 – Multiaxial portion of the simultaneous fit to Usibor data for the work hardening field model.

We see that the switch to stress defined hardening provides a significant gain to the quality of our fits. We now “refresh” the hardening rate upon a change in load direction and thus are able to capture a significant feature of martensite mechanics. However, this model is not a true Masing model; in order to do that, we must allow the hardening field to warp (via translation). By doing this we capture another important event that is occurring at the microstructure. The event is the differential yielding of the various microstructural elements (laths) that results in the development of microscopic residual stresses. We address this next in fully developed multisurface plasticity.

3.4.5 Multi Surface Plasticity

In the last section we saw that defining the hardening purely by stress state is not sufficient to achieve a strong fit to the experimental data. Ideally, we would want to include both the plastic history and stress state into the hardening rate. A surface based model of this type likely will provide the highest fidelity possible from a macroscopic constitutive model. This model is an abstract implementation of Masing behaviour however; phenomenologically, from a conceptual standpoint, a multisurface plasticity model is well suited for describing martensite. From a plot of the effective hardening rate for pre-strained tensile samples in Figure 3.72 below, we see that if we were to compare such behaviour to a prestrained multisurface plasticity state, many features are consistent between both. Namely, the onset of plasticity occurs sooner as the load orientation is rotated from the original strain direction. Additionally, the amount of hardening potential increases as the load orientation is rotated from the original strain direction.

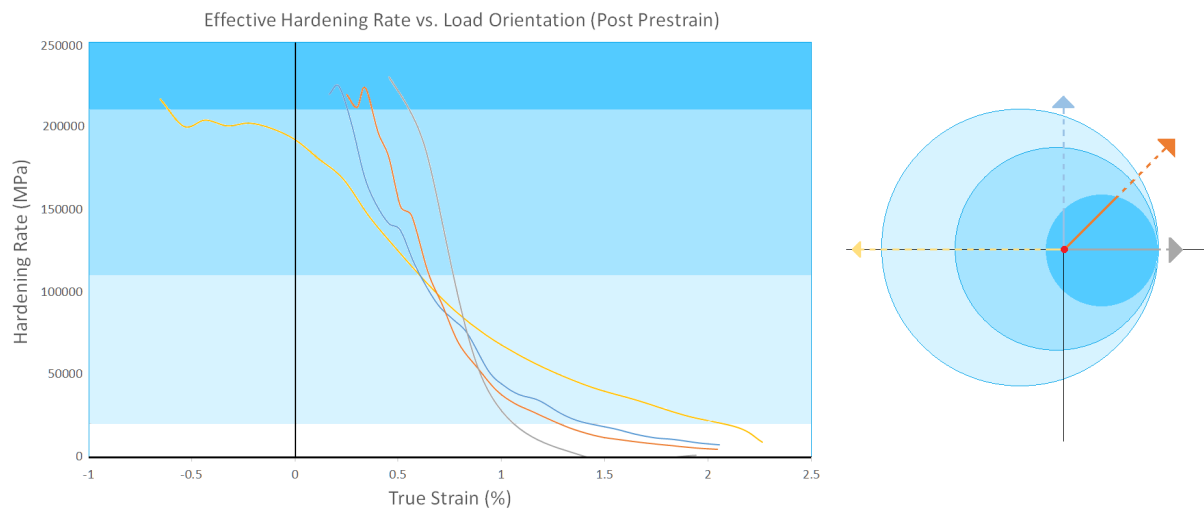


Figure 3.72 – A depiction of how a multi-surface plasticity model corresponds to the experimentally measured work hardening rates of pre-strained martensitic steel (0.24wt.%C). The amount of time spent pre-yield corresponds to the proximity of the orientation to the original load direction; a feature shared in the multisurface plasticity model. Additionally, orientations with lower initial yielding show a longer time spent at high work hardening rates; this is also captured in a multisurface plasticity model. Note that the data is from samples spanning multiple production batches; as such, there are small variations in chemistry and properties, however, the material is always Usibor 0.24wt.%C and the trends are clearly visible regardless.

To see such a comparison conceptually is very reassuring; even if such a comparison is purely phenomenological. Nonetheless, many of the microstructural mechanisms one would expect to occur in martensite are “broad-stroked” in such a model as discussed in Section 3.2.2. We can see how the model performs in reality in both Bauschinger and full multiaxial loading in Figures 3.73 and 3.74.

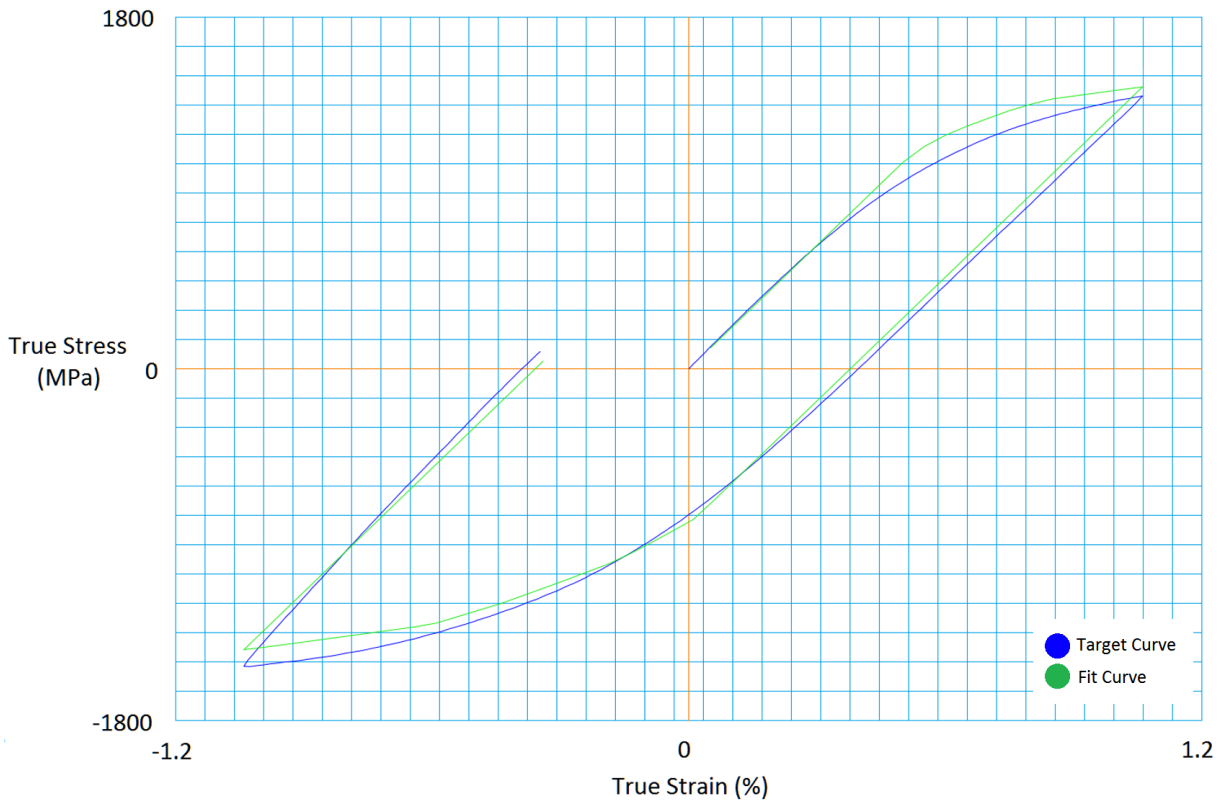
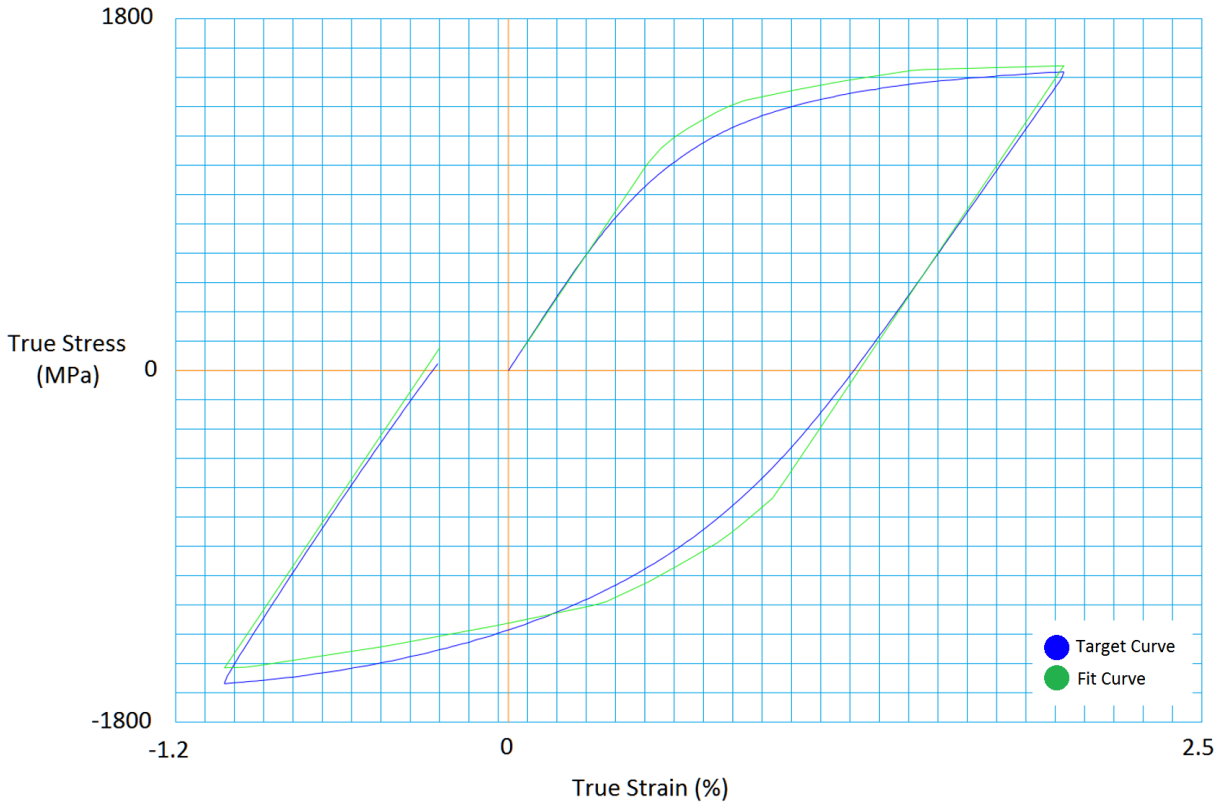


Figure 3.73 – Bauschinger portion of simultaneous fit to Multisurface Model (Usibor)

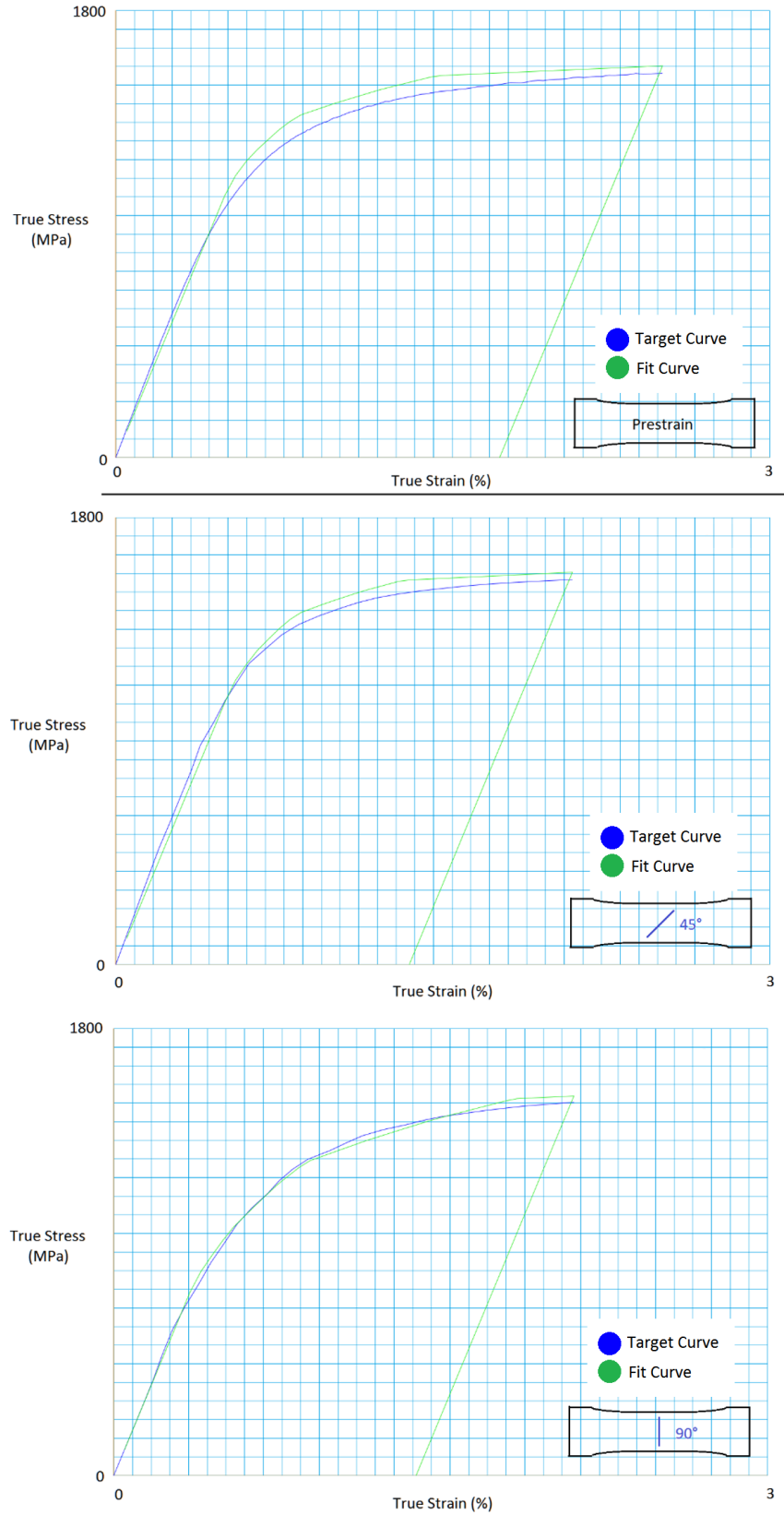
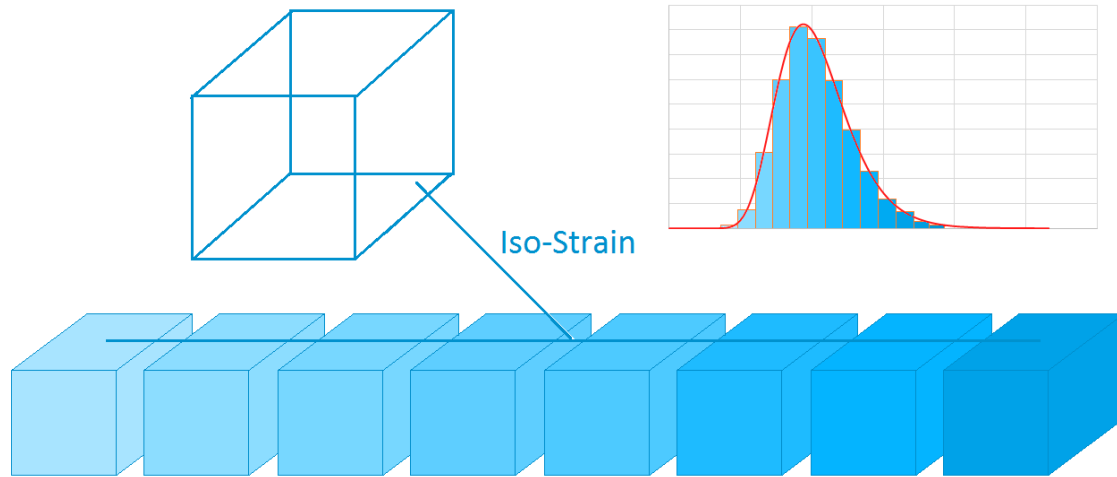


Figure 3.74 – Multiaxial portion of simultaneous fit to Multisurface Model (Usibor)



3.5 Direct Masing Model

We discussed the use of an iso-strain continuous composite⁹ model as a tool to capture the large elastoplastic transition in martensitic steels. Often when we see such methods discussed (Allain, Bouaziz, and Takahashi 2012; Badinier 2013), the model is constructed only in one dimension and applicable to simple loading (as Masing originally envisaged). In this section, we take the essence of this formulation and apply it to three dimensional finite elements, thus making a fully consistent iso-strain model that is applicable to general loading. Unlike the first three models which are freely applicable to a finite element solver, this model must have special considerations. It is not possible to simply substitute the logic into a constitutive subroutine. In essence, what this model will become is a model that is many subelements operating in parallel and the result is a combination of them all. We will redefine the finite element expression for incorporating this model.

In presenting this model, we will see that it has many parallels with the multisurface plasticity model in the last section (it is effectively a less abstract representation of that model). As opposed to multiple plasticity surfaces that reflect on the plastic activation of various elements, we explicitly define such elements with their own yield point and keep track of their strain state; the only caveat being that the elements are operating in an iso-strain configuration. Operating in this manner allows us to keep track of the residual stresses that develop between elements; a function that was modelled via backstress evolution in the multisurface plasticity model.

⁹ We use the terms: Continuous Composite Model, CC Model, and Masing Model interchangeably.

3.5.1 Building a Continuous Composite Model

A continuous composite model has its roots in the area of fiber-based materials. Since these materials consist of one-dimensional fibers with strengths that deviate around an average value, it makes sense to generate material descriptions based upon the relative motion of such fibers. In general, these models make a constitutive assumption of how the straining relates to the fiber orientation. For instance, iso-stress for one dimensional-loading normal to the fiber orientation; iso-strain for loading parallel to the fiber orientation; and more exotic methods such as localization and iso-work (Allain et al. 2012; Bouaziz and Buessler 2004) for less clearly defined fiber orientation.

Martensite is thought of as a sort of nanocomposite by many people; it makes sense then to attempt to use a continuous composite model in the material description. This has been attempted in the literature; however, the authors generally tend to limit themselves to one dimensional loading and do not consider, or even formulate, their expressions in general three-dimensional loading (Allain et al. 2012; Badinier 2013).

In building our model, we begin by considering a one dimensional finite element and comparing it to a classical composite description. By understanding how a Masing solid is supposed to behave, and looking at how the finite element is formulated, we modify the basic finite element equations to model the Masing behaviour. Subsequently, we will expand our reasoning to a fully three-dimensional continuum element that fulfills the iso-strain assumption of the Masing model.

Continuous Composite in One Dimensional Finite Elements

The CC model is very easy to interpret for one dimensional finite elements because the model itself is one dimensional. Ultimately, the Masing model says that when a bundle of material is pulled in an iso-strain configuration, the stresses experienced by each ‘strand’ are different because the properties of the strands vary in a continuum. Macroscopically however, the observed stress is the area average of the stresses in each strand. Additionally, each strand may have a different material

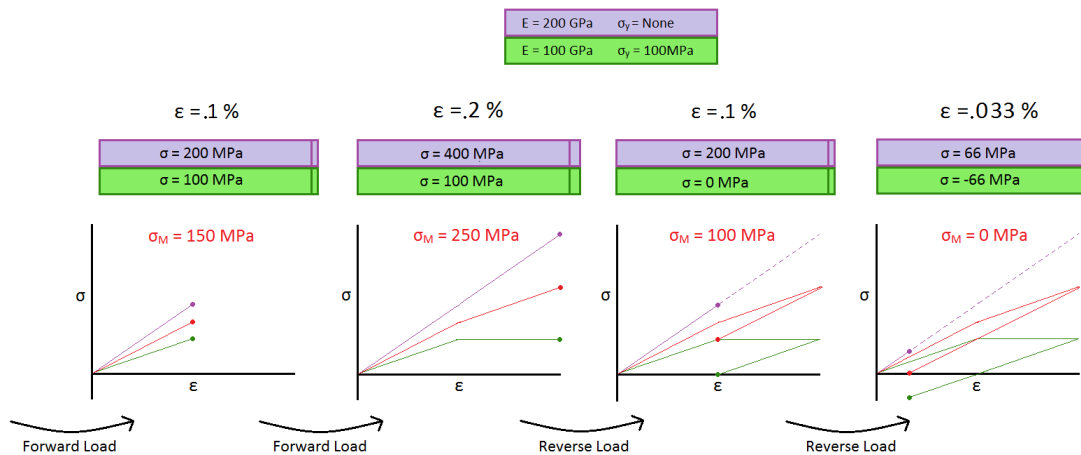


Figure 3.75 – Process illustrating the formation of residual stresses in a discretized one dimensional Masing solid after a forward and reverse loading. Note that when the material ends up macroscopically unloaded, the two components both have balancing residual stresses within.

constitutive law which may or may not contain inelastic components. This is crucial because differences in the constitutive laws leads to the ability for residual stresses to form inside the strands after unloading has occurred. Figure 3.75 depicts a two-component discretized CC model. It illustrates how the stress states vary within all the components of the solid as well as how the macroscopic stress state is obtained.

Our goal for the one dimensional finite element is for it to capture all the qualities of a composite model; namely, the ability to keep track of individual component qualities. This applies to the unique constitutive law that each component maintains and consequently, the unique stress state therein.

The fact that the solid is comprised of many component regions is a good starting point for the creation of the finite element. It implies that this finite element must store all the component data. When we consider a one-dimensional finite element and compare it to a composite solid, we see that the Masing element is actually just an assemblage of rods that behave in iso-strain configuration. Each of the component rods maintains its own physical state variables. The macroscopic stress state is simply a volume average of the constituents (see Figure 3.76).

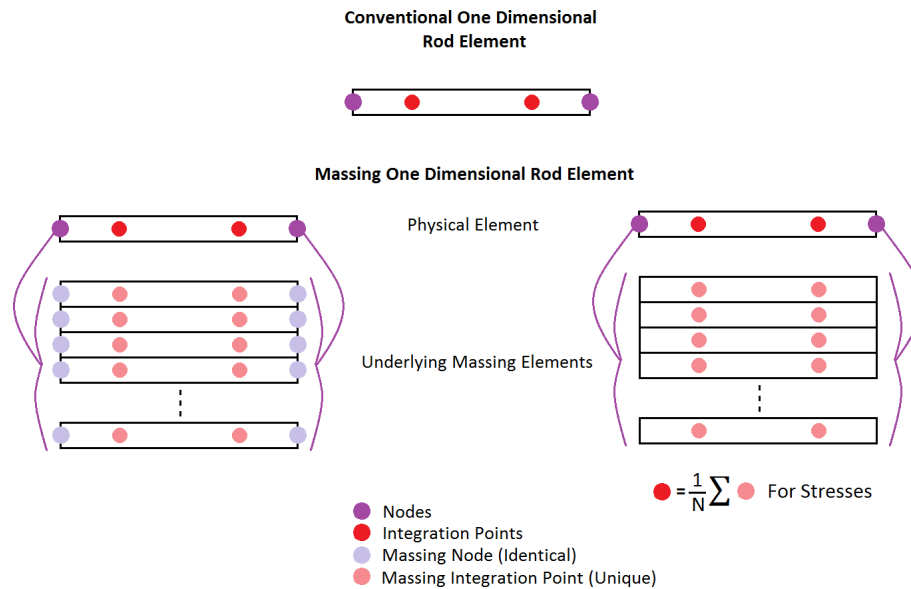


Figure 3.76 – Philosophy of a one-dimensional Masing element. The rod element is actually an assemblage of overlaid elements that all share the same nodal degrees of freedom; this ensures the iso-strain condition of the Masing model. Each sublayer has unique integration points with their own constitutive model and physical state quantities; however, the global macroscopic stress state viewed on the mesh element is the average of the stress states of the underlying Masing integration points.

Figure 3.76 shows the hidden layers (Masing Elements) of the solid. Notice that these hidden layers have their own stress integration points in order to preserve their constitutive individuality, however, they all share the same nodal points to preserve the identical strain field they all experience. In transforming this model to a three-dimensional element, all of these properties hold; however, we will not be able to visualize the underlying fibers as being stacked adjacently; in actuality we will have to understand them as being stacked on top of each other or rather, operating in parallel to one another. We are just able to conceptualize the problem easier if we stack the elements, as opposed to layer them in one dimension.

Masing Solid in Three Dimensional Finite Elements

As we saw in the previous section, a three dimensional continuum element will in fact be, in actuality, many elements stacked upon each other that share the same nodal degrees of freedom; while preserving their own stress integration state. The global(macroscopic) stress state is a fractional sum of each; with each sub-element contributing its volume represented stress state in the actual solid.

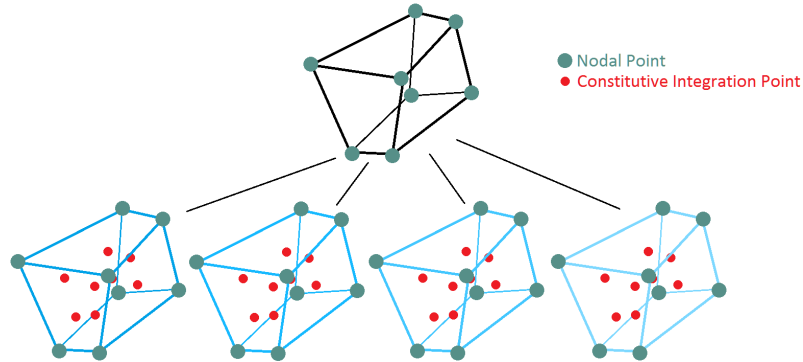


Figure 3.77 - Superimposed subelements defining a three dimensional Masing superelement; each with their own constitutive integration points. Notice the deformation/strain field in each subelement is identical.

We will now rework the virtual work expression for finite elements with our new definition for macroscopic stress in mind (Equation 3.54). In this expression, k represents the number of subelements used.

Stress Combination Formula – Equation 3.54

$$\sigma_{ij}^M = \frac{1}{k} \sum_k \sigma_{ij}^k$$

Virtual Work Expression – Equation 3.55

$$\int_{V_0} \delta \varepsilon_{ij}^T \sigma_{ij}^{t+\Delta t} dV = \delta u^T F_{ext} \rightarrow \int_{V_0} \delta \varepsilon_{ij}^T \frac{1}{k} \sum_k \sigma_{ij}^k dV = \delta u^T F_{ext}$$

Finite Element Equation – Equation 3.56

$$\int_{V_0} B^T \frac{1}{k} \sum_k D^k B[u] dV = F_{ext} - \int_{V_0} B^T \frac{1}{k} \sum_k \sigma_{ij}^{k(t)} dV$$

From the examination of the virtual work expression, we see that virtually any expression can be substituted for the macroscopic stress at any given integration point in the material. However, a volume average is the most physical function to use. A point of interest in the finite element equation is that the solver still requires an appropriate tangent modulus to evaluate $\Delta \sigma_{ENG}^M$. A tangent modulus could be assembled via linear combination of the sub-tangent moduli; that is, using the same function as the

stress weighting. However, in this thesis, we will use a linear elastic tangent modulus to converge upon the results (Initial Stiffness Method) due to its robustness.

A second point of interest is that the macroscopic stress could sum to zero even if all the sub-stresses are not zero. This is truly in the spirit of microscopic residual stresses and is a desirable feature for our model. In theory, one could initialize such stresses to non-zero when performing a fit as a mechanism of capturing non-isotropic behaviour that may exist in the material; similar to offsetting the yield surface from the origin in the multisurface model. We will attempt this momentarily but first we will examine the performance of the model without this effect.

3.5.2 Masing Model Performance

We are now in a position to present the results of a Masing fit to the experimental data. A simultaneous fit to all the Usibor strain data is presented in Figures 3.78 and 3.79. A 40-layer Masing model was used with isotropic hardening permitted for each subelement. Notice the ability of this model to capture gradual yielding, the Bauschinger effect, and anisotropy without defining such phenomena explicitly.

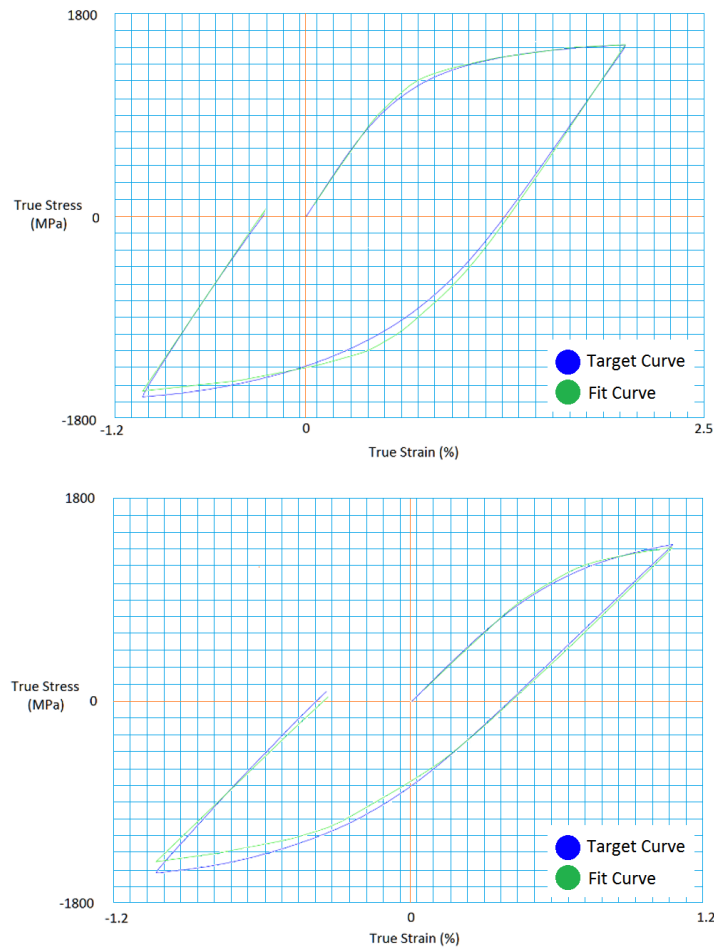


Figure 3.78 – Bauschinger portion of simultaneous fit to the Direct Masing Model (Usibor)

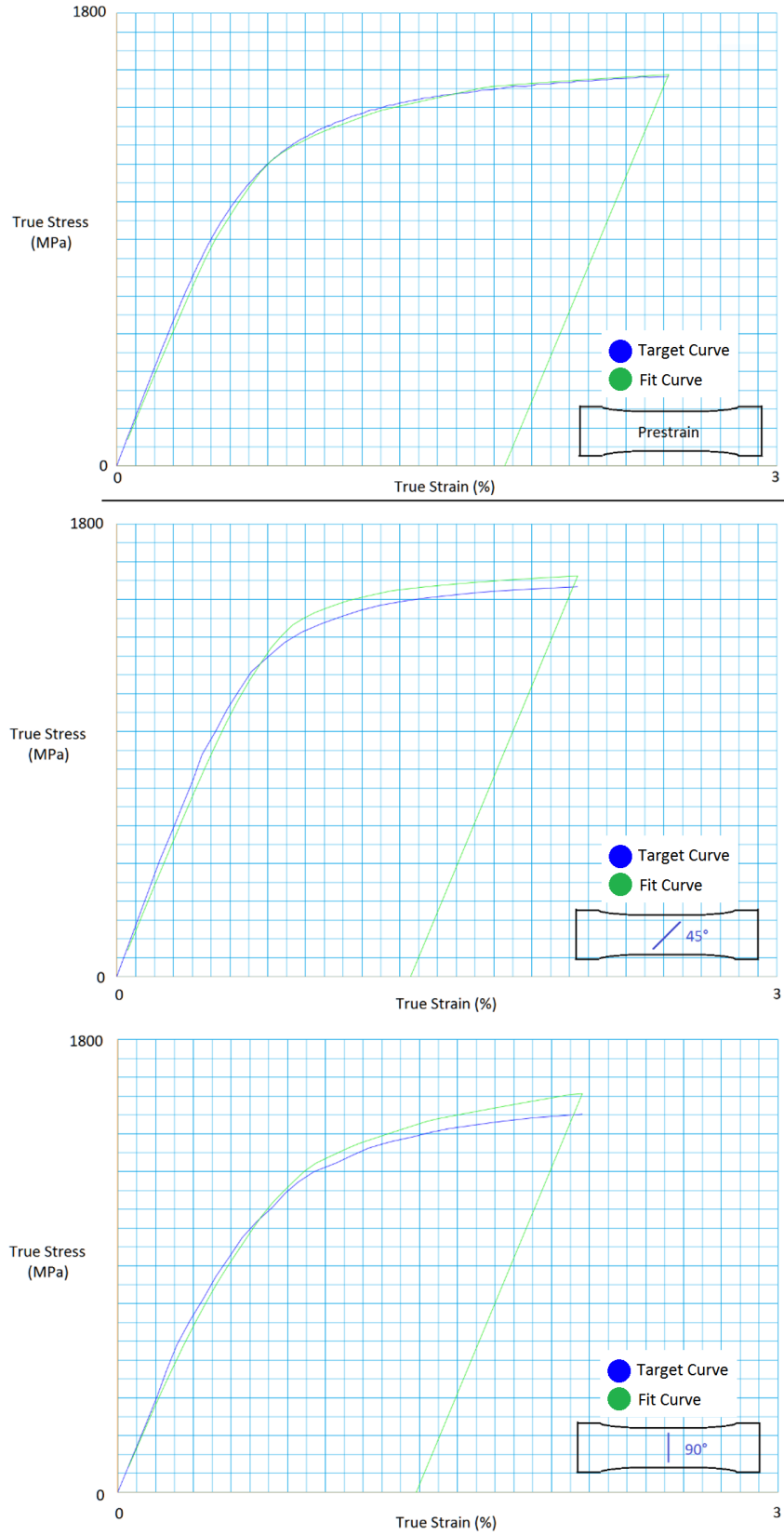


Figure 3.79 – Multiaxial portion of simultaneous fit to the Direct Masing Model (Usibor)

3.5.3 Anisotropic Behaviour and Tempering Behaviour

Up till now, we have fit our data assuming that the material is isotropic. As such, there are no texture or complicated residual stress effects that would give the material different properties in other directions. Tensile testing of as-quenched Usibor cut from sheets with a different orientation to the rolling direction strongly confirm this; as Figure 3.80 below depicts. Of course, there is no way to know if these properties hold in the direction perpendicular to the sheet.

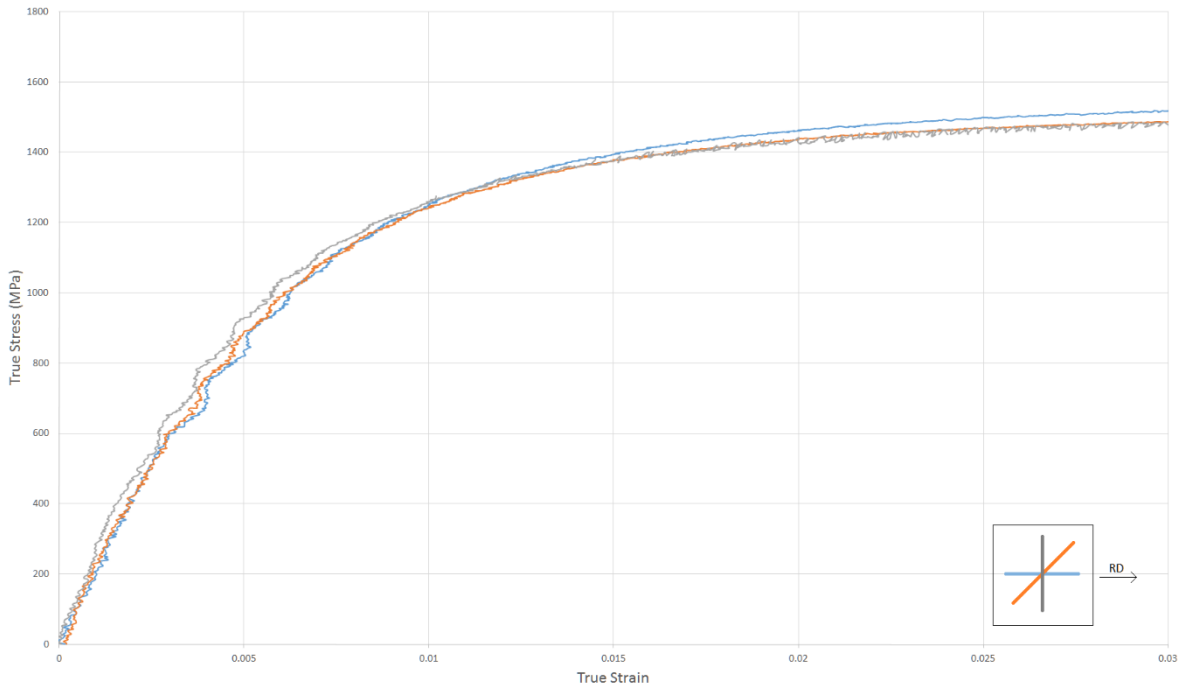


Figure 3.80 – Tensile tests at 0°, 45°, and 90° to the roll direction for as-quenched Usibor (0.24wt.%C).

Although the tensile tests are very similar in all directions, compression tests depict a different story. Upon comparison between stress/strain curves of a tensile and compression specimen, it is apparent that the material is harder in compression. There are a couple plausible reasons why this may be the case; firstly, this anisotropy may be caused by macroscopic residual stresses induced from quenching. This is possible because the compression and Bauschinger samples are made thick to prevent buckling upon compression. Another explanation is that the microscopic residual stress state favors yielding under forward loading. Although microscopic residual stresses are balanced; the distribution of tension and compression stress states may not be evenly distributed among hard and soft points in the microstructure. If this were the case, this tension/compression anisotropy would be the natural result. Figure 3.81 demonstrates this idea in a two element system in which the tensile/compressive behaviour split is numerically illustrated. The presence of internal stresses at some scale is confirmed from Tension/Compression test comparisons of as-quenched and tempered martensite. From Figure 3.82, we see that the difference between the tension and compression curves is reduced upon tempering; with a one hour 300°C temper effectively eliminating this anisotropy.

Two Element System

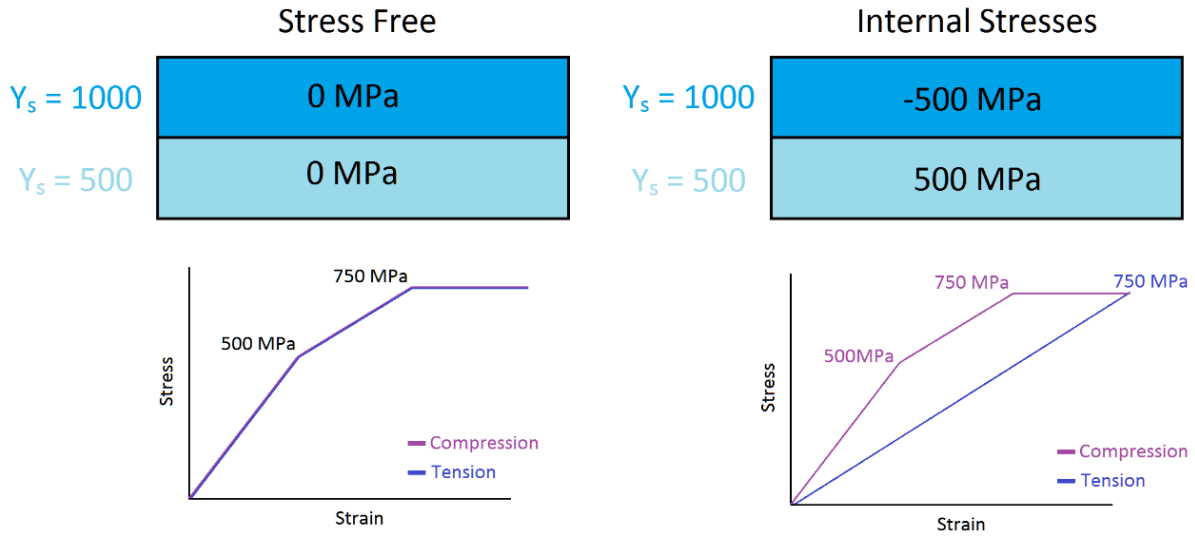


Figure 3.81 – One-dimensional numerical depiction of how internal stresses can cause forward/reverse loading anisotropy

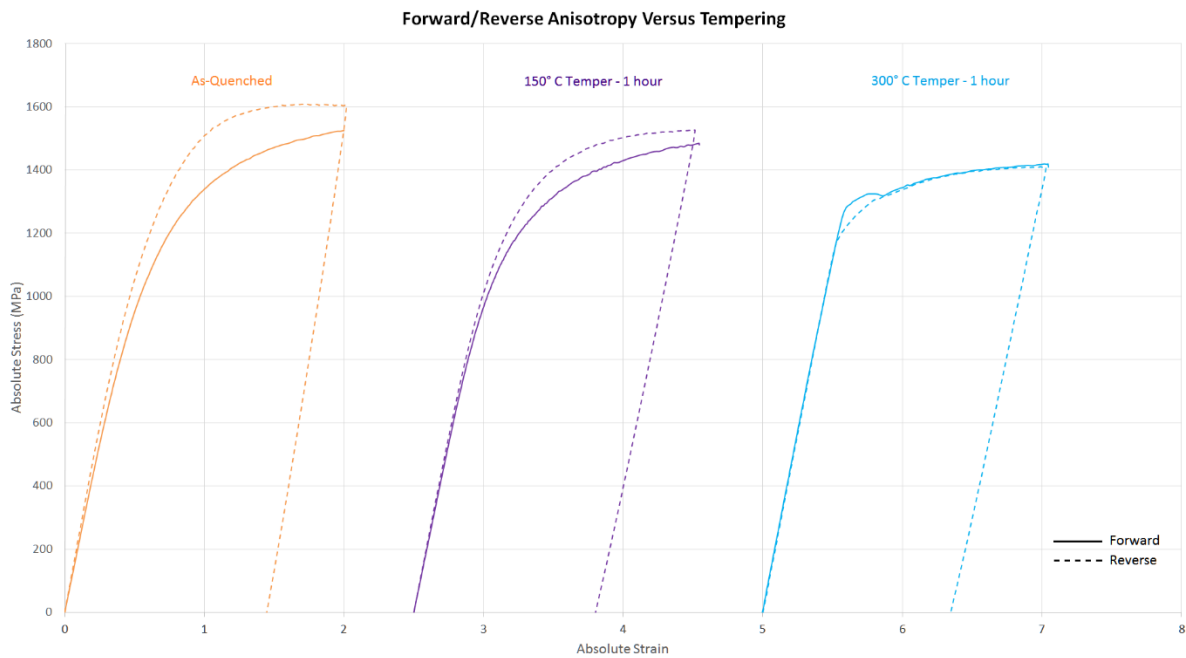


Figure 3.82 – Comparison of forward (tension) and reverse (compression) loading curves for Usibor 0.24wt.% Carbon for different degrees of tempering. Testing data courtesy Reza Roumina.

Modelling Anisotropy with Masing

We can model the anisotropy that exists in unstrained specimens with a Masing model by assuming that the subelements are prestrained; that is, they are under internal stresses in their resting state. Since there is no load on the macroscopic sample as a whole, these internal stresses must balance to zero. Previously, our genetic algorithm performed a search for a collection of yield strengths and hardening parameters that best described the data. If we are to now include the compression data (that effectively adds the reality of anisotropy), we must now allow the algorithm to search for stress components as well. Specifically, for each subelement, we are searching for a yield strength (Y_s), isotropic hardening parameter (linear hardening) (H_{ISO}), and stress state (S_{ij}). Additionally, equilibrium must be enforced between the subelements. Note that the addition of the pre-stress state to the subelements is equivalent to shifting the yield surfaces in the previous models presented.

A second concern that arises when dealing with anisotropy is that an anisotropic material model will intrinsically behave differently in different directions; even if that behaviour is not necessarily desired. For this reason, we will fit the entire data set rotated in plane on a sheet at an angle of 0° , 45° , and 90° . We are doing this because Figure 3.80 suggests that there is no difference in behaviour with regard to in-sheet angle. Since we have no data regarding mechanical behaviour outside the plane of the sheet, we will allow this to vary freely. Figure 3.83 below summarizes the fitting set that we will use. In summation, we will fit the 1% Bauschinger Test, 2% Bauschinger Test, and 2% Compression Test at in-plane angles of 0° , 45° , and 90° . Three different fits will be performed; for as-quenched Martensite, 150°C Tempered Martensite, and 300°C Tempered Martensite so that we can see how the internal stresses evolve between them. The data presented will use a 50-Subelement Masing model. The fitting collections for this defined test set are shown on the next several pages from Figures 3.84 to 3.92. Note that these graphs are all part of the same fit for each temper condition.

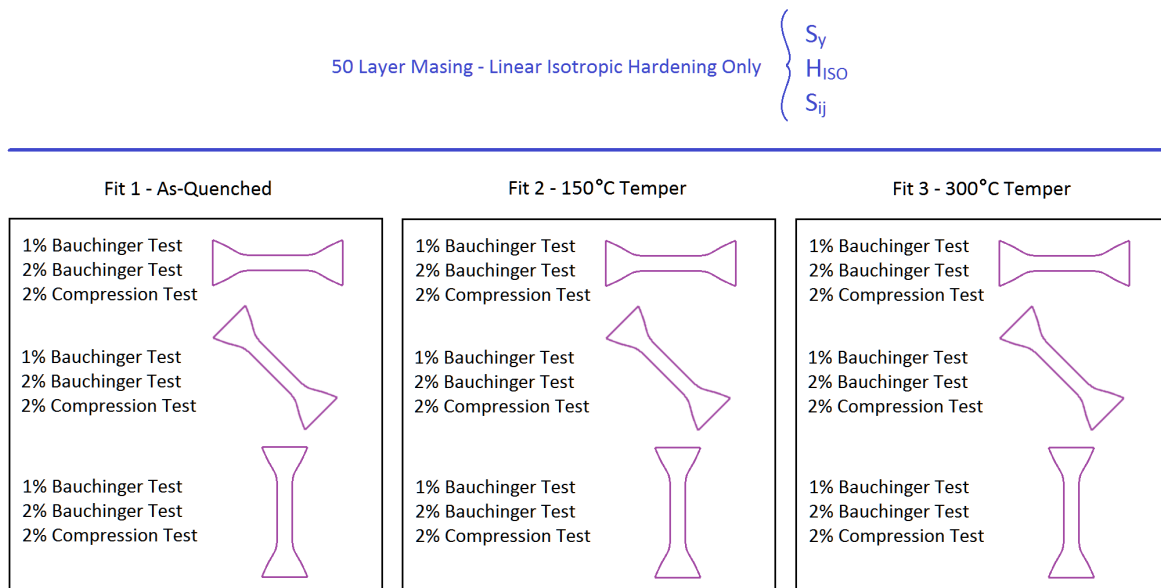


Figure 3.83 – Summary of fitting method used to model anisotropy in Usibor 0.24wt.%C Steel. Three different fits are conducted; each for different temper conditions. Internal stress states are permitted in the Masing subelements and are actively searched during the fitting procedure.

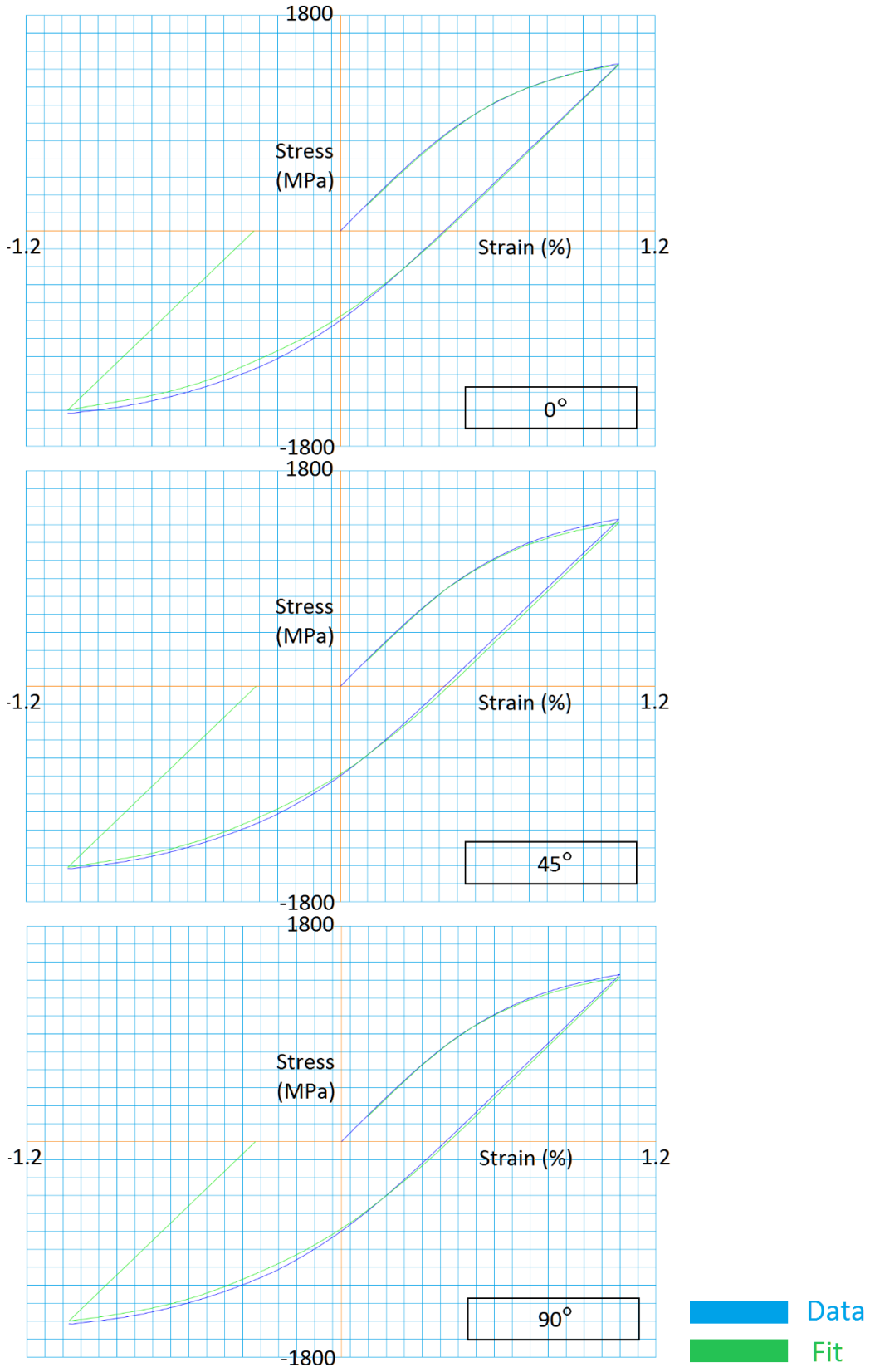


Figure 3.84 – AS-QUENCHED – 1% Bauschinger Test – USIBOR 0.24 wt.%C

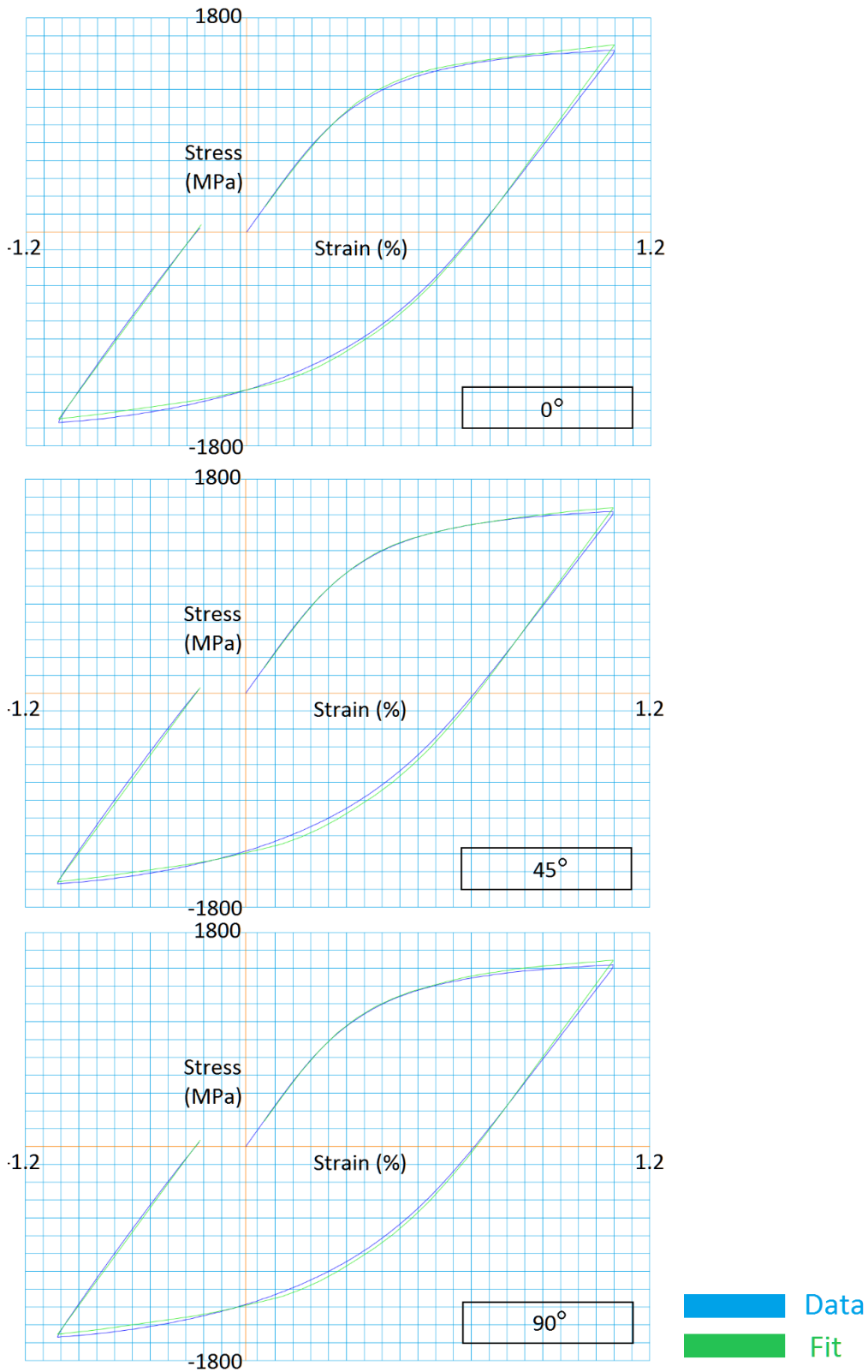


Figure 3.85 – AS-QUENCHED – 2% Bauschinger Test – USIBOR 0.24 wt.%C

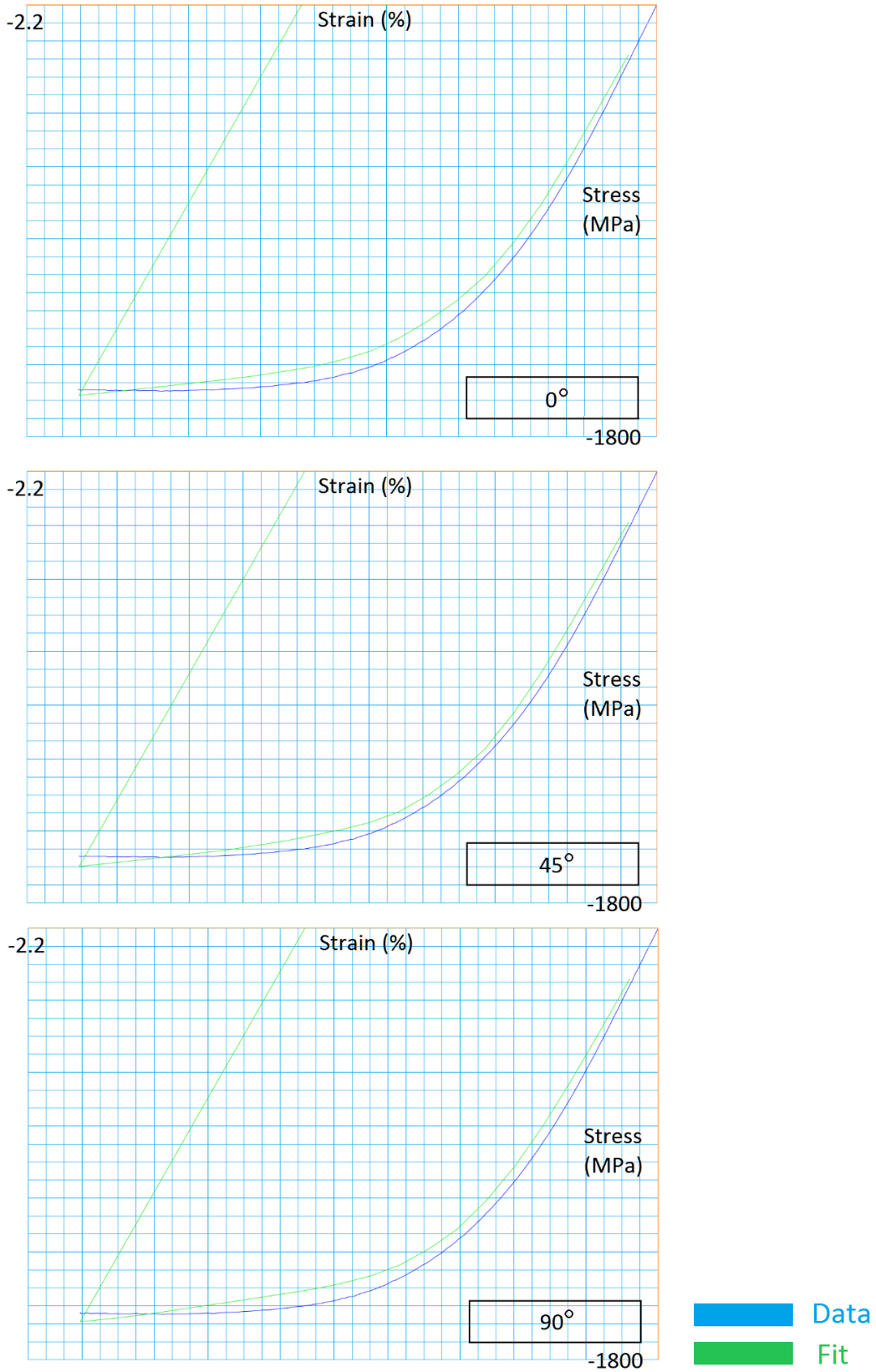


Figure 3.86 – AS-QUENCHED – 2% Compression Test – USIBOR 0.24 wt.%C

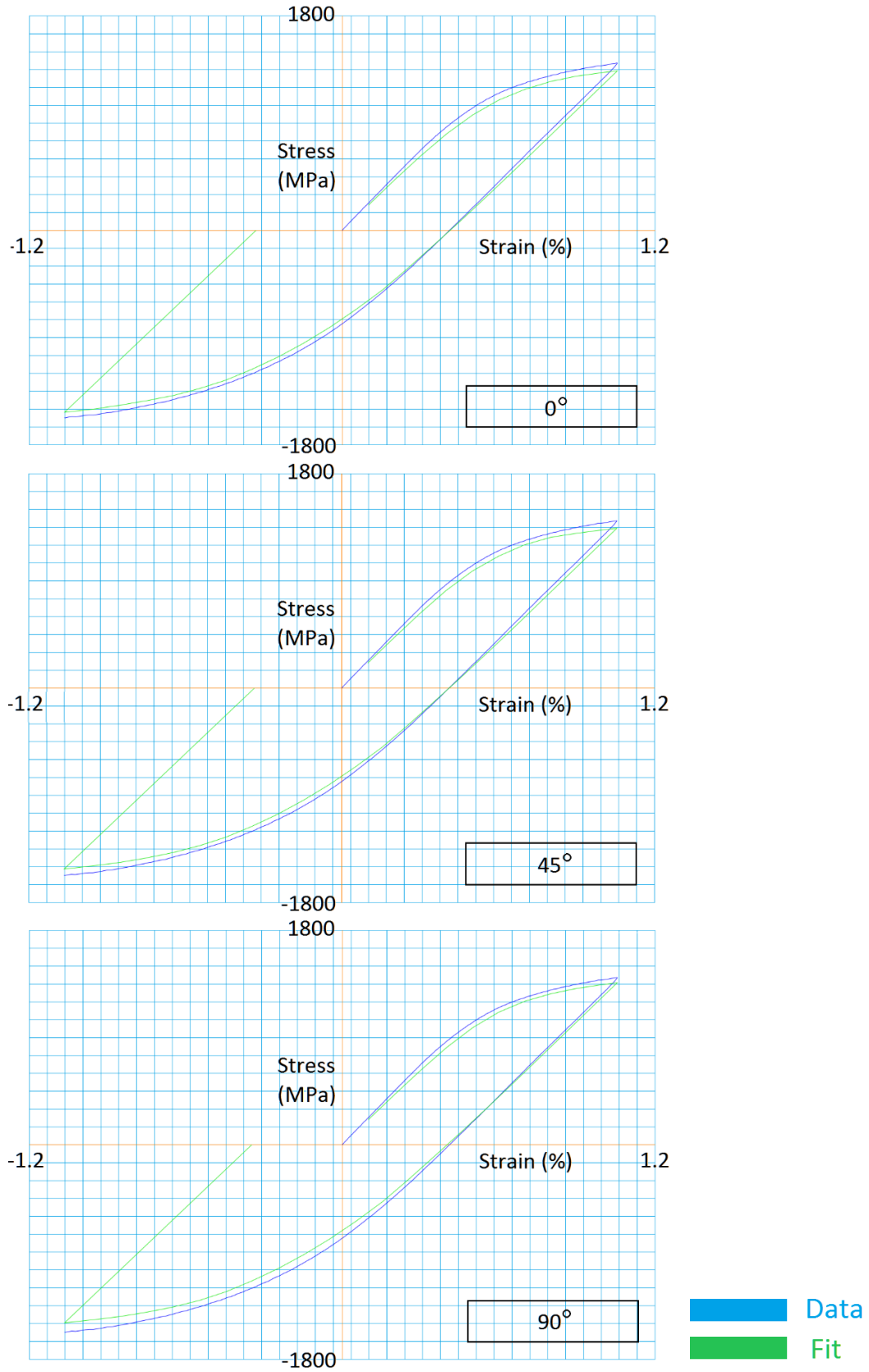


Figure 3.87 – 150°C TEMPER - 1 HOUR – 1% Bauschinger Test – USIBOR 0.24 wt.%C

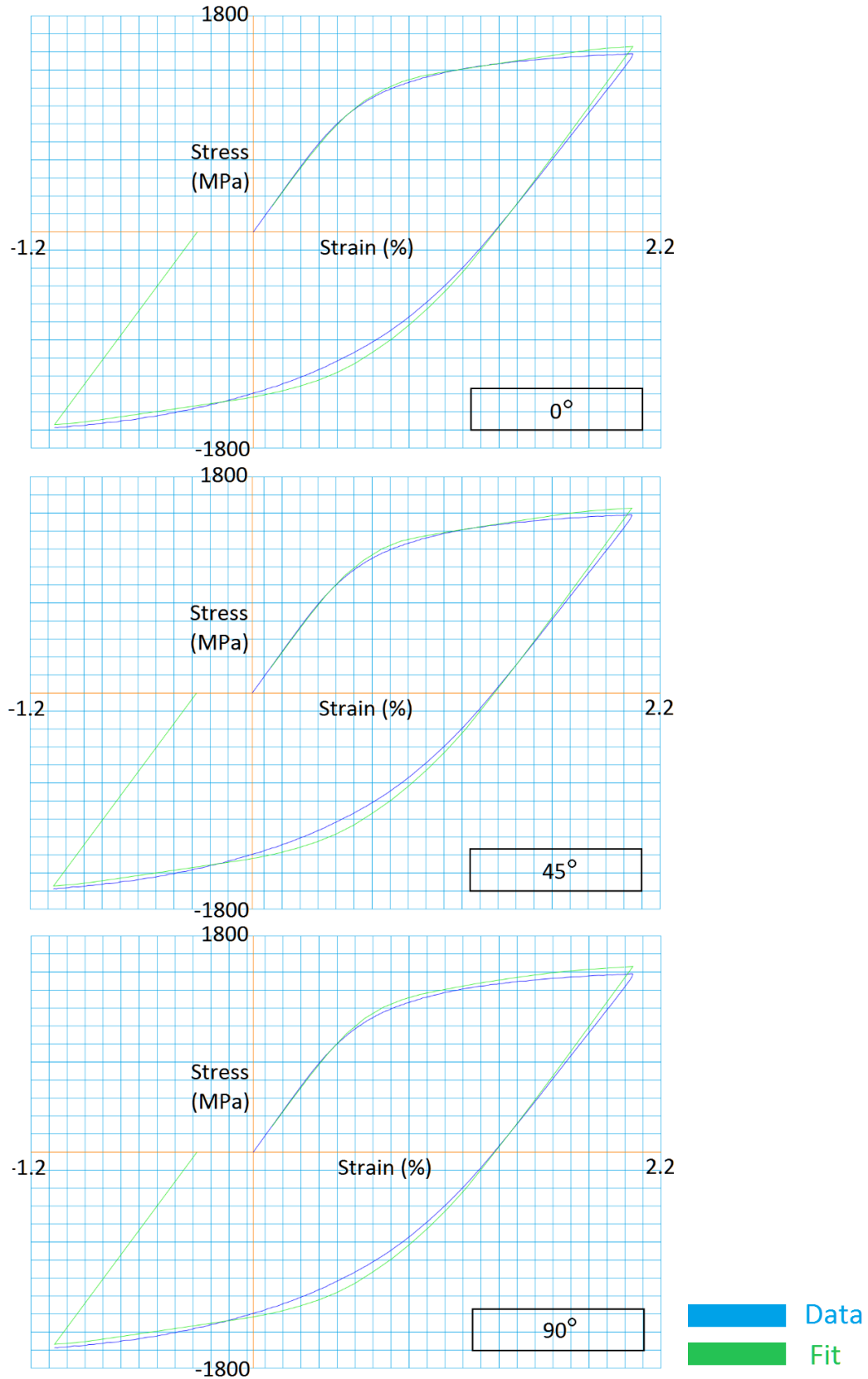


Figure 3.88 - 150°C TEMPER - 1 HOUR - 2% Bauschinger Test - USBOR 0.24 wt.%C

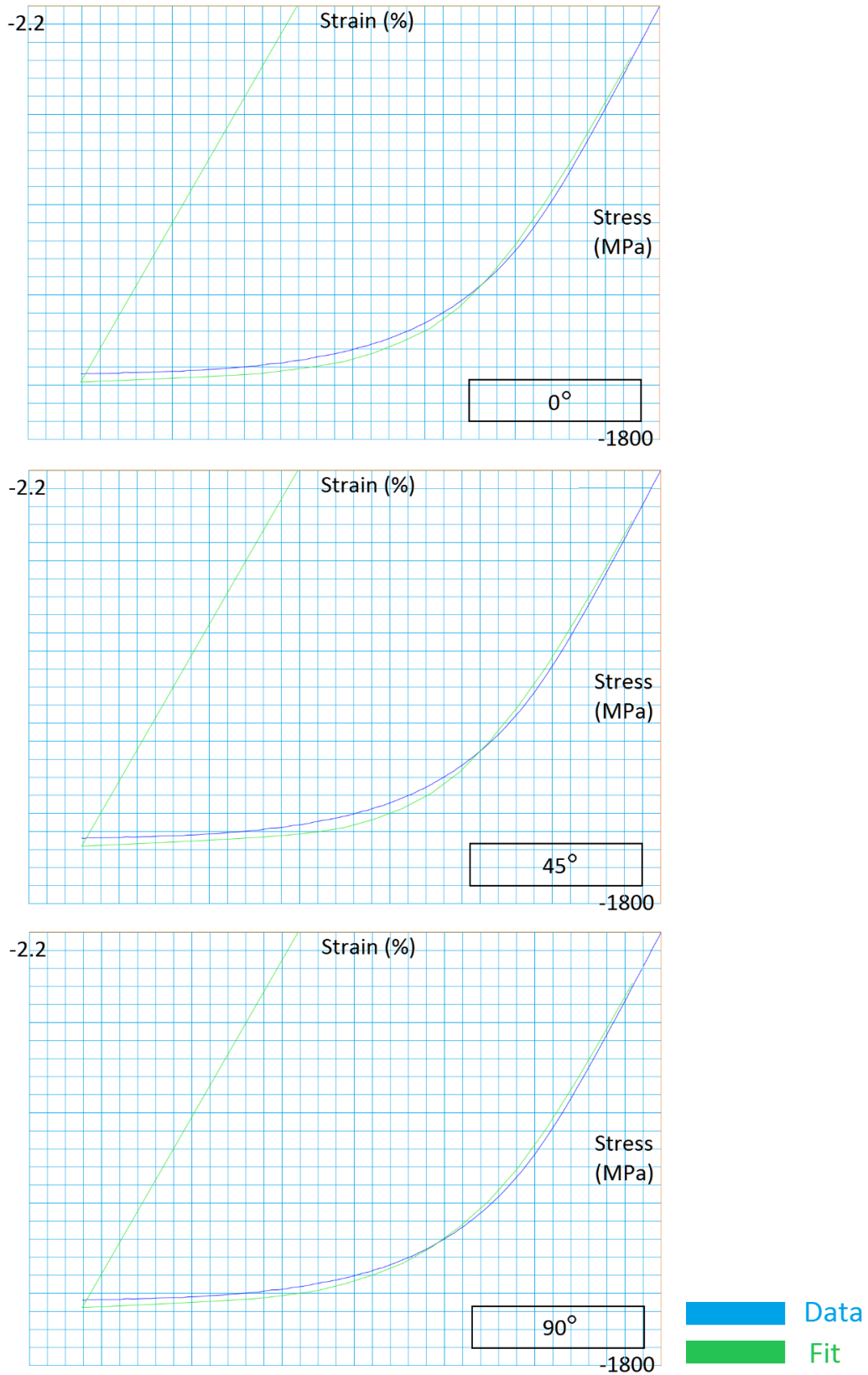


Figure 3.89 - 150°C TEMPER - 1 HOUR – 2% Compression Test – USIBOR 0.24 wt.%C

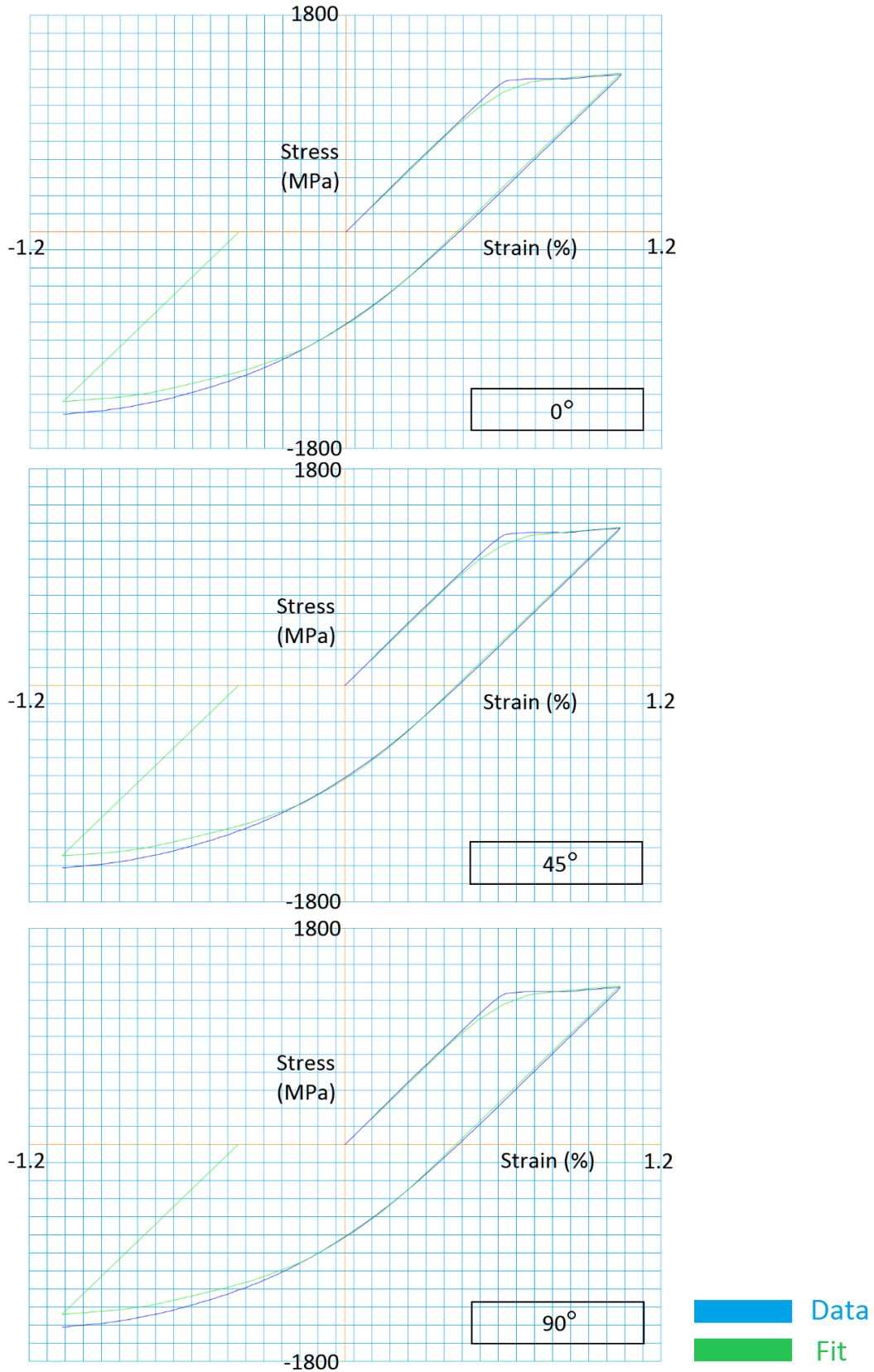


Figure 3.90 - 300°C TEMPER - 1 HOUR – 1% Bauschinger Test – USIBOR 0.24 wt.%C

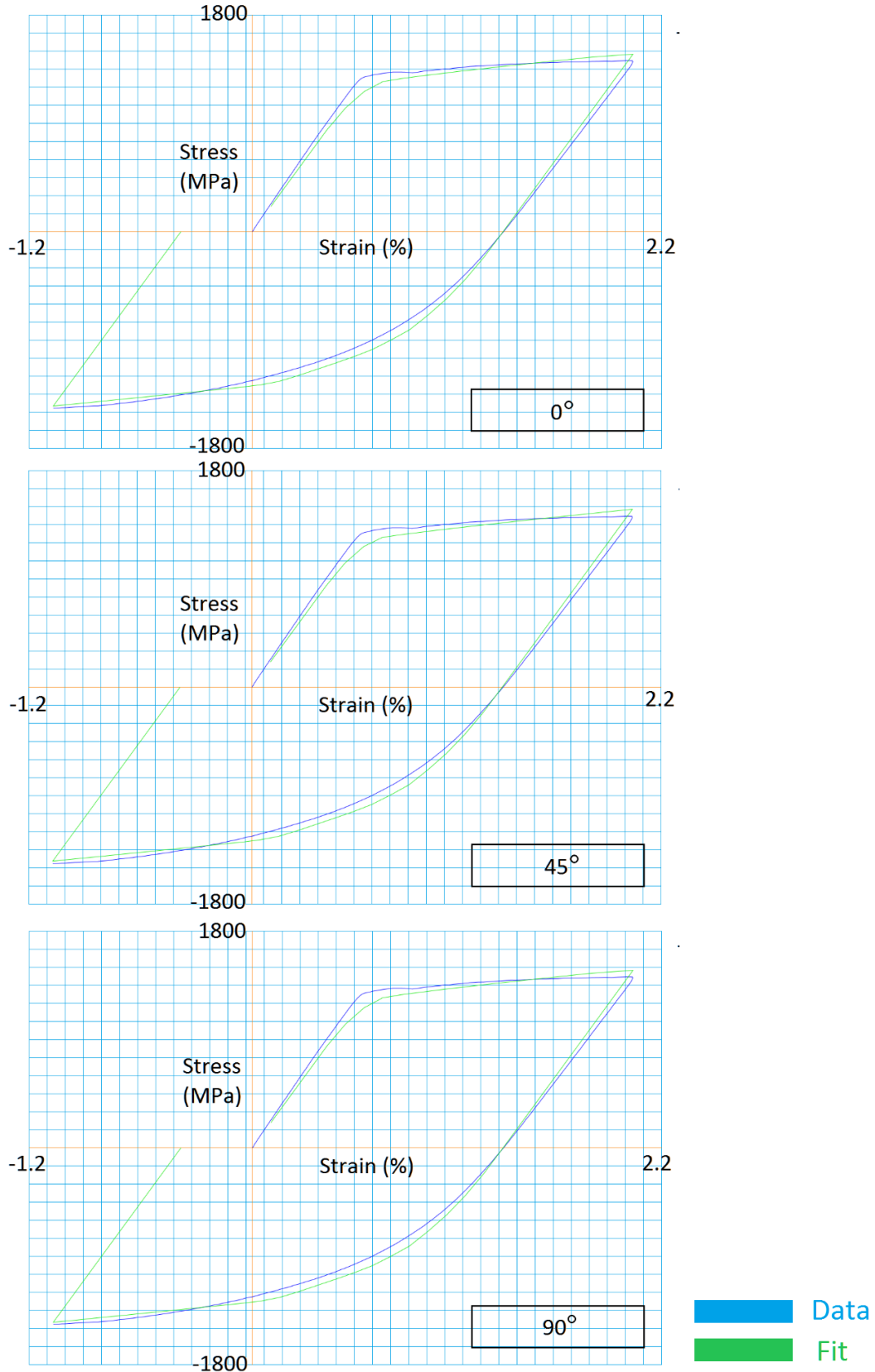


Figure 3.91 - 300°C TEMPER - 1 HOUR - 2% Bauschinger Test - USIBOR 0.24 wt.%C

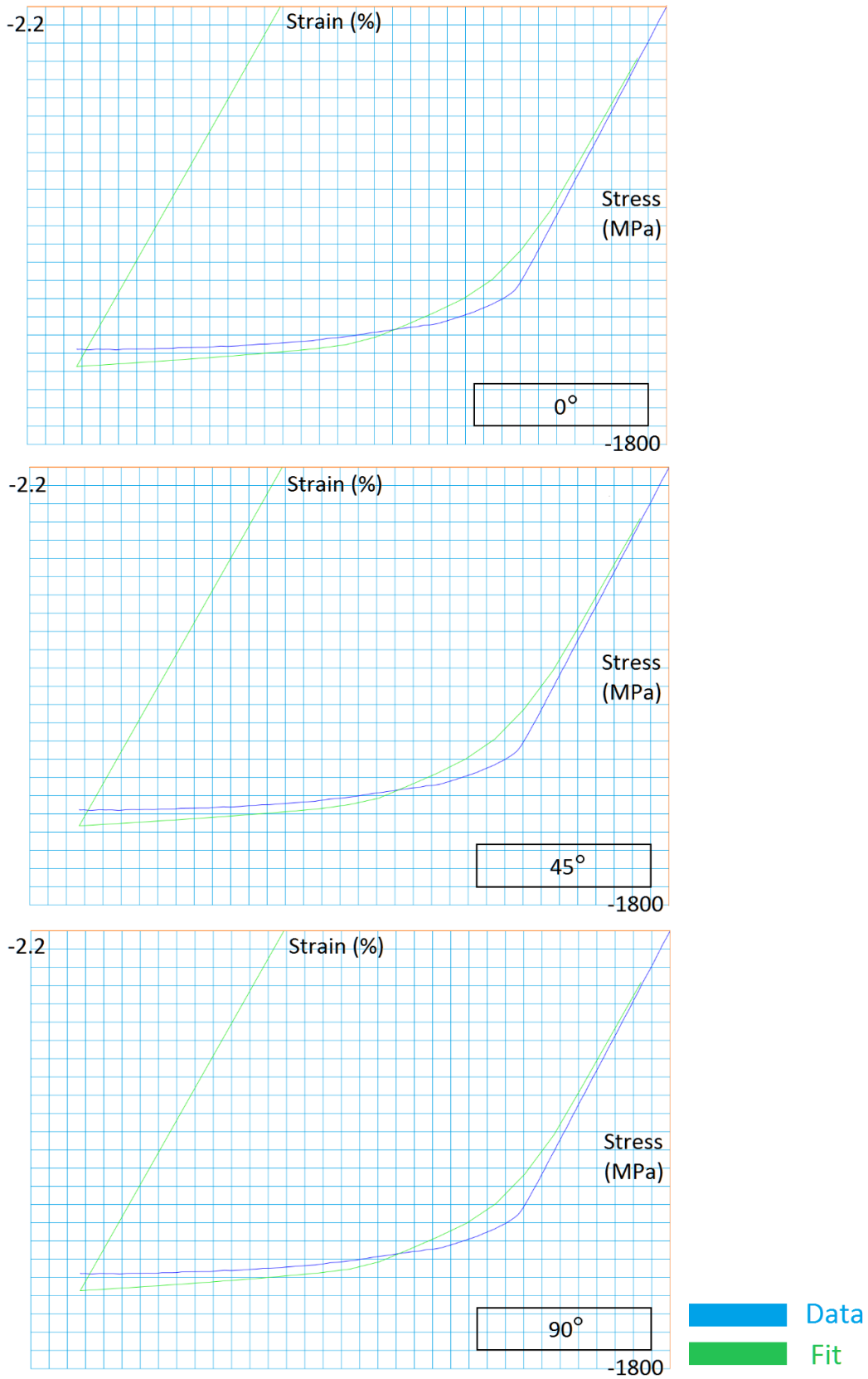


Figure 3.92 - 300°C TEMPER - 1 HOUR - 2% Compression Test – USIBOR 0.24 wt.%C

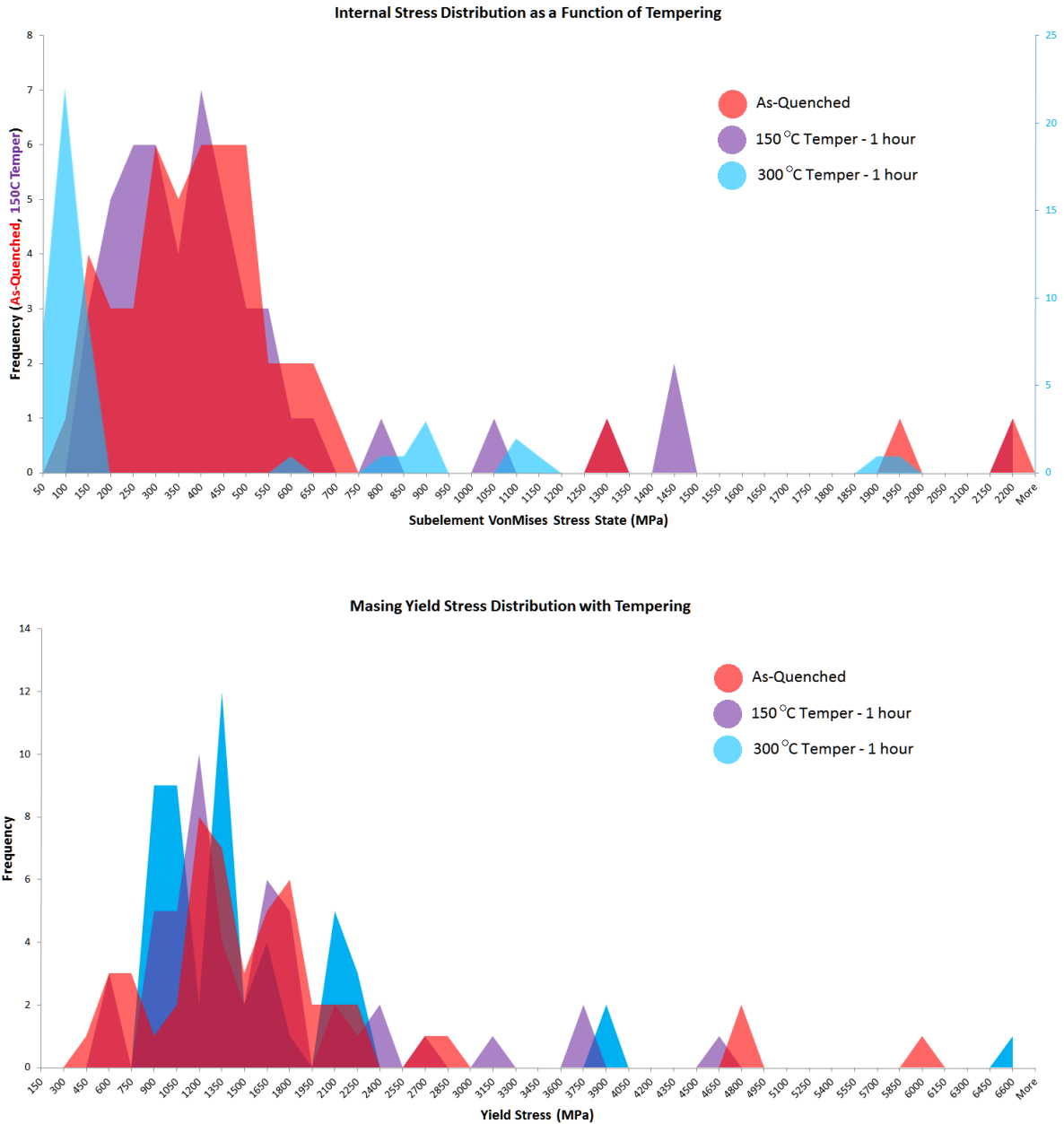
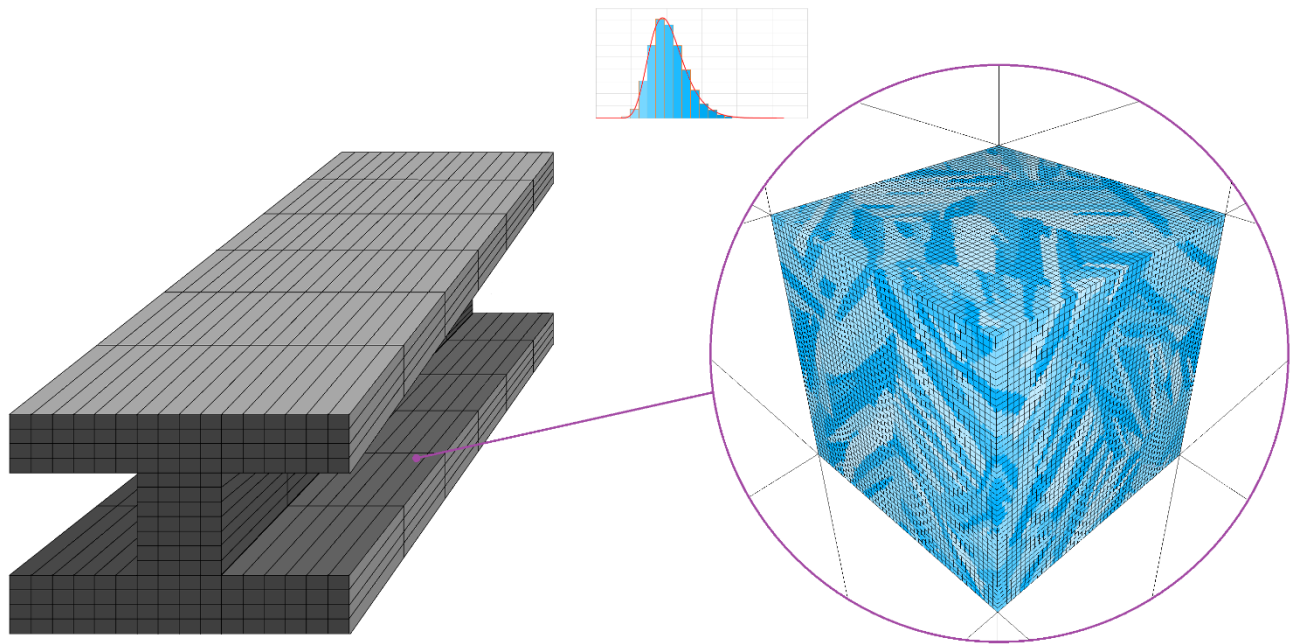


Figure 3.93 – Distributions of vonMises Stress(top) and Yield Strengths(bottom) for Masing subelements fitted to experimental data of various temper conditions (shown in previous figures).

From cursory inspection, we see that the fits we have obtained are of quite good quality. However, the really enlightening information does not lie in the curves themselves. but rather, can be gleamed from statistical trends in the fitted quantities. For instance, if we were to plot subelement yield stresses, and subelement vonMises stress states (Figure 3.93), we see some definitely interesting behaviour. Firstly, it is clear that the intensity of the internal stresses drops with tempering along with a tightening of the distribution. Additionally, the yield stress distribution does not shift, but rather, it becomes more intensified around a peak of approximately 1300 MPa for Usibor 0.24wt.%C. Such behaviour makes sense from a microstructural point of view since internal stresses would expect to be relieved with exposure to high temperatures; if the relief mechanism is at all creep like, regions with

higher stresses should relieve fastest; thus resulting in a tightening of the distribution. The yield stress normalization is consistent as well since we are removing the material differences in lath phase distribution. Specifically, we are eliminating differences in microstructure that stem from different auto-temper times in an as-quenched material.

These observations are of particular interest to one who would like to construct a model for mechanical behaviour as a function of different tempering temperatures and times. It would be of interest to run the same analysis for a model consisting of more layers than 50 so that the statistical shape of the yield and internal stress distributions could be more clearly defined. If this were done for a variety of tempering conditions, it may be possible to construct parameter transformation functions that rely on temper time and temperature as input. Such work is outside the scope of this thesis and for now, we focus our investigations into purely as-quenched martensite.



3.6 Martensitic Micro-Cell Model

In the last section, we took our first steps into building a representative microstructural model via the definition of a simple stress averaging function; that is, a stress average of multiple subelements that represent micro-regions within the material. In this section, we take things a step further. Instead of defining a simple representative function to operate as the connection between macroscopic stress and subelement internal stresses, we ask the question, what if the function were in fact a simulation of its own? That is to say, at each integration point in the material, we run a micromechanical simulation of the microstructure of the martensite defined via a periodic unit cell. This simulation effectively acts as a constitutive model; accepting a strain increment that is applied to the cell and returning the cell average stress state. By doing this, we effectively eliminate the iso-strain assumption of Masing, and instead allow each subelement to have spatial resolution; we rigorously enforce deformation consistency between subelements.

The use of this technique has been demonstrated in the literature for a number of materials and is referred to as first order homogenization. Before constructing the specific model, we will study the theory of this technique, how it's been implemented in finite element literature, and the requirements for proper implementation

3.6.1 Macro-Meso Connection¹⁰

In conventional finite element analysis, at each step or iteration, a strain increment is evaluated at each integration point and partitioned into its appropriate elastic and inelastic components via a constitutive model. This model is either of closed form, as is the case in elasticity; or is incrementally defined as is the case in conventional macroscopic plasticity models. These constitutive models are based on the idea of homogenization of material behaviour; the heterogeneous microscale can be homogenized at the macroscopic scale (Hill 1984). In this section we do the same thing, however, the constitutive model is no longer a simple function, or defined analytically, but rather a simulation of a microscopic fraction of the macroscopic material that is extended to infinity via periodic boundary conditions; this microscopic representation is called a Representative Volume Element (RVE).

Conceptually, one can imagine this type of model being performed to represent isotropic elasticity. If a periodic unit cell consisting of many grains with their own anisotropically-oriented elastic behaviour were simulated with the application of a global strain, one would expect to recover the macroscopic constitutive model if the average stress in the unit cell were calculated. In essence, we are building a macroscopic constitutive model that has a microscopic mechanical simulation being run “under the hood”, with the idea that a good macroscopic description can be formulated by tracking events occurring on a scale below. This is referred to as the macro-meso connection and the procedure for its implementation in Finite Element Analysis is illustrated in Figure 3.94 below.

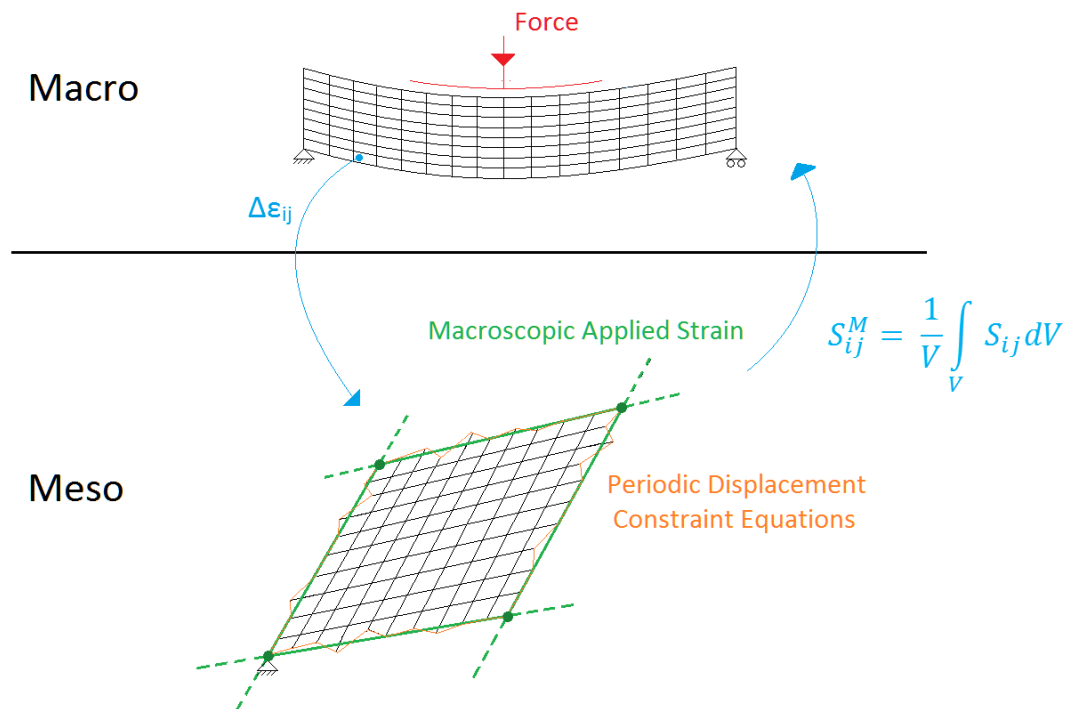


Figure 3.94 - Depiction of the Macro-Meso connection paradigm. The strain increment is transferred to the meso-level via equivalent displacement boundary conditions. The deformed cell is then solved for equilibrium with periodic displacement constraint equations enforced. After equilibrium, the volume stress average is returned to the macro level as the macroscopic stress state.

¹⁰ More appropriately named the meso-micro connection in the context of this thesis.

The figure shows how macroscopic strains are transferred to the mesoscale and simulated via periodic displacement boundary conditions. The stress state in the unit cell is averaged and this macroscopic stress is returned to the macro level as output for the constitutive model. This type of model has been implemented in the literature for the study of heterogeneous materials such as polycrystals (Miehe, Schotte, and Schröder 1999), porous materials (Kouznetsova et al. 2001), and concrete (Gitman et al. 2008). As such, it would appear to be a good type of candidate model for a nanocomposite such as martensite.

Evolution of a Masing Type Macro-Meso Connection

The Direct Masing model we used in the last section can be considered on the representative volume element level. In this context, the RVE element is a single “element” with layered subelements superimposed (Figure 3.95). This RVE effectively reduces to the stress averaging formula we saw in the last section. Of course, we can now ask the question of what happens when we define the representative volume element less abstractly and give it structure. To this regard, two structures are proposed; a structure in which the Masing subelements are laid out in a grid, and a structure in which the subelements are laid out in an arrangement approximating the block structure of martensite (Figure 3.97). The additional model resolution provided by these structures should improve the quality of the fit due to the ability for plastic strain to be localized in the material. We will test the two spatially resolved structures and compare performance against the Masing approach. In order to do this, we will have to define how the unit cells will be constructed and fitted with the genetic algorithm. The reason for this is that in addition to the subelement properties, we must now define their position in space in a manner consistent with the rules of a representative volume element.

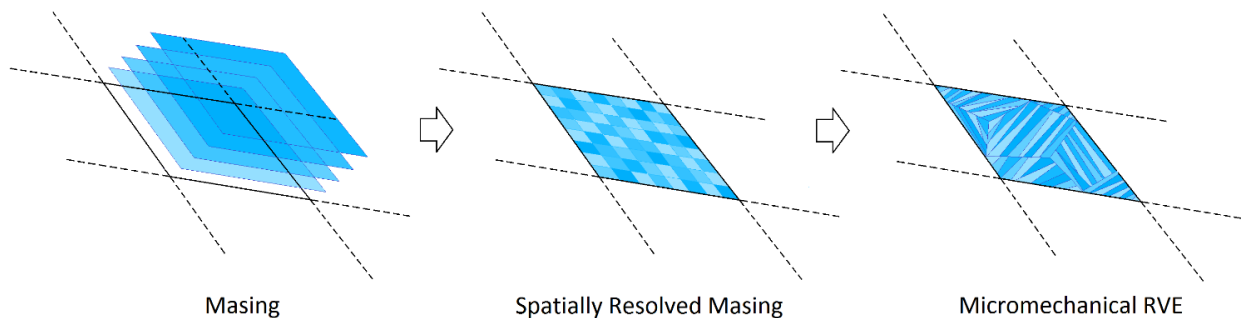


Figure 3.95 – Representative Volume Elements (Two Dimensional Analogs) for a Masing Model and two models in which the Masing subelements are spatially resolved; one in a grid pattern and another in a block like structure pattern.

3.6.2 Spatially Resolved Masing Assembly and Fitting Procedure

This type of model is relatively easy to construct due to the cubic nature of the cells. Periodicity of the unit cell is automatically enforced since the subelement boundaries lie on the cell boundaries. With regard to the fitting, we fit the subelement properties as we did in the last section for the Direct Masing model; however, we additionally assign each subelement a position in the RVE. When marching

forward in the genetic algorithm, new trial parameter sets (gene sets) will inherit different positions from the parent sets; thus, different arrangements of cells will be explored in the search. In performing this optimization, we will use the results of the Direct Masing optimization to seed the parent generation (with a small deviation of $\pm 20\%$ permitted). The reason for doing this is because the extreme cost of a simulation of this type precludes using a random parent seed.

3.6.3 Micromechanical RVE Assembly and Fitting Procedure

Unlike the last model, we will now try to define a unit cell that is representative of martensite in its structure. When assembling the unit cell to represent martensite, the first question we might ask is “What scale do we wish to represent?” Recall that there are many length scales that define lath martensite (Figure 3.53). The largest scale is the prior austenite and should be represented within the unit cell; however, representing the prior austenite alone is not sufficient because there is no real mechanical heterogeneity between prior austenite grains. In fact, the mechanical heterogeneity is expected to exist all the way at the bottom; at the lath level. We saw previously that the laths are expected to have different hardness as well as variations in internal stress state. This would average-out at the prior austenite level. The problem with representing both laths and prior austenite grains simultaneously is that the difference in scales is approximately 1000 times at the extremes. This difference is too extreme for modern day computational resources as it would imply a simulation of one billion finite elements would need to be performed; at each integration point of a macroscopic model nonetheless! As such, we compromise and scale back to the block level; the level above the laths. At this level, the difference in length scales varies from 10-100 times; a more reasonable feat. As such, the subelements of the model are now effectively the block structure of martensite. We will construct a periodic unit cell that closely approximates the block structure and assign each subelement to a block in the cell. The genetic algorithm fitter will play with the material properties of each subelement (block) as it did in the Direct Masing model.

Packet Tessellation

The prior austenite grains of martensite are really defined as a collection of packets. These packets are fairly random in size, positioning, and structure as shown from an experimental map in Figure 3.96. In order to build a good representation of this structure, Veronoi tessellation is used generate a random packet seed grid. After this step, the Veronoi cells are agglomerated randomly in order to better represent the structure. Any random grouping of packets is representative of a prior austenite grain; however, such a distinction adds no real value to the analysis unless one were to keep track of variants. Also note that unlike the schematic example shown, the actual Veronoi mesh enforces periodicity at the boundaries.

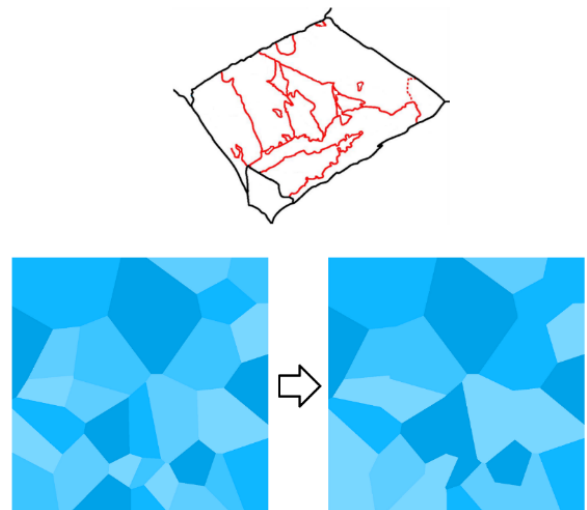


Figure 3.96 - (Top) Experimental map from (Kitahara et al. 2006) depicting prior austenite (black lines) and packet boundaries (red lines). (Below) Veronoi tessellation using random seeds before and after agglomeration

Block Assembly

Now that we have the packet structure of the martensite, we must now define the block structure within the packets. We know schematically that the blocks tend to be relatively aligned within the packets and have a plate-like 3D structure. Additionally, the thickness of the plates tends to vary considerably and they tend to grow until they reach a packet boundary or a previously transformed region. With this in mind, we progress by assigning each packet a random global block orientation. Each block will have this orientation of growth with a small random deviation permitted. Additionally, each block is given a random thickness. As more blocks are assigned, the untransformed space diminishes and the thickness of future blocks is necessarily reduced to fit. These blocks stand as proxies for the laths in this respect as this is more characteristic of lath growth. Figure 3.97 shows a single packet with the block structure that is generated via this algorithm.

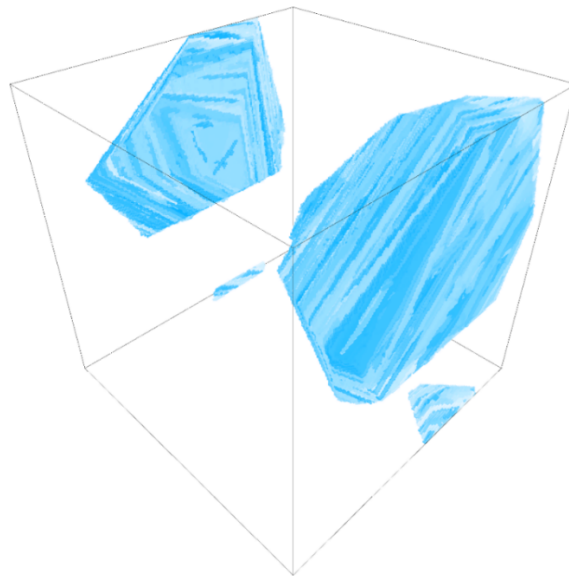


Figure 3.97 – Procedurally generated block structure of a single martensite packet. Notice that the blocks are plate-like with varying thickness and small deviations in orientation. Also, notice that the cell is indeed periodic.

Constitutive Applicability

In assembling our Representative Volume Element (RVE), we assign different yield strengths for each of the blocks present; this is the legacy of the Masing model and was justified in previous sections. Each of the blocks is treated as elastically isotropic and flows under classical J-2 plasticity. Comparing this constitutive assumption for the blocks to the reality of martensite, it is clear that we are making some assumptions for simplicity. It is untrue that the blocks would exhibit true isotropic behaviour and continuum plastic flow; however, based on the variant assignment of 6 possible variants per packet (Kitahara et al. 2006), quasi-isotropic behaviour could be expected as well as somewhat continuum-like plastic flow. It is no doubt that the assignment of the anisotropic crystal elastic constants as well as implementing a crystal plasticity model would give better fidelity to reality; however, this is a complication we forgo at the moment.

3.6.4 Solving for Equilibrium in the Microcell

We've already discussed how the representative volume element acts as the constitutive model at each integration point of the model. Upon application of the macroscopic strain to the RVE, we would then solve for equilibrium within the cell to find the average stress. In solving for equilibrium, one would naively think that we could apply the same quasi-static solver presented in Chapter 2; however, since this is a cell with periodic boundary conditions, the bandwidth of the stiffness matrix would be prohibitive due to the coupling equations on each edge of the cell (this effectively removes the sparseness of the matrix). For this reason, we have opted for an explicit dynamic solution scheme which forgoes the use of a global stiffness matrix. By using this scheme, we are solving for the dynamic solution and running the time until the system reaches its equilibrium state (the static solution).

$$[M][\ddot{u}] + [C][\dot{u}] + [K][u] = [F]$$

Forward Euler $\left(\frac{1}{\Delta t^2}[M] + \frac{1}{2\Delta t}[C]\right)[u]^{t+\Delta t} = [F]_{ext} - [F]_{int} + \frac{2}{\Delta t^2}[M][u]^t - \left(\frac{1}{\Delta t^2}[M] - \frac{1}{2\Delta t}[C]\right)[u]^{t-\Delta t}$

Equation 3.57 – Explicit Dynamic solution time-stepping procedure.

The actual implementation of an explicit dynamic solver to periodic cells is quite simple. In fact, the only consideration we have to make is that the internal forces are periodic (shown red above); thus we must be sure to apply internal forces that act on boundary nodes to equivalent nodes. With this done, we do not even need to apply any essential boundary conditions to the problem when seeking equilibrium! As we see in Figure 3.98, we apply the macroscopic strain as a displacement field to the cell. Afterwards, we seek equilibrium with the appropriate periodicity of internal forces as previously discussed. We do not need any constraints on the cell in this stage because the cell is guaranteed to maintain its global strain state during equilibrium; this is because the corner nodes will always have the same forces acting on them and thus, will always move by the same amounts; that means a cell comprising just the corner nodes is only able to move as a rigid body.

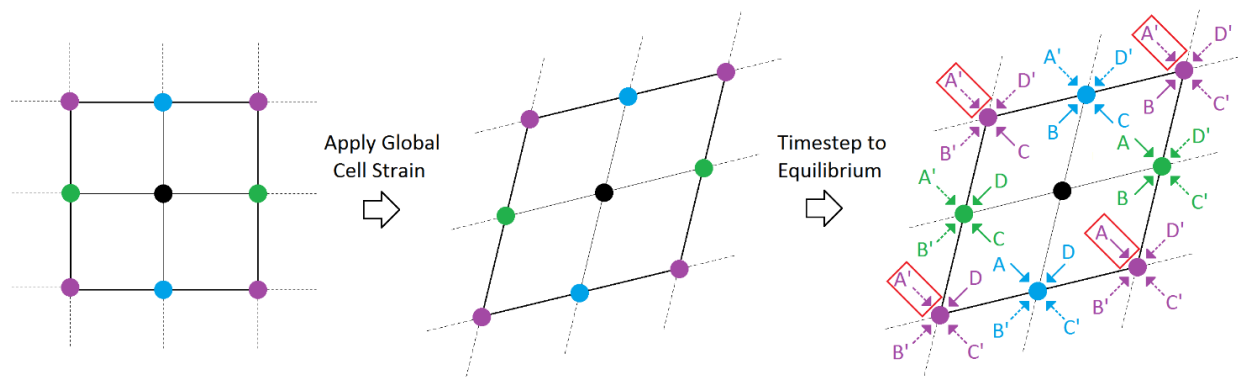


Figure 3.98 – Application of the macroscopic strain is applied to the cell via nodal displacements. This can be applied to the entire cell uniformly, or at just the corner nodes prior to seeking equilibrium. Equilibrium is found by progressing the dynamic solution in time until a static arrangement is obtained; periodic internal forces are maintained on the boundary of the cell. No nodes need to be fixed during the equilibrium phase.

3.6.5 Fit to Experimental Data

We quantitatively evaluate the suitability of each of the Representative Volume Elements in describing martensite. Due to the extreme computational cost of fitting the RVE's, only the 1% and 2% Bauschinger tests were used as fitting data. The summary of the fit performance is shown in Table 3.3 below, normalized to Masing.

Model	Performance	Number of Fits	Fit Time
Masing	1.0	512,000	1 hour
Spatial Resolved Masing	0.66	3,200	1 week
Microstructural RVE	0.89	1,600	2 weeks

Table 3.3 – Relative Fit quality of Various RVE's and associated qualities of the relevant fits. Notice that the more advanced RVE's took significantly more resources while achieving better fits. The number of fits corresponds to the number of tested parameter sets.

It is interesting that the more complex RVE's did manage to perform better than Masing. However, this performance increase is small and comes at a significant increase in computational cost. It is quite clear that diminishing returns sets in as the model is further refined. In fact, it can be argued that a Masing model performs unjustifiably well considering its vague approximation of the microstructure. However, the performance to cost ratio of a Masing model is orders to magnitude higher than for the more refined models. As such, we will rely on a Masing model in the subsequent chapter.

The fits obtained for each model type are shown in Figure 3.99. The improvements provided by the more advanced representative volumes are small but noticeable; this is due to the ability of these models to deviate from ideal Masing behaviour. It is clear that further gains will not be possible without resorting to more refined descriptions of the microstructure. Such descriptions will inevitably need to make use of crystal plasticity, and anisotropic elasticity. Further refinements will of course come at increase cost; in Section 3.8 we will take a close examination of such cost scaling and see how these ideas will become relevant in the future.

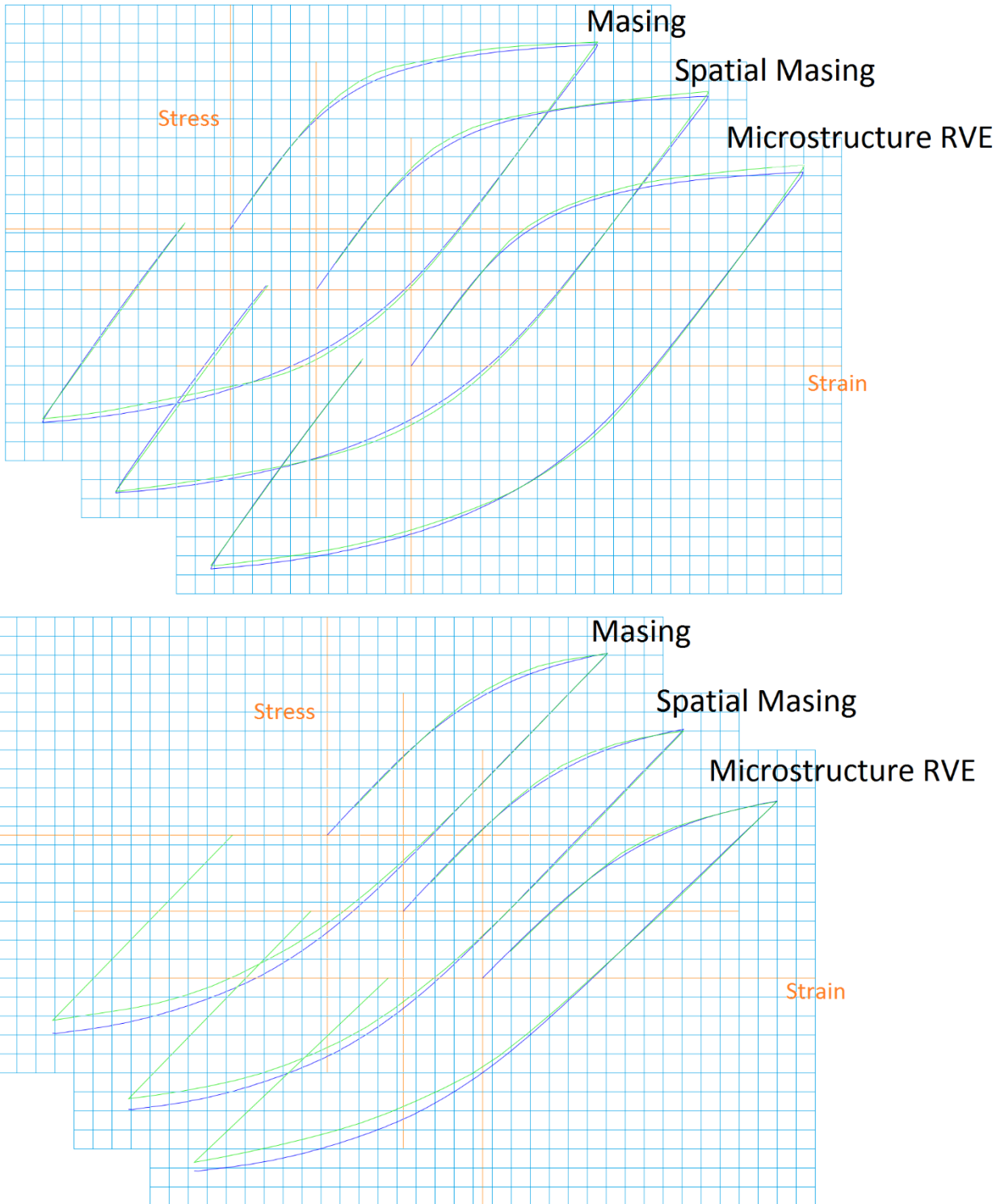


Figure 3.99 – Fits of various representative volume elements to the 0.24wt.% Usibor data (**Top** – 2% Bauschinger test, **Bottom** – 1% Bauschinger test). The 1% and 2% Bauschinger tests are fitted simultaneously. Fitted curves are shown in green and experimental data is in blue.

Relative fit values: Masing – 1.68, Spatial Masing - 1.09, Microstructure RVE - 1.45. (0 = perfect fit)

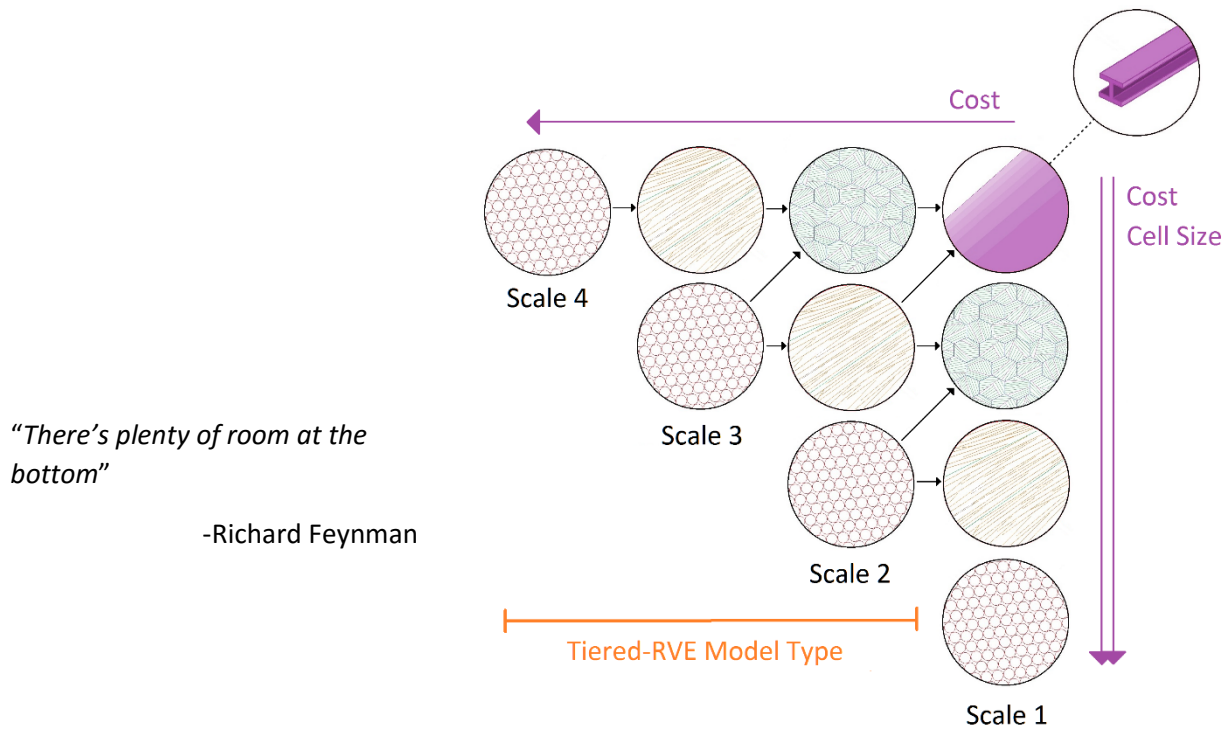
3.7 Model Comparisons and Conclusions

In this chapter, what we really did was examine very closely the concept of a meso-micro connection as it pertains to martensite (or more generally a bridge between length scales). We began by looking at the simplest models in which classical J-2 plasticity models were used to homogenize the microscale to a smooth macroscopic continuum. We saw that these are wholly inadequate for martensite as the nuances of the elastoplastic transition are neglected. We continued by modeling the microscale as a collection of elastoplastic elements deforming in parallel; as introduced by Masing. These models performed very well with a minimal increase in cost over mixed hardening models. Interestingly, the work-hardening field model performed slightly better than the multisurface plasticity model and direct Masing model, despite not being a true representation of Masing’s model. This behaviour was not planned and just a fortunate surprise; however, not entirely unexpected, as we saw that a Masing model should not represent martensite perfectly. Finally, we refined our definition of the microscopic scale to something much more sophisticated than Masing in which we constructed a representative volume element to keep track of plasticity at the microscale; this model significantly improves our representation of the microscale, albeit at a very large increase in cost. Nonetheless, the increase in performance generated by this technique may be useful in certain situations; such as in more critical areas of a model. One important point of note is that the multisurface plasticity model was rated as performing slightly worse than the Direct Masing model; this is a consequence of the fact that we did not allow any isotropic hardening in the multisurface model whereas we did in the Direct Masing model. We saw that some isotropic hardening of the material is necessary as was depicted by the ideal homology factors of approximately 2.2. Theoretically, the multisurface model should perform identically to the Direct Masing model, however, from a personal point of view in implementing both models, the Direct Masing model was far more simple to implement and much more intuitive than the multisurface model.

This chapter has completed the groundwork for the next chapter in which we attempt to model compositionally graded martensitic steel that has undergone multi-strain path loading. Recall that such a material will have the quench induced residual stresses from Chapter Two superimposed on the part. We will rely on the Masing Model in the next chapter due to the prohibitive cost of the RVE model. By using the Masing Model to capture mesoscopic constitutive behaviour (through Masing’s meso-micro connection) and our quench model to capture macroscopic residual stresses, we will have a strong physical justification for modelling the room temperature behaviour of as-quenched martensitic steel.

Model	Performance	Relative Computational Cost
Mixed Hardening	10.3	0.1
Work Hardening Field	0.85	1
Multi-Surface Plasticity (No Isotropic Hardening)	1.7	1
Direct Masing	1	1
Representative Volume Element	0.6-0.7	1000-1,000,000

Table 3.4 – Model Comparisons normalized to the Direct Masing model. The performance comparison is a measure of fit quality with zero representing a perfect fit (lower is better). The computational time is a measure of the time required to evaluate the constitutive model (lower is better).



3.8 Tiered Modeling Techniques

In an ideal world in which computational power is unlimited, one can imagine populating the entire domain by the smallest scale features of the material; atoms (or smaller). Of course the number of such elements would be so astronomically large that such a computation would be practically impossible in the real world; as such, compromises have to be made. We’ve explored the idea of bridging length scales as a means of capturing events that occur at various levels of a materials’ structure. The simplest models use a single bridge between the macroscale and a sub-scale; not only this, but the subscale is usually analytically homogenized such that this bridge is not traversed explicitly; this is the case with isotropic elasticity and J2-plasticity for example. In the previous section we constructed an explicit bridge between the meso-scale and micro-scale with both our Masing model, which idealizes the microscale as a collection of spring-slider elements, and a microscopic representative volume element model.

In this section, we explore the idea of extending this bridge to even smaller length scales and creating multiple tiers of bridges. For example, it is conceivable that we can go from meso to micro to nano to atomic constitutively. Of course being possible and feasible are two different criteria; as such, we will quantitatively examine the costs of doing such analyses.

3.8.1 Representative Volume Element Cost Scaling

This thesis has considered a number of representative volume elements of various structure and size. Here, we consider the relative costs in terms of time and memory required for various gauss point models; be it conventional macroscopic elasticity/plasticity, a Masing model, a finite element mesh RVE, and even molecular dynamics. Such costs are summarized in Table 3.5 below.

Gauss Point Model	Solution Points	Relative Timestep Size	Relative Solution Time	Memory (MB)
Conventional	(1)	-	0.00001	0.000080
100-Layer Masing Type	100	-	0.001	0.016
3k DOF RVE (10x10x10) nodes	5,830 2,460	1 0.25	1 1.69	0.466 0.197
30k DOF RVE (22x22x22) nodes	69,300 29,200	0.438 0.110	27.1 45.6	5.54 2.34
300k DOF RVE (46x46x46) nodes	749,000 316,000	0.198 0.0496	648 1,090	59.9 25.3
3000k DOF RVE (100x100x100) nodes	7,760,000 2,380,000	0.0909 0.0253	14,600 16,100	621 190
30000k DOF RVE (215x215x215) nodes	78,900,000 33,300,000	0.0420 0.0100	322,000 570,000	6,310 2,660
MD RVE – 100nm cube (417x417x417) atoms	72,300,000 ¹¹	(.001) ¹²	12,400,000	5,780
MD RVE – 100µm cube (417,000x417,000x417,000) atoms	7.23x10 ¹⁶	(.0000001)	10 ²⁰	10 ¹²

(8-Node Trilinear Elements) - (27-Node Triquadratic Elements)

Table 3.5 – Cost Analysis for various Gauss Point models

¹¹ Assuming Atomic Diameter of 2.4 Å (Kadav et al. 2001a)

¹² Assuming Timestep Size of 1 femtosecond and FEA RVE of equivalent dimensions (for relative comparison)

3.8.2 Tiered Model Costs

We just considered the cost of various gauss point constitutive models. Now we will consider the cost of constructing entire model simulations of various size at the macroscale, and tiering at the gauss point level. Table 3.6 summarizes such complete model assemblies with relative time cost and approximate compute time required in 2016 in order to get a true feeling for the orders of magnitude in time scaling.

Costs for Hierarchical Schemes (Linear Elements)

Top-Tier Model Size	Gauss Model Type	Relative Time Cost	2016 Time¹³ (Per Step)
3k DOF	Conventional	1	0.01s
-	Masing (100 layers)	100	1s
-	3K DOF Meso RVE	100×10^3	.278 hours
-	300k DOF Meso RVE	64.8×10^6	7.5 days
-	MD (Meso)	10^{28}	32 Billion Gya
-	3K DOF RVE (Meso) + 3k RVE (Nano)	10.0×10^9	3.17 years
-	300K DOF RVE (Meso) + 300k RVE (Nano)	4.20×10^{15}	1.33 Mya
-	3K DOF RVE (Meso) + MD (Nano)	124×10^{15}	39 Mya
-	300K DOF RVE (Meso) + MD (Nano)	80.3×10^{18}	25 Gya
30k DOF	Conventional	11.9	.119s
-	Masing	1.19×10^3	11.9s
-	3K DOF Meso RVE	11.9×10^6	3.31 hours
-	300k DOF Meso RVE	772×10^6	.245 years

¹³ Using High-End Personal Computer with GPU Processing. For CPU computation, add an order of magnitude. For supercomputing, remove one to three orders of magnitude.

-	MD (Meso)	10^{29}	320 Billion Gya
-	3K DOF RVE (Meso) + 3k RVE (Nano)	119×10^9	37.7 years
-	300K DOF RVE (Meso) + 300k RVE (Nano)	50.0×10^{15}	15,800 years
-	3K DOF RVE (Meso) + MD (Nano)	148×10^{16}	464 Mya
-	300K DOF RVE (Meso) + MD (Nano)	956×10^{18}	298 Gya
300k DOF	Conventional	128	1.28s
-	Masing	12.8×10^3	2.13 min
-	3K DOF Meso RVE	12.8×10^6	35.5 hours
-	300k DOF Meso RVE	8.29×10^9	2.63 years
-	MD (Meso)	10^{30}	4 Trillion Gya
-	3k DOF RVE (Meso) + 3k RVE (Nano)	1.13×10^{12}	406 years
-	300K DOF RVE (Meso) + 300k RVE (Nano)	537×10^{15}	170,000 years
-	3K DOF RVE (Meso) + MD (Nano)	158×10^{17}	5 Gya
-	300K DOF RVE (Meso) + MD (Nano)	103×10^{20}	3200 Gya

Table 3.6 – Cost projections for various model cell sizes of various tiering. Green cells indicate one tier, yellow cells indicate two tiers, and red cells indicate three tiers.

3.8.3 Computational Feasibility

The last section made some very startling realizations regarding the inadequacy of current compute power in tackling most RVE based problems. However, if one were to consider the projections of computer power versus time, it is readily apparent that these types of models will become feasible in the near future. Figure 3.100 below depicts how our tiered models would perform on the world’s fastest supercomputers dated from 1993 to 2013. From the trend, it is not unreasonable to extrapolate that multi-tiered modeling could become very prevalent in as little as a decade. In fact, any model that does not use Molecular Dynamics could be feasible within the next 25 years.

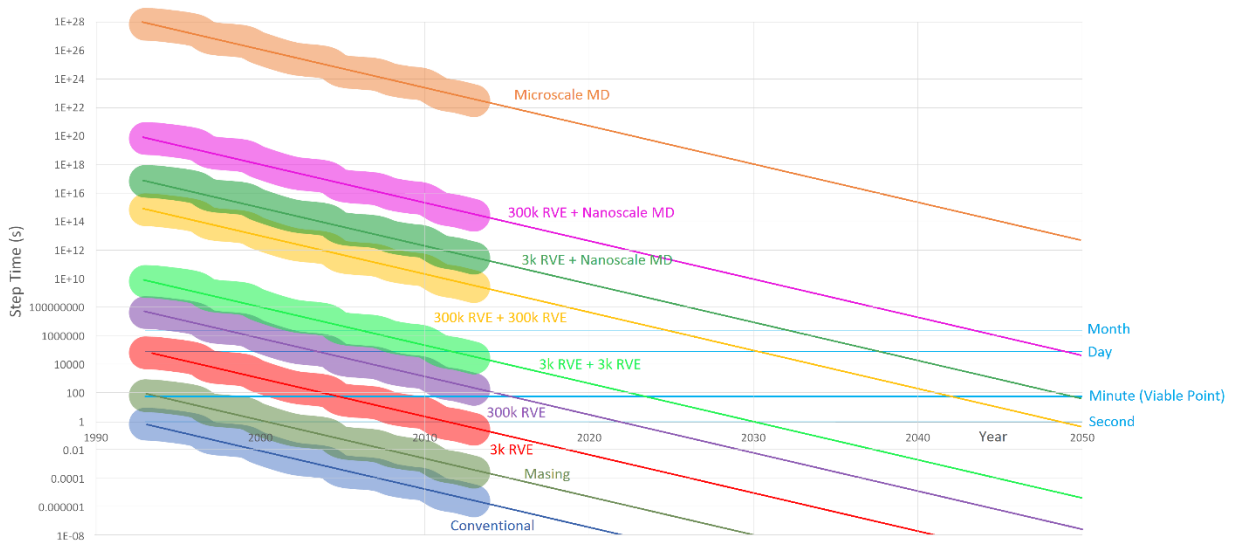
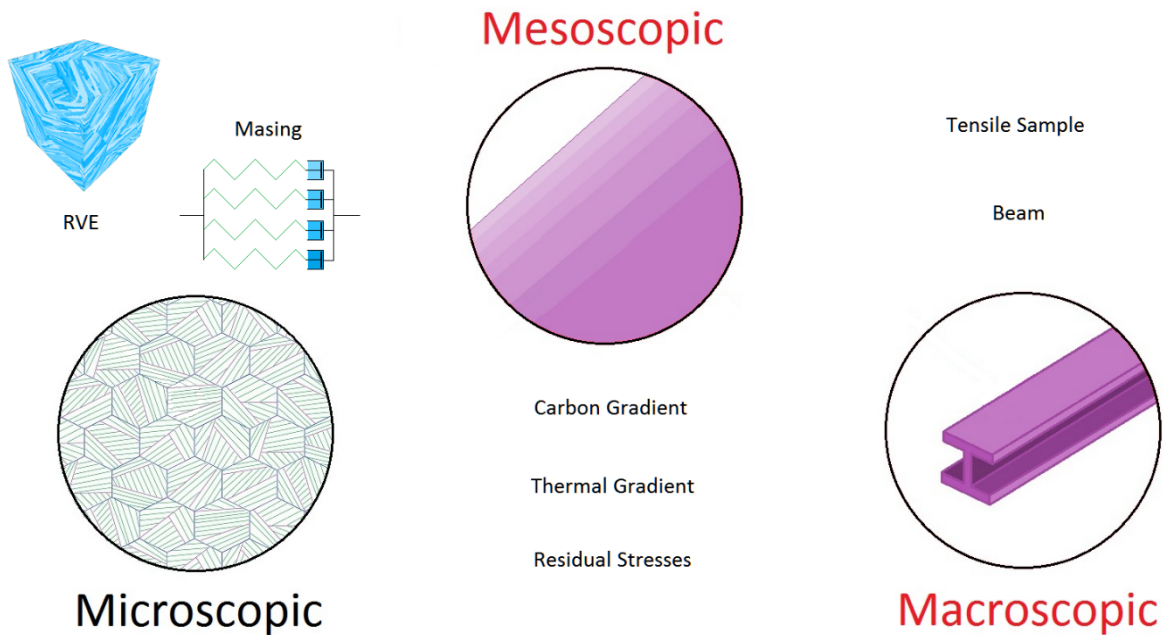


Figure 3.100 - Evaluation of models summarized in Table 3.6 with predicted performance on the worlds top supercomputers from 1993 to 2013; assuming linear scaling of performance. Future extrapolations are shown depicting viability of model types in the future.



Chapter 4 – Multi-Scale Coupled Simulations

The work presented up till now has given us a lot of insight into the various modelling considerations that exist when working with compositionally graded martensite. In Chapter 2, we looked at features that exist on the largest scale of the material that are also explainable with general macroscopic material descriptions. In particular, we know that the phenomena of carbon diffusion and quench-induced residual stresses are things that can be modelled by considering the material to be a simple homogenous continuum; describable with macroscopic empirical data for mass diffusion, thermal conductivity, and heat capacity. Additionally, the mechanical behaviour is modelled in this context in the same manner due to the small plastic strains during quenching. In Chapter 3, we saw that we need a mechanical model for events that are occurring at the microstructure if we are to extend a mechanical description to moderate plastic strains. Models based upon a Masing description are the first true attempts to model the meso scale with parameters that track events at the micro scale. In this model we saw that the microscale is a collection of elements with different strengths that are being pulled in parallel; the macroscopic stress/strain behaviour is the result of differential yielding of the elements combined with the residual stresses that evolve between them. Of course we then took our description a step further by modelling the microstructure with a representative volume element of block-like elements.

In this chapter, we combine everything we have done and consider the behaviour of compositionally graded macroscopic materials that are subjected to moderate strains. It is here where we see the true power of this multiscale modelling technique and its potential for understanding complex materials such as martensite.

4.1 Constitutive Scaling

Our compositionally graded martensite features a spatially varying carbon content. Since the mechanical properties of martensite vary very strongly with carbon content, it is necessary for us to scale our meso-micro constitutive model to different carbon contents (Recall that we fit our model to a 0.24wt.%C Usibor). This could potentially be a very difficult task depending on how increased carbon truly affects the microstructure, however, there are certain hypotheses we can test in our microscopic model.

4.1.1 Homologous Scaling of the Stress/Strain curve

A large amount of literature data exists for the monotonic behaviour of martensite. In particular, we have access to tensile data for the 43xx series of steel. A good first question to look at when examining this data is “Are the stress strain curves geometrically similar?”. Specifically, we are asking if the stress/strain curve for one can be obtained from a simple axis rescaling of the other. To examine this, we have performed a homologous scaling of the Usibor 0.24wt.% steel to the Yield Strength (0.2% offset) and UTS of 4320, 4330, 4340 and 4350. This data is presented in Figure 4.101 below.

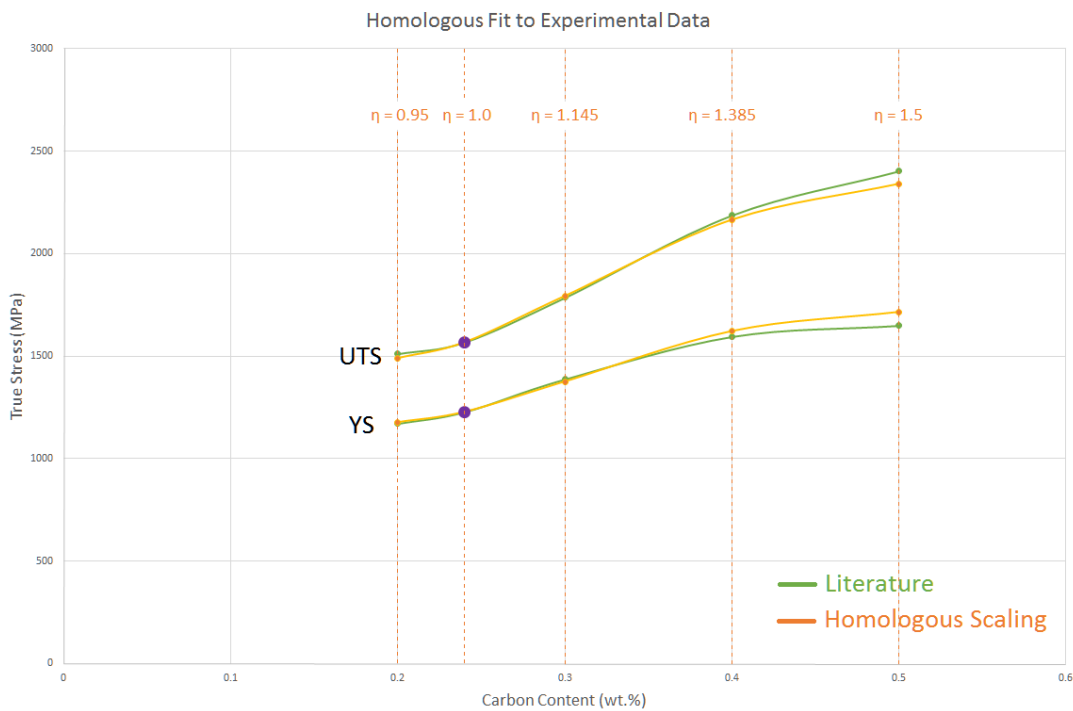


Figure 4.101 – A comparison of the Yield Strengths and Ultimate Tensile Strengths of literature 43xx series steel compared to those obtained from homologous scaling of the stress/strain curve of Usibor 0.24wt.%. The scaling parameter is shown in orange.

The data in this figure is quite remarkable. In fact, it tells us that the stress strain curves are in fact quite geometrically similar; especially below, 0.4wt.% Carbon. What is even more remarkable is that the Usibor is geometrically similar to the 43xx steels despite small differences in alloying. This bodes well for us, as it implies we can simply rescale our constitutive model and still have excellent material agreement. Figure 4.102 depicts the rescaled curves on the next page.

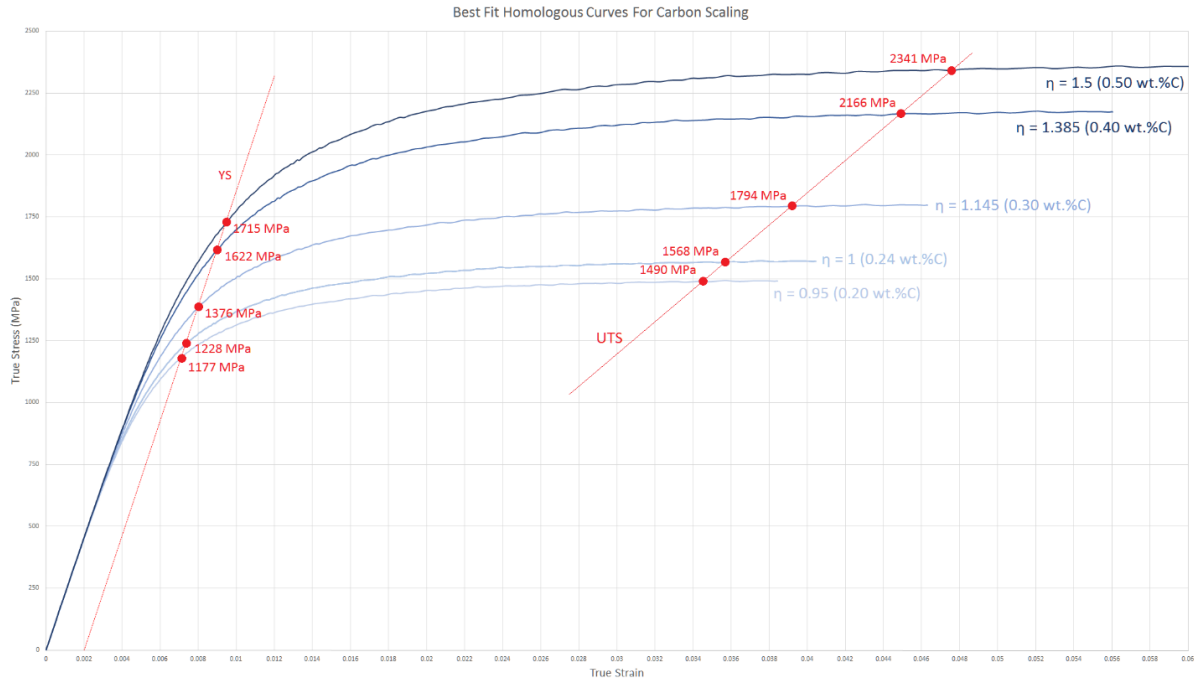


Figure 4.102 – Homologous Stress/Strain curves to Usibor 0.24wt.% C. The scaling of Yield Stress and Ultimate Tensile Stress are shown for different homology factors (η), appropriate to various carbon contents.

The variation in homology parameter as a function of carbon content is shown below in Figure 4.103. It is noted that the scaling relationship is very linear.

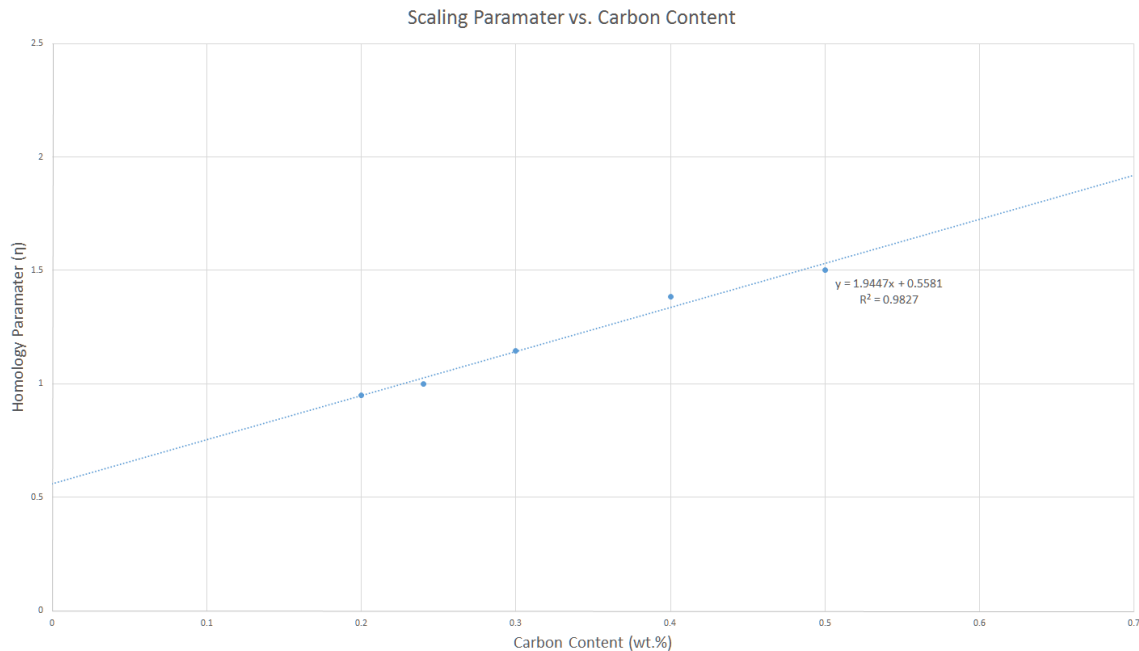


Figure 4.103 – Scaling parameter as a function of carbon content with linear trend depicted

The linear relationship depicted in Figure 4.103 is given by Equation 4.58. It depicts the scaling from the reference of 0.24wt.% Carbon to any other Carbon content.

$${}_{0.24}\eta(C) = 1.9447 * C + 0.5581 \quad \text{Eq. 4.58}$$

4.1.2 Homologous Scaling of the Constitutive Model

We have seen how the stress/strain curve for various martensite grades scales geometrically. We must now apply this scaling to the constitutive model that is used to generate these curves in the first place. In this chapter, we will use a Masing model to govern our constitutive relation due to its good behaviour in multiaxial loading and cost. The RVE model does perform slightly better, however the cost would be absolutely prohibitive in the context of a full simulation at the present time.

Recall that a Masing model consists of a microscopic arrangement of elements being deformed in parallel; each with different strengths. In order to scale the model, we must scale the distribution of element strengths. Figure 4.104 shows this scaling applied to an example log-normal distribution. Notice how the elements shift and stretch in the stress space.

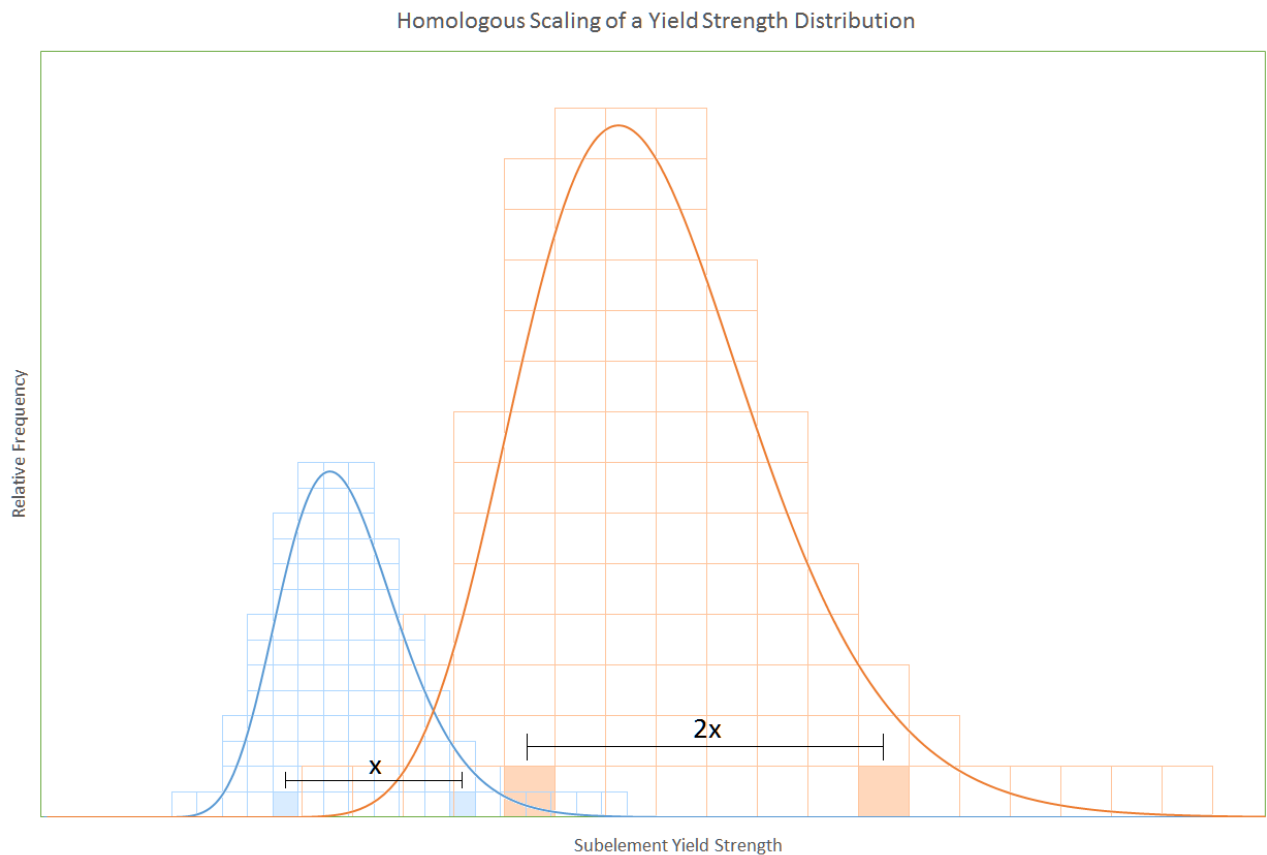


Figure 4.104 – Homologous scaling of a Masing distribution of element strengths. This example shows the scaling of a log-normal distribution by a factor of 2. Note how this effectively shifts and stretches the distribution.

4.2 Case Studies

It is here where we are now able to perform complete simulations of diffusion, quenching, and loading of various compositionally graded martensitic structures. In this section we will examine four case studies. Two of these case studies are concerning beams with different carbon distributions that are loaded in 3-point bending. The remaining two case studies concern a plate and a square rod that are decarburized and loaded through a Bauschinger test.

4.2.1 Bending Test of an Asymmetrically Graded Beam

Our first fully coupled simulations involve asymmetrically carburized beams. We treat the beams through the diffusion, quenching and processing stages with the respective applicable models active. For these experiments, we oil quench during the quench phase and apply a 20-layer Masing model with appropriate constitutive scaling during the loading phase. The Total Lagrange Formulation is used for these experiments due to rotations. The summaries of both simulations are depicted in Figures 4.105 and 4.106. The first features a beam that is decarburized at the top and carburized at the bottom. It is interesting that after quenching and before loading, the macroscopic residual stress state is effectively a wave; this governs the further beam bending performance. The second simulation features a beam that is decarburized on one side only. The residual stress state for this carbon profile is a skewed well shape.

Both beams evolve differently during loading as a result of these carbon profiles and residual stress states. As we have been positing all along, the potential for structure optimization is enormous with mechanical behaviour traversing a wide possibility space. This will be emphasized further in the next section where we perform Bauschinger test simulations of different plate structures.

4.2.2 Bauschinger Testing of a Decarburized Plate

In this section we perform Bauschinger tests of both a decarburized plate that has been symmetrically decarburized on both sides, and a decarburized rod that has been decarburized and quenched on all four sides. Like the previous tests, a 20-layer Masing constitutive model is used for the loading phase. These experiments are summarized in Figures 4.107 and 4.108 respectively. The evolution of macroscopic internal stresses is plotted as a function of progress of the Bauschinger test so that insight into the governing mechanisms is visible. It is interesting in both tests that unloading after the first load phase results in an inversion of the stress state. Such mechanical deformations may be useful in the future for further engineering of the internal stress state. For example, a beam may be preloaded in tension before being shipped to obtain a more favorable stress state in bending behaviour. Indeed, the possibilities are endless and there exists a large potential for products that are tweaked to very high performance specifications.

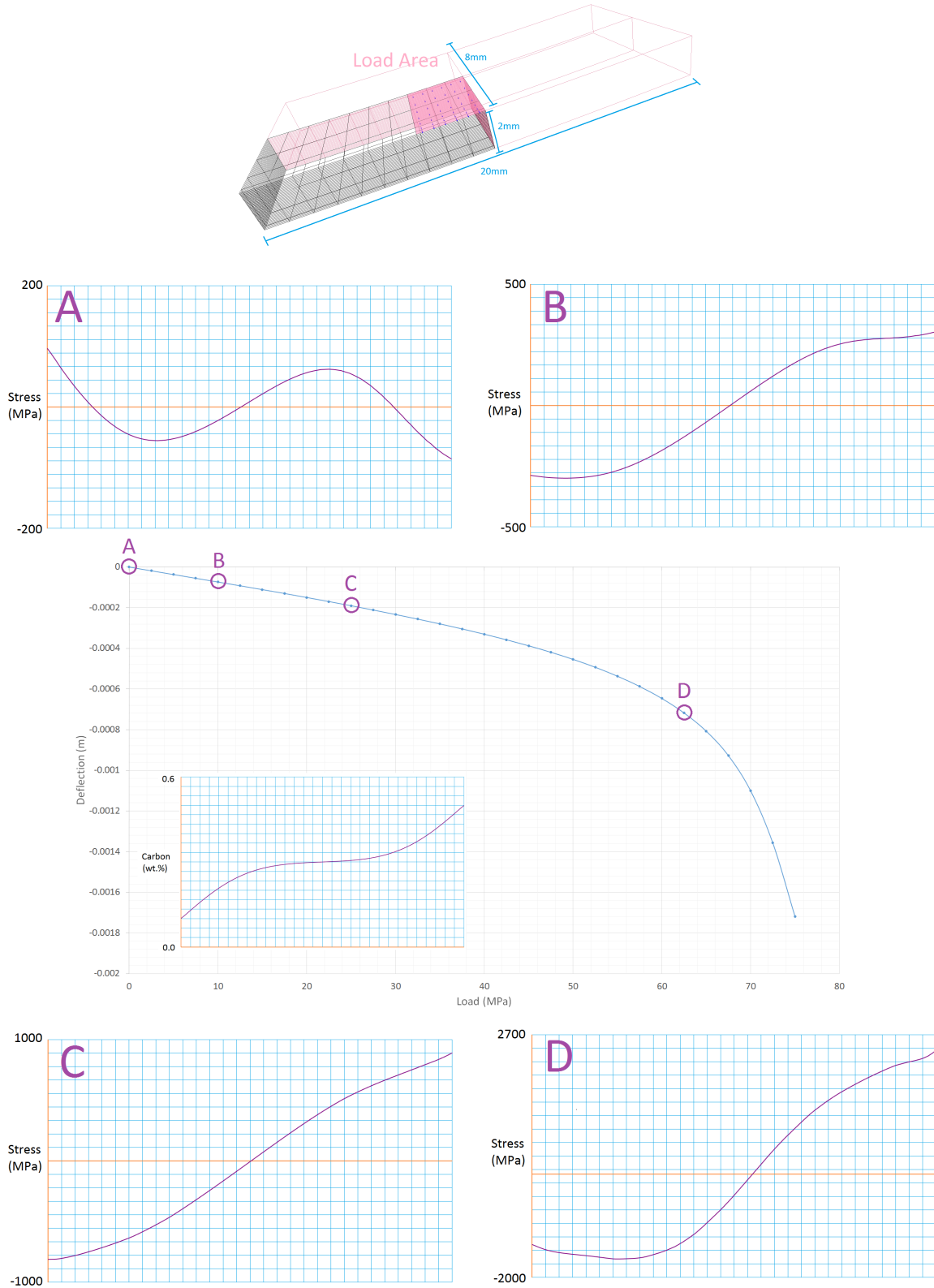


Figure 4.105 – Force/Deflection plot of an asymmetrically carburized beam and associated cross-sectional stress states (axial). A 20-layer Masing constitutive model is used at each integration point. (A) As-quenched stress state before any loading. (B)(C)(D) Axial stresses as an increasing center load is applied.

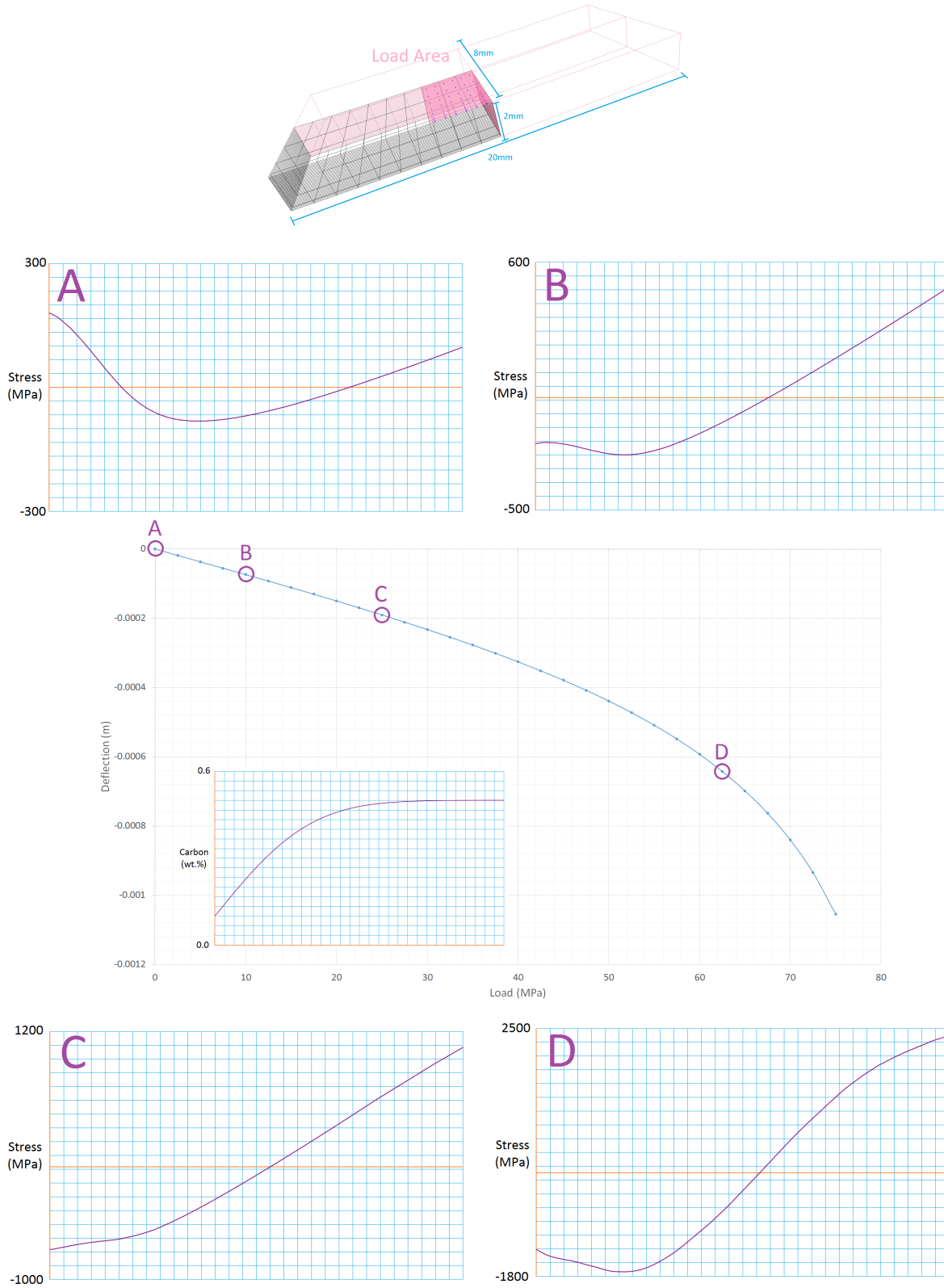


Figure 4.106 – Force/Deflection plot of an asymmetrically decarburized beam and associated cross-sectional stress states (axial). A 20-layer Masing constitutive model is used at each integration point. (A) As-quenched stress state before any loading. (B)(C)(D) Axial stresses as an increasing center load is applied.

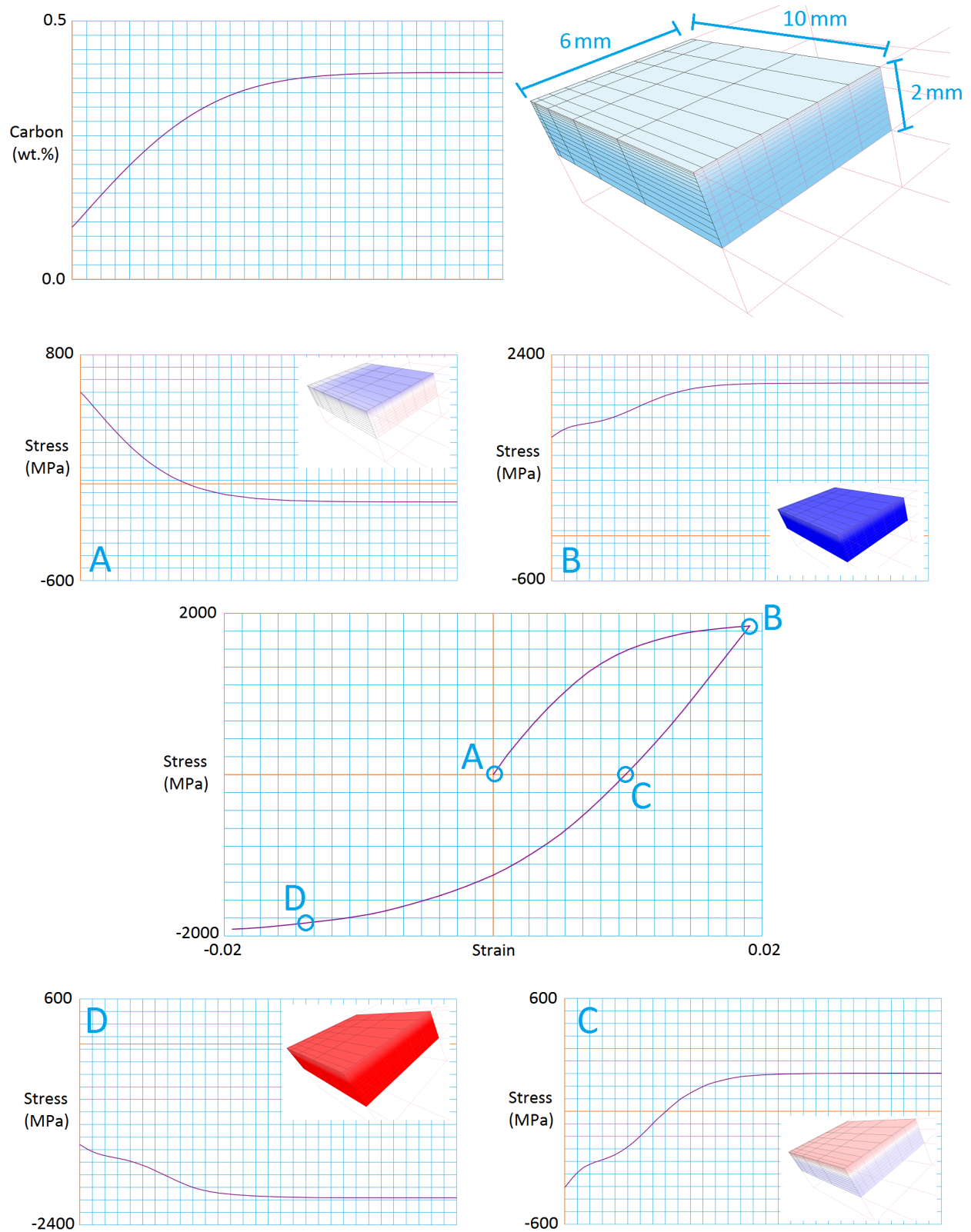


Figure 4.107 – Bauschinger test of a decarburized plate that is decarburized/quenched from two sides (symmetric about thickness). A 20-layer Masing constitutive model is used at each integration point. (A) As-quenched in-plane stress state depicted through half-thickness. (B)(C)(D) Depiction of axial stresses as the plate is loaded axially through a Bauschinger test.

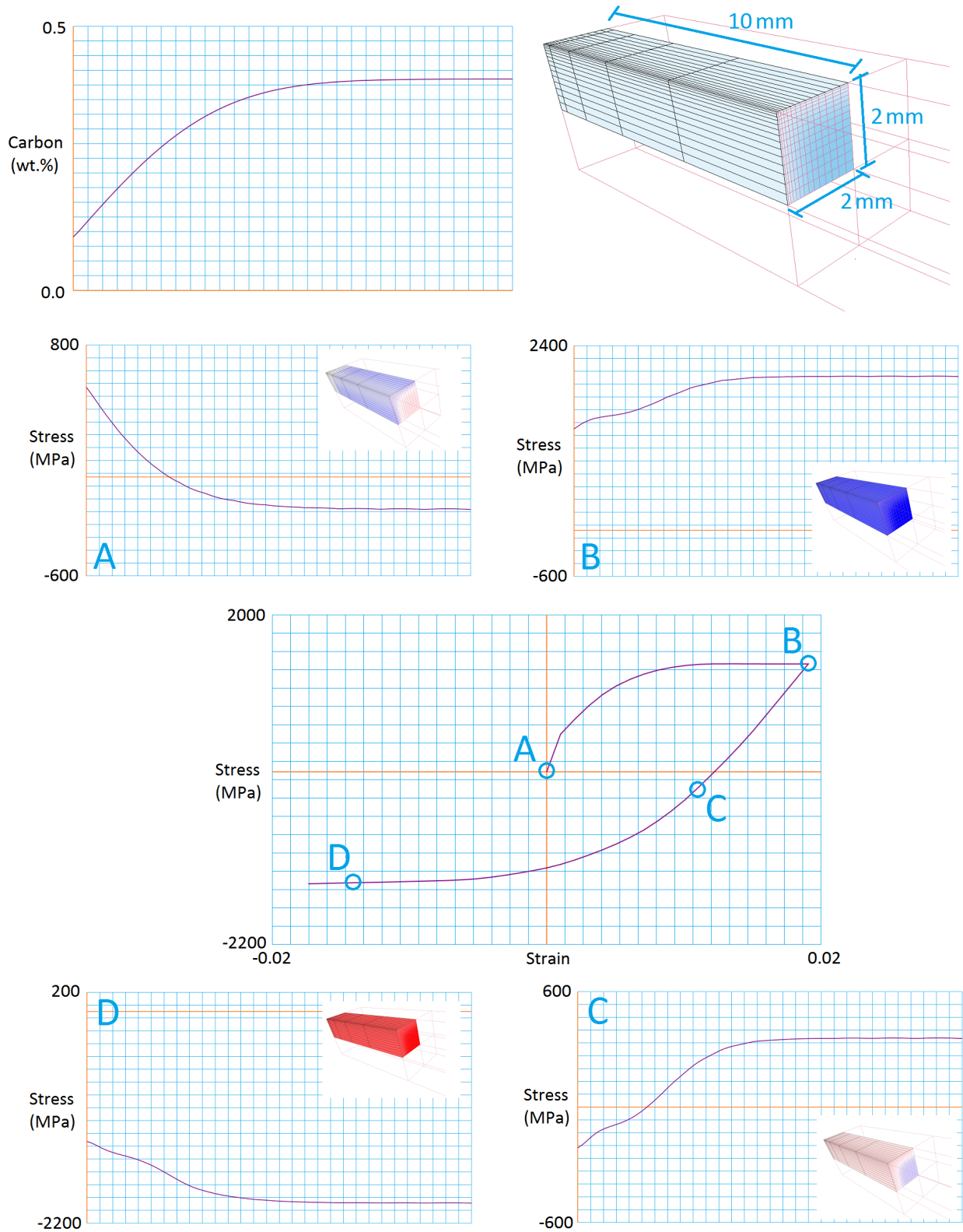


Figure 4.108 – Bauschinger test of a decarburized square rod that is decarburized/quenched from four sides. A 20-layer Masing constitutive model is used at each integration point. (A) As-quenched axial stress state depicted through half-thickness. (B)(C)(D) Depiction of axial stresses as the rod is loaded axially through a Bauschinger test.

4.2.3 Examination of Presented Case Studies

The case studies of compositionally graded martensitic structures that we have just presented are indicative of the complexity of working with such materials. In the case of a loaded beam (Figures 4.105 and 4.106), we see that despite the beams being of the same geometry, their as-quenched stresses and general loading behaviour are very different due to the carbon composition profile. What is interesting is that although the stresses evolve differently during loading, they end up in a configuration that is very similar. That is to say, the effect of the internal stresses becomes washed out as the object plastifies. The largest difference between the two cases occurs for intermediate loads. We see the beam depicted in Figure 4.105 initially has high resistance to bending, but then fails rapidly as load is increased beyond a specific point; whereas the beam in Figure 4.106 has a very gradual failure behaviour.

In the case studies of the two-sided decarburized plate and four-sided decarburized rod (Figures 4.107 and 4.108), we see that the presence of internal stresses augments the gradual yielding seen in the material. That is to say, we see additional effects on gradual yielding that are not just from the Masing constitutive model at each individual integration point, but also from the overlaid quench induced stress state. The surface of the material is under considerable tension and since it is much softer than the core, yielding begins very earlier, causing a very rounded stress/strain curve. As in the case of the beam example, the stress evolution during Bauschinger loading is unique to the sample owing to the combination of internal stresses and material strength differences throughout the geometry.

4.3 Closing Remarks

The work presented in this thesis was done with the express aim of convincing the reader that there is indeed much that can be done to optimize materials further than what is currently available. The ability to mesoscopically grade the composition of martensitic steels leads to some very exciting and intriguing possibilities regarding mechanical performance.

We saw that the intrinsically tiered scaling of features in a compositionally graded martensite requires some more advanced modeling techniques than those that are conventionally used for metals. Specifically, the modeling needed to match the tiering of the material. While conventional models were acceptable for the quenching process simulation due to the small strains, they were seen to be inadequate for room temperature plastic straining of the material. In this regard, we investigated models that were designed to represent the microstructural scale of the material. Of these models, a Masing model was seen to very effective and computationally inexpensive. More complex models based upon representative volume elements were seen to provide slightly better material descriptions with the price of an extremely inflated computational overhead. Nonetheless, a detailed analysis of the costs associated with these models shows that their implementation will become feasible in the coming decades.

On the point of computational resources, we were able to model each step of the material processing and loading procedure satisfactorily with the computer resources of the current day. As such, we were able to virtually prototype parts and make predictions regarding their mechanical behaviour. If an engineer wanted to optimize a part for a specific loading scenario, they would be able to experiment numerically before real life testing. However, at this point in time, an engineer's intuition is still required to anticipate which modifications to the processing parameters may improve the properties. In the future, with more compute power available, it may be possible for a computer to permute through many different processing properties and obtain an optimum procedure and structure for a given goal. Such machines would permute possibilities in the diffusion stage, quench stage, and even in a preloading stage, as was proposed in the last section, using global optimization techniques that we discussed in this thesis.

With these regards in mind, I leave you with a quote from Klaus-Jürgen Bathe, one of the fathers of the modern finite element method. "Progress in design of new structures seems to be unlimited". The future of material structures is indeed very magnificent and we should expect that structures will exploit the ideas discussed in this thesis to bring engineered constructs to the next generation.

References

- Abrassart, J. B. 1972. "Influence Des Transformation Martensitic Sur Les Proprietes Mechaniques Des Alliages Du System Fe-Ni-Cr-C." Universite de Nancy.
- Allain, Sebastien, Olivier Bouaziz, and Manabu Takahashi. 2012. "Toward a New Interpretation of the Mechanical Behaviour of As-Quenched Low Alloyed Martensitic Steels." *ISIJ International* 52(4):717–22.
- Anderoglu, Osman. 2004. "Residual Stress Measurement Using X-Ray Diffraction." Texas A&M University.
- Badinier, G. et al. 2015. "Microstructural Heterogeneity and Its Relationship to the Strength of Martensite." *Materials Science and Engineering: A* 638:329–39.
- Badinier, Guillaume. 2013. "Effect of Carbon Segregation and Carbide Precipitation on the Mechanical Response of Martensite." University of British Columbia.
- Barlat, F. 2007. "Constitutive Modeling for Metals." in *Advanced Methods in Material Forming*, edited by D. Banabic.
- Bathe, KJ. 1986. "Finite Element Procedures for Solids and Structures - Nonlinear Analysis." *MIT Video Course*.
- Bathe, Klaus-Jurgen. 2006. *Finite Element Procedures*. Prentice Hall.
- Besseling, J. F. 1958. "A Theory of Elastic, Plastic and Creep Deformations of an Initially Isotropic Material Showing Anisotropic Strain Hardening, Creep Recovery and Secondary Creep." *Journal of Applied Mechanics* 25(4):529–36.
- Bhadeshia, H. K. D. H. 1981. "Diffusion of Carbon in Austenite." *Metal Science* 15(April):477–79.
- De Borst, Rene., Mike. A. Crisfield, Joris J. C. Remmers, and Clemens V. Verhoosel. 2012. *Non-Linear Finite Element Analysis of Solids and Structures*. John Wiley and Sons Ltd.
- Bouaziz, O. and P. Buessler. 2004. "Iso-Work Increment Assumption for Heterogeneous Material Behaviour Modelling." *Advanced Engineering Materials* 6(12):79–83.
- Bruker. 2009. "Residual Stresses." in *Diffraction Leptos 7 - User Manual*.
- Capdevila, C., F. G. Caballero, and C. García De Andrés. 2003. "Analysis of Effect of Alloying Elements on Martensite Start Temperature of Steels." *Materials Science and Technology* 19(5):581–86.
- Chun, B. K., H. Y. Kim, and J. K. Lee. 2002. "Modeling the Bauschinger Effect for Sheet Metals, Part II: Applications." *International Journal of Plasticity* 18(5-6):597–616.

- Cicoria, Robert, Bechir Chehab, and Hatem Zurob. 2013. "Diffusion as a Method for Producing Architected Materials." *Scripta Materialia* 68(1):17–21.
- Deng, Xiaohu and Dongying Ju. 2013. "Modeling and Simulation of Quenching and Tempering Process in Steels." *Physics Procedia* 50:368–74.
- E. Gautier, J. S. Zhang and X. M. Zhang. 1995. "Martensitic Transformation under Stress in Ferrous Alloys. Mechanical Behaviour and Resulting Morphologies." *Journal de Physique IV* 5(C8):41–50.
- Fischer, F. D. et al. 2000. "A New View on Transformation Induced Plasticity." *International Journal of Plasticity* 16:723–48.
- Fischer, F. D., E. R. Oberaigner, K. Tanaka, and F. Nishimura. 1998. "Transformation Induced Plasticity Revised An Updated Formulation." *International Journal of Solids and Structures* 35(18):2209–27.
- Fischer, F. D., Q. P. Sun, and K. Tanaka. 1996. "Transformation-Induced Plasticity (TRIP)*." *Appl. Mech. Rev.* 49(6):317–64.
- Fisher, F. D. 1997. *Modelling and Simulation of Transformation Induced Plasticity in Elasto-Plastic Materials*. edited by M. Berveiller and F. D. Fischer. Springer-Verlag Wien.
- Fitzpatrick, Me et al. 2005. "Determination of Residual Stresses by X-Ray Diffraction - Issue 2." *Measurement Good Practice Guide* 52(2):74.
- Ganghoffer, J. F. et al. 1991. "Micromechanical Simulation of a Martensitic Transformation By Finite Elements." *Journal de Physique IV* 1:77–82.
- Ganguly, S., S. Datta, P. P. Chattopadhyay, and N. Chakraborti. 2009. "Designing the Multiphase Microstructure of Steel for Optimal TRIP Effect: A Multiobjective Genetic Algorithm Based Approach." *Materials and Manufacturing Processes* 24(1):31–37.
- Gitman, I. M., H. Askes, and L. J. Sluys. 2008. "Coupled-Volume Multi-Scale Modelling of Quasi-Brittle Material." *European Journal of Mechanics, A/Solids* 27(3):302–27.
- Goldberg, David E. and Chie Hsiung Kuo. 1987. "Genetic Algorithms in Pipeline Optimization." *Journal of Computing in Civil Engineering* 1(2):128–41.
- Greenwood, J. W. and R. H. Johnson. 1964. "The Deformation of Metals under Small Stresses under Phase Transformations." *Proceedings of the Royal society of London. Series A, Mathematical and Physical Sciences* 283:403–22.
- Hachisu, T., T. Sakai, and K. Taguchi. 1981. "Transient Temperature Distribution in Circular Cylinders during Quenching." *Heat Transfer - Jpn. Res.* 10(1):52–64.
- Hauk, Viktor. 1997. *Structural and Residual Stress Analysis by Nondestructive Methods*. Elsevier.

- Hill, R. 1984. "On Macroscopic Effects of Heterogeneity in Elastoplastic Media at Finite Strain." *Mathematical Proceedings of the Cambridge Philosophical Society* 95(3):481–94.
- International Nickel Inc. n.d. *Isothermal Transformation Diagrams of Nickel Alloy Steel*.
- Iwan, W. D. 1967. "On a Class of Models for the Yielding Behavior of Continuous and Composite Systems." *Journal of Applied Mechanics* 34(3):612–17.
- Kadau, K., P. Entel, T. C. Germann, P. S. Lomdahl, and B. L. Holian. 2001a. "Large-Scale Molecular-Dynamics Study of the Nucleation Process of Martensite in {F}e- $\{N\}$ i Alloys." *Journal de Physique {IV}* 11:17–22.
- Kadau, K., P. Entel, T. C. Germann, P. S. Lomdahl, and B. L. Holian. 2001b. "Large-Scale Molecular-Dynamics Study of the Nucleation Process of Martensite in Fe-Ni Alloys." *Journal de Physique IV* 11(8):17–22.
- Karabelchtchikova, Olga and Richard D. Sisson. 2006. "Carbon Diffusion in Steels: A Numerical Analysis Based on Direct Integration of the Flux." *Journal of Phase Equilibria & Diffusion* 27(6):598–604.
- Kitahara, Hiromoto, Rintaro Ueji, Nobuhiro Tsuji, and Yoritoshi Minamino. 2006. "Crystallographic Features of Lath Martensite in Low-Carbon Steel." *Acta Materialia* 54(5):1279–88.
- Koistinen, D. P. and R. E. Marburger. 1959. "A General Equation Prescribing the Extent of the Austenite-Martensite Transformation in Pure Iron-Carbon Alloys and Plain Carbon Steels." *Acta Metallurgica* 7(1):59–60.
- Kojić, Miloš and Klaus-Jürgen Bathe. 1987. "The 'effective Stress Function' Algorithm for Thermo-Elasto Plasticity and Creep." *International Journal for Numerical Methods in Engineering* 24(8):1509–32.
- Kolednik, O. 2000. "The Yield Stress Gradient Effect in Inhomogeneous Materials." *International Journal of Solids and Structures* 37(5):781–808.
- Kouznetsova, V., W. a M. Brekelmans, and F. P. T. Baaijens. 2001. "Approach to Micro-Macro Modeling of Heterogeneous Materials." *Computational Mechanics* 27(1):37–48.
- Krauss, George. 1999. "Martensite in Steel: Strength and Structure." *Materials Science and Engineering: A* 273-275:40–57.
- Krieg, R. D. 1975. "A Practical Two Surface Plasticity Theory." *Journal of Applied Mechanics* 42(3):641–46.
- Leblond, J. B., J. Devaux, and J. C. Devaux. 1989. "Mathematical Modelling of Transformation Plasticity in Steels I : Case of Ideal - Plastic Phases." *International journal of Plasticity* 5:551–72.
- Lee, Seok Jae and Young Kook Lee. 2008. "Finite Element Simulation of Quench Distortion in a Low-Alloy Steel Incorporating Transformation Kinetics." *Acta Materialia* 56(7):1482–90.

- Lee, Seok-Jae and Young-Kook Lee. 2009. "Latent Heat of Martensitic Transformation in a Medium-Carbon Low-Alloy Steel." *Scripta Materialia* 60(11):1016–19.
- Lemaitre, J. and J.L. Chaboche. 1990. *Mechanics of Solid Materials*. University of Cambridge.
- Magee, C. L. 1966. "Transformation Kinetics, Microplasticity, and Aging of Martensite in Fe-31Ni." Carnegie Institute of Technology.
- Marketz, F. and F. D. Fischer. 1999. "Micromechanical Modelling of Stress-Assisted Martensitic Transformation." *Modelling and Simulation in Materials Science and Engineering* 2(5):1017–46.
- Masing, G. 1923. "Zur Heyn'schen Theorie Der Verfestigung Der Metalle Durch Verbor- Gen Elastische Spannungen." *Wissenschaftliche Veröffentlichungen aus dem Siemens- Konzern* 3(1):231–39.
- Masing, G. 1926. "Eigenspannungen Und Verfestigung Beim Messing." *Proceedings of the Second International Congress of Applied Mechanics*, 332–35.
- Miehe, Christian, Jan Schotte, and Jörg Schröder. 1999. "Computational Micro–macro Transitions and Overall Moduli in the Analysis of Polycrystals at Large Strains." *Computational Materials Science* 16(1-4):372–82.
- Montans, Francisco J. and Ronaldo I. Borja. 2002. "Implicit J2-Bounding Surface Plasticity Using Prager's Translation Rule." *International Journal for Numerical Methods in Engineering* 55(10):1129–66.
- Morris, John W., Chris Kinney, Ken Pytlewski, and Y. Adachi. 2013. "Microstructure and Cleavage in Lath Martensitic Steels." *Science and Technology of Advanced Materials* 14:014208.
- Morsdorf, L., C. C. Tasan, D. Ponge, and D. Raabe. 2015. "3D Structural and Atomic-Scale Analysis of Lath Martensite: Effect of the Transformation Sequence." *Acta Materialia* 95:366–77.
- Mróz, Z. 1967. "On the Description of Anisotropic Workhardening." *Journal of the Mechanics and Physics of Solids* 15(3):163–75.
- Nikishkov, Gennadiy. 2010. *Finite Element Equations for Heat Transfer*.
- Pan, J. 2002. "Factors Affecting Final Part Shaping." Pp. 159–82 in *Handbook of Residual Stress and Deformation of Steel*, edited by G. Totten, M. Howes, and T. Inoue.
- Parris, D. C. and R. B. McLellan. 1976. "The Diffusivity of Carbon in Austenite." *Acta Metallurgica* 24:523–28.
- Passarella, Diego N., Adriana Aparicio, Fernando Varas, and Elena B. Ortega. 2014. "Heat Transfer Coefficient Determination of Quenching Process." *Mecanica Computacional XXXIII*:2009–21.
- Patel, J. R. and M. Cohen. 1953. "Criterion for the Action of Applied Stresses in the Martensitic Transformation." *Acta Metallurgica* 1(5):531–38.

- Prager, W. 1955. "The Theory of Plasticity: A Survey of Recent Achievements." *Proceedings of The Institution of Mechanical Engineering* 169(1):41–57.
- Prawoto, Y., N. Jasmawati, and K. Sumeru. 2012. "Effect of Prior Austenite Grain Size on the Morphology and Mechanical Properties of Martensite in Medium Carbon Steel." *Journal of Materials Science & Technology* 28(5):461–66.
- Price, R. F. and A. J. Fletcher. 1980. "Determination of Surface Heat Transfer Coefficients during Quenching of Steel Plates." *Metals Technology* 7(1):203–11.
- Reti, T. 2002. "Residual Stresses in Carburized, Carbonitrided, and Case-Hardened Components." Pp. 189–208 in *Handbook of Residual Stress and Deformation of Steel*, edited by G. Totten, M. Howes, and T. Inoue.
- Roumina, R., J. D. Embury, O. Bouaziz, and H. S. Zurob. 2013. "Mechanical Behavior of a Compositionally Graded 300M Steel." *Materials Science and Engineering A* 578:140–49.
- Ruud, C. 2002. "Measurement of Residual Stresses." Pp. 99–117 in *Handbook of Residual Stress and Deformation of Steel*, edited by G. Totten, M. Howes, and T. Inoue.
- Sherby, Oleg D., Jeffrey Wadsworth, Donald R. Lesuer, and Chol K. Syn. 2008. "Revisiting the Structure of Martensite in Iron-Carbon Steels." *Materials Transactions* 49(9):2016–27.
- Simsir, Canaer. 2008. "3D Finite Element Simulation of Steel Quenching in Order to Determine the Microstructure and Residual Stresses." Middle East Technical University.
- Şimşir, Caner and C. Hakan Gür. 2010. "A Simulation of the Quenching Process for Predicting Temperature, Microstructure and Residual Stresses." *Strojniski Vestnik/Journal of Mechanical Engineering* 56(2):93–103.
- Sivanandam, S. N. and S. N. Deepa. 2008. *Introduction to Genetic Algorithms*. Springer.
- Smit, R. J. M., W. a. M. Brekelmans, and H. E. H. Meijer. 1998. "Prediction of the Mechanical Behavior of Nonlinear Heterogeneous Systems by Multi-Level Finite Element Modeling." *Computer Methods in Applied Mechanics and Engineering* 155(97):181–92.
- Souza, Ester C. De, Luiz F. O. Friedel, George E. Totten, and Lauralice C. F. Canale. 2013. "Quenching and Heat Transfer Properties of Aged and Unaged Vegetable Oils." *Journal of Petroleum Science Research* 2(1):41–47.
- De Souza Neto, E. A., D. Peric, and D. R. J. Owen. 2008. *Computational Methods For Plasticity Thoery and Applications*. John Wiley and Sons Ltd.
- Stuwe, H. P. 1997. "Interaction of Stresses and Strains with Phase Changes in Metals: Physical Aspects." in *Mechanics of Solids with Phase Changes*, edited by F. D. Fischer and M. Berveiller. Springer-Verlag Wien.

- Sussman, Theodore and Klaus-Jurgen Bathe. 1986. "Studies of Finite Element Procedures - Stress Band Plots and the Evaluation of Finite Element Meshes." *Engineering Computations* 3(3):178–91.
- Tseng, N. T. and G. C. Lee. 1983. "Simple Plasticity Model of Two Surface Type." *Journal of Engineering Mechanics* 109(3):795–810.
- Wolpert, David H. and William G. Macready. 1997. "No Free Lunch Theorems for Optimization." *IEEE Transactions on Evolutionary Computation* 1(1):67–82.
- Yamanaka, Akinori, Tomohiro Takaki, and Yoshihiro Tomita. 2010. "Elastoplastic Phase-Field Simulation of Martensitic Transformation with Plastic Deformation in Polycrystal." *International Journal of Mechanical Sciences* 52(2):245–50.
- Zhang, Jian Min, Yan Zhang, Ke Wei Xu, and Vincent Ji. 2008. "General Compliance Transformation Relation and Applications for Anisotropic Cubic Metals." *Materials Letters* 62(8-9):1328–32.
- Zhu, R. et al. 2006. "Atomistic Calculation of Elastic Moduli in Strained Silicon." *Semiconductor Science and Technology* 21:906–11.
- Ziegler, H. 1959. "A Modification of Pragers Hardening Rule." *Quarterly of Applied Mathematics* 17:55–65.

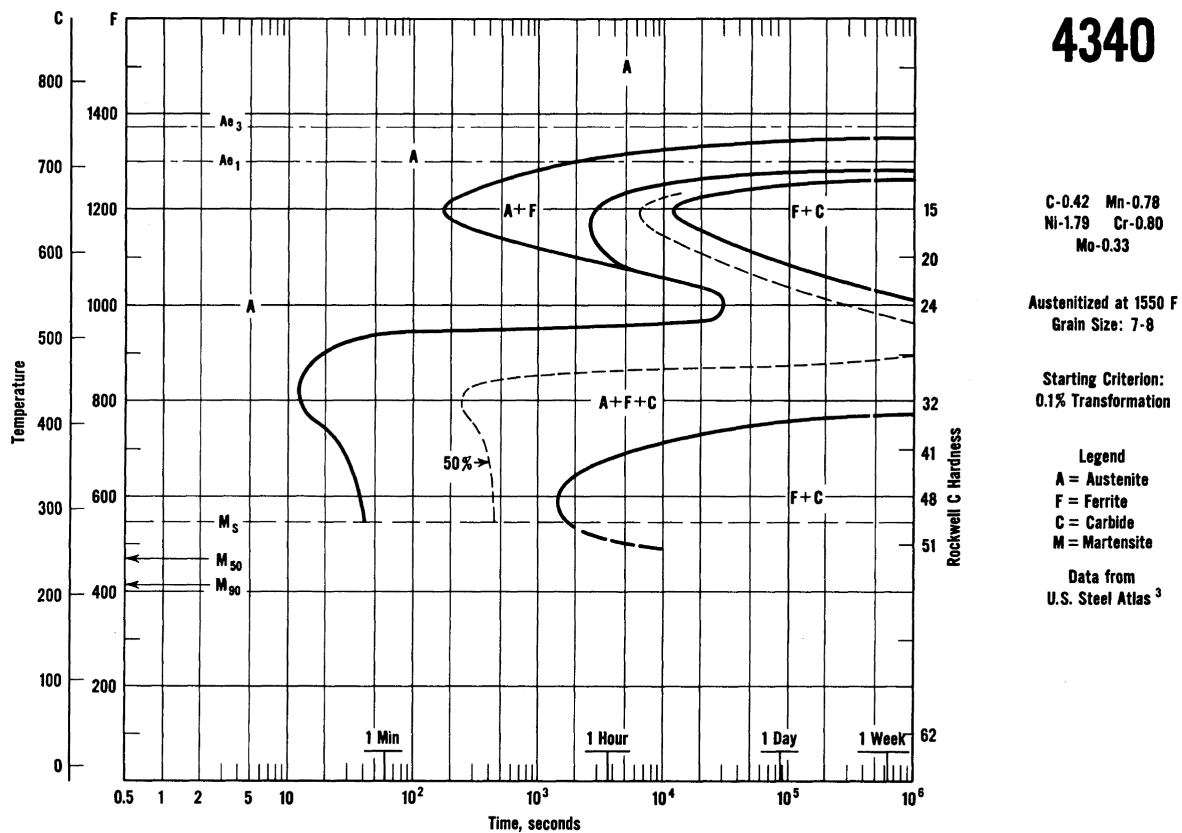
Appendix – Material Properties Reference

Composition of Relevant Steel Grades (wt.%)

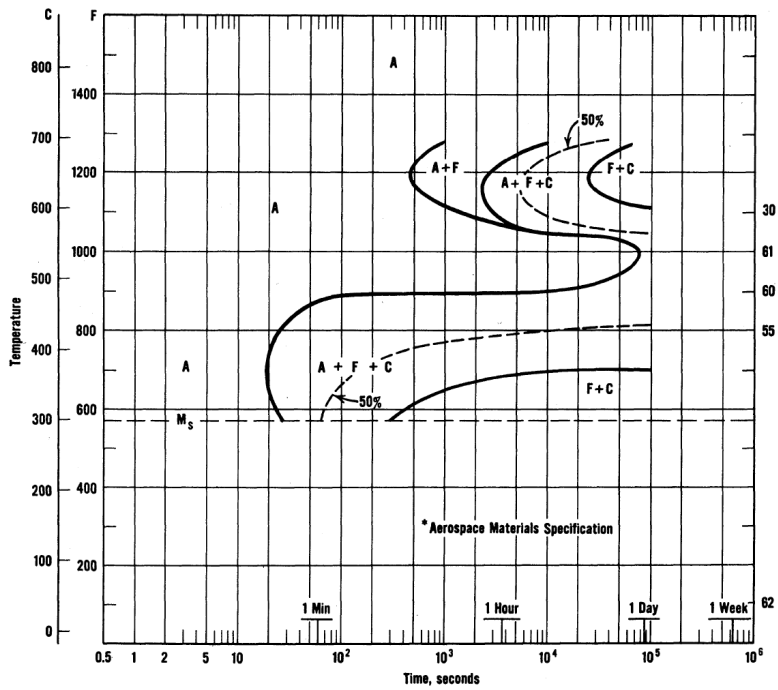
Grade	C	Si	Ni	Cr	V	Mo	Mn	Ti
Usibor 1500	0.24	0.65	0.02	0.19	--	--	1.13	0.03
300M	0.42	1.62	1.82	0.82	0.05	0.47	0.75	0.4
4340	0.42	0.22	1.79	0.80	--	0.33	0.78	--

Available Transformation Diagrams

TTT – 4340 (International Nickel Inc. n.d.)



TTT – 300M (International Nickel Inc. n.d.)



AMS* 6416
(300-M)

C-0.43 Mn-0.83
Si-1.55 Ni-1.84
Cr-0.91 Mo-0.40
V-0.12

Austenitized at 1575 F
Grain Size: 5-7

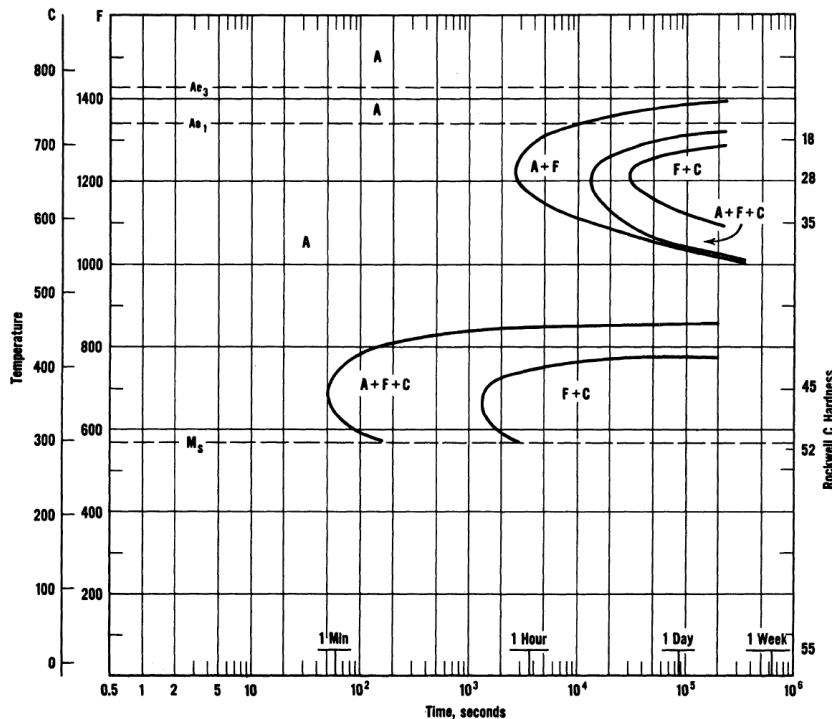
Starting Criterion:
0.5% Transformation

Legend
A = Austenite
F = Ferrite
C = Carbide
M = Martensite

Data from
Bethlehem Steel Co.

TTT – 4340 + Si + V (Effectively a Decarburized 300M)

(International Nickel Inc. n.d.)



4330
Modified
(Si+V)

C-0.34 Mn-0.98
Si-1.37 Ni-1.82
Cr-0.95 Mo-0.42
V-0.14

Austenitized at 1650 F
Grain Size: 4

Starting Criterion:
1% Transformation

Legend
A = Austenite
F = Ferrite
C = Carbide
M = Martensite

Data from
J. W. Forney, Frankford
Arsenal, Report R-1627,
April 1962

CCT – Usibor 1500 (Arcelor)

